TECHNICAL UNIVERSITY OF CRETE
SCHOOL OF PRODUCTION ENGINEERING & MANAGEMENT

Particle acceleration using a high intensity Laser facility and the role of gas dynamics

Επιτάχυνση σωματιδίων με τη χρήση διάταξης Laser υψηλής έντασης και ο ρόλος της αεριοδυναμικής

By

Georgia Andrianaki

A dissertation submitted in partial fulfilment of the
requirements for the degree of
Doctor of Philosophy (PhD)

Advisor: Dr. Ioannis K. Nikolos, Professor
Co-Advisors: Michael Tatarakis, Professor; Nektarios Papadogiannis, Professor

Chania, November, 2023

The implementation of the doctoral thesis was co-financed by Greece and the European Union (European Social Fund-ESF) through the Operational Programme «Human Resources Development, Education and Lifelong Learning» in the context of the Act “Enhancing Human Resources Research Potential by undertaking a Doctoral Research” Sub-action 2: IKY Scholarship Programme for PhD candidates in the Greek Universities.

Ευρωπαϊκή Ένωση
European Social Fund

Operational Programme
Human Resources Development, Education and Lifelong Learning
Co-financed by Greece and the European Union

ΕΣΠΑ
2014-2020
ανάπτυξη - εργασία - αλληλεγγύη

TECHNICAL UNIVERSITY OF CRETE
SCHOOL OF PRODUCTION ENGINEERING & MANAGEMENT

Particle acceleration using a high intensity Laser facility and the role of gas dynamics

Επιτάχυνση σωματιδίων με τη χρήση διάταξης Laser υψηλής έντασης και ο ρόλος της αεριοδυναμικής

By **Georgia Andrianaki**

Supervised and approved by:	**Approved by:**
Dr. Ioannis K. Nikolos Professor, Advisor Technical University of Crete School of Production Engineering & Management	**Dr. Anargyros I. Delis** Professor Technical University of Crete School of Production Engineering & Management
Dr. Michael Tatarakis Professor, Co-Advisor Hellenic Mediterranean University	**Dr. Georgios Arampatzis** Associate Professor Technical University of Crete School of Production Engineering & Management
Dr. Nektarios Papadogiannis Professor, Co-Advisor Hellenic Mediterranean University	**Dr. Georgios Karatzas** Professor Technical University of Crete School of Chemical & Environmental Engineering
	Dr. Vasilios Dimitriou Professor Hellenic Mediterranean University

ΕΠΤΑΜΕΛΗΣ ΕΞΕΤΑΣΤΙΚΗ ΕΠΙΤΡΟΠΗ

Τίτλος (ελληνικά/αγγλικά): Επιτάχυνση σωματιδίων με τη χρήση διάταξης Laser υψηλής έντασης και ο ρόλος της αεριοδυναμικής / Particle acceleration using a high intensity Laser facility and the role of gas dynamics.

ΔΙΔΑΚΤΟΡΙΚΗ ΔΙΑΤΡΙΒΗ

Γεωργία Ανδριανάκη

ΤΡΙΜΕΛΗΣ ΣΥΜΒΟΥΛΕΥΤΙΚΗ ΕΠΙΤΡΟΠΗ:

1. **Ιωάννης Κ. Νκολός, Καθηγητής, Σχολή ΜΠΔ, Πολυτεχνείο Κρήτης.**
2. **Μιχαήλ Ταταράκης, Καθηγητής, Ελληνικό Μεσογειακό Πανεπιστήμιο.**
3. **Νεκτάριος Παπαδογιάννης, Καθηγητής, Ελληνικό Μεσογειακό Πανεπιστήμιο.**

Εγκρίθηκε από την επταμελή εξεταστική επιτροπή την: 22 / 11 / 2023.

1. **Δρ. Ιωάννης Κ. Νκολός, Καθηγητής, Σχολή ΜΠΔ,** **(υπογραφή)**

   Πολυτεχνείο Κρήτης (Επιβλέπων).

   Ioannis Nikolos Digitally signed by Ioannis Nikolos
   Date: 2023.11.22 18:00:39 +02'00'

2. **Δρ. Μιχαήλ Ταταράκης, Καθηγητής, Ελληνικό Μεσογειακό Πανεπιστήμιο (Συνεπιβλέπων).**

   MICHAIL TATARAKIS MICHAIL TATARAKIS
   22.11.2023 21:36

3. **Δρ. Νεκτάριος Παπαδογιάννης, Καθηγητής, Ελληνικό Μεσογειακό Πανεπιστήμιο (Συνεπιβλέπων).**

   NEKTARIOS PAPADOGIANNIS NEKTARIOS PAPADOGIANNIS
   23.11.2023 14:57

4. **Δρ. Ανάργυρος Δελής, Καθηγητής, Σχολή ΜΠΔ, Πολυτεχνείο Κρήτης.**

   Anargyros Delis Digitally signed by Anargyros Delis
   Date: 2023.11.23 10:44:41 +02'00'

5. **Δρ. Γεώργιος Αραμπατζής, Αναπληρωτής Καθηγητής, Σχολή ΜΠΔ, Πολυτεχνείο.**

   Georgios Arampatzis Digitally signed by Georgios Arampatzis
   Date: 2023.11.24 08:51:11 +02'00'

6. **Δρ. Γεώργιος Καρατζάς, Καθηγητής, Σχολή ΧΗΜΗΠΕΡ, Πολυτεχνείο Κρήτης.**

Digitally signed by
Georgios Karatzas
Date: 2023.11.23
17:54:16 +02'00'

7. **Δρ. Βασίλειος Δημητρίου, Καθηγητής, Ελληνικό Μεσογειακό Πανεπιστήμιο.**

VASILEIOS DIMITRIOU VASILEIOS DIMITRIOU
23.11.2023 17:00

List of Symbols

A	Vector potential
a_0	Normalized peak vector potential
B	Magnetic field
c	Light speed
c_p	Specific heat with constant pressure
c_v	Specific heat with constant volume
E	Electric field
e	Electron charge
E_c	Betatron radiation critical energy
e_{in}	Specific internal energy
E_L	Pulse energy
e_t	Specific total energy
g	Gravity constant
h	Specific enthalpy
I_L	Laser Intensity
k	Wavenumber
K_B	Boltzmann constant
K_n	Knudsen Number
L_{acc}	Acceleration Length
L_d	Dephasing length
L_{diff}	Diffraction length
L_{dp}	Depletion length
M	Mach Number
m_e	Electron mass
M_i	Molecular weight
N_a	Avogadro Number
n_c	Critical density
n_e	Electron density
p	Pressure
P	Momentum
P_L	Laser power
q	Specific heat
R	Specific gas constant
r_b	Bubble radius
s	Specific entropy
T	Temperature
t	Time
u_g	Group velocity
u_{ph}	Phase velocity
V	Volume
w	Work per unit mass
w_0	Beam waist
z_R	Reyleigh length
α	Sound speed
β	Normalized velocity
γ	Lorentz factor
ε_0	Vacuum permittivity
η_p	Refractive index of plasma
κ	Adiabatic index
λ_0	Laser central wavelength
λ_D	Debye length
λ_p	Plasma wavelength
λ_B	Betatron wavelength
μ	Dynamic viscosity
ρ	Density
$\overline{\overline{\tau}}$	Viscous stress tensor
τ_0	Laser pulse duration
Φ	Scalar potential
ω_0	Laser central angular frequency
ω_p	Plasma frequency

List of Acronyms

ASE	Amplified Spontaneous Emission
CAD	Computer Aided Design
CAM	Computer Assisted Manufacturing
CCD	Charge Coupled Device
CD	Convergent Divergent
CFD	Computational Fluid Dynamics
CNC	Computer Numerical Control
CPA	Chirped Pulse Amplification
EM	ElectroMagnetic
FCC	Future Circular Collider
FDM	Fused Deposition Modeling
FFT	Fast Fourier Transform
FVM	Finite Volume Method
FWHM	Full Width at Half Maximum
IDEA	Interferometrical Data Evolution Algorithms
IPPL	Institute of Plasma Physics and Lasers
LHC	Large Hadron Collider
LINAC	LINear ACcelerator
LMD	Laser Metal Deposition
LPA	Laser Plasma Acceleration
LWFA	Laser WakeField Acceleration
MOC	Method Of Characteristics
MS	Magnetic Spectrometer
NIF	National Ignition Facility
PIC	Particle in Cell
PLIF	Planar Laser Induced Fluorescence
PWFA	Particle WakeField Acceleration
RF	RadioFrequency
SLA	StereoLithogrAphy
SRSI	Self-Referenced Spectral Interferometry
STP	Standard Temperature and Pressure
TUC	Technical University of Crete

Abstract

Laser WakeField Acceleration (**LWFA**) is a method to accelerate electrons up to the GeV level. The concept involves electron injection and acceleration in the same setup, creating an accelerator of ultra-high electric field ($\sim GeV/m$), and tiny size, ranging from few mm to few cm lengths. This is nowadays achievable with table-top lasers, or in university-scale facilities. As the size and cost of an accelerator based on Laser Wakefield technology are reduced compared to conventional technology, scientists over the globe are working hard in this field.

In LWFA experiments, an ultra-fast ($\tau_0 \sim fs$), ultra-intense ($I_L \sim 10^{18}\ W/cm^2$) laser pulse interacts with a gaseous target, forming a plasma channel. When specific conditions are fulfilled, some background electrons are injected into the rear side of the channel in the shape of a bunch. In this channel, plasma waves are formed, which create an accelerating field at the laser propagation direction. The electron bunch is accelerated due to this field in relativistic velocities and its energy according to state-of-the-art experiments exceeds some GeV within few cm. The acceleration is more efficient when the driving laser pulse length is smaller than the plasma wavelength ($c\tau_0 < \lambda_p$). The relativistic electron bunch has a small size and angular divergence; however, its energy spread is high. Also, electron bunches accelerated via the LWFA mechanism still need to be more stable and controllable. In this context, the goal is to optimize LWFA, regarding electron bunch stability, energy, and energy spread.

This dissertation studies the role of the gas density profile in controlling the characteristics of LWFA electron beams. Multiple scientific groups extensively study the role of the gas nature, the gas density, and the gas density profile in LWFA. In this dissertation a gas jet assembly, namely a pulsed gas valve with an interchangeable nozzle attached, is used. A set of different geometry nozzles incorporated into the gas valve was studied as a final integrated design. Initially, Computational Fluid Dynamic (CFD) simulations of the gas flow for the integrated designs were performed. Selected nozzles were subsequently 3D-printed, and experimental density evaluation measurements via interferometry were conducted. Also, constructed non-axisymmetric nozzles were evaluated via tomography.

Several nozzles were used for LWFA experiments, and the results are presented in detail. Increasing the length of the gaseous target increased the peak electron energy

and energy range. Using N_2 as a gaseous target and increasing the backing pressure, the mean total charge, mean maximum energy, and angular divergence of the electron beam increased, while the mean saturated energy decreased. Some of the experimental results were further investigated with PIC simulations, conducted by Dr. Anastasios Grigoriadis. Although the non-symmetric nozzle was not experimentally tested, the behavior expected was studied by conducting 2D PIC simulations.

Finally, an identification study of Betatron radiation, a collimated, soft x-ray beam produced concurrently and collinearly to the electron beam, is presented. Measurements of x-ray signals by varying x-ray source position and the gas backing pressure, revealed a directional x-ray beam, produced only when LWFA conditions were fulfilled.

Περίληψη

Η μέθοδος επιτάχυνσης ηλεκτρονίων με τη χρήση laser, γνωστή ως **Laser WakeField Acceleration** (**LWFA**) παράγει πειραματικά δέσμες ηλεκτρονίων με ενέργεια μερικών GeV. Στη μέθοδο αυτή, με τη χρήση ενός υπερ-ισχυρού λέιζερ, δημιουργείται ένας μικροσκοπικός επιταχυντής πλάσματος με μέγεθος που κυμαίνεται από λίγα mm έως λίγα cm, ο οποίος υποστηρίζει εξαιρετικά ισχυρά ηλεκτρικά πεδία της τάξεως των GeV/m. Επιπλέον, τα ηλεκτρόνια που εισέρχονται σε αυτόν προέρχονται από το ίδιο το πλάσμα που δημιουργήθηκε, οπότε η μέθοδος μπορεί να λάβει χώρα ακόμα και με τη χρήση ενός σύγχρονου, επιτραπέζιου λέιζερ ή με τη χρήση εγκαταστάσεων πανεπιστημιακής κλίμακας. Το βασικό πλεονέκτημα της μεθόδου είναι ότι το μέγεθος και το κόστος ενός επιταχυντή που βασίζεται στην τεχνολογία αυτή είναι μειωμένο, σε σύγκριση με τη συμβατική τεχνολογία επιταχυντών.

Εν συντομία, η μέθοδος LWFA διεξάγεται πειραματικά όταν ένας εξαιρετικά υπερ-βραχής ($\tau_0 \sim fs$) υψηλής έντασης ($I_L \sim 10^{18}\ W/cm^2$)) παλμός λέιζερ αλληλοεπιδρά με έναν αέριο στόχο, δημιουργώντας ένα κανάλι πλάσματος. Όταν δημιουργηθούν οι κατάλληλες συνθήκες, κάποια από τα ηλεκτρόνια του περιβάλλοντος πλάσματος εισέρχονται στο κανάλι με τη μορφή δέσμης. Στο κανάλι σχηματίζονται κύματα πλάσματος, που δημιουργούν ένα ηλεκτρικό πεδίο ικανό να τα επιταχύνει στην κατεύθυνση διάδοσης του λέιζερ σε σχετικιστικές ενέργειες. Η επιτάχυνση είναι πιο αποτελεσματική όταν το μήκος παλμού του λέιζερ είναι μικρότερο από το μήκος κύματος του πλάσματος που δημιουργείται ($c\tau_0 < \lambda_p$). Η σχετικιστική δέσμη ηλεκτρονίων έχει ενδιαφέροντα χαρακτηριστικά, όπως μικρό μέγεθος και γωνιακή απόκλιση, όμως έχει μεγάλο ενεργειακό εύρος. Επιπλέον, λόγω του επιτόπιου σχηματισμού του επιταχυντή κατά την αλληλεπίδραση, παρατηρούνται προβλήματα στην σταθερότητα και στον έλεγχο των ιδιοτήτων της δέσμης. Πολλές ερευνητικές ομάδες ανά τον κόσμο έχουν επικεντρώσει την έρευνά τους στην βελτιστοποίηση της μεθόδου, ώστε να παράγονται σταθερές και ρυθμιζόμενες δέσμες ηλεκτρονίων από τη μέθοδο αυτή.

Σε αυτή τη διατριβή εξετάζεται ο ρόλος του προφίλ του αέριου στόχου στον έλεγχο των χαρακτηριστικών της δέσμης των ηλεκτρονίων, που παράγονται με τη μέθοδο LWFA, που, όπως προκύπτει από την βιβλιογραφική επισκόπηση, είναι ένα αρκετά σημαντικό ερευνητικό ζήτημα. Η μελέτη ενός συστήματος που ελέγχει και διαμορφώνει τη ροή του αερίου αποτελούμενο από μια βαλβίδα και ένα σύνολο από διαφορετικής γεωμετρίας ακροφύσια, παρουσιάζεται μέσα από προσομοιώσεις Υπολογιστικής Ρυεστοδυναμικής (CFD – Computational Fluid Dynamics). Τα ακροφύσια που μελετήθηκαν, κατασκευάστηκαν με τη χρήση τεχνολογίας τριδιάστατης εκτύπωσης (3D-printed), ενώ τα παραγόμενα προφίλ πυκνότητας μελετήθηκαν πειραματικά με συμβολομετρία. Επιπλέον, κατασκευάστηκαν μη συμμετρικά ακροφύσια, για τα οποία εφαρμόστηκε η μέθοδος της τομογραφίας.

Στη συνέχεια, τα ακροφύσια χρησιμοποιήθηκαν σε πειραματική διάταξη που αναπτύξαμε για την επιτάχυνση ηλεκτρονίων με τη μέθοδο LWFA και τα αποτελέσματα αυτής της μελέτης παρουσιάζονται στην παρούσα Διατριβή. Η χρήση ακροφυσίων, που δημιούργησαν μακρύτερα προφίλ πυκνότητας, οδήγησε στην αύξηση της μέγιστης ενέργειας, καθώς και του ενεργειακού εύρους των ηλεκτρονίων. Επιπλέον, πραγματοποιήθηκε παραμετρική μελέτη με τη χρήση ενός μόνο ακροφυσίου και αεριού N_2, που έδειξε ότι αυξάνοντας την ασκούμενη πίεση στο σύστημα βαλβίδας-ακροφυσίου το μέσο συνολικό φορτίο, η μέση μέγιστη ενέργεια και η γωνιακή απόκλιση της δέσμης ηλεκτρονίων αυξήθηκαν, ενώ η μέση κορεσμένη ενέργεια μειώθηκε. Για περεταίρω διερεύνηση, μερικά από τα πειραματικά αποτελέσματα μελετήθηκαν και με τη χρήση PIC κώδικα από το συνάδερφο Αναστάσιο Γρηγοριάδη, τα οποία αποτελέσματα επίσης παρουσιάζονται. Σύμφωνα με αυτή τη μελέτη, τα πειραματικά αποτελέσματά αναπαράγονται ποιοτικά, ενώ τα αναμενόμενα αποτελέσματα για τη χρήση του μη-συμμετρικού ακροφυσίου 1 είναι επίσης σημαντικού ενδιαφέροντος.

Επιπλέον, ταυτόχρονα και στην ίδια κατεύθυνση με τη δέσμη των ηλεκτρονίων παράγεται και μια δέσμη μικρής γωνιακής απόκλισης, σύμφωνων χωρικά ακτινών χ, που ονομάζεται ακτινοβολία Βήτατρον. Στα πλαίσια αναγνώρισης και διαχωρισμού αυτής της ακτινοβολίας από ακτίνες χ που παράγονται στο πλάσμα από άλλους μηχανισμούς, πραγματοποιήθηκε ένα πείραμα του οποίου τα αποτελέσματα επίσης παρουσιάζονται στην παρούσα Διατριβή.

Publications related to this dissertation.

Publications in Journals

- J.F. Ong, A.C. Berceanu, A. Grigoriadis, **G. Andrianaki**, V. Dimitriou, M. Tatarakis, N.A. Papadogiannis, and E.P. Benis," Non-linear QED approach of betatron radiation in a laser wakefield accelerator", submitted to *Scientific Reports*
- **G. Andrianaki**, A. Grigoriadis, A. Skoulakis, I. Tazes, D. Mancelli, I. Fitilis, V. Dimitriou, E. P. Benis, N. A. Papadogiannis, M. Tatarakis, and I.K. Nikolos, "Design, manufacturing, evaluation and performance of a 3D-printed, custom-made nozzle for laser wakefield acceleration experiments", *Review of Scientific Instruments,* **94**, 103309 (2023). https://doi.org/10.1063/5.0169623
- A. Grigoriadis, **G. Andrianaki**, I. Tazes, V. Dimitriou, M. Tatarakis, E. P. Benis, and N. A. Papadogiannis. "Efficient plasma electron accelerator driven by linearly chirped multi-10-TW laser pulses," *Scientific Reports,* **13**, 2918 (2023). https://doi.org/10.1038/s41598-023-28755-1
- A. Grigoriadis, **G. Andrianaki**, M. Tatarakis, E. P. Benis, and N. A. Papadogiannis, "The role of laser chirp in relativistic electron acceleration using multi-electron gas targets," *Plasma Physics and Controlled Fusion,* **65**, 044001 (2023). DOI 10.1088/1361-6587/acbb25
- A. Grigoriadis, **G. Andrianaki**, I. Fitilis, V. Dimitriou, E.I. Clark, N.A. Papadogiannis, E.P. Benis and M. Tatarakis, "Improving a high-power laser-based relativistic electron source: the role of laser pulse contrast and gas jet density profile." *Plasma Physics and Controlled Fusion,* **64**, 044007 (2022). DOI 10.1088/1361-6587/ac4b06
- E. Clark, A. Grigoriadis, S. Petrakis, I. Tazes, **G. Andrianaki**, A. Skoulakis. Y. Orphanos, E. Kaselouris, I. Fitilis, J. Chatzakis, E. Bakarezos, V. Dimitriou, E. P. Benis, N. A. Papadogiannis & M. Tatarakis, "High-intensity laser-driven secondary radiation sources using the ZEUS 45 TW laser system at the Institute of Plasma Physics and Lasers of the Hellenic Mediterranean University Research Centre," *High Power Laser Science and Engineering,* **9**, E53 (2021). doi:10.1017/hpl.2021.38
- A. Grigoriadis, **G. Andrianaki**, M. Tatarakis, E. P. Benis, N. A. Papadogiannis, "Betatron-type laser-plasma x-ray sources generated in multi-electron gas targets," *Applied Physics Letters,* **118** (13): 131110 (2021). doi.org/10.1063/5.0046184

Contributions to Conferences with Proceedings

- **G. Andrianaki**, A. Grigoriadis, I. Tazes, I. Fitilis, V. Dimitriou, E.P. Benis, I.K. Nikolos, N.A. Papadogiannis and M. Tatarakis, "Custom-made 3d printed nozzles for Laser Wakefield Acceleration (LWFA) experiments in the Institute of Plasma Physics and Lasers (IPPL)", 3rd International Conference in Electronic Engineering, Information Technology & Education (EEITE), Chania, Crete 28-30/09/2022. https://eeite2022.hmu.gr/eeite2022-proceedings-2/ p. 106.
- **G. Andrianaki**, A. Grigoriadis, I. Tazes, I. Fitilis, V. Dimitriou, E.P. Benis, I.K. Nicolos, N. A. Papadogiannis, M. Tatarakis, "The design and performance of an asymmetrical nozzle in Laser Wake Field electron acceleration," 48th European Physics Society (EPS) Plasma Conference, online (27/06-01/07/2022). ISBN 9781713863236
- **G. Andrianaki**, A. Grigoriadis, E. P. Benis, and N.A. Papadogiannis, "Pointing characteristics of x-rays generated by relativistic electron acceleration via 45 TW

fs laser-he plasma", 22nd International Conference on Ultrafast Phenomena, Optical Society of America (OSA), virtual event 16-19/11/2020. OSA Technical Digest (Optica Publishing Group, 2020), paper Tu4A.12.

Table of Contents

List of Symbols....ix

Abstract....xi

Περίληψη....i

Table of Contents....vi

List of Figures....ix

List of Tables....xvii

Statement of Original Authorship....xviii

Acknowledgements....xix

Ο μηχανισμός επιτάχυνσης ηλεκτρονίων Laser WakeField Acceleration (LWFA)....xxi

Chapter 1: Introduction....1

1.1 Background....1

1.2 LWFA and Betatron Radiation....4
  1.2.1 Role of gas density in LWFA and Betatron Radiation experiments....5

1.3 Gas density studies oriented in LWFA....9
  1.3.1 Design and characterization of nozzles....9
  1.3.2 Design and characterization of other gaseous targets....10
  1.3.3 Gas density studies for ion acceleration....11

1.4 LWFA and Betatron radiation potential applications....11

1.5 High Power Laser Experiments conducted in IPPL....13

1.6 Motivation....14

1.7 Thesis Outline....15

Chapter 2: Fluid dynamics for Compressible flow....17

2.1 Ideal gas equation of state....17

2.2 Energy Conservation law....18
  2.2.1 Important thermodynamic quantities....18

2.3 Second thermodynamic law....19

2.4 1D steady flow along a tube....19

2.5 Compressible flow....20

2.6 Quasi-1D isentropic model for a supersonic Nozzle....21

2.7 Supersonic flow characteristic formations....23

2.8 A general form of conservation equations....25

2.9 numerical methods....26

Chapter 3: LWFA theory 28

3.1 A Gaussian laser pulse in a vacuum and important laser QUANTITIES 28

3.2 Single electron motion in the laser field 30

3.3 Propagation of em waves in a plasma 31

3.4 Plasma waves 32

3.5 LWFA regimes 33
  3.5.1 The Bubble regime 33

3.6 laser modulation in a plasma 34
  3.6.1 Self-focusing 34
  3.6.2 Self-compression 35
  3.6.3 Filamentation 35

3.7 wavebreaking and electron injection 35
  3.7.1 Ionization injection 36
  3.7.2 Injection in a density down-ramp 36
  3.7.3 Optical injection 37

3.8 Energy gain in the plasma wave 37
  3.8.1 Electron dephasing length 37
  3.8.2 Pump depletion length 38
  3.8.3 Laser diffraction limitation 38

3.9 betatron radiation 38

3.10 pic simulations 40

Chapter 4: CFD simulations setup and results for conical Nozzles 43

4.1 Physical problem 43

4.2 Simulation Geometry Mesh and Boundary conditions 44

4.3 Density based solver 45

4.4 Simulation results 46
  4.4.1 Kinetic theory model 50
  4.4.2 Density calculation with Peng-Robinson real gas model 53

4.5 Effect of Gas Pressure 55
  4.5.1 Inlet pressure parametric study 55
  4.5.2 Outlet pressure 57

4.6 nozzles 2-5 58

4.7 Remarks 60

Chapter 5: Experimental setups 61

5.1 Zeus laser system 62

5.2 measurements of laser characteristics 63

5.3 LWFA experimental setup 65
  5.3.1 Operation of the EM valve and synchronization 66

5.3.2 Shadowgraphy technique 67
5.3.3 Magnetic spectrometer (MS) 67

5.4 Interferometry technique 68
5.4.1 Phase shift 70
5.4.2 Axisymmetric nozzles: Abel Inversion 71
5.4.3 Non axisymmetric nozzles: Tomographic reconstruction 72

5.5 X-ray detection 73

Chapter 6: Nozzle manufacturing and density measurements 75

6.1 NOZZLE MANUFACTURING WITH 3d printing 75
6.1.1 Comments on printing procedure 78

6.2 Results for axisymmetric nozzles 79

6.3 Results for non-axisymmetric nozzles 83

Chapter 7: LWFA experimental results by varying gas density profile 88

7.1 Nozzle 0 89

7.2 Nozzle 1 89
7.2.1 PIC simulations for Nozzle 1 90

7.3 Nozzle 2 92
7.3.1 Nozzle 2 - PIC simulations results 92

7.4 Nozzle NS 1 2d-PIC simulations 93

7.5 Remarks 94

7.6 N_2 target-pressure scan 95

Chapter 8: X-ray Betatron identification experiment 99

8.1 The betatron radiation identification setup 99

8.2 Pressure scan 101

8.3 x ray pointing 102

Chapter 9: Conclusions and perspectives 105

Appendices 109

Funding 121

Bibliography 123

List of Figures

Figure 1-1: left) LHC top view and a schematic map of a possible location for the next generation, the so-called FCC (Https://Home.Cern/Science/Accelerators/Future-Circular-Collider). right) The progress of particle accelerators over the years is known as the Livingston curve (Bingham et al., 2004). 3

Figure 1-2: Maximum electron beam energy achieved by multiple different experiments combined as a function of a) laser power in TW, b) accelerator length in m and c) plasma density in $cm - 3$. Adopted from (Mangles, 2017). 5

Figure 1-3: Electron energy spectrum and the simultaneously Betatron radiation profile, obtained with a gas cell with adjustable length from $3 - 40\ mm$. Adopted from (Wood et al., 2017). 5

Figure 1-4: (a) The transition injection mechanism, realized using a blade downstream the nozzle exit. The density profile measured presents a peak that drops fast (Tsai et al., 2018). (b) The down-ramp mechanism was realized using two nozzles. The density down-ramp created is long (Hansson et al., 2015). 7

Figure 1-5: (left) The use of the LWFA electron source to irradiate electronic board in collaboration with Democritus University of Thrace; (right) A gel emulating human tissue constructed by the group of the Medical School of Crete and the University Hospital of Crete. One of the containers was irradiated by high-energy electrons (blurred one), and the other one was used as a reference one (Fitilis et al., 2022). 13

Figure 2-1: A sound wave with velocity α crosses a tube with gas density ρ. 20

Figure 2-2: 1D isentropic model: A backing pressure reservoir with known initial conditions ρ_0, T_0 and p_0 is given. The gas flows through a nozzle with a minimum cross-section At (at the throat) and exhausts a gas jet at the exit where the cross-section is Ae. 22

Figure 2-3: Ratio of the nozzle exit to the nozzle throat as a function of M for noble and diatomic gasses. 23

Figure 2-4 Sketch of a flow across an oblique shock and an expansion fan. 24

Figure 2-5: Flow structures due to high-pressure exhaust of a gas with exit pressure Pe in a chamber with lower pressure Pa. Figure adopted from: (Https://Aerospaceweb.Org). 24

Figure 2-6: Flow lines along a conceptual volume, the control volume, fixed in space, surrounded by the control surface. 25

Figure 3-1: The spatial evolution of a Gaussian pulse at focus. The beam waist $w0$ and the Rayleigh length zR are highlighted. 29

Figure 3-2: Electron relativistic trajectories in the laser field in the laser frame (left) and in the laboratory frame for $a0 = 1$ and $a0 = 4$. 31

Figure 3-3: Behind the laser pulse a bubble, void from electrons is formed. Electrons are injected from its rear side and accelerated. Adopted by (Malka, 2013). 33

Figure 3-4: Electrons injected in the bubble oscillate transversely and emit x-ray photons of small divergence at the laser propagation direction. This radiation is known as Betatron. Adopted from (Jinchuan, 2013). 39

Figure 4-1: Concept of the simulation: Using a pressure regulator the backing pressure is set. The gas flows via a metallic pipe to a pulsed gas valve and exhausts to the vacuum chamber via a nozzle. The pressure gauge located at one of the chambers' ports measures an indicative pressure value, related to the outlet pressure. 43

Figure 4-2: left: Conceptual Flow Domain. Right: The exact dimensions at various locations. 44

Figure 4-3: The 2D mesh is unstructured, quadrilateral dominant. The mesh after the close to the wall area is finer, to capture viscous effects. 45

Figure 4-4: Steps of the Density Based solver of ANSYS Fluent. 46

Figure 4-5: Detail of the simulation domain inside Nozzle 1: density map (top) and Mach number map (bottom). Flow formations inside the inner valve and nozzle region are highlighted: a barrel shock, followed by a diamond-like shock are observed inside the nozzle. Maximum values of Mach number are in the order of 10. 48

Figure 4-6: Density (black) and Mach number (blue) along the symmetry axis of the simulation domain (bottom), for He and $40\ bar$ backing pressure. 48

Figure 4-7: Gas density profiles $200, 400, 600, 800\ and\ 1000\ \mu m$ downstream the Nozzle 1 exit for He, Ne and Ar, for $40\ bar$ backing pressure and outlet pressure $1\ mbar$). Density along the axis of symmetry, for the 3 gases. 49

Figure 4-8: Density along axis for He, Ne and Ar $1mm$ downstream the Nozzle 1 exit. A small density increase is noticed, due to the reflections of the expansion waves to the shear layer. The selected area is zoomed, as being the mostly used in LWFA experiments. 49

Figure 4-9: Pressure and temperature in the flow domain. The values vary significantly and upstream the Mach disk the static pressure is below the critical value, while the temperature is slightly above. 50

Figure 4-10: Lennard-Jones potential characteristic form; σ is the distance at which the potential is equal to zero, and ε is the depth of the well. 51

Figure 4-11: The comparison of the quantities a) Cp, b) μ, c) k, d) ρ, e) M and f) p for two different simulation cases. In case 1 the values of cp, μ and k are constant (bottom), while in case 2, are calculated by the kinetic theory model. Although the values of μ and k vary almost two orders of magnitude, the variation of ρ, M and p is below the resolution of the contour maps. 52

Figure 4-12: Top: Particle density (left) and Mach number (right) profiles $400\ \mu m$ downstream the nozzle exit; Bottom: Mach number and density variation along the axis, for constant values of the gas properties according to table 2 (green) and for properties calculated according to the kinetic-theory model (black). 53

Figure 4-13: p-T phase diagram of ^{4}He. The critical point is at $pc = 2.27\ bar$ and $Tc = 5.2\ K$ (Slenczka & Toennies, 2022). 53

Figure 4-14: Particle density (left) and Mach number (right) profiles $400\ \mu m$ downstream the nozzle exit. Bottom: Mach number and density variation along flow axis for the density calculated from the ideal gas equation of state (green) and for the density calculated from the Peng-Robinson real gas equation of state (black). 55

Figure 4-15: Density contour maps for He for $50\ bar$ (top) and $25\ bar$ (bottom) backing pressure. Similar flow features are formed. The overall density decreases by decreasing backing pressure, as also the length of the jet. 56

Figure 4-16: Particle density $400\ \mu m$ downstream the nozzle's exit, for $25\ to\ 50\ bar$ backing pressures. The peak to minimum value ratio is increased, as well as the distance between the peaks, as the backing pressure increases. 56

Figure 4-17: Particle density along axis for $25\ to\ 50\ bar$ backing pressures. The flow features after the first barrel shock are moving slightly downstream as the pressure increases. 57

Figure 4-18: Density contour maps for Nozzle 1 with He, at $40\ bar$ backing pressure. From top to bottom, outlet pressure increases from $1\ to\ 10\ mbar$, initially without a great effect on density values, especially at the area close to the nozzle exit. Progressively diamond-like shocks with increasing periodicity are formed. 57

Figure 4-19: Density contour maps of Nozzles 2, 3, 4 and 5, for He, with $40\ bar$ backing pressure, and $1\ mbar$ at the outlet. Their dimensions are presented in Table 1. 58

Figure 4-20: Particle density of all Nozzles of Table 1, $400\ \mu m$ downstream each nozzle's exit, for He, with $40\ bar$ backing pressure and $1\ mbar$ at the outlet. The profile lengths vary according to the exit diameter of each nozzle. The density profiles of Nozzles 2 & 4 are smoother. 59

Figure 4-21: Particle density of all Nozzles of Table 1, along axis of symmetry, from $1\ mm$ upstream the exit to $14\ mm$ downstream, for He, with $40\ bar$ backing pressure, and $1\ mbar$ at the outlet. 60

Figure 5-1: IPPL facility of HMU hosted at Rethymnon (top). The 45 TW laser system Zeus (bottom). 61

Figure 5-2: General layout of laser Zeus. The basic modules necessary to amplify the pulse up to 1.4 J energy using the CPA technique, are highlighted. 62

Figure 5-3: a) Table of laser diagnostics. Off-line measurements highlight the laser condition, resulting in potential corrections which also are used as reference for the following experiments. b) Pulse duration measured by the Wizzler. c) Contrast ratio measurement with and without the additional saturable absorber, placed before the first amplifier. 64

Figure 5-4: The spatial density profile of the focal spot at beam waist position. Its lineouts measured by the two perpendicular profiles at FWHM is $26.4\ \mu m$. 64

Figure 5-5: The laser is entering the experimental chamber via a vacuum tube. A gate valve placed at the tube provides the opportunity to keep the compressor chamber under vacuum conditions, while exposing the experimental chamber to atmospheric pressure. A turbo pump (accompanied by a mechanical pump) on top of the chamber's topping provides high vacuum conditions during the experiments. Two CCD cameras are highlighted: CCD camera for MS is dedicated to the detection of the trace of the electrons, after their path in the Magnetic Spectrometer (MS), and one for the shadowgraphy setup, placed on the optical diagnostic table. On the optical beam table, all the optics necessary to drive the probe beam are set. Finally, the pulse generator that controls the delays among the laser pulse, the gas valve opening, and the CCD cameras' opening time, is highlighted. 65

Figure 5-6: left) The pair of magnets of the MS. Right) The EM gas valve with a plastic, 3D printed nozzle attached. 66

Figure 5-7: Synchronization diagram of the temporal delays of the gas jet assembly and the CCD cameras. A pulse generator triggered by the laser is used to adjust the time delays. 66

Figure 5-8: a) Operating principle of shadowgraphy technique. Probe beam of laser Zeus with an incoming intensity $I0$ crosses the interaction area perpendicularly and the disturbed beam Id is captured by a CCD camera. The density gradient resulting in different refractive indexes $\eta x, y, z$ causes the light to refract, revealing density structures formed by the interaction. b) A typical shadowgram captured in a LWFA experiment. 67

Figure 5-9: Operating principle of MS. Relativistic electrons cross a magnetic field of 0.4 T and are dispersed with respect to their velocity perpendicular to their initial direction. Their interaction with a scintillating screen produces photons of 545 nm wavelength, which are recorded to a CCD camera. The analysis of the recorded signal via a spectrum analysis code produces electron energy spectrum. 68

Figure 5-10: Operating principle of Nomarski interferometry set-up: The beam of a CW laser is driven over the 3D-printed nozzle, where the gas exhausts. Then, the beam crosses a Wolaston prism, where two spatially separated perpendicularly polarized beams are formed, which then cross a polarizer. The interference signal of the two beams is recorded onto a CCD camera. 69

Figure 5-11: Steps for obtaining a phase shift map. For the reported steps IDEA software was used (Hipp et al., 2004). 70

Figure 5-12: Abel Inversion reference geometry. The laser propagates parallel to the x-axis and passes through an area containing the axial symmetric gas jet. The projection of the phase shift F(y) is recorded on the CCD camera chip. 71

Figure 5-13: Reference geometry for tomography. Laser beam crosses the gas jet by various angles, creating the projections hp, θ, which are used to calculate local phase shift distribution via the relation 5.16. 73

Figure 5-14: a) The photodiode Morros Compton CA with active area 1.2 cm. b) The x-ray photodiode was reverse biased (-300 V) and connected to the oscilloscope. c) Al foil x-ray transmission curves (Https://Henke.Lbl.Gov/Optical_constants). 74

Figure 6-1: CAD drawing and prototype of Nozzle 1, printed via FDM technique. 75

Figure 6-2: Nozzles produced via FDM 3D-printing. 76

Figure 6-3: Nozzles printed via SLA process. a) Printing of half section of a nozzle to test the ability of the Anycubic SLA printer to reproduce inner nozzle details. Printing under an angle destroyed the bottom flatness. (b) Inverse-Z printing. The top area is rough after removing the supportive material. 77

Figure 6-4: a) Printing chamber of Meltio M450 metallic 3D-printer, filled with gas Ar, through the protective window while printing. The laser is melting the 1 mm wire which is welded on the special bed. b) The welded part was unsuccessfully printed. 78

Figure 6-5: Phase shifts of Nozzle 1 ($2\ mm$ exit diameter) (a, b), and Nozzle 2 ($3\ mm$ exit diameter) (c, d), for He, at $40\ bar$ (a, c) and $50\ bar$ (b, d) backing pressure. Nozzle 2 systematically produced less symmetric phase shifts. Results obtained with IDEA software (Hipp et al., 2004). 79

Figure 6-6: Bottom: Particle density contours in $cm-3$ for Nozzle 1 for Ne, Ar and N_2 at $40\ bar$ backing pressure, measured with interferometry technique. Top: Particle density contours in $cm-3$ for Nozzle 1 for He at $40\ bar$ backing pressure, measured with interferometry technique and respective CFD simulation for He at $40\ bar$ backing pressure and 10 mbar outlet pressure. 80

Figure 6-7: Density profiles for He (top), Ne (middle) and Ar (bottom) at $40\ bar$ backing pressure for Nozzle 1. Magenta lines are experimental results 300 (left) $500\ \mu m$ (right) downstream the nozzle's exit, and green lines are simulated values at the same distance respectively, for $40\ bar$ backing pressure and $1\ mbar$ at the outlet. 81

Figure 6-8: The peak density value variation of gas He with respect to the backing pressure applied at the valve for Nozzle 1, $300\ \mu m$ downstream the nozzle exit. Green spots and respective fitting curve is for the experimental results and red spots and respective fitting curve is for the CFD simulations. 81

Figure 6-9: Experimental (left) and simulated (right) particle density contours for Nozzle 2, for He at $40\ bar$ backing pressure (1 mbar for the pressure outlet). 82

Figure 6-10: Particle density profiles for Nozzles 2 (blue line), 3 (orange line) and 4 (yellow line), $400\ \mu m$ downstream each nozzle exit for gas He, at $40\ bar$ backing pressure. 83

Figure 6-11: Bottom: Section view of NS1. Initially consists of a cylindrical area, elongated as an ellipse from one side and rectangular from the other side. Top: Side view of NS1 exit. 83

Figure 6-12: a) The experimental setup during interferometry experiments. The optics necessary to realize a Nomarski interferometer, as described in Figure 5-8, are highlighted. The base design, together with the long and stiff metallic pipe was annulling the ability to turn the nozzle at will. b) Nozzle AS1 and the phase shifts obtained at $0°, 47°, 70°, 90°$......... 84

Figure 6-13: Density contour maps downstream the non-symmetric nozzle for N_2 at $30\ bar$ backing pressure $200, 400, 600, and\ 800\ \mu m$ downstream the nozzle exit. 85

Figure 6-14: (Left) N_2 density profiles for 30 bar backing pressure along the black line displayed in Figure 6.8 at $200\ \mu m$, corresponding to the laser propagation direction for $200, 400, 600, and\ 800\ \mu m$ downstream the exit of Nozzle NS 1 and N_2 density profile for $30\ bar$ backing pressure $200\ \mu m$ downstream the exit of Nozzle 2. (Right) density along the grey line displayed in Figure 6.8 at $200\ \mu m$ for $200, 400, 600, and\ 800\ \mu m$ downstream the exit of Nozzle NS 1............... 85

Figure 6-15: Density profiles at 200 (blue), 400 (green), 600 (yellow) and 800 (magenta) μm downstream the exit of NS 1 along the black line noted at the $200\ \mu m$ contour map of Figure 6-13. The density decreases by increasing the distance. Although pressure increases from $35\ to\ 50\ bar$ peak density remains almost unchanged.......... 86

Figure 6-16: New base designs for asymmetrical nozzles. The designs are suitable for rotation at will in 6 or more equidistant angles, without rotating the gas jet assembly. 87

Figure 7-1: Layout of the experimental chamber during the LWFA experiments. Laser Zeus is driven and focused above the gas nozzle. The generated electron beam travels along the laser propagation direction and crosses the magnetic spectrometer. The electrons, dispersed according to their energy, are imaged on a scintillating screen. The probe beam travels perpendicular to the interaction area, to image the plasma channel formed by the interaction via shadowgraphy technique. 88

Figure 7-2: a) Electron energy spectra for 5 shots using Nozzle 0 (shots 1-5 from top to bottom). b) Spectra projection to the energy axis. The Semi-monoenergetic beams are produced with high stability. c) Picture of Nozzle 0. 89

Figure 7-3: a) Electron energy spectra for 5 shots using Nozzle 1 (shots 1-5 from top to bottom). b) Spectra projection to the energy axis. c) shadowgram at the end of the interaction. The plasma channel has broken into sub-channels at the higher intensity area. 90

Figure 7-4: PIC simulation results for Nozzle 1. The density profile for $40\ bar$ backing pressure was approximated as fully ionized He (top left). In sub-plots A), to D) the snapshots of the plasma density, when the laser has crossed points A to D in the density profile, are plotted. At B) the beam is broken into beamlets, which drive additional waves. In the main accelerating structure of B), we see injected electron bunches, which further accelerate at C) and D), resulting in a wide energy spectrum with 3 distinct peaks (top right).......... 91

Figure 7-5: Electron energy spectra for 5 shots using Nozzle 2. High energy spread, high-energy beams are produced with good stability. b)

Spectra projection to the energy axis. c) Shadowgram at the end of the interaction. The plasma channel is uniform. 92

Figure 7-6: PIC simulations results for Nozzle 2. The density profile for $40\ bar$ backing pressure was approximated (top left). The resulting electron spectrum is plotted (top-right). In sub-plots A to D the snapshots of the plasma density when the laser has crossed points A to D in the density profile are plotted. First and second bubbles are elongated at B), where injection starts. In C) and D) the first bubble still expands in the longitudinal direction and injection continues. 93

Figure 7-7: PIC simulations results for NS 1. The density profile used for fully ionized He was utilized (top left). The resulting electron spectrum is plotted (top-right). In sub-plots A) to D) the snapshots of the plasma density, when the laser has crossed points A to D in the density profile, are plotted. The first bubble formed is elongated at C), where electrons are injected. In D) the bubble is additionally stretched but no further injection occurs. 94

Figure 7-8: left) The shadowgrams at the end of the interaction for $30 - 45\ bar$ backing pressure. The length of the break noticed, increases with backing pressure increase. Right) The N_2 density profiles for Nozzle 2 at a distance $1.1\ mm$ downstream the nozzle exit, for $30 - 45\ bar$ backing pressure, measured with interferometry technique off-line. 96

Figure 7-9: 4 representative electron spectra for $30, 35, 40\ and\ 45\ bar$ backing pressure. At $30\ bar$ lies the injection threshold, where high energy - low charge beams were detected. 97

Figure 7-10: Mean total charge, mean maximum energy, and mean saturated maximum energy of electrons produced with an N_2 gas target for $30 - 45\ bar$ backing pressure. Charge increases significantly with backing pressure and creates the beam loading effect. 98

Figure 8-1: Layout of the experimental chamber during the Betatron radiation identification experiment. Laser Zeus is driven and focused above the gas nozzle. Laser final focusing optic (off-axis parabola) and the gas jet assembly are placed on a motorized base, permitting the source to move as a whole along the green array from -4 to $4\ mm$. Two photodiodes D1 and D2 are set, D1 at the laser propagation direction, D2 under various angles placed at the same distance from the source. The electron beam generated travels along the laser propagation direction and crosses the magnetic field of the spectrometer, which deflects them out of the active area of D1. The photodiodes were appropriately shielded and filtered from photons with energy below $1\ keV$, as presented in section 5.5. 100

Figure 8-2: Quantum efficiency of D1 and D2 for stable photon source. 100

Figure 8-3: Signal (V) with respect to time for D1 (bottom) and D2 (top). In D1 the signal is distinguished from noise for a backing pressure higher than 35 bar. 101

Figure 8-4: Integrated signal (a.u.) over time is plotted with respect to backing pressure applied to the EM valve. 102

Figure 8-5: The signal over time recorded by D2 (left) and D1 (right) for source translation from $4\ to\ -1\ mm$ ($67\ to\ -17\ mrad$) with respect to D1 centre. Signal in D2 is not affected by the source translation, while signal in D1 is dropping by increasing the angle. 102

Figure 8-6: Integrated signal over time for D1 and D2, with respect to the translation position of the x-ray source relative to D1 centre. 103

Figure 9-2: Particle density $200\ \mu m$ over the nozzle exit for Nozzle 1, with gas He at $40\ bar$ backing pressure. 110

Figure 9-3: The relative difference percentage for the 3 test meshes relative to the selected one. The relative difference of the finer mesh with the utilized one is below 1%. 111

List of Tables

Table 1: Geometric features of the designed nozzles 45

Table 2: gas properties for p=1 bar and T=300 K (Https://Www.Engineeringtoolbox.Com/; Https://Www.Engineersedge.Com) 47

Table 3: Refractive indexes of the gasses at STP (*Https://Www.Engineeringtoolbox.Com/Refractive-Index-D_1264.Html*, n.d.) 72

Statement of Original Authorship

The work contained in this thesis has not been previously submitted to meet requirements for an award at this or any other higher education institution. To the best of my knowledge and belief, the thesis contains no material previously published or written by another person except where due reference is made.

Signature: Georgia Andrianaki

Date: 22/11/2023

Acknowledgements

This dissertation is the result of a long an intense period, where the conditions to conduct research were not always ideal. For instance, given that large part of this work was experimental, and experiments are a teamwork, Covid 19 created many complications that only human interaction could help to overcome! I want to acknowledge the contribution of my supervisors, colleagues and family, first for being there!

First of all, I want to thank my advisor Prof. Ioannis K. Nikolos for his continuous support in multiple ways. His scientific contribution was great, especially in the CFD part, where he also provided me with the necessary equipment and plenty of space to perform my simulations. Also, although super-busy, he was always responding in the most helpful way. In addition, I want to thank him for being a very understandable person, who could encouraged me a lot in many difficult moments.

I want to also thank the IPPL Director Prof. Michael Tatarakis, for being the first person who motivated me to conduct a PhD. His continuous support and guidance all these years was of great importance. In addition, I want to thank Prpf. Nektarios Papadogiannis and Prof. Emmanuel Benis, who both provided scientific support and especially for the great collaboration we had in the x-ray Betatron project.

Special thanks to Dr. Eugene Clark, who guided the experimental campaigns at first and shared his knowledge with patience. In addition, I want to thank Prof. Vasilios Dimitriou, who always supported me with motivating scientific conversations and for providing important equipment. I want to thank Dr. Ioannis Fitilis and Stelios Petrakis for all the experimental support and guidance with the laser. In addition, I want to thank the members of the lab group Anastasios Grigoriadis and Ioannis Tazes, who were always there under ideal and difficult conditions for any kind of help, experimental or even existential! Especially Anastasios Grigoriadis was an ideal lab partner during all the years. In addition, I specially thank Alexandros Skoulakis, who always shared his wisdom with me and other colleagues. I also wish to thank IPPL stuff and students, who collaborated in a good atmosphere, E. Bakarezos, I. Chatzakis, V. Kasselouris, I. Orphanos, S. Vlachos and E. Vrouvaki. Also, I wish to thank TUC PhD candidates Stavros N. Leloudas and Angelos Klothakis, for providing software and technical support.

To efficiently arrive to this point, the most crucial role was played by my partner Donaldi Mancelli, my parents Athina Palioudaki and Michalis Andrianakis, and my sisters Maria and Argyro Andrianaki.

The experimental part of this work was conducted at the Institute of Plasma Physics and Lasers of the Hellenic Mediterranean University of Crete at Rethymnon, Greece. The computational part was conducted at the Turbomachines & Fluid Dynamics Laboratory at the School of Production Engineering & Management of the Technical University of Crete in Chania, Greece. The funding of this research is presented at a special section after the bibliography.

Επιτάχυνση σωματιδίων με τη χρήση διάταξης Laser υψηλής έντασης και ο ρόλος της αεριοδυναμικής.

Ο μηχανισμός επιτάχυνσης ηλεκτρονίων Laser WakeField Acceleration (LWFA)

Ο μηχανισμός Laser WakeField Acceleration (LWFA) χρησιμοποιείται ευρέως για την επιτάχυνση ηλεκτρονίων σε ενέργειες που φτάνουν μερικά GeV, μέσα σε πολύ μικρή απόσταση. Όσο τα ηλεκτρόνια επιταχύνονται στη κατεύθυνση διάδοσης του λέιζερ, ταυτόχρονα ταλαντώνονται εγκάρσια, παράγοντας φωτόνια στην περιοχή των ακτίνων χ. Μεγάλο ερευνητικό ενδιαφέρον εστιάζεται σε αυτό το μηχανισμό, όχι μόνο λόγω της ενδιαφέρουσας φυσικής που προκύπτει από την αλληλεπίδραση ενός υπερ-ισχυρού λέιζερ με την ύλη, αλλά και λόγω του μικρού μεγέθους, άρα και κόστους ενός τέτοιου επιταχυντή, σε σχέση με τους λεγόμενους συμβατικούς. Η προοπτική να χρησιμοποιηθεί το LWFA σε εφαρμογές που σήμερα χρησιμοποιούνται για παράδειγμα γραμμικοί επιταχυντές, εξετάζεται ήδη σε ερευνητικό επίπεδο, όπως και σε μελέτες σκοπιμότητας.

Πειραματικά το LWFA λαμβάνει χώρα όταν ένας υπέρ-βραχύς ($\tau_0 \sim 10s\ fs$), υπέρ-ισχυρός παλμός ($P \sim TW$) εστιάζεται σε πολύ μικρή περιοχή διαμέτρου μερικών δεκάδων μm δημιουργώντας ένα παλμό έντασης $I > 10^{18}\ W/cm^2$. Στην περιοχή εστίασης απελευθερώνεται ένας πίδακας αερίου κατάλληλης πυκνότητας. Υποθέτοντας ως αέριο το ήλιο που συνηθίζεται σε αυτή την κατηγορία πειραμάτων, το αέριο θα έχει πλήρως ιονιστεί ήδη από τον προ-παλμό μικρότερης έντασης που παράγει το λέιζερ, η οποία όμως ξεπερνά το κατώφλι ιονισμού των 2 ηλεκτρονίων του ηλίου. Έτσι, όταν ο κύριος παλμός του λέιζερ φτάνει, τα ηλεκτρόνια φεύγουν από την περιοχή, λόγω της δύναμης ponderomotive, δημιουργώντας μια φούσκα ιόντων, τα οποία παραμένουν ακίνητα, ενώ τα ηλεκτρόνια ταλαντώνονται με μια συχνότητα ταλάντωσης γνωστή ως συχνότητα πλάσματος, η οποία εξαρτάται από την πυκνότητα του πλάσματος. Η φυσαλίδα με τα κύματα πλάσματος ακολουθεί την διάδοση του παλμού. Εξαιτίας των κυμάτων, η τιμή του ηλεκτρικού πεδίου κατά τη διεύθυνση διάδοσης του λέιζερ φτάνει τα GeV/m. Κατά τη διάδοση το πλάτος του ηλεκτρικού πεδίου συνεχίζει να αυξάνεται, μέχρι που φτάνει το άνω όριο του ‘wavebreaking’. Τότε, μέρος των ηλεκτρονίων εισέρχονται στη φυσαλίδα, και επιταχύνονται λόγω του ηλεκτρικού πεδίου που δημιουργείται από τα κύματα πλάσματος στη κατεύθυνση διάδοσης του λέιζερ. Τα ηλεκτρόνια αυτά έχουν χαρακτηριστικά δέσμης, με μικρό ενεργειακό εύρος και γωνιακή απόκλιση. Στην περίπτωση αυτή έχουμε είσοδο των ηλεκτρονίων στη δομή επιτάχυνσης με το μηχανισμό self-injection.

Όμως τα ηλεκτρόνια μπορεί να εισέλθουν στη δομή επιτάχυνσης και με άλλους μηχανισμούς, όπως το ionization injection, ή το down-ramp injection. Στην περίπτωση του ionization injection, έχουμε αέριο μεγαλύτερου ατομικού αριθμού και ενώ τα εξώτερα ηλεκτρόνια ιονίζονται από τον προ-παλμό και δημιουργούν τα κύματα πλάσματος, κάποια από τα ηλεκτρόνια των εσωτερικών στοιβάδων ιονίζονται μέσα στη φούσκα, είτε από τον κύριο παλμό, είτε λόγω φαινομένων διάδοσης, όπως την αυτό-εστίαση του λέιζερ λόγω μεταβολών της πυκνότητας και του δείκτη διάθλασης του πλάσματος. Αυτό πειραματικά οδηγεί κυρίως σε μεγαλύτερο συνολικό φορτίο στη δέσμη των ηλεκτρονίων. Στην περίπτωση του down-ramp injection, χρησιμοποιείται ένα προφίλ πυκνότητας όπου στην αρχή έχει μια κορυφή πυκνότητας, η οποία ακολουθείται από μια πτώση της πυκνότητας, το λεγόμενο down-ramp. Κατά την πάροδο του λέιζερ από την περιοχή αυτή, λόγω της χαμηλότερης πυκνότητας, το μήκος κύματος του πλάσματος μεγαλώνει, η φούσκα επιμηκύνεται και ηλεκτρόνια μπορούν να εισέλθουν ευκολότερα από το πίσω μέρος της φούσκας και να επιταχυνθούν. Πειραματικά, τέτοια προφίλ ακολουθούμενα από μια μικρότερη, σταθερή πυκνότητα μετά από το down-ramp, η οποία βελτιστοποιεί την επιτάχυνση, έχουν οδηγήσει στη βελτίωση των χαρακτηριστικών της δέσμης ηλεκτρονίων.

Μετά την είσοδο των ηλεκτρονίων στη δομή επιτάχυνσης, τα ηλεκτρόνια κερδίζουν ενέργεια μέχρι να φτάσουν κάποια όρια της μεθόδου, όπως για παράδειγμα το pump depletion length, όπου η ενέργεια του παλμού δεν είναι πλέον ικανή να οδηγήσει τα κύματα που δημιουργούν το ηλεκτρικό πεδίο και η επιτάχυνση σταματά. Ένας απλουστευμένος τρόπος προσέγγισης του υπολογισμού της συνολικής ενέργειας των ηλεκτρονίων είναι ο πολλαπλασιασμός της μέγιστης τιμής του ηλεκτρικού πεδίου επί το μήκος επιτάχυνσης. Αυτό θα οδηγούσε σε μονοενεργειακές δέσμες που έχουν κερδίσει τη μέγιστη ενέργεια από το πεδίο, κάτι το οποίο πειραματικά δεν παρατηρείται, αφού για παράδειγμα δεν εισέρχονται όλα τα ηλεκτρόνια στην ίδια θέση και η τιμή του ηλεκτρικού πεδίου δεν είναι σταθερή, αφού εξαρτάται από την πυκνότητα. Επιπλέον και άλλα φαινόμενα λαμβάνουν χώρα, όπως το filamentation του λέιζερ ή το beam loading. Όταν συμβαίνει το φαινόμενο που αποκαλείται filamentation, η δέσμη λέιζερ σπάει σε μικρότερες δέσμες, δημιουργώντας περισσότερες από μια δομές επιτάχυνσης, διαιρώντας όμως την ενέργεια που τις οδηγεί, με αποτέλεσμα μικρότερης έντασης ηλεκτρικό πεδίο ή και την είσοδο και επιτάχυνση πολλαπλών δεσμών ηλεκτρονίων από τις επιπλέον δομές. Όταν συμβαίνει το φαινόμενο που αποκαλείται beam loading, το φορτίο της δέσμης ηλεκτρονίων που εισέρχεται στη δομή επιτάχυνσης είναι πολύ μεγάλο και ικανό να παραμορφώσει τα πεδία της, με αποτέλεσμα να επιταχύνονται δέσμες ηλεκτρονίων με χαμηλότερης ποιότητας χαρακτηριστικά (μεγάλο φορτίο, αλλά μεγάλο ενεργειακό εύρος όπως και γωνιακή απόκλιση). Γενικά, πρόκειται για μια μη γραμμική αλληλεπίδραση του λέιζερ με το πλάσμα, η οποία εξελίσσεται στο χρόνο και η προσέγγιση της αναλυτικά είναι αδύνατη. Γι' αυτό το λόγο, στον σχεδιασμό νέων πειραμάτων ή στην ανάλυση πειραματικών δεδομένων χρησιμοποιούνται κώδικες PIC, οι οποίοι επιλύουν τις εξισώσεις του Maxwell σε ένα δομημένο πλέγμα, μεγέθους κατάλληλου για να περιγράψει τα συλλογικά φαινόμενα του πλάσματος για ένα περιορισμένο αριθμό ψευδο-σωματιδίων, που αντιπροσωπεύουν κατανομές φορτίων.

Ο ρόλος της πυκνότητας

Στη διατριβή αυτή μελετάται η δυνατότητα ελέγχου των χαρακτηριστικών των δεσμών ηλεκτρονίων μέσα από την πυκνότητα του αερίου. Όπως ήδη αναφέρθηκε, η πυκνότητα του πλάσματος, η φύση του αεριού, το μήκος επιτάχυνσης, καθώς και η μορφή του προφίλ παίζουν κυρίαρχο ρόλο στη δημιουργία της δομής επιτάχυνσης, όπως και στην εισαγωγή των ηλεκτρονίων σε αυτήν. Έτσι, σχεδιάστηκαν και μελετήθηκαν ένα σύνολο από ακροφύσια κατάλληλα να διαμορφώσουν την πυκνότητα του αερίου στην περιοχή της αλληλεπίδρασης και να παράγουν διαφορετικά μεταξύ τους προφίλ, στην περιοχή ενδιαφέροντος για το LWFA. Τα ακροφύσια που συνήθως χρησιμοποιούνται είναι συγκλίνοντα-αποκλίνοντα, για παράδειγμα τύπου De Laval, και παράγουν υπερηχητικές ροές στην έξοδό τους.

Για τη μελέτη τέτοιων ακροφυσίων υπάρχει διαθέσιμο στη βιβλιογραφία ένα ευρέως χρησιμοποιούμενο μοντέλο, που προσεγγίζει τη ροή ως ισεντροπική. Το μοντέλο αυτό υπολογίζει τις τιμές καταστατικών μεγεθών όπως η πίεση, η πυκνότητα και η θερμοκρασία μέσα στο ακροφύσιο με βάση τις αρχικές τους τιμές και τον λόγο της διατομής της μικρότερης επιφάνειας του ακροφυσίου, του λεγόμενου λαιμού, προς την επιφάνεια του ακροφυσίου στη συγκεκριμένη θέση. Το μοντέλο αυτό δεν λαμβάνει υπόψη τυχόν ασυνέχειες, όπως τον σχηματισμό κυμάτων κρούσης, ή την τυρβώδη ροή που αναπτύσσεται κυρίως στα τοιχώματα του ακροφυσίου. Όμως, σύμφωνα με τη βιβλιογραφία και προκαταρκτικές προσομοιώσεις, η μελέτη κάθετων και πλάγιων κυμάτων κρούσης, όπως και ασυνεχειών επαφής αλλά και της τυρβώδους ροής είναι καθοριστικής σημασίας.

Για να περιγράφουν πλήρως όλες οι φυσικές διεργασίες που λαμβάνουν χώρα σε όλη την περιοχή ενδιαφέροντος, οι εξισώσεις της συνέχειας, καθώς και της διατήρησης της ορμής και της ενέργειας πρέπει να λυθούν, μαζί με μια καταστατική εξίσωση που περιγράφει το αέριο, καθώς και τον δεύτερο θερμοδυναμικό νόμο. Επειδή η επίλυση τέτοιων συστημάτων αναλυτικά είναι επιτεύξιμη μόνο για πολύ απλοποιημένα προβλήματα, στην μελέτη αυτή χρησιμοποιήθηκε ο κώδικας υπολογιστικής ρευστοδυναμικής ANSYS Fluent. Στην περίπτωση αυτή οι εξισώσεις διακριτοποιούνται και επιλύεται το παραγόμενο αλγεβρικό σύστημα πάνω στους κόμβους ενός πλέγματος που δημιουργείται κάνοντας χρήση κάποιας μεθόδου διακριτοποίησης, στην περίπτωσή μας τη μέθοδο πεπερασμένων όγκων.

Προσομοιώσεις για τον υπολογισμό της πυκνότητας μέσα από τα σχεδιαζόμενα ακροφύσια

Για τις προσομοιώσεις σχεδιάστηκαν οι κατάλληλες γεωμετρίες, οι οποίες περιλαμβάνουν μέρος και της βαλβίδας που ελέγχει τη ροή του αερίου. Αυτό διότι η ίδια η βαλβίδα περιλαμβάνει μια πολύ μικρής διατομής περιοχή, η οποία επιλέχτηκε να παίξει το ρόλο του λαιμού. Έτσι, τα ακροφύσια που δημιουργήθηκαν ήταν κατά βάση αποκλίνοντα (κωνικά), όπως φαίνεται στην εικόνα 1, όπου παρουσιάζεται το χωρίο επίλυσης του προβλήματος. Χρησιμοποιήθηκε ο βασισμένος στην πυκνότητα επιλύτης, όπου λύνει τις εξισώσεις της συνέχειας της διατήρησης της ορμής και της ενέργειας σε ένα βήμα, καθώς και το μοντέλο τυρβώδους ροής στο επόμενο βήμα (k-ω SST) επαναληπτικά, μέχρι να ικανοποιηθεί το κριτήριο σύγκλισης. Έγινε χρήση της αξονικής συμμετρίας του προβλήματος, ώστε να επιλυθεί ως αξονοσυμμετρικό-2D και προσεγγίστηκε ως σταθερή ροή.

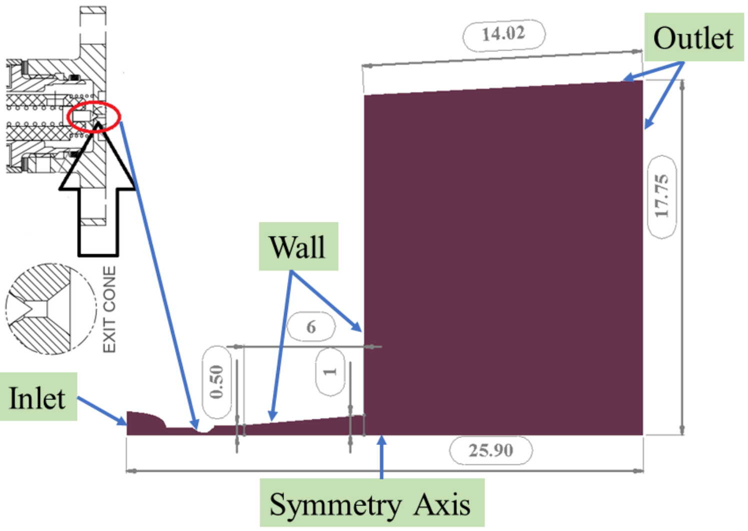

Εικόνα 1: Το χωρίο επίλυσης του προβλήματος. Στην είσοδο μια περιοχή σταθερής πίεσης (reservoir) ακολουθείται από μικρό τμήμα της βαλβίδας και στη συνέχεια το σχεδιαζόμενο ακροφύσιο 1. Η ροή συνεχίζεται στον θάλαμο κενού, όπου η τιμή πίεσης εξόδου είναι 1 $mbar$.

Τυπικά αποτελέσματα των προσομοιώσεων παρουσιάζονται στην εικόνα 2. Εφαρμόζοντας πίεση εισόδου 40 bar αερίου He, σε μια περιοχή που συμβολίζει τη δεξαμενή σταθερής πίεσης και πίεση εξόδου 1 $mbar$, το αέριο περνά μέσα από μέρος της βαλβίδας και όταν φτάσει στην πρώτη μικρή αποκλίνουσα περιοχή ξεκινά η απότομη πτώση της πυκνότητας και σχηματίζεται ένα τύπου barrel shock, του οποίου ο δίσκος Mach βρίσκεται μέσα στο κυλινδρικό τμήμα του σχεδιαζόμενου ακροφυσίου. Κύματα εκτόνωσης αποκλίνουν από την περιοχή αυτή και εφόσον ανακλαστούν στο τοίχωμα του ακροφυσίου αλλάζουν κατεύθυνση προς το κέντρο της ροής δημιουργώντας ένα νέο τύπου diamond shock. Η ροή συνεχίζεται και τα αποκλίνοντα κύματα εκτόνωσης από το diamond shock επανασυγκλίνουν μετά από την ανάκλασή τους στο εσωτερικό του ακροφυσίου και στο στρώμα διάτμησης, προκαλώντας μια μικρή αύξηση της πυκνότητας στην περιοχή που χρησιμοποιείται για τα πειράματα του LWFA (από την έξοδο του ακροφυσίου και για $1\ mm$).

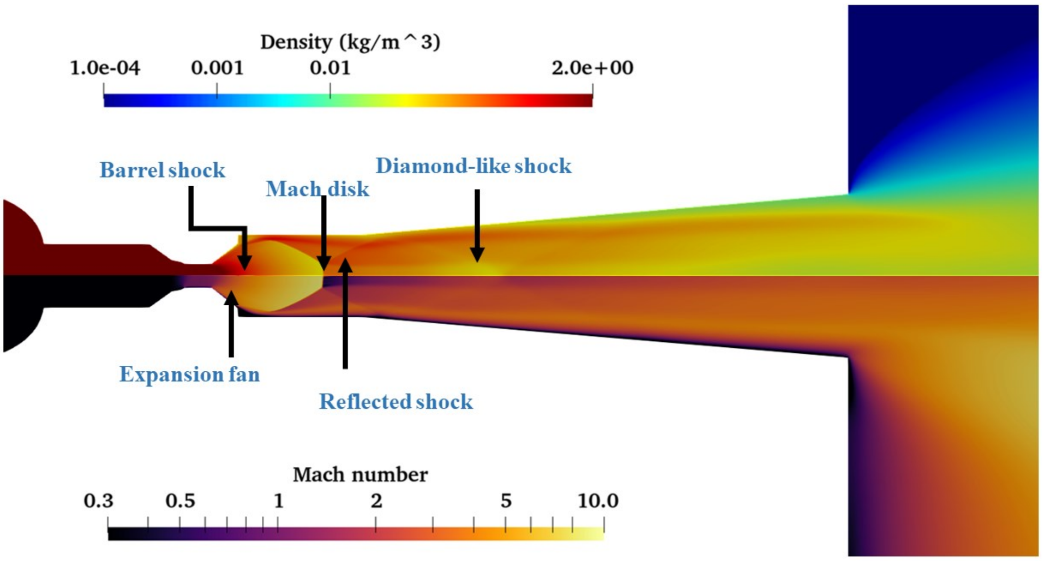

Εικόνα 2: Τυπικά αποτελέσματα των προσομοιώσεων με τον κώδικα ANSYS Fluent. Η πτώση της πυκνότητας μετά την περιοχή του λαιμού είναι απότομη και ένα τύπου barrel shock σχηματίζεται μέσα στην κυλινδρική περιοχή του σχεδιαζόμενου ακροφυσίου. Ανακλώμενα κύματα εκτόνωσης συγκλίνουν λίγο αργότερα και σχηματίζεται ένα δεύτερο τύπου diamond shock. Η ροή συνεχίζεται και στην περιοχή αμέσως μετά την έξοδο παρατηρείται μια τελευταία, μικρή αύξηση της πυκνότητας.

Το μοντέλο επίλυσης περιλάμβανε την καταστατική εξίσωση ιδανικού αερίου και επιλύθηκε για σταθερές τιμές του ιξώδους, της θερμικής αγωγιμότητας και της ειδικής θερμοχωρητικότητας με σταθερή πίεση. Η ίδια μελέτη επαναλήφθηκε για μεταβολή των παραπάνω μεγεθών σύμφωνα με την κινητική θεωρία των αερίων χωρίς ιδιαίτερη επίπτωση στις τιμές των μεγεθών αναφοράς (πυκνότητα, αριθμός Mach). Επιπλέον, επειδή παρατηρήθηκαν τοπικά τιμές πυκνότητας και πίεσης κοντά στις κρίσιμες (που μπορεί να οδηγήσουν σε συνθήκες για αλλαγή φάσης), μελετήθηκε η επίλυση του μοντέλου με τη χρήση της εξίσωσης πραγματικού αερίου Peng-Robinson. Σε αυτή την περίπτωση παρατηρήθηκε μεταβολή των μεγεθών αναφοράς <8%.

Η μελέτη αυτή διενεργήθηκε για 4 διαφορετικά αέρια (He, Ne, Ar και N_2), για 5 διαφορετικής γεωμετρίας ακροφύσια (Πίνακας 1) των οποίων τα σχέδια παρατίθενται στο Appendix B, και για ένα σύνολο παραμέτρων όπως η πίεση εισόδου στη δεξαμενή και η πίεση εξόδου στο θάλαμο που εκτονώνεται το αέριο. Τα προφίλ της πυκνότητας όλων των ακροφυσίων για οριακές συνθήκες ίδιες με τις παραπάνω παρουσιάζονται στην εικόνα 3, για $400\ \mu m$ απόσταση από την έξοδο του ακροφυσίου, περιοχή ενδιαφέροντος για τα πειράματα. Όπως φαίνεται, παρουσιάζουν κορυφές στην άκρη και πτώση στη μέση.

Ακροφύσιο	1	2	3	4	5
Cone length (mm)	6	8	3	6	6
Base length (mm)	1.5	3	1.5	1.5	2
Exit diameter (mm)	2	3	2	2.5	3
Straight part (mm)	-	-	-	-	2

Πίνακας 1: Διαστάσεις των ακροφυσίων που μελετήθηκαν.

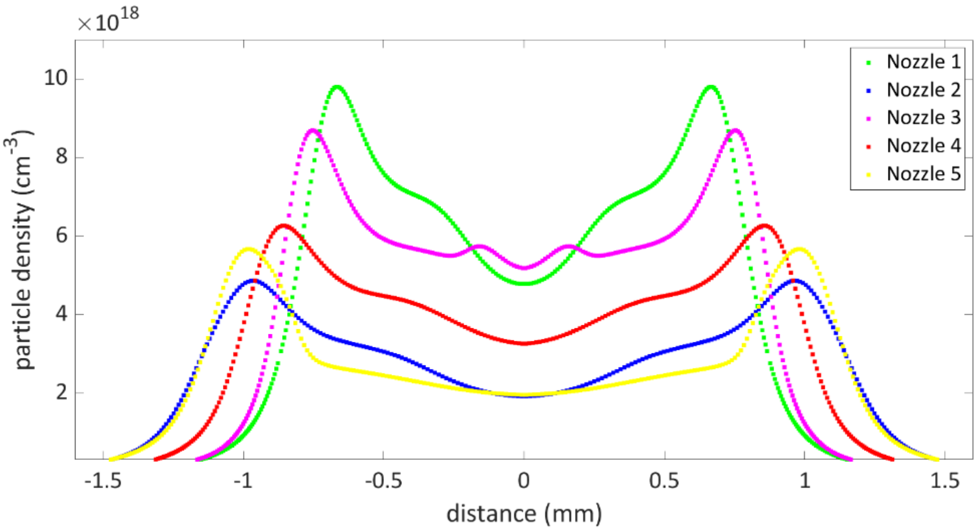

Εικόνα 3: Η τιμή της σωματιδιακής πυκνότητας του αερίου He $400\,\mu m$ από την έξοδο κάθε ακροφυσίου (Πίνακας 1) για αέριο He, $40\ bar$ πίεση στην είσοδο και $1\ mbar$ στην έξοδο.

Επιπλέον, σχεδιάστηκαν και μη συμμετρικά ακροφύσια με σκοπό τη δημιουργία ενός προφίλ πυκνότητας κατάλληλου για LWFA με τη μέθοδο down-ramp injection, των οποίων τα σχέδια παρατίθενται στο Appendix B. Όλα τα ακροφύσια κατασκευάστηκαν με τη μέθοδο της τριδιάστατης εκτύπωσης. Δοκιμάστηκαν τρεις διαφορετικές τεχνικές, οι FDM, SLA και LMD.

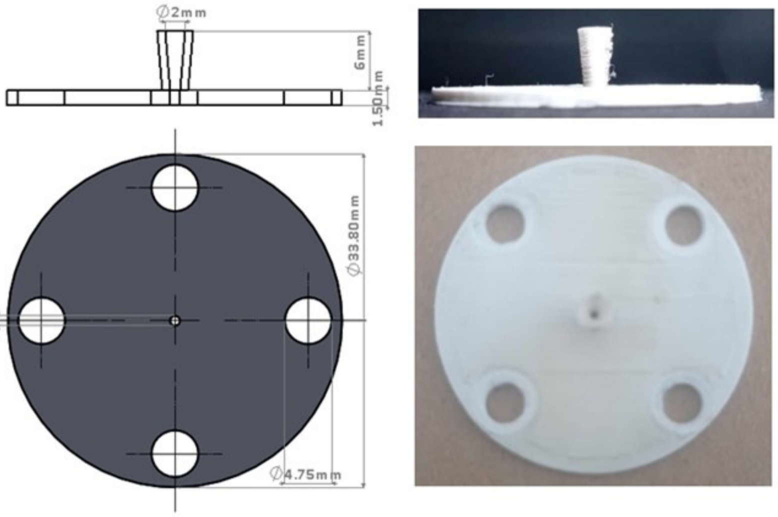

Εικόνα 4: σχέδιο και φωτογραφίες από το εκτυπωμένο με FDM ακροφύσιο 1.

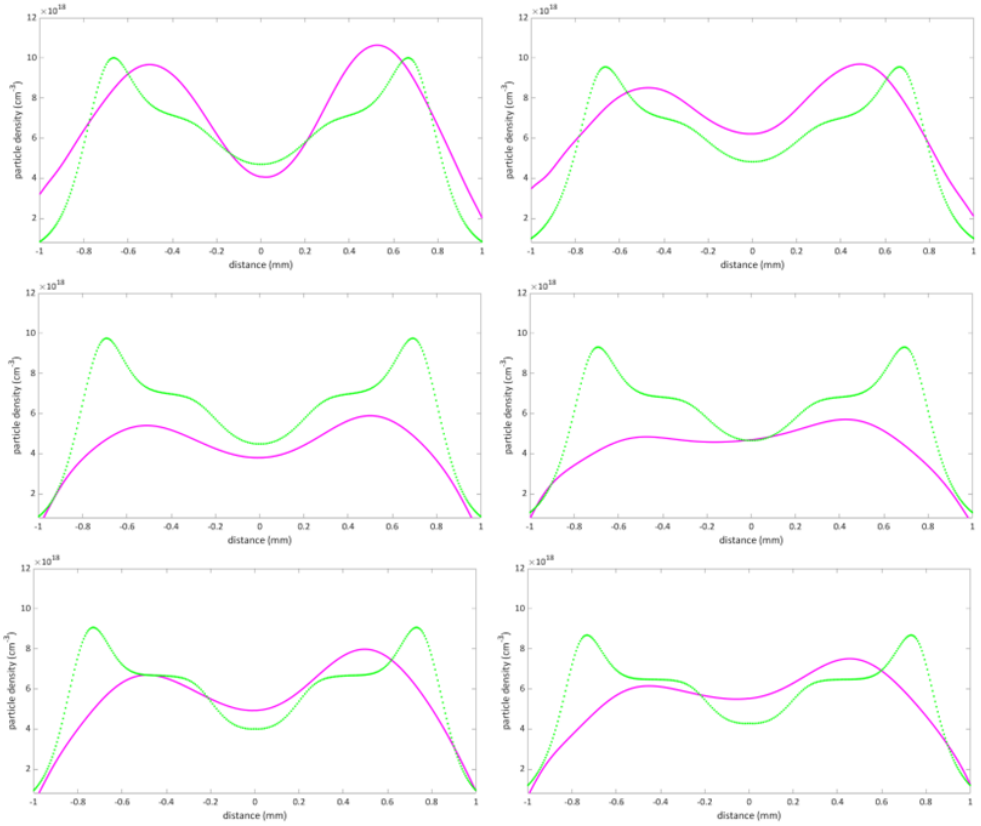

Εικόνα 5: Προφίλ πυκνότητας, που προέκυψαν από συμβολομετρικές μετρήσεις (μωβ γραμμή) από το ακροφύσιο 1 για He (πάνω) Ne (μέση) και Ar (κάτω) με 40 bar πίεση στην είσοδο συγκρίνονται με αυτή που προέκυψε από την προσομοίωση (πράσινη γραμμή) για απόσταση $300\ \mu m$ (αριστερά) και $500\ \mu m$ (δεξιά) από την έξοδο του ακροφυσίου. Για τις μετρήσεις αναπτύχθηκε συμβολόμετρο τύπου Νομάρσκι.

Στη συνέχεια μετρήθηκε η πυκνότητα του αερίου που προκύπτει για κάθε ακροφύσιο, για 4 διαφορετικά αέρια και για διάφορες πιέσεις στην είσοδο της βαλβίδας με τη μέθοδο της συμβολομετρίας. Αναπτύχθηκε συμβολόμετρο τύπου

Νομάρσκι και η ανάλυση των αποτελεσμάτων έγινε με τη χρήση κώδικα που επέτρεπε την ανάδειξη ασυμμετριών στη ροή του αερίου. Έγινε σύγκριση των αποτελεσμάτων των μετρήσεων με τις προσομοιώσεις και βρέθηκαν κατά βάση σε καλή συμφωνία. Για παράδειγμα, στην εικόνα 5 παρουσιάζονται αποτελέσματα από το ακροφύσιο 1 όπου η πυκνότητα που μετρήθηκε για He, Ne και Ar με 40 bar πίεση στην είσοδο συγκρίνονται με αυτή που προέκυψε από την προσομοίωση για απόσταση 300 και $500\ \mu m$ από την έξοδο του ακροφυσίου.

Επιπλέον, για τα μη συμμετρικά ακροφύσια, ελήφθησαν εικόνες συμβολής από 4 διαφορετικές γωνίες, προκειμένου να γίνει υπολογισμός της πυκνότητας με τη μέθοδο της τομογραφίας. Στην εικόνα 6 παρουσιάζονται αποτελέσματα των προφίλ της πυκνότητας που προέκυψαν από το ακροφύσιο NS 1 για διάφορες αποστάσεις από την έξοδο του. Αριστερά, παρουσιάζονται τα προφίλ που προέκυψαν στην κατεύθυνση διάδοσης του λέιζερ, τα οποία δημιουργούν το προσδοκώμενο down-ramp, ακολουθούμενο από μια περιοχή χαμηλής αλλά σχεδόν σταθερής πυκνότητας. Δεξιά παρουσιάζεται η τιμή της πυκνότητας κάθετα από την κατεύθυνση διάδοσης του λέιζερ. Σύμφωνα με τη βιβλιογραφία, μέχρι τώρα τα προφίλ αυτά παράγονται με τη χρήση διαδοχικών ακροφυσίων με διαφορετικό προφίλ αερίων ή με τη χρήση εμποδίου μικρών διαστάσεων (π.χ. ξυράφι) πάνω από το ακροφύσιο. Η δημιουργία ενός τέτοιου προφίλ πυκνότητας με τη χρήση ενός μόνο ακροφυσίου είναι σημαντική διότι απλοποιεί την πειραματική διάταξη.

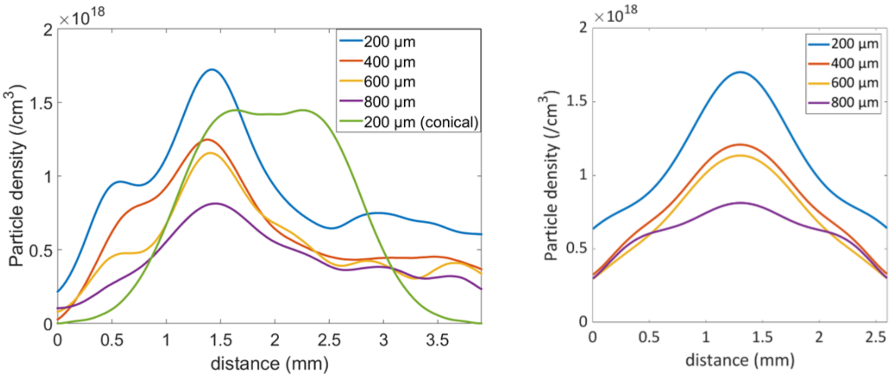

Εικόνα 6: Προφίλ πυκνότητας που προέκυψαν από συμβολομετρικές μετρήσεις κατά μήκος (αριστερά) και κάθετα (δεξιά) στην κατεύθυνση διάδοσης του λέιζερ για το μη συμμετρικό ακροφύσιο NS 1 σε διάφορες αποστάσεις από την έξοδο του ακροφυσίου.

Πειράματα επιτάχυνσης ηλεκτρονίων

Τα ακροφύσια σχεδιάστηκαν με σκοπό την επίτευξη ελέγχου των χαρακτηριστικών της δέσμης των ηλεκτρονίων μέσα από τα προφίλ της πυκνότητας. Εφόσον χαρακτηρίστηκαν με συμβολομετρία, κάποια από αυτά χρησιμοποιήθηκαν και σε πειράματα LWFA. Τα πειράματα που παρουσιάζονται διεξήχθησαν με τη διάταξη που σχεδιάσαμε και υλοποιήσαμε στο Ινστιτούτο Φυσικής Πλάσματος και

Λέιζερ (ΙΦΠΛ) του Ελληνικού Μεσογειακού Πανεπιστημίου. Όπως φαίνεται στην εικόνα 7, η δέσμη του λέιζερ Ζευς διαμέτρου 5.5 cm, χρονικής διάρκειας παλμού 25 fs και ενέργειας $\sim 1\,J$ εστιάζεται πάνω από τον πίδακα (jet) αερίου σε ένταση μεγαλύτερη από $10^{19}\,W/cm^2$. Εκεί συναντά τον πίδακα αερίου που απελευθερώνεται από μια ηλεκτρομαγνητική βαλβίδα, η οποία ανοίγει κατόπιν σήματος που έρχεται από το λέιζερ και διαμορφώνεται από ακροφύσιο της επιλογής μας. Η αλληλεπίδραση παράγει ένα κανάλι πλάσματος το οποίο, λόγω της μεταβολής της πυκνότητας του πλάσματος, παρουσιάζει περιοχές διαφορετικής φωτεινότητας και στη διάταξη αυτή καταγράφεται με τη μέθοδο της σκιαγραφίας. Τα ηλεκτρόνια που επιταχύνονται στη κατεύθυνση διάδοσης του λέιζερ περνούν μέσα από ένα ζεύγος μαγνητών σταθερού μαγνητικού πεδίου και εκτρέπονται ανάλογα με την ενέργειά τους από τη δύναμη Lorentz κάθετα στο μαγνητικό πεδίο και στην αρχική τους ταχύτητα. Έτσι, το φάσμα της δέσμης των ηλεκτρονίων απεικονίζεται σε μια κάμερα όπως και η γωνιακή της απόκλιση. Αποτελέσματα του πειράματος παρουσιάζονται στις εικόνες 8, 9 και 10 για τη χρήση των ακροφυσίων 0, 1 και 2. Το ακροφύσιο 0 είναι κυλινδρικό με διάμετρο 0.8 mm και παραδόθηκε μαζί με την βαλβίδα. Τα ακροφύσια 1 και 2 σχεδιάστηκαν και εκτυπώθηκαν στα πλαίσια αυτής της διατριβής και έχουν διάμετρο 2 και 3 mm αντίστοιχα, όπως φαίνεται στον Πίνακα 1.

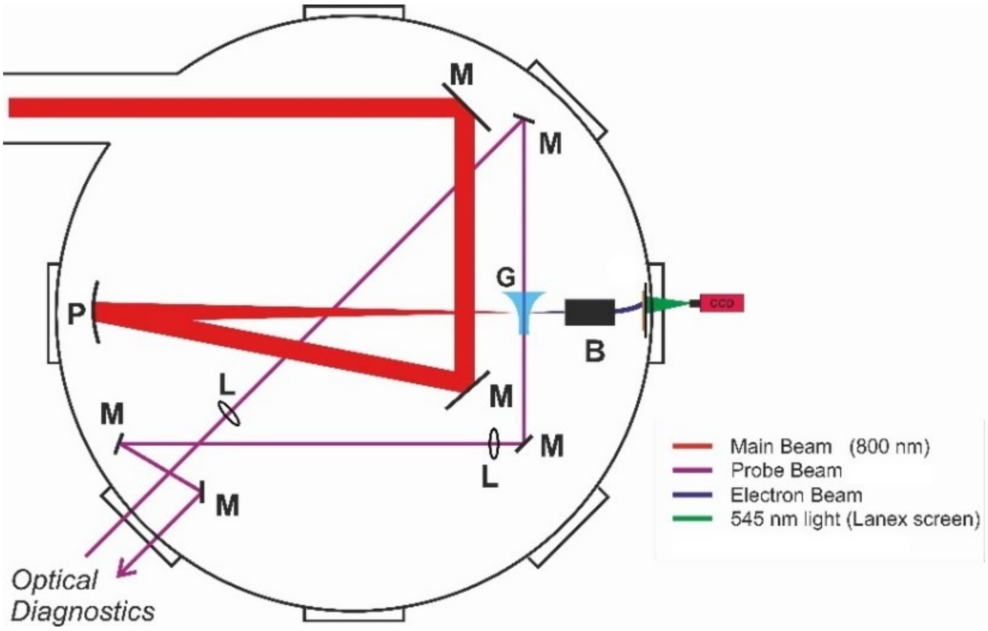

Εικόνα 7: Σχέδιο της πειραματικής διάταξης που αναπτύξαμε στο κεντρικό θάλαμο κενού του ΙΦΠΛ. Το λέιζερ εισέρχεται στο θάλαμο και εστιάζεται πάνω από τον πίδακα αερίου. Ο μηχανισμός LWFA λαμβάνει χώρα όταν το λέιζερ εστιάζεται πάνω από την έξοδο της ηλεκτρομαγνητικής βαλβίδας όπου ένα ακροφύσιο διαμορφώνει τη ροή του αερίου. Η δέσμη ηλεκτρονίων υψηλής ενέργειας που παράγεται διασχίζει ένα ισχυρό μαγνητικό πεδίο και εκτρέπεται ως συνάρτηση της ενέργειας των ηλεκτρονίων. Το αποτύπωμα της αλληλεπίδρασης της δέσμης των ηλεκτρονίων με μια φθορίζουσα οθόνη καταγράφεται σε μια κάμερα και με τη χρήση κατάλληλου κώδικα υπολογίζεται το ενεργειακό φάσμα. Μια δευτερεύουσα δέσμη του λέιζερ περνά κάθετα από την περιοχή αλληλεπίδρασης και χρησιμοποιείται για την απεικόνιση της σκιάς του καναλιού πλάσματος που δημιουργείται.

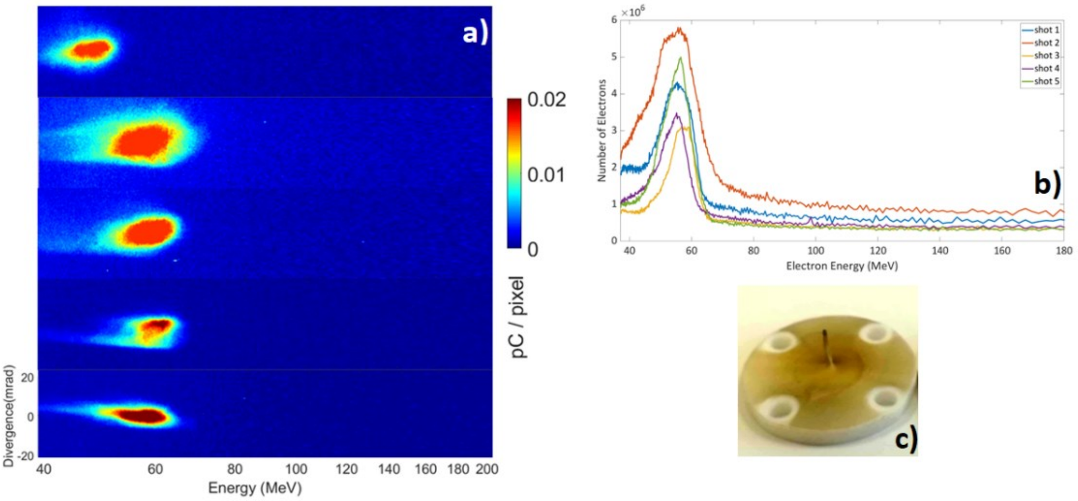

Εικόνα 8: a) Φάσματα ενέργειας των ηλεκτρονίων και b) η προβολή τους στον άξονα της ενέργειας c) με τη χρήση του κυλινδρικού ακροφυσίου με διάμετρο εξόδου $0.8\ mm$ για αέριο He με πίεση στην είσοδο $12\ bar$.

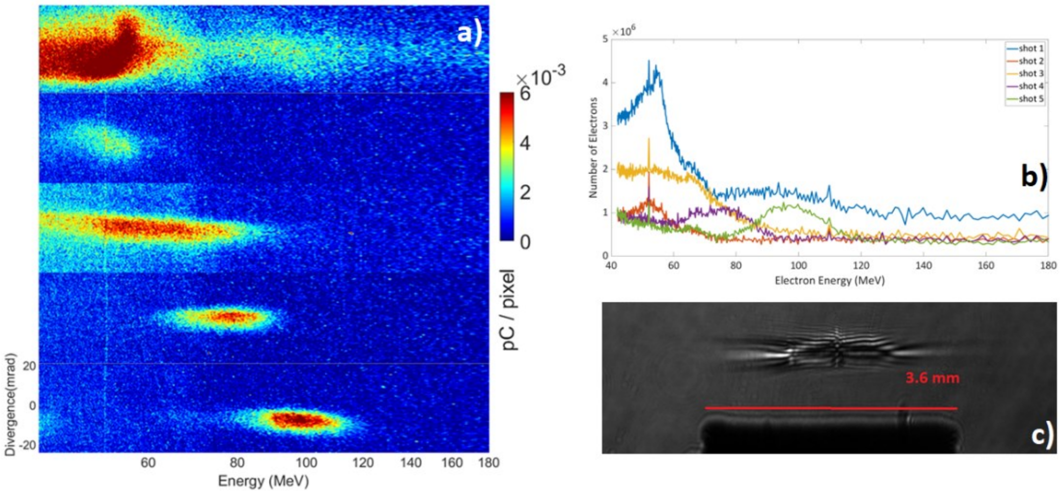

Εικόνα 9: a) Φάσματα ενέργειας των ηλεκτρονίων και b) η προβολή τους στον άξονα της ενέργειας με τη χρήση του ακροφυσίου 1 με διάμετρο εξόδου $2\ mm$ για αέριο He με πίεση στην είσοδο $40\ bar$. c) Ενδεικτικό κανάλι πλάσματος με τη μέθοδο της σκιαγραφίας.

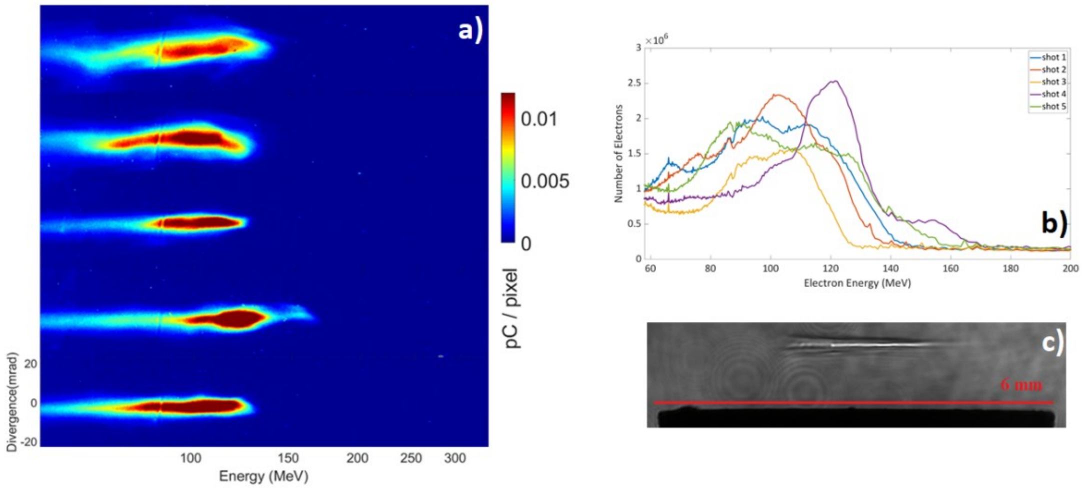

Εικόνα 10: a) Φάσματα ενέργειας των ηλεκτρονίων και b) η προβολή τους στον άξονα της ενέργειας με τη χρήση του ακροφυσίου 2 με διάμετρο εξόδου 3 mm για αέριο He με πίεση στην είσοδο 35 bar. c) Ενδεικτικό κανάλι πλάσματος με τη μέθοδο της σκιαγραφίας.

Συγκρίνοντας τα ενεργειακά φάσματα των εικόνων 8-10 παρατηρούμε ότι η ενέργεια της δέσμης των ηλεκτρονίων όπως και το εύρος της μεγαλώνει όσο μεγαλώνει το μήκος του ακροφυσίου. Η μέθοδος αυτή επιτρέπει να αυξηθεί η μέγιστη ενέργεια όσο το μήκος παραμένει μικρότερο από τα όρια που αναφέρθηκαν νωρίτερα.

Επιπλέον παρατηρήσαμε στην εικόνα 9 (c) ότι στην σκιαγραφία για το ακροφύσιο 1 εμφανίζονται πολλαπλά κανάλια πλάσματος αντί για 1. Επιπλέον, στις PIC προσημειώσεις για προφίλ πλάσματος που προέκυψε από τη μέτρηση πυκνότητας για το ακροφύσιο 1 στα 40 bar αερίου He, φάνηκε ότι στην περίπτωση αυτή είχαμε filamentation του λέιζερ.

Οι PIC προσημειώσεις διεξήχθησαν επίσης για προφίλ πλάσματος που προέκυψε από τη μέτρηση πυκνότητας για το ακροφύσιο 2 στα 40 bar αερίου He και του NS 1 σε αντίστοιχες συνθήκες. Τα αποτελέσματα έδειξαν και στις 3 περιπτώσεις ότι η είσοδος των ηλεκτρονίων στην δομή επιτάχυνσης συνέβη μετά την πάροδο του λέιζερ από την πτώση πυκνότητας που παρατηρείται στα προφίλ και εφόσον σε αυτήν την περιοχή η φούσκα επιμηκύνθηκε, όπως δηλαδή συζητήθηκε για το μηχανισμο down-ramp injection. Στην περίπτωση του NS 1 όπου το πείραμα δεν έχει διεξαχθεί ακόμα, το αναμενόμενο ενεργειακό φάσμα φαίνεται να παρουσιάζει αρκετό ενδιαφέρον. Επιπλέον ένα βασικό πλεονέκτημα που καταγράφεται στη βιβλιογραφία για τέτοιου είδους προφίλ είναι η αυξημένη επαναληψιμότητα, το οποίο είναι σημαντικό χαρακτηριστικό για τη χρήση των ηλεκτρονίων σε εφαρμογές.

Στη συνέχεια παρουσιάζονται τα πειραματικά αποτελέσματα από την ίδια διάταξη για τη χρήση του ακροφυσίου 2 εξετάζοντας ένα εύρος πιέσεων εισόδου $30 - 45\ bar$ με αέριο N_2. Κατά τη διεξαγωγή του πειράματος η ενέργεια του λέιζερ μετρήθηκε μικρότερη, οπότε η μέγιστη ένταση αγγίζει τα $5\ 10^{18}\ W/cm^2$. Η δέσμη ηλεκτρονίων εμφανίζεται για πρώτη φορά πάνω από τα 30 bar, όπως είναι αναμενόμενο αφού υπάρχει ένα κατώφλι πυκνότητας για την εισαγωγή ηλεκτρονίων στο μηχανισμό LWFA, ενώ όσο αυξάνεται η πίεση, άρα και η πυκνότητα, η μέση μέγιστη κορεσμένη ενέργεια πέφτει, ενώ το φορτίο και η μέση μέγιστη ενέργεια αυξάνονται. Στην εικόνα 11 παρουσιάζονται μέσες τιμές των μεγεθών αυτών για πολλαπλά φάσματα (8-12 φάσματα ανά πίεση). Επιπλέον, από τα 40 και κυρίως στα $45\ bar$ παρατηρείται το φαινόμενο του beam loading, όπου το φορτίο είναι τόσο μεγάλο που τα ηλεκτρόνια χάνουν πλέον τα χαρακτηριστικά μορφής δέσης και μοιάζουν περισσότερο με ένα συνεχές ρεύμα.

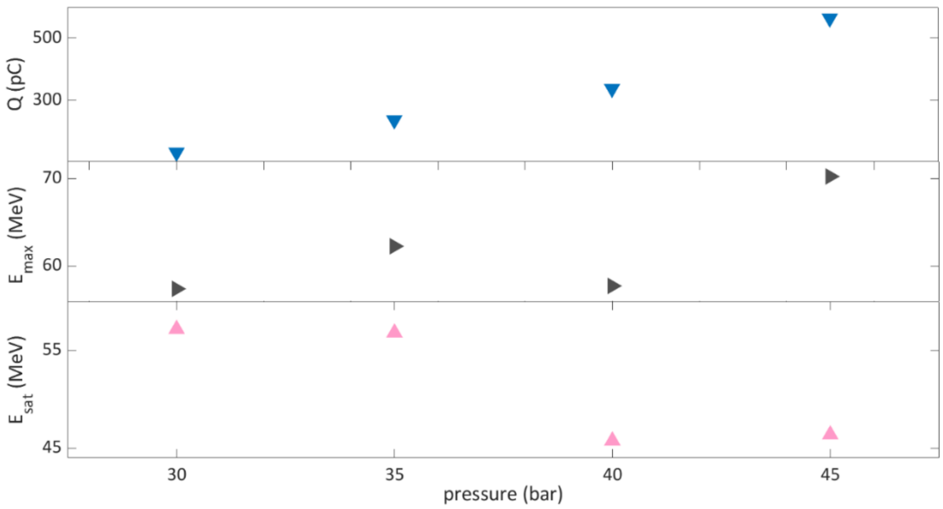

Εικόνα 11: Μέση τιμή του φορτίου (πάνω), μέγιστης ενέργειας (μέση) και μέγιστης κορεσμένης ενέργειας (κάτω) για πολλαπλά φάσματα σε συνάρτηση με την πίεση.

Δυστυχώς στην περίπτωση αυτή δεν διενεργήθηκαν PIC προσομοιώσεις, διότι η χρήση N_2 που συνδέεται με το μηχανισμό ionization injection είναι υπολογιστικά πολύ κοστοβόρα. Επιπλέον, με βάση τα προφίλ πυκνότητας που μετρήθηκαν με συμβολομετρία για αυτές τις συνθήκες και τα αποτελέσματα των παραπάνω προσομοιώσεων υποθέτουμε ότι και εδώ ο μηχανισμός down-ramp injection έχει παίξει ρόλο στην είσοδο των ηλεκτρονίων στη δομή επιτάχυνσης.

Πείραμα ταυτοποίησης της ακτινοβολίας Βήτατρον

Επιπλέον παρουσιάζεται ένα πείραμα ταυτοποίησης της Βήτατρον ακτινοβολίας ακτίνων χ. Η ακτινοβολία αυτή εκπέμπεται ταυτόχρονα και συγγραμμικά με την δέσμη ηλεκτρονίων που παράγεται με τον μηχανισμό LWFA καθώς τα ηλεκτρόνια μέσα στη φούσκα ταλαντώνονται εγκάρσια στη κατεύθυνση του λέιζερ και όταν αυτά αλλάζουν κατεύθυνση, εκπέμπουν φωτόνια στην περιοχή των ακτίνων χ. Το αποτέλεσμα είναι μια δέσμη ακτίνων χ με μικρή γωνιακή απόκλιση. Η δέσμη αυτή παράγεται μόνο όταν οι συνθήκες του LWFA πληρούνται και ηλεκτρόνια έχουν εισαχθεί στη δομή επιτάχυνσης. Επειδή η ακτινοβολία

Βήτατρον παράγεται από μια πολύ μικρή περιοχή, έχει μεγάλο βαθμό συμφωνίας και σε συνδυασμό με την πολύ μικρή διάρκεια της αποκτά χαρακτηριστικά επιθυμητά για εφαρμογές στην απεικόνιση μικροσκοπικών δομών.

Τροποποιώντας την υφιστάμενη διάταξη για την ανίχνευση ηλεκτρονίων στο ΙΦΠΛ διενεργήσαμε πειράματα για τη μελέτη αυτής της ακτινοβολίας. Αρχικά, διενεργήθηκε μια προκαταρκτική μελέτη προκειμένου να ταυτοποιήσουμε τα χαρακτηριστικά αυτής της δέσμης και να αποκλείσουμε άλλους μηχανισμούς παραγωγής ακτίνων χ από το πλάσμα.

Η μελέτη αυτή διενεργήθηκε με τη χρήση κατάλληλων φωτοδιόδων. Η διάταξη για την παραγωγή ακτίνων χ είναι παρόμοια με εκείνη για LWFA με τη διαφορά ότι τοποθετήθηκαν δύο φωτοδίοδοι κατάλληλα φιλτραρισμένες από κάθε άλλου είδους ακτινοβολία μέσα στο θάλαμο, η μια στην θέση που αναμένονται οι ακτίνες χ τύπου Βήτατρον και η άλλη σε διάφορες θέσεις αλλά ίση απόσταση, ενώ τα αποτελέσματα που παρουσιάζονται εδώ είναι για κάθετα σε την πρώτη. Το ζεύγος μαγνητών παρέμεινε ώστε να εκτρέψει τα ηλεκτρόνια μακριά από την ενεργό επιφάνεια της φωτοδιόδου, όμως δεν υπήρχε η δυνατότητα απεικόνισης του φάσματος τους. Σε πρώτη φάση μετρήσαμε τα σήματα των φωτοδιόδων αυξάνοντας την πίεση εισόδου στη βαλβίδα με το ακροφύσιο 2 από 15 έως 42 bar, ενώ το αέριο ήταν He.

Στην εικόνα 12 παρουσιάζεται το συνολικό σήμα μετρημένο στη φωτοδίοδο κάθετα (πάνω) και στη κατεύθυνση διάδοσης του λέιζερ (κάτω). Στην πρώτη περίπτωση το σήμα ανεβαίνει γραμμικά με την πίεση (άρα και την πυκνότητα, ενώ στη δεύτερη το σήμα εμφανίζεται πρώτη φορά από τα 30 bar και πάνω, παρουσιάζοντας συμπεριφορά κατωφλίου όπως συμβαίνει και με το LWFA.

Επιπλέον προκειμένου να ελέγξουμε την κατευθυντικότητα των φωτονίων μεταβάλλαμε την θέση της ‘πηγής’ και στην εικόνα 13 αντίστοιχα παρουσιάζονται τα συνολικά σήματα στις δυο φωτοδιόδους. Εφόσον το τελευταίο οπτικό εστίασης καθώς και η βαλβίδα που ελέγχει τη ροή του αερίου ήταν τοποθετημένα σε μηχανοκίνητες βάσεις που μετακινούνται με ακρίβεια μm, τις μετακινήσαμε ισόποσα, παράλληλα, σε απόσταση μέχρι και 4 mm εκατέρωθεν της αρχικής θέσης. Με αυτό τον τρόπο παρατηρήσαμε ότι η το σήμα κάθετα παρέμεινε σταθερό, ενώ στην κατεύθυνση διάδοσης έπεσε μόλις απομακρύνθηκε πάνω από 1 mm.

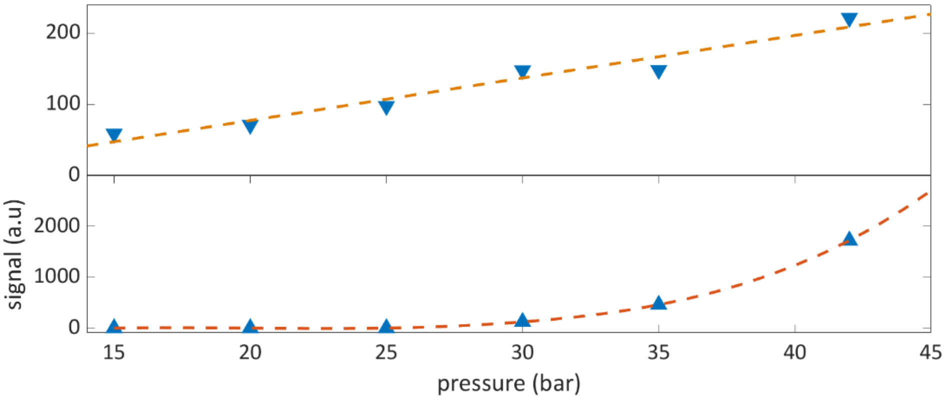

Εικόνα 12: Συνολικό σήμα στη φωτοδίοδο κάθετα (πάνω) και στη κατεύθυνση διάδοσης του λέιζερ (κάτω) ως συνάρτηση της πίεσης εισόδου στη βαλβίδα. Στην πρώτη περίπτωση το σήμα ανεβαίνει γραμμικά ενώ στη δεύτερη ξεκινάει να εμφανίζεται στα $30\ bar$ και αυξάνεται μη γραμμικά.

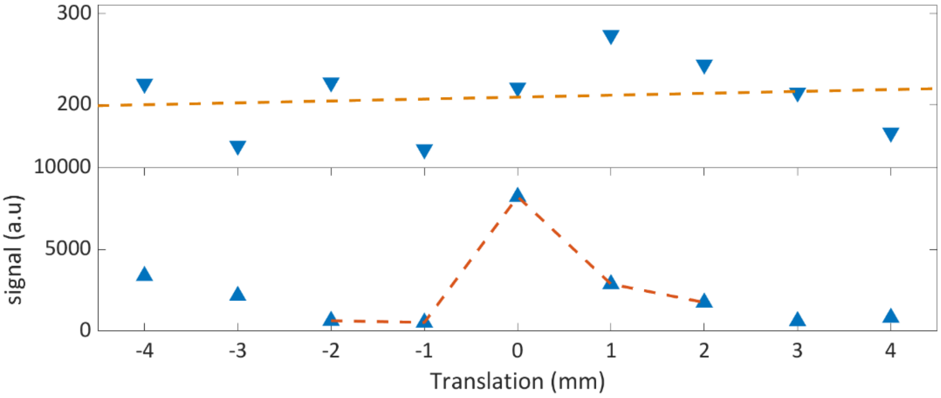

Εικόνα 13: Συνολικό σήμα στη φωτοδίοδο κάθετα (πάνω) και στη κατεύθυνση διάδοσης του λέιζερ (κάτω) ως συνάρτηση της θέσης της πηγής. Στην πρώτη περίπτωση το σήμα παραμένει σταθερό ενώ στη δεύτερη μεταβάλλεται απότομα για μετακίνηση της πηγής των φωτονίων κάθετα στην διεύθυνση διάδοσης της ακτινοβολίας Βήτατρον.

Από την προκαταρκτική μελέτη προέκυψε ότι η ακτινοβολία που μετρήθηκε στην κατεύθυνση που αναμενόταν η ακτινοβολία Βήτατρον παρουσιάζει μη γραμμική συμπεριφορά ως προς την πυκνότητα, ενώ είναι και είναι κατευθυντική, χαρακτηριστικά που αποδίδονται σε ακτινοβολία τύπου Βήτατρον. Αντίθετα, στην φωτοδίοδο που βρισκόταν κάθετα, τα σήματα επέδειξαν γραμμική μεταβολή με την πίεση καθώς και δε μεταβλήθηκαν με τη μεταβολή της θέσης της πηγής, άρα ο μηχανισμός παραγωγής τους είναι διαφορετικός.

Συμπεράσματα

Ο μηχανισμός LWFA βασίζεται στη μη γραμμική αλληλεπίδραση του λέιζερ με αέριο στόχο για την επιτάχυνση ηλεκτρονίων σε σχετικιστικές ταχύτητες και την παραγωγή ακτίνων χ τύπου Βήτατρον. Η αλληλεπίδραση εξαρτάται από τα χαρακτηριστικά του λέιζερ και το προφίλ της πυκνότητας του αερίου. Στην διατριβή αυτή παρουσιάζεται μια μελέτη για το σχεδιασμό και την κατασκευή ακροφυσίων που παράγουν προφίλ κατάλληλα για πειράματα με το συγκεκριμένο μηχανισμό. Τα προφίλ της πυκνότητας μετρήθηκαν και συγκρίθηκαν με τις προσομοιώσεις και στη συνέχεια κάποια από αυτά χρησιμοποιήθηκαν σε πειράματα LWFA, όπου διαπιστώθηκε ότι επετεύχθη σε ένα βαθμό ο έλεγχος κάποιων χαρακτηριστικών των δεσμών ηλεκτρονίων που παράγονται. Ο έλεγχος της πηγής των ηλεκτρονίων είναι ένα κρίσιμο βήμα για την χρήση της σε εφαρμογές. Επιπλέον, διαπιστώθηκε η ύπαρξη δέσμης ακτίνων χ τύπου Βήτατρον.

Chapter 1: Introduction

This dissertation explores the interaction between high-intensity laser pulses and plasmas generated by gaseous targets, aiming at accelerating electrons via the LWFA method and produce x-ray radiation. Experiments took place at the Zeus laser facility at the Institute of Plasma Physics & Lasers (IPPL) of the Hellenic Mediterranean University Centre of Research & Innovation. The laser pulses used have ultrashort duration ($\tau_0 < 25\,fs$), near-infrared wavelength ($\lambda_0 = 0.8\,\mu m$), up to $1.2\,J$ of energy, and high repetition rates (up to $10\,Hz$). The plasma sources applied are from gaseous targets, i.e. lie in the underdense plasma regime. With the high-repetition-rate capability, optimization of certain parameters of the interaction including the nozzle geometry, benefits for the development of a well-defined and stable electron source for applications.

In this chapter, the background of such interactions is presented, as well as the state-of-the-art works in this field, especially focusing on the role of the gas density profile. In addition, the advantages of a LWFA relativistic electron source in comparison to conventional accelerators and its potential applications are discussed.

1.1 BACKGROUND

When someone talks about lasers, any audience is thinking of several devices. Lasers are simultaneously daily life objects, such as pointers or medical devices for regular eye surgery, and also massive complex systems, enclosed in specially designed buildings that support state-of-the-art research, such the most energetic laser in Europe the Laser Mega Joule (LMJ) which delivers energy $> 1\,MJ$ to its targets. The acronym LASER stands for Light Amplification by Stimulated Emission of Radiation, a device first built 60 years ago (Maiman T. H., 1960). The basic idea is that when a material, the so-called gain medium (e.g., gas, liquid, crystal), is pumped by an external energy source, its electrons are excited to higher energy levels for a very short time and then decay back to their initial energy level, emitting a photon, carrying energy equal to the difference of energy of the two energy levels. When early enough specific energy photons seed the gain medium, stimulated emission happens, and photons from the medium are emitted in the same direction as the seeded photons and present the same characteristics (polarization, energy, and phase). Finally, the seeded light is amplified, resulting in a temporally and spatially coherent light source. Based on the laser operating principle, technology evolved rapidly and offered outstanding achievements, while the term now is more generic. There are lasers of various wavelengths (up to x-rays), pulse durations (down to attoseconds), beam energy (up to MJ), and operating frequency (up to kHz), providing support in various scientific fields, laser-plasma interactions being among them.

Plasma is the fourth state of matter, where ions coexist with electrons in a mixture governed by electric and magnetic fields. Plasma is the most abundant state in the universe; for example, stars are plasma balls. The plasma state is not easy to preserve on earth as, without the action of an external force, ions and electrons of the plasma quickly recombine and result in neutral atoms. However, during a lightning strike, the powerful electrical discharge creates plasma in the atmosphere, which emits the light we observe. Also, if someone is lucky to travel and meet polar auroras, he will see the light emitted because of the plasma, as solar plasma coming from the solar wind enters the earth's magnetosphere and excites or ionizes the atmosphere's particles, which then recombine and emit the light.

Given the abundance of plasma in the universe, there is a considerable interest in comprehending and governing it. The finest art we want to learn from plasma studies is fusion. The Sun is Earth's most trustworthy power supplier, providing a continuous energy flow. The energy is produced by the fusion of light nuclei, such as H, He, and their isotopes, a fuel easy to produce everywhere on earth, while the products of the reactions are easy to handle (mostly He and neutrons). These two reasons make fusion the most democratic and ecological solution at the same time.

In the laboratory, plasma is created for studies using, e.g., electrical discharge devices, such as Plasma Focus (Auluck et al., 2021; Haines, 2011) or Plasma Z-Pinch (Haines, 2011), but also via the interaction of matter with high-power lasers (C. Liu et al., 2019). Plasma is extensively studied, by many groups worldwide, building a community that had to adapt or develop the necessary experimental and theoretical tools to interpret their results.

Last year was a milestone for laser-plasma physics and laser-driven fusion groups, as a historical, scientific breakthrough was achieved. Many years after the theoretical prediction for the laser-driven fusion scheme, the National Ignition Facility (NIF) in the USA, after applying massive efforts in multidisciplinary fields, such as the engineering of new lasers, the design, and construction of the interaction area, the targets, and the necessary diagnostics, based on laborious experimental campaigns and theoretical studies along with numerical simulations, they succeeded for the first-time net energy gain during the interaction (Atzeni et al., 2022).

Another fascinating result, which emerged from laser-plasma interaction, is particle acceleration. From the year 2000, when three groups reported acceleration of ions up to some tens of MeV (Clark et al., 2000; Maksimchuk et al., 2000; Snavely et al., 2000) and then, ion and electron acceleration based on laser-plasma interaction are successively breaking their high-energy records and improving their beam characteristics. It's been more than a hundred years since particle accelerators[1] were first built, and they have offered their services countless times in fundamental physics, new technology, and applications. For a linear particle accelerator (LINAC), the basic idea is to inject a particle beam in successive RadioFrequency (RF) cavities and, by applying RF pulses, create ElectroMagnetic (EM) fields that accelerate the injected beam. The accelerating fields, developed at each cavity, are limited by the cavity's materials breakdown limits to $\sim 50\, MeV/m$. Thus, to achieve higher acceleration, longer LINACs, composed of more and more RF cavities, are necessary, or circular accelerators, where the particle beams circulate for multiple rounds, bent by huge magnetic fields. However, circular accelerators suffer from losses, as when the relativistic charged particles are perpendicularly accelerated, emit light. This light is known as synchrotron radiation, and although it is a deficiency for the circular accelerator, as it is an energy loss for charged particles, on the other hand, it is also a precious light source, useful in many experiments. Their contribution to particle physics is unique and unnegotiable, and up to now, it has motivated whole-continent collaboration projects with huge budgets, such as the Large Hadron Collider (LHC), the most significant and most expensive device ever constructed.

---

[1] For description of the operation principle of LINACS and circular accelerators see: https://en.wikipedia.org/wiki/Particle_accelerator

This continuous evolution was not only based on the spirit of knowledge, as all the intermediate steps have resulted in other great investments and achievements, applicable in fields like medicine and industry. Particle therapy is one of the most essential applications of LINACs, which are hosted in almost any peripheral hospital. However, regarding the demands for ongoing research, the idea of creating an even greater and more expensive device than LHC faces skepticism among scientists. In Figure 1-1 left) a top view of the LHC area and a possible Future Circular Collider (FCC) position is displayed (Https://Home.Cern/Science/Accelerators/Future-Circular-Collider).

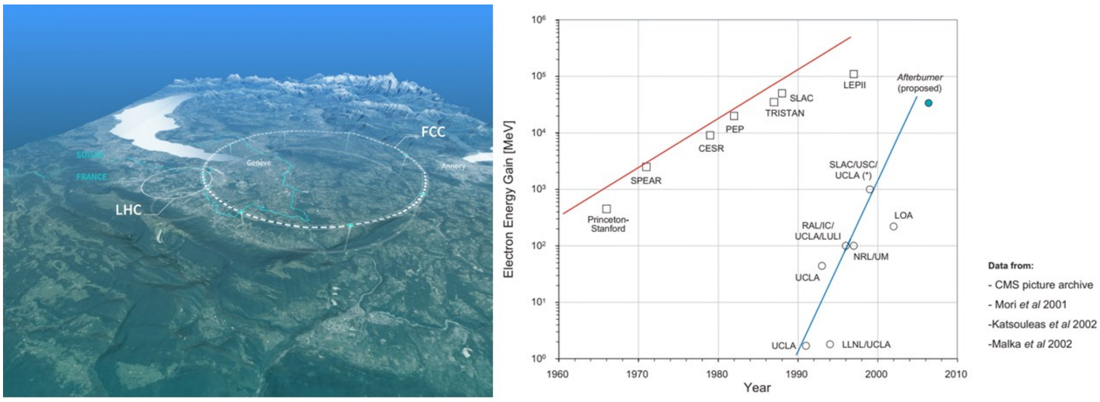

Figure 1-1: left) LHC top view and a schematic map of a possible location for the next generation, the so-called FCC (Https://Home.Cern/Science/Accelerators/Future-Circular-Collider). right) The progress of particle accelerators over the years is known as the Livingston curve (Bingham et al., 2004).

On the other hand, the size of laser-based particle accelerators is university-scaled, and their cost is more affordable. Therefore, they are a good candidate for medical applications, or as the first accelerator stage for a conventional particle accelerator (Joshi et al., 2020). In Figure 1-1 right) the particle acceleration evolution in terms of particle energy over time is displayed, a curve known as the Livingston curve (Bingham et al., 2004). After the '90s, the Laser-Plasma Accelerators (LPA) entered the game and have proven to be good competitors.

1.2 LWFA AND BETATRON RADIATION

The most well-known process for laser-induced-electron acceleration is called Laser WakeField Acceleration. The LWFA concept was introduced theoretically in 1979 by Tajima and Dawson (Tajima & Dawson, 1979) in a work that proposed two novel processes for electron acceleration that would significantly reduce an accelerator's length, compared to conventional accelerators. The second process, also laser based, will not be discussed here, as it is out of the scope of this dissertation. LWFA experimental realization was only feasible once laser technology permitted. The development of Ti: Sa lasers (Moulton, 1986) together with the Chirp Pulse Amplification (CPA) technique (Strickland & Mourou, 1985) which was awarded the Physics Nobel Prize in 2018, resulted in the development of high-power lasers. The basic idea of CPA technique is to stretch the ultra-short pulse temporally, then amplify the stretched pulse, while keeping its power below the damage threshold of the amplifier's materials and finally re-compress it to the fs level. LWFA was first realized in 2004 by three independent groups, which achieved electron bunches with energies up to $100\ MeV$ (Geddes et al., 2004; Mangles et al., 2004; Faure et al.,2004).

In an LWFA experiment, a gaseous target interacts with an ultra-short, high-intensity laser pulse, to accelerate electrons. As the laser pulse propagates through the gas, electrons are expelled out of a region called a bubble, while ions remain stable. Then electrons oscillate due to the space-charge force, forming an electron density wave with strong longitudinal electric fields exceeding $100\ GV/m$. Electrons injected from the rare side of the bubble are accelerated by the electric field at the laser propagation direction to ultra-relativistic energies over distances thousands of times shorter than in conventional particle accelerators. These electrons, when properly injected, present beam-like properties.

During the last 19 years, many groups studied this process and various ideas and techniques have been implemented, resulting in significant improvements in electron beam properties. To name a few, electron energy has increased significantly over the years (Leemans et al., 2006), especially after the appearance of PW lasers, with today's record at $8\ GeV$ obtained by the group of (Gonsalves et al., 2019). In addition, great improvements in beam characteristics, such as smaller charge, stable pointing, energy, and energy spread fluctuations, are reported when the density value is closest to the matching conditions (Mangles et al., 2007a). Higher beam pointing stability is reported by improving laser contrast (Mangles et al., 2006), or by installing an aperture transverse to the laser beam path, before the focusing optic (Nakanii et al., 2023). Higher average current is achieved via kHz repetition rate with mJ lasers (Gustas et al., 2018), and higher charge per shot (Couperus et al., 2017).

In 2004 the existence of an x-ray beam, resulting from the oscillation of the relativistic electrons in the WakeField was also demonstrated experimentally (Rousse et al., 2004). The x-ray beam is emitted at the laser and electron propagation direction, so-called Betatron radiation. As a photon source, Betatron radiation presents interesting characteristics, such as coherence, small angular divergence, and directionality. Experimental studies have reported significant improvements in this field, aiming to maximize the photon yield (Fourmaux et al., 2017; Mishra et al., 2022; Tomkus et al., 2020).

1.2.1 Role of gas density in LWFA and Betatron Radiation experiments

From the conceptual description of LWFA, it is evident that the basic components of an experiment are the high-power laser and the gaseous target. Globally, there are many laser facilities hosting lasers of some to multi-TW power and fewer hosting PW class lasers. LWFA is a kind of "resonant" process, as some matching conditions must be fulfilled to optimize the laser interaction with the gas, as discussed in Chapter 3. For multi-TW or PW lasers, the resonant conditions can be met by regulating the energy of the laser pulse; however, when few TW are only available, usually the maximum laser power must be exploited to accelerate electrons efficiently.

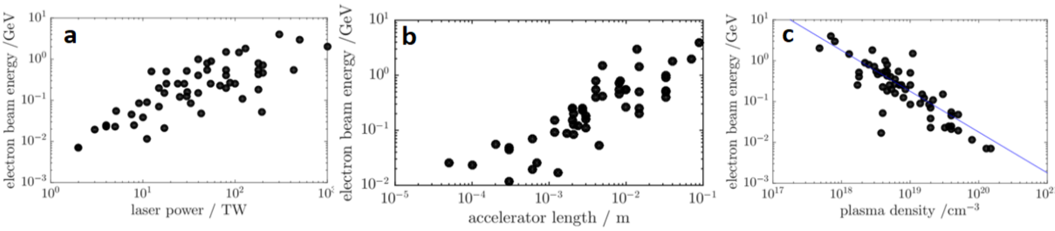

Figure 1-2: Maximum electron beam energy achieved by multiple different experiments combined as a function of a) laser power in TW, b) accelerator length in m and c) plasma density in cm^{-3}. Adopted from (Mangles, 2017).

Figure 1-2 combines the results of many LWFA experiments that took place in various facilities from a review presentation (Mangles, 2017), providing an idea of its scaling. According to Figure 1-2 a, one way to increase electron beam energy is by increasing laser power. At the same time, the gas density profile is a way to control and/or optimize the interaction (Figure 1-2 b & c). The accelerator length is related to the gaseous target length, and the plasma density is associated with the gaseous target density and composition. It is important to clarify that for the experimental points of Figure 1-2 b) and c), apart from the accelerator's length and plasma density, other parameters, such as laser power or focal spot size differ for several of the points. The connection between the gas density and the final electron beam energy, although described by a single relation according to various theoretical or simulation models, is highly complicated.

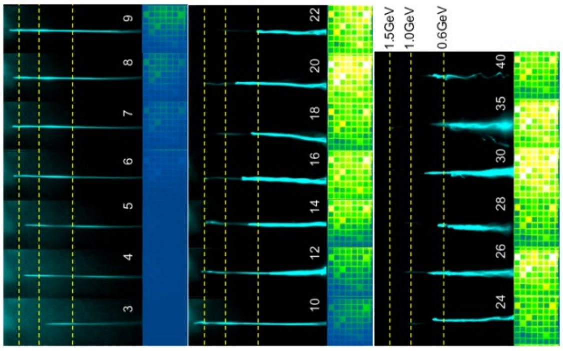

Figure 1-3: Electron energy spectrum and the simultaneously Betatron radiation profile, obtained with a gas cell with adjustable length from $3 - 40\ mm$. Adopted from (Wood et al., 2017).

In (Wood et al., 2017) a study of the resulting electron beam using an adjustable-length gas cell as a gaseous target was presented. According to the experimental results, a wide energy range electron source is created. Figure 1-3 shows that while the length increases from 3 to $10\,mm$, the maximum electron energy increases, providing numerous electrons with a small angular divergence. However, a further increase of the gas cell length from 12 to $40\,mm$ leads to a maximum electron energy decrease and a higher angular divergence in lower energy electrons. Next to the electron spectrum, the x-ray, Betatron beam profile is presented. A gradual increase in the number of photons with the gas cell length is shown. However, the number of photons is still growing at $12\,mm$ and further, where the energy of electrons begins to decrease. According to (Ferri et al., 2018) , the optimum conditions for LWFA and Betatron radiation do not coincide.

Typically, the electrons resulting from LWFA experiments suffer from wide energy spread and lack of pointing stability and reproducibility in terms of energy, angular divergence, and charge per shot (Maier et al., 2020; Mangles et al., 2006, 2007). Contrary to conventional accelerators, in LWFA the accelerator is recreated for each laser shot, transferring laser and gas fluctuations to the result. Also, the driving laser properties change during a long-term experimental session. To improve the stability and reproducibility of the process, multiple experimental implementations have been tested. A general idea that must be introduced here is that the optimum conditions for electron injection and electron acceleration via LWFA are different. High electron density is preferred for efficiently injecting a populated electron bunch into the wake, while the acceleration process is more efficient when the electron density is low (Golovin et al., 2016).

Gas density profile can affect the LWFA in multiple ways. The neutral gas density can be controlled by varying the backing pressure applied to the gas valve. Electron beams produced by the interaction of a laser with a gas jet target were studied by (Mangles et al., 2007). The gas used was He, while the pressure was varying, producing a top hat electron density profile, $2\,mm$ long, in a range $e = 0.5 - 5\ 10^{19}$ cm^{-3}. This group stated that the reproducibility of the electron beam in terms of charge, pointing, energy, and energy spread, were minimized at low densities, while the electron production was only happening above a density threshold.

The length of the plasma channel can change by changing the gas jet diameter, or the gas cell length, providing controllability over the accelerator's length, as shown in Figures 1-2 b) and 1-3. In (Huntington et al., 2011) nozzles of various exit diameters are examined at the same irradiation conditions. Although the energy initially increases when the nozzle of $500\ \mu m$ exit diameter, is replaced by one of $1\,mm$, a further increase in exit diameter up to $5\,mm$ results in multiple electron beams, attributed to filamentation, a non-linear phenomenon that will be explained in section 3.6.3.

The composition of the plasma can vary according to the gas, or gas mixture used. Many groups explore also LWFA with multi-electron gas targets, namely high-Z gases, or gas mixtures. In this case, an alternative injection mechanism is also taking place, the ionization injection mechanism (Malka, 2012), explained in section 3.7.1. The use of Ar gas in comparison to He, under the same irradiation conditions, produced more stable, low energy and divergence electron beams (Mori et al., 2009). N_2 and

Ne, as also mixtures with a small percentage of high-Z gas with He have been studied (Huang et al., 2016; S. Li et al., 2014; Pak et al., 2010). Typically, wide energy, high charge electron beams are produced.

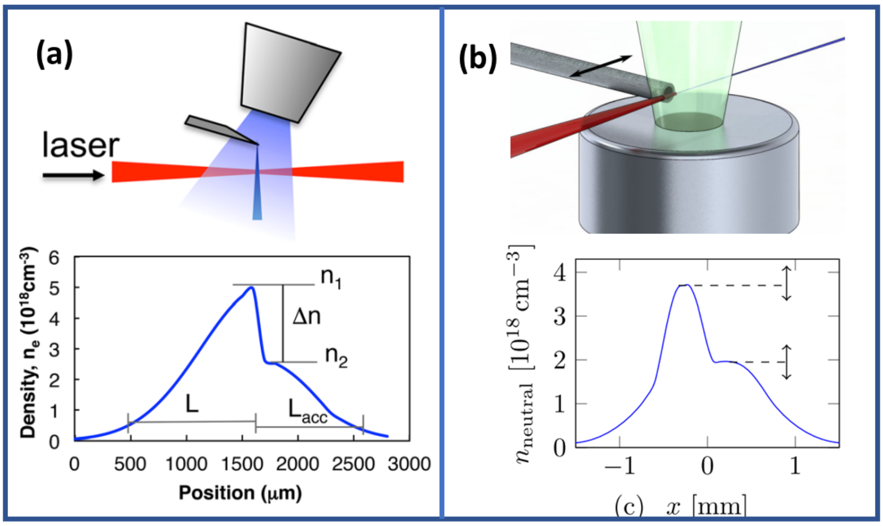

Figure 1-4: (a) The transition injection mechanism, realized using a blade downstream the nozzle exit. The density profile measured presents a peak that drops fast (Tsai et al., 2018). (b) The down-ramp mechanism was realized using two nozzles. The density down-ramp created is long (Hansson et al., 2015).

Also, the nozzle's shape defines the uniformity of the gas jet profile, e.g., a cylindrical nozzle provides a high-density, high-gradient gas jet, while a convergent-divergent nozzle (De Laval) provides a more uniform one. Initially, uniform density profiles were preferred according to (Malka et al., 2000; Semushin & Malka, 2001). However, even before the experimental realization of LWFA, some groups based on analytical calculations and Particle In Cell (PIC) simulations (Bulanov et al., 1998; Hemker et al., 2002; Suk et al., 2001) proposed the use of gas targets with a decreasing density at the laser propagation direction, followed by a low and constant density area. In this way, the electron injection is forced to happen locally at the position where the density drops from the peak value to a plateau, offering controllability. The so-called **down-ramp injection mechanism** (Malka, 2012), which is introduced in more detail in section 3.7.2, has been achieved with short or long ramp lengths, leading to two sub-mechanisms, the **density transition or shock injection**, and the **long down-ramp**. For the density transition injection mechanism, a high-gradient density followed by a constant density is produced. This has been realized with the use of a blade positioned downstream of the gas jet emanating from a nozzle, which creates a shock front (Buck et al., 2013; Ekerfelt et al., 2017; Schmid et al., 2010; Thaury et al., 2015; Tsai et al., 2018). These groups have studied electron beams resulting from using a gas jet without any distortions and from the same gas jet when a blade intervenes in the gas flow. Practically, the blade is positioned on a translation stage, permitting its motion in different heights over the nozzle and along the nozzle propagation direction, resulting in different nozzle coverages (Figure 1-4 (a)).

On the other hand, long down-ramps are realized using two consecutive gas nozzles, which provide different gas density profiles that interfere. In (Hansson et al., 2015), the second, smaller-diameter nozzle, exhausts perpendicularly to the regular nozzle (Figure 1-4 (b)). By varying the gas density of the second nozzle the electron injection was controlled within a specific range, and by varying the distance between the two nozzles, the acceleration distance was changed, resulting in electron energy tunability. In (Golovin et al., 2015, 2016), two consecutive nozzles with different exit diameters were used. The group examined various cases, such as exchanging the position of the two nozzles, using different gas mixtures in each nozzle, and varying the gas density separately. They state that independent controllability of the charge and energy spread was achieved.

Experimentally, not only do the setups provide some tunability over electron beam characteristics, but also the reproducibility, which depends on the injection mechanism, is greatly enhanced (Hansson et al., 2015). This is why extensive PIC studies have been conducted on how ramp characteristics (e.g., length, height, position) improve the produced electron beams (Hue et al., 2022; Massimo et al., 2017). However, in practice, the laser-gas interaction area in LWFA experiments is small, and the additional equipment is hard to establish in some configurations. Also, complex and expensive equipment (translation stages and/or extra valves) are required to control the relative positions (Tomkus et al., 2020).

The injection along a density drop, however by using a parabolic density profile was also examined via PIC simulations in refs. (Hafz et al., 2003; Kim et al., 2004). In this case, the injection occurs along the ramp, however along the laser propagation axis instead of a lower density plateau, an up-ramp follows, which could lead the electrons faster in the de-acceleration phase. According to their results the electrons mainly remained in the acceleration phase, thus the up-ramp of the parabolic profile was not an obstacle. In this context, their idea was experimentally tested using a gas jet and a secondary, machining laser beam. The machining beam arrived at the gas jet, perpendicularly to the main laser propagation direction 1 to $2\,ns$ before the interaction. Examining the gas profile at the main laser pulse propagation direction, the machining beam creates an area of lower density, enclosed by two distinct density peaks. Thus, along the first peak injection occurs and then acceleration of narrow energy beams is reported (Faure et al., 2010), as also, by controlling the position of the lower density area tuning of the electron energy was achieved (Brijesh et al., 2012).

Another elegant setup has been examined, providing up-ramp density profiles. In this work, by simply tilting the gas jet, in a way that the density profile creates an up-ramp at the laser propagation direction, the mean, and maximum energy increased and improved tunability were achieved (Aniculaesei et al., 2019). According to (Guillaume et al., 2015), following a similar idea they created an up-ramp by positioning a blade at the end of the gas jet, this ramp caused the re-phashing of electrons, and kept them longer in the accelerating field, providing higher energy electrons.

In addition, (Ferri et al., 2018) proposed a two stage, hybrid scheme, to enhance Betatron Radiation. The first stage consisted of a low-density gas jet ($\sim 10^{18}\ cm^{-3}$), used to optimize the electron beam characteristics via LWFA process. Then, the electron beam is injected in a second, higher density gas jet ($\sim 10^{20}\ cm^{-3}$), where the electron beam creates itself a wakefileld, a regime known as Particle WakeField Acceleration (PWFA). In the second, denser plasma wake, the electrons oscillate with higher amplitude, resulting to higher energy photons. The electron beam characteristics after this stage were inferior, but the photon source was improved in terms of photon energy and total number.

According to (L. M. Chen et al., 2013), they succeeded a $x10$ enhancement of the number of Betatron photons by using a clustering medium instead of a gaseous target. Clusters formed under specific gas expansion conditions lead to areas of higher electron density, where laser energy absorption is locally higher.

1.3 GAS DENSITY STUDIES ORIENTED IN LWFA

1.3.1 Design and characterization of nozzles

In LWFA experiments the interaction area is small, creating complications to the laser-target alignment and installation of diagnostics. Although gas cells provide longer acceleration lengths, in a low, controllable density environment, in many experimental setups gas jets are preferred as they pose minimum limitations.

For these reasons, many groups have studied gas jets theoretically, and experimentally, also by conducting CFD simulations of the gas flow by modifying backing pressure, gas composition, and nozzle geometry (Couperus et al., 2016; Lemos et al., 2009; Q. S. Liu et al., 2021; Lorenz et al., 2019; Malka et al., 2000; Semushin & Malka, 2001; Zhou et al., 2021). In addition, there is a necessity to study the non-axisymmetric gas density profiles, which have been used in LWFA experiments (Hansson et al., 2015)or PIC simulations (Bulanov et al., 1998; Kim et al., 2004). Such density profiles are more complicated to produce experimentally, model via CFD results, or even measure, as the most common techniques, e.g., interferometry, takes advantage of the rotational symmetry of the gas jet. In this paragraph, we will present the pioneering and most important studies in the design, optimization, and measurements of such profiles. For brevity reasons, we omit the density measurements accompanying almost every LWFA experiment.

In the context of LPA, the group of (Malka et al., 2000) explored neutral Ar gas density, using a Mach-Zehnder interferometer[2] for a wide range of backing pressures for a cylindrical and a De Laval nozzle. One year later, based on their findings, they extended their research by conducting CFD simulations to design and optimize uniform gas density profiles, resulting from cylindrical and De Laval nozzles (Semushin & Malka, 2001). In this latter work, they proposed a simplified design for a De Laval nozzle, where the convergent part is conical instead of parabolic.

The design of supersonic nozzles of a long exit diameter based on an “interactive computer program” provided by (Atkinson & Smith, 1995) was examined by (Lemos et al., 2009). In this program, fluid equations are solved using the Method of Characteristics (MOC) over the area where thermal transfer and viscous effects can be ignored (isentropic part), while a boundary layer is defined, where viscous effects are considered. Following this approach, some nozzle designs were compared, and two were experimentally characterized.

---

[2] Mach-Zehnder interferometer is an elegant setup, where a laser beam is split to two, which follow different but equal optical paths, one of them crosses the studied object, while the reference one remains undisturbed. Arriving simultaneously at a camera, the two beams interfere, and their phase difference contains information related to various physical quantities (https://physicsopenlab.org/2020/05/28/mach-zehnder-interferometer/).

The difficulties in gas density measurement of axisymmetric and non-axisymmetric nozzles were studied in (Landgraf et al., 2011). In the routine procedure for axisymmetric nozzles, an interferometric image containing fringe shifts due to the gas expansion is reconstructed via the Abel Inversion method to obtain the gas density (see section 5.4). However, the nozzles, either by construction or by use, sometimes do not deliver the symmetry assumed. Their work applies a tomographic reconstruction method, where interferometric images under variable angles are obtained and analyzed together, to highlight any asymmetries produced. Also, non-axisymmetric nozzles used in LWFA experiments are characterized, using the latter method.

Another important work that highlights the inaccuracy of the assumption of rotational symmetry and presents the characterization of a non-axisymmetric slit nozzle, is the one conducted by (Couperus et al., 2016). In addition, they explore the influence of the gas on the density profile. A common practice is to rely on high refractive index gas, which facilitates the measurement to infer lower refractive index gases behavior that are most used in the LWFA experiments. The different forms of density profiles resulting from the same nozzle are presented for applying the same backing pressure for Ar and He.

From the nozzle designing perspective, the most fundamental conducted by (Schmid & Veisz, 2012). In their publication, they present the behavior of supersonic De Laval nozzles with exit diameter from some mm down to $150\ \mu m$ via CFD simulations, and some interferometry measurements for validation. Studying various simulation setups in ANSYS Fluent, their conclusions were afterward used by various groups in the field (Henares et al., 2019; Lorenz et al., 2019). The influence of the nozzle geometry, backing pressure, and boundary layer formation are extensively examined.

In (Lorenz et al., 2019), a multi-configuration nozzle specially designed and constructed is studied via CFD simulations and tomography. The ability to change the density profile by modifying the nozzle shape is discussed. In (Q. S. Liu et al., 2021), a gas density characterization of four different geometry nozzles for five gasses commonly used in LWFA experiments is conducted. In (Aniculaesei et al., 2019), a tilted nozzle is used to provide an up-ramp density profile in LWFA experiments. The density profiles have been simulated using ANSYS Fluent and measured via interferometry.

In addition, in (Zhou et al., 2021) they examine the effect of the curvature of the divergent section of a CD nozzle (concave, straight and convex) on the shocks formed in this part, and consequently on the density profiles downstream its exit. They reported uniform gas profiles by optimizing straight and trumpet-like convergent geometries, while bell-like geometry was reported to create high-density regions far from the nozzle.

1.3.2 Design and characterization of other gaseous targets

In LWFA experimental setups, other types of gaseous targets have been also used and studied. Although out of the scope of this thesis, we will include some studies for completeness. In (Brandi et al., 2016) they study the behavior of a gas cell by measuring online gas density via second harmonic interferometry. The gas density was adjusted by modifying the cell orifice diameter. In (Kononenko et al., 2016), transient

CFD simulations were conducted for a two-stage gas cell of adjustable length. The first stage of the cell acts as an electron injector, while the second one as an accelerator. By tuning backing pressure of each stage separately, a transition-injection density profile was created. In (Aniculaesei et al., 2018), a novel gas target design, the 'SlitCell', which is a combination of a slit exhausting in a gas cell, was designed and optimized via the conduction of CFD simulations. The 'SlitCell' has an adjustable length, and its performance was characterized. In (Gonsalves et al., 2011), the electron injector, namely a nozzle releasing He, was attached exactly before the accelerator, namely a capillary with one slit at each edge, permitting to fill the capillary with H_2. A discharge current was applied to create plasma in the capillary.

1.3.3 Gas density studies for ion acceleration

Laser-induced ion acceleration was initially achieved using foils as targets (Clark et al., 2000; Maksimchuk et al., 2000; Snavely et al., 2000). Despite the method's efficiency, a significant drawback is the necessity for target replacement, as the foil is sublimated. However, this requires refocusing the laser beam to the new foil area, which is time-consuming and prevents operation in high repetition. At the same time, the debris created by the foil was polluting the vacuum chamber, and sophisticated optics were damaged regularly. Nowadays, gaseous targets are extensively studied by many groups (Prencipe et al., 2017). The gas target design for ion acceleration, although shares standard methodology, serves a different scope, as ultra-high density, very small diameter gas jets are preferred.

In (Sylla et al., 2012) they developed an apparatus that can operate safely and reliably in high repetition with a backing pressure of up to 400 bar. A pneumatic pressure booster was connected to a new technology electrovalve, delivering ultra-high density, sub-millimetric gas jets. The time response and the peak density for different geometry nozzles were measured. In (Henares et al., 2019), CFD simulations of a specific nozzle design and strioscopy[3] measurements have been conducted for gases H_2 and N_2 for a very wide range of pressures (1-1000 bar). Also, the system's time evolution (gas valve with nozzle) was characterized. The specific system had already accelerated ions up to 2 MeV. In (Rovige et al., 2021) the use of a symmetric shock developed over a sub-millimetric nozzle as a target was proposed. Simulations via CFD and experimental results agreed well, regarding the position of the shock. Also, the idea of a non-axisymmetric nozzle was discussed.

1.4 LWFA AND BETATRON RADIATION POTENTIAL APPLICATIONS

Electrons accelerated by LWFA mechanism can potentially be utilized in any application already supported by conventional accelerators, such as scientific research, semiconductor manufacturing, or imaging. In particular, LWFA electrons have been already used for diffraction imaging (He et al., 2013), and positron beams generation (Sarri et al., 2017). A very interesting application, which is extensively studied, is the use of LWFA electrons for cancer therapies. Up to now, such therapies are conducted mainly by LINACs, providing few MeV electrons, which are established for example in Greece, in peripheral basis. However, few MeV electrons deposit their energy in outer layers and are not suitable for deep-seated tumor irradiation. The electron beams produced via LWFA mechanism which are typically at the $100's\ MeV$ range are nowadays tested via simulations or phantoms, in the context of Very High Energy Electrons (VHEE). The idea of using VHEE in therapies is that since the higher energy beams due to relativistic effects experience reduced scattering, under specific conditions of electron beam focusing this may enable irradiation of deep-seated tumors (Kokurewicz et al., 2019). Another scheme is the so-called FLASH irradiation, where an ultra-high dose must be delivered unfractionated, in the order of $40\ Gy/s$, a dose still not available by current technology; however, LWFA which is very quickly developed, is considered as a possible candidate. For this outstanding application, feasibility studies are conducted (Labate et al., 2020).

---

[3] A flow visualization technique known also as Schlieren. The word "strioscopie" (strioscopy) is widely used in French. (A. Hirschberg, "Schlieren and shadowgraph techniques: Visualizing phenomena in transparent media: G.S. Settles (Springer-Verlag, Berlin, Germany, 2001),", European Journal of Mechanics B-fluids (2002)).

The generation of gamma rays is also achieved when LWFA relativistic electrons cross a high-Z material and, as they interact (usually with a metallic bulk), their velocity changes emitting photons, known as Bremsstrahlung radiation (Lemos et al., 2017). Bremsstrahlung Radiation produces high number, high energy photons, however non-directional, so its performance as a photon source is limited. Also, LWFA is discussed as a part of a hybrid scheme for electron acceleration, where the LWFA electron beam is injected in a second gas jet, generating its own wakefield via the PWFA. This combination is discussed to improve the resulting electron bunches with high charge and low angular divergence (Hidding et al., 2019). Another popular hybrid scheme proposes the injection of the relativistic electrons produced via LWFA to a conventional accelerator, to reduce the size of the latter, or to an undulator[4] for hard x-ray production (Joshi et al., 2020; Malka V., 2013).

Betatron x-rays are produced in a small area ($\sim\mu m$), thus present high spatial coherence. Their use as an imaging tool in LPA experiments is already established (Wood et al., 2018). Another outstanding achievement is their use for tomographic medical imaging, where a human bone was imaged with a resolution below $50\ \mu m$ (Cole et al., 2015).

All the above applications are still under investigation, as an important problem arising in all LWFA experimental campaigns is the reproducibility of the electron beam characteristics. To resolve this issue, extensive long-lasting experiments have been conducted, to quantify the reasons and design active stabilization tools (Maier et al., 2020).

---

[4] An undulator is a device consisting of consecutive magnetic dipoles used e.g. in Synchrotrons where injected electrons are forced to oscillate and consequently irradiate collimated photons (https://en.wikipedia.org/wiki/Undulator).

1.5 HIGH POWER LASER EXPERIMENTS CONDUCTED IN IPPL

Institute of Plasma Physics and Lasers (IPPL) is one of the Innovation Centres of the Hellenic Mediterranean University, a research facility in Rethymno which hosts the most powerful laser in Greece, laser Zeus (section 5.1). IPPL opened in 2015, while this research initiated in 2018, by participating in a series of high-power laser experiments using laser Zeus. In 2018 we mainly conducted ion acceleration experiments, using foil targets for ion acceleration (Clark et al., 2021) via TNSA mechanism (Clark et al., 2000).

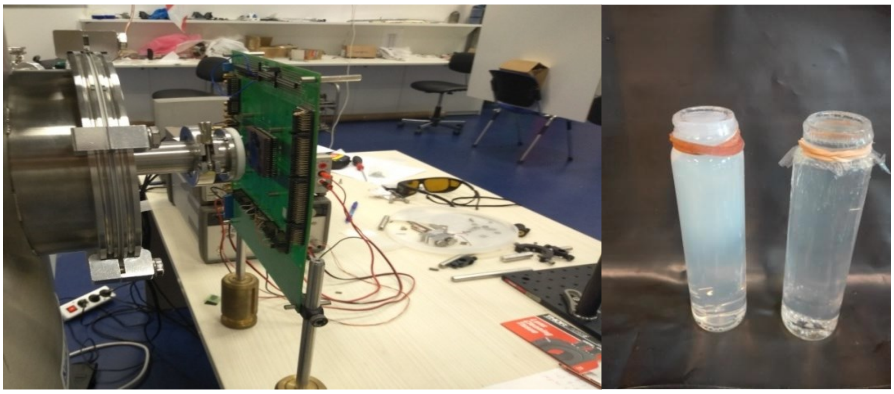

Figure 1-5: (left) The use of the LWFA electron source to irradiate electronic board in collaboration with Democritus University of Thrace; (right) A gel emulating human tissue constructed by the group of the Medical School of Crete and the University Hospital of Crete. One of the containers was irradiated by high-energy electrons (blurred one), and the other one was used as a reference one (Fitilis et al., 2022).

During the last years, at IPPL was developed an electron and Betatron x-ray source (Clark et al., 2021). Research has been conducted on the creation, establishment, and continuous improvement of the sources and related diagnostics. The ability to offer a reliable, tunable high-energy electron or x-ray photon source has been examined in many ways. The study of the ionization injection mechanism was examined (Grigoriadis et al., 2021) using multi-electron gas targets. By changing the pulse temporal profile using a saturable absorber, the reproducibility of the electron source was increased (Grigoriadis et al., 2022). The influence of the variation of the chirp of the laser pulse, to control electrons' energy was also illustrated (Grigoriadis, Andrianaki, Tatarakis, et al., 2023; Grigoriadis, Andrianaki, Tazes, et al., 2023).

In addition, the electron source was utilized to irradiate targets and study how they were influenced. For example, in Figure 1-5 (left) an experiment conducted in collaboration with the Democritus University of Trace is depicted. Their group has developed an electronic board with a set of sensors for the European Space Agency. Their product had to undergo special irradiation tests, as an emulation of cosmic radiation that a sensor would receive on a space trip. Such tests usually take place in the few synchrotron facilities existing worldwide, increasing their complexity (e.g. beam time arrangement, complicated protocols) and cost (travel abroad, cost of the beam time). The experiment was an investigation to see whether the IPPL facility could support the conduction of the test. In this case, in order to emulate the cosmic radiation, an overall high charge was required; thus, a high repetition, high-charge bunch was necessary, regardless of its energy (above a threshold permitting the electrons to cross the board).

Also, the idea to use LWFA electrons instead of the electrons coming from LINACs in radiotherapy, as discussed before, was tested via preliminary experiments (Kokurewicz et al., 2019; Labate et al., 2020). In this context, in collaboration with the Medical School of Crete and the University Hospital of Crete, specially manufactured polymer dosimetry gels have been irradiated, having a specific chemical composition that emulates human tissue. The corresponding results, using electrons resulting from the irradiation of foils, are presented in (Fitilis et al., 2022).

1.6 MOTIVATION

During this work, I was fascinated by the ways that the gas density profile was affecting the experiment. Initially, only one nozzle, Nozzle 0 was provided with the gas valve. Due to its small diameter ($800\ \mu m$) the acceleration process resulted in a stable, low-energy, semi-monoenergetic electron bunch, as discussed in section 7.1. Its reproducibility was remarkable, however some tunability was needed. This tunability, as already discussed, is partially offered by modifying gas density profiles.

The idea to test longer diameter gas jets was the first step, as according to calculations the laser energy was not fully depleted along the existing nozzle (see section 3.8). The gas target manufacturing via 3D printing, although was recently implemented (Döpp et al., 2016; Vargas et al., 2014), was not a trivial task. 3D-priting manufacturing technology for a special application requires some kind of expertise; as for example in LPA, the high-vacuum and high laser power conditions are unsuitable for many materials. Typically, targets are purchased from specialized companies, and their commission takes a long time and is expensive. Moreover, the most common techniques employed in target nozzle fabrication do not facilitate non-axisymmetric designs, which may be of a great interest (Döpp et al., 2016; Prencipe et al., 2017).

In this context, we conducted a study on the design, the simulation of the gas flow, the manufacturing of prototypes, the density profile characterization, and the use in LWFA experiments of a set of axisymmetric nozzles. After the successful operation of the first set, 3 non-axisymmetric nozzles were also produced. The design of non-axisymmetric nozzles was aiming to the creation of a down-ramp density profile, by just the use of one nozzle, omitting extra complexity provided by other setups (e.g. second nozzle, blade over a nozzle, machining beam). As presented later, this profile was successfully achieved. As already discussed in section 1.2.1, down-ramps are reported to improve electron bunches controllability and reproducibility, properties necessary for further use in potential applications.

Practically, a complete study would follow a workflow, which includes one more essential step, the conduction of PIC simulations before prototyping. PIC simulations are a key tool, which reveals information about the laser-gas interaction. This will be the subject of further research, due to time-constraints. However, some of the most important density profiles were used in PIC simulations by my colleague Anastasios Grigoriadis, to provide some understanding of our experimental results.

1.7 THESIS OUTLINE

In Chapter 2 the theoretical background is presented, including gas behavior, the state variables and their relations, the conservation laws, and the quasi 1D isentropic model for a gas flow via a nozzle. Important 2D formations, resulting from a supersonic flow via a nozzle, such as normal oblique shocks, are introduced. The full set of equations necessary to calculate the flow properties, including viscous effects, is presented. To solve the complicated, non-linear differential equations, numerical methods are applied.

In Chapter 3 some basic relations, necessary to describe the LWFA mechanism and the scaling of Betatron radiation, are presented. Specifically, the interaction of a gas with the laser, the resulting plasma quantities, the waves formed in the plasma and laser propagation effects in the plasma, are discussed. Other important mechanisms, like electron injection and energy gain limitations, are presented. In addition, the scaling of Betatron radiation is discussed.

In Chapter 4 the setup and results from the conducted CFD simulations are presnted. A set of axisymmetric nozzles is examined. The ideal gas and real gas model are used. The influence of backing and outlet pressure is examined.

In Chapter 5 the laser, its diagnostics, and the experimental setups, used to perform the experiments, are discussed. The Nomarski interferometer, the method to reconstruct the density via Abel Inversion and tomography and the basic equipment necessary to conduct a LWFA experiment are presented.

In Chapter 6 the nozzles' evaluation study is presented. Some details for the manufacturing procedure via 3D printing and the experimental measurements of density profiles are illustrated. The experimental results are compared with CFD simulations.

In Chapter 7 the results of the LWFA experiments for 3 different Nozzles are discussed. The effect of the gas density profile to the electron beam characteristics, such as the maximum energy and energy range, are presented. Additionally, some PIC simulation results are presented. Furthermore, the behavior of the electron source by conducting a backing pressure parametric study for gas N_2 is examined.

In Chapter 8 the experiment conducted for the identification of Betatron radiation is presented.

Finally, the conclusions and perspectives of this work are discussed.

Chapter 2: Fluid dynamics for Compressible flow

The term gas jet refers to the flow of gas released from a device such as a nozzle, opening, or pipe. Typically, it involves the discharge of pressurized gas, resulting in a concentrated, directional flow. To study the behaviour of a gas jet factors such as the gas properties, nozzle design, and ambient conditions are crucial. When the jet is released from a device at a pressure higher (smaller) than the ambient pressure, then we have an under-expanded (over-expanded) flow (Franquet et al., 2015). Gas jets are commonly used in various applications, including industrial processes, heating and cooling systems, and propulsion systems. The importance of gas jets in aeronautics caused their extensive study. During the last years their study became a hot topic also in laser-matter interaction experiments, as discussed in section 1.3. In the context of this work, modified De Laval-type nozzles with applied backing pressure exceeding $25\ bar$ exhaust to a vacuum chamber. The free jet flow to the chamber is highly under-expanded.

In this chapter, we discuss the theory and basic tools to study such a flow. Important relations that are essential to the description of a gas as a system and of compressible fluid flow are discussed. A quasi-1D simplified model for axisymmetric nozzles that is used to achieve a good estimate for the density in the nozzle ignoring 2D effects is presented. Finally, the set of equations that must be solved to calculate the density value at any position, including viscosity and thermal conductivity effects, is presented.

2.1 IDEAL GAS EQUATION OF STATE

Gas properties macroscopically are investigated in terms of state variables, such as temperature $T\ (K)$, pressure $p\ (Pa)$ and density $\rho\ (m^{-3})$. State variables are connected through a general category of equations known as equations of state. Any state variable is a function of two others, e.g., $T = T(p, \rho)$. For many gases the ideal gas law is typically used, described by the relation:

$$pV = \rho RT \qquad 2.1$$

$R = \frac{\mathcal{R}}{M_i} (J/kg\ K)$ is the specific gas constant for a gas with molar mass M_i where $\mathcal{R} = N_a k_B = 8.31\ \ (J/Kmol)$, *is the gas constant*, $N_a = 6.022\ 10^{23} mol^{-1}$ is the Avogadro number and $k_B = 1.38\ 10^{-23}\ J/K$ is the Boltzmann's constant. The assumptions made for the ideal gas approximation are that the gas particles have negligible volume and equal size, and that intermolecular forces are negligible. In addition, any collision among particles is considered elastic, without energy loss. For noble gases and many other gases under a wide range of conditions, these assumptions are justified.

2.2 ENERGY CONSERVATION LAW

If we consider an amount of gas in a container as a system, energy remains constant either can be offered, or consumed by the system in exchange with the environment. The quantity used to measure the energy content per unit mass of a gas is called specific internal energy e_{in} (J/kg). Specific internal energy is defined as the sum of the kinetic energy of particles and their potential energy (per unit mass) and is a state variable. Especially for an ideal gas, where intermolecular forces are negligible, and ignoring gravity, the specific internal energy is a function only of temperature, $e_{in} = e_{in}(T)$. Heat per unit mass (specific heat) q (J/kg), is transferred either from or to the gas system by interacting with another system with a different temperature T'. Also, the work per unit mass (specific work) conducted by the gas due to the gas pressure p by moving one of its walls with surface A, for a distance ds is given by the relation:

$$w = \frac{p\,Ads}{m} = \frac{p\,dV}{m} = p\,dv = p\,d(\frac{1}{\rho}) \qquad 2.2$$

where V (m^3) is the volume, v is the specific volume and ρ $(kg\,m^{-3})$ is the density. The conservation of energy equation or the First Thermodynamic Law for a closed system can be expressed per unit mass as:

$$dq = de_{in} + pd(\frac{1}{\rho}). \qquad 2.3$$

2.2.1 Important thermodynamic quantities

In thermodynamics, the most studied ways to transfer heat to a gas, are by keeping the pressure constant, or by keeping the volume constant. This is why, specific heat capacity with constant pressure, c_p, and specific heat capacity with constant volume, c_v $(J/(kg\,K))$, are defined for each gas, as the amount of heat, necessary to raise the gas (of unitary mass) temperature by $1\,K$, *or more precisely* by the following relations:

$$c_p = \left(\frac{\partial q}{\partial T}\right)_p \qquad c_v = \left(\frac{\partial q}{\partial T}\right)_v = \left(\frac{\partial e}{\partial T}\right)_v. \qquad 2.4$$

Also, specific enthalpy, h is defined as:

$$h = e + \frac{p}{\rho} \text{ thus, } c_p = \left(\frac{\partial h}{\partial T}\right)_p. \qquad 2.5$$

Another important quantity is the adiabatic index, or specific heat capacity ratio κ,

$$\kappa = \frac{c_p}{c_v} \text{ or } \kappa = \frac{2+f}{f}. \qquad 2.6$$

Relation 2.6 is connecting the adiabatic index to the equipartition theorem of kinetic theory, as f stands for the total degrees of freedom of a molecule (e.g., $f = 3$ for noble gasses which can only transfer, $f = 5$ for diatomic gasses like N_2, which can also rotate). Finally, from equation 2.5 and for an ideal gas the following relation results (where the 0 subscript corresponds to the ideal gas):

$$c_{p0}\, dT = c_{v0}\, dT + R\, dT \rightarrow c_{p0} - c_{v0} = R. \qquad 2.7$$

2.3 SECOND THERMODYNAMIC LAW

Entropy is a state variable defined as:

$$ds \equiv \left(\frac{\delta q}{T}\right)_{REV} \qquad 2.8$$

where the subscript (REV) stands for a reversible procedure, while the (δ) symbol is used to define the differential of specific heat, which is not a state variable. Starting from the First Thermodynamic Law, the first of the Gibbs' Relations results as:

$$ds = \frac{de + pd(\frac{1}{\rho})}{T}. \qquad 2.9$$

From entropy's definition (relation 2.8), results that a reversible and adiabatic process $(\delta q = 0)$ *is an* isentropic process $(ds = 0)$. For a reversible adiabatic process of an ideal gas (with constant values for specific heat capacities), we have:

$$pv^{\kappa} = C. \qquad 2.10$$

Thus, considering relation 2.10 the thermodynamic properties are connected via the following set of relations (for a reversible adiabatic process of an ideal gas with constant values for specific heat capacities):

$$\frac{p_2}{p_1} = \left(\frac{T_2}{T_1}\right)^{\frac{\kappa}{\kappa-1}} \qquad 2.11$$

$$\frac{p_2}{p_1} = \left(\frac{\rho_2}{\rho_1}\right)^{\kappa} = \left(\frac{v_1}{v_2}\right)^{\kappa} \qquad 2.12$$

$$\frac{\rho_2}{\rho_1} = \frac{v_1}{v_2} = \left(\frac{T_2}{T_1}\right)^{\frac{1}{\kappa-1}}. \qquad 2.13$$

2.4 1D STEADY FLOW ALONG A TUBE

The steady flow between points 1 and 2 along a constant-surface tube, assuming no external forces or viscous effects, can be described by the following conservation laws(Anderson, 2003):

1 D steady Mass conservation: $\rho_1 u_1 = \rho_2 u_2$ 2.14

1 D steady Momentum conservation:

$$p_1 + \rho_1 u_1^2 = p_2 + \rho_2 u_2^2 \tag{2.15}$$

1 D steady Energy conservation:

$$h_1 + \frac{1}{2} u_1^2 = h_2 + \frac{1}{2} u_2^2 \tag{2.16}$$

where u denotes the velocity along x-axis. Since the actual distance of points 1 and 2 is not considered, this derivation is valid for both continuous and discontinuous variations (for a distance tending to zero).

2.5 COMPRESSIBLE FLOW

One way to classify fluids, is compressibility. A flow is compressible when a fluid experiences significant changes in density when subjected to large variations e.g., in pressure.

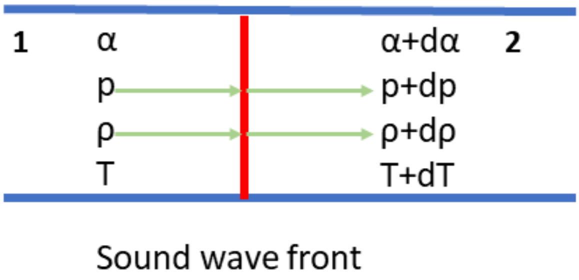

Figure 2-1: A sound wave with velocity α crosses a tube with gas density ρ.

Let us consider a sound wave moving with a velocity a along a tube full of gas of density ρ, according to Figure 2-1. Sound waves are characterized as weak waves, thus, assuming the wave to be stationary, the fluid velocity in region 1 moves towards the wave with a velocity a, while the fluid of region 2 moves away with a velocity $a + da$, where da is infinitesimal small velocity variation due to the sound wave. There is also a variation in pressure, density, and temperature, symbolized as dp, $d\rho$ and dT, respectively. According to 2.14, in this case:

$$\rho a = \rho a + a d\rho + \rho da + d\rho \, da \tag{2.17}$$

where the second order term $d\rho \, da$ is very small, thus ignored. Hence,

$$\alpha = -\rho \frac{da}{d\rho}. \tag{2.18}$$

Using 2.15,

$$p + \rho a^2 = (p + dp) + (\rho + d\rho)(a + da)^2. \tag{2.19}$$

By equalizing with zero the products of infinitesimal quantities and solving for the velocity variation da, one obtains:

$$d\alpha = -\frac{dp + a^2 d\rho}{2\alpha\rho}. \tag{2.20}$$

By substituting 2.20 to 2.18:

$$\alpha = \rho\left[\frac{dp + a^2 d\rho}{2\alpha\rho d\rho}\right]. \tag{2.21}$$

Solving for a^2:

$$\alpha^2 = \frac{dp}{d\rho}. \tag{2.22}$$

For an ideal gas, the speed of sound is expressed by:

$$\alpha = \sqrt{\frac{\kappa p}{\rho}} = \sqrt{\kappa RT}. \tag{2.23}$$

Finally, the Mach number is defined as the ratio of the fluid velocity v to the speed of sound in a medium, a:

$$M = \frac{v}{\alpha}. \tag{2.24}$$

To distinguish a gas flow as compressible, the gas density variation happening due to a pressure change along the flow should be too large to be neglected. To quantify that, a common convention is when Mach number of the flow is higher than 0.3. When the flow is incompressible, the flow is described using continuity and momentum conservation equations. However, when the flow is compressible, thus more complicated, the energy conservation equation must be solved too.

2.6 QUASI-1D ISENTROPIC MODEL FOR A SUPERSONIC NOZZLE

When a gas flows through a nozzle of varying area A, its molecules are deflected by the walls. In an incompressible flow case, the gas density remains constant while the velocity increases (for a convergent nozzle). However, as the speed of the flow v, approaches the speed of sound in the gas a, compressibility effects become important. Considering flow through a convergent-divergent nozzle, as shown in Figure 2-2, the flow is gradually compressed as the nozzle area decreases and then gradually expanded as the nozzle area increases. Considering also adiabatic walls (no heat exchange through the walls), thus an isentropic process takes place. For this case, a quasi-1D isentropic model is discussed extensively in the bibliography as a cour(Anderson, 2003; Zucker & Biblarz, 2002)n(Anderson, 2003; Zucker & Biblarz, 2002). According to this model equations 2.14 to 2.16 are replaced by the following set:

Quasi-1 D steady Mass conservation:	$d(\rho VA) = 0$	2.25
Quasi-1 D steady Momentum conservation:	$dp = -\rho u\, du$	2.26
Quasi-1 D steady Energy conservation:	$dh + udu = 0$	2.27

Based on 2.25-2.27 and the ideal gas equation of state, the following relations are derived:

$$\frac{A_t}{A} = M\left[1 + \frac{\kappa - 1}{\kappa + 1}(M^2 - 1)\right]^{-\frac{\kappa+1}{2(\kappa-1)}} \qquad 2.28$$

$$\frac{T}{T_0} = (1 + \frac{\kappa - 1}{2}M^2)^{-1} \qquad 2.29$$

$$\frac{p}{p_0} = (1 + \frac{\kappa - 1}{2}M^2)^{-\frac{\kappa}{\kappa-1}} \qquad 2.30$$

$$\frac{\rho}{\rho_0} = (1 + \frac{\kappa - 1}{2}M^2)^{-\frac{1}{\kappa-1}}. \qquad 2.31$$

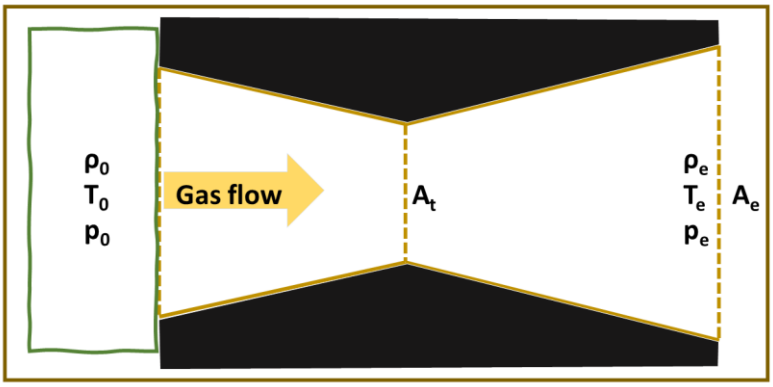

Figure 2-2: 1D isentropic model: A backing pressure reservoir with known initial conditions ρ_0, T_0 and p_0 is given. The gas flows through a nozzle with a minimum cross-section A_t (at the throat) and exhausts a gas jet at the exit where the cross-section is A_e.

They permit to calculate state variables ρ, T and p at any position with a varying cross-section A along the inner area of the nozzle. The variables in equations 2.29-2.31 are expressed only as a function of Mach number M and their initial values ρ_0, T_0 and p_0 at the reservoir. The initial values are also called stagnation parameters.

According to equation 2.28, known as the area-Mach number relation (Anderson, 2003), Mach number at any location is calculated by considering the local surface area A and the smallest surface area A_t, known as the throat of the nozzle. In Figure 2-3 the ratio of the nozzle exit to the nozzle throat is plotted as a function of M for noble and diatomic gases.

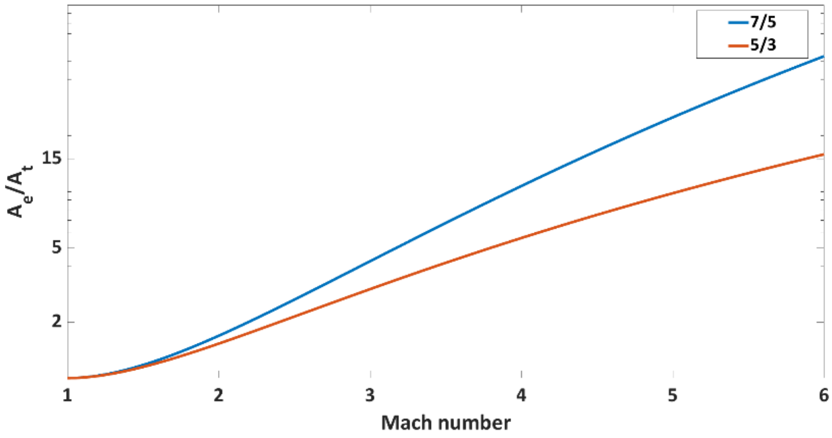

Figure 2-3: Ratio of the nozzle exit to the nozzle throat as a function of M for noble and diatomic gasses.

At the nozzle throat, where $A = A_t$, and $M \approx 1$ the flow is sonic, while at the divergent part, the flow becomes supersonic ($M > 1$). According to this model, the Mach number of a given geometry is only affected by the gas nature.

With the 1D isentropic model only values in the inner nozzle area are calculated. Also, other essential effects are ignored.

2.7 SUPERSONIC FLOW CHARACTERISTIC FORMATIONS

According to (Anderson, 2003) supersonic flows are characterized by the existence of normal or oblique shocks, expansion, and compression waves. For example, in a tube, normal shock waves are formed when a disturbance is moving through a compressible medium at a speed greater than the local speed of sound. This disturbance creates a compression of the medium downstream, leading to an abrupt increase in pressure, and a rarefaction or expansion behind it, expressed by a sudden decrease in pressure. The significant change in pressure and other flow properties (e.g. density, temperature) across the shock front creates a distinct boundary between the regions of compressed and expanded medium and the process is no more isentropic. In case of a normal shock, the 1D steady flow description is adequate, as the so-called Rankine-Hugoniot equations are used to relate upstream and downstream variables, across the shock:

Normal Shock- Mass conservation:

$$\rho_1(u_1 - a) = \rho_2(u_2 - a) \tag{2.32}$$

Normal Shock- Momentum conservation:

$$p_1 + \rho_1(u_1 - a)^2 = p_2 + \rho_2(u_2 - a)^2 \tag{2.33}$$

Normal Shock- Energy conservation:

$$h_1 + \frac{1}{2}(u_1 - a)^2 = h_2 + \frac{1}{2}(u_2 - a)^2 \tag{2.34}$$

where a is the shock velocity, 1 is the position upstream and 2 downstream the shock, while u_1 and u_2 are the uniform fluid velocities at each side, in the shock reference frame (Laney, 1998)

On the other hand, in a nozzle oblique shocks or expansion waves are happening when the flow meets a change on the wall direction, which are inherently 2D effects. When a concave corner is met, as in Figure 2-4 left, an oblique shock is formed. The flow direction changes and becomes parallel to the concave boundary. The Mach number decreases, and the density increases across the shock wave. If the shock is weak, we refer to oblique wave, where the flow properties vary continuously.

Expansion waves arise when the corner is convex. In Figure 2-4 right an expansion fan is formed, along which the direction of the flow changes according to the convex boundary and Mach number increases, while density decreases. Expansion waves are related to smooth variation flow properties and obey isentropic relations. When the corner is sharp and the expansion fan is centered (as in Figure 2-4) the expansion waves are also called Prandtl-Meyer waves, named after Prandtl and his student Meyer who worked on the theory of such waves.

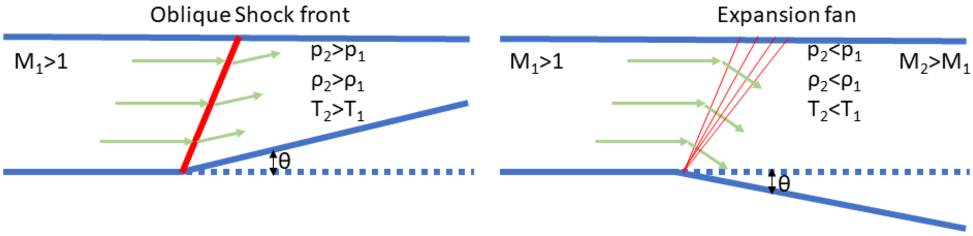
Oblique Shock front
$M_1>1$
$p_2>p_1$
$\rho_2>\rho_1$
$T_2>T_1$
θ
Expansion fan
$M_1>1$
$p_2<p_1$
$\rho_2<\rho_1$
$T_2<T_1$
$M_2>M_1$
θ

Figure 2-4 Sketch of a flow across an oblique shock and an expansion fan.

In addition, a contact discontinuity can be formed, known as slip line or slip surface in multidimensional flows. In the 1D case, normal velocity and pressure are continuous across the discontinuity $(u_1 = u_2$ and $p_1 = p_2)$, however energy, density and temperature may increase or decrease. The fluid can't cross such a discontinuity, however it moves with the fluid. Contact discontinuity separates areas with different entropy and their appearance originate either to the initial conditions, or to the intersection of 2 shocks (Laney, 1998).

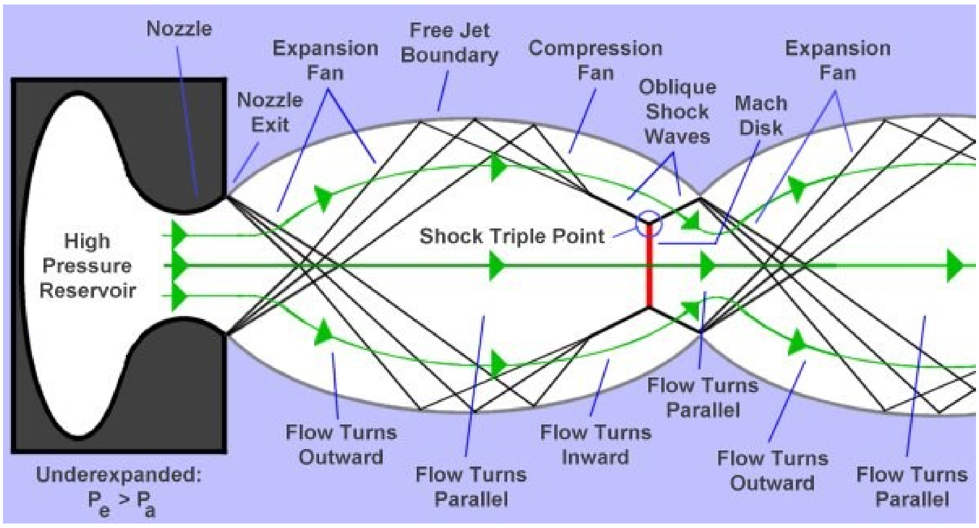
Nozzle
Expansion Fan
Free Jet Boundary
Compression Fan
Oblique Shock Waves
Mach Disk
Expansion Fan
Nozzle Exit
High Pressure Reservoir
Shock Triple Point
Flow Turns Outward
Flow Turns Parallel
Flow Turns Inward
Flow Turns Parallel
Flow Turns Outward
Flow Turns Parallel
Underexpanded:
$P_e > P_a$

Figure 2-5: Flow structures due to high-pressure exhaust of a gas with exit pressure P_e in a chamber with lower pressure P_a. Figure adopted from: (Https://Aerospaceweb.Org).

To stress the complexity of a flow via a nozzle in Figure 2-5 a sketch for an under-expanded flow is presented. Multiple formations, such as expansion waves which are reflected and turning inwards forming compression waves due to the pressure difference at the free jet boundary are highlighted. Such formations are well described and experimentally captured in an extensive study conducted by *NASA Langley Research Center* (Inman et al., 2009; Wilkes et al., 2005, 2006)

Moreover, across the shocks high temperature gradients are developed and thermal conduction becomes important. The flow along the nozzle's inner area is also affected by turbulence effects, developed mainly along the walls (Schmid, 2009). To capture such flow structures, which finally define the gas density profiles obtained by the designed nozzles, the solution of the governing system equations, containing the respective terms is necessary over a volume area.

2.8 A GENERAL FORM OF CONSERVATION EQUATIONS

We have already seen the sets of equations 2.14-2.16, 2.25-2.27 and 2.32-2.34 which express simplified editions of the general forms of the conservation equations in an 1D and quasi-1D approximation and across a normal shock (1D). Here, some of the most important equations in fluid dynamics, the well-known Navier-Stokes equations, formulated by Claude-Louis Navier and George Gabriel Stokes are discussed. This set of partial differential equations allows for the calculation of fluid behavior based on initial conditions and boundary conditions ((Zucker & Biblarz, 2002)). Literally speaking, only one of them, the momentum conservation equation is formulated from Navier and Stokes, however in modern literature all together they are frequently referred as the complete set of Navier-Stokes equations.

Continuity equation

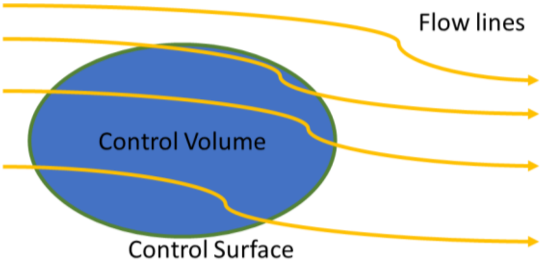

Figure 2-6: Flow lines along a conceptual volume, the control volume, fixed in space, surrounded by the control surface.

The continuity equation is given in differential form as:

$$\frac{\partial \rho}{\partial t} + \nabla \cdot \rho \boldsymbol{v} = 0 \qquad 2.35$$

where, as already introduced, ρ is the fluid density, $\boldsymbol{v}$ is its velocity vector, and t is time. This equation, when solved for a fixed Control Volume (CV), namely a conceptual volume related to a geometry studied, states that the rate of increase of density at this volume and the rate of mass flux passing through the Control Surface (CS) surrounding the control volume, are conserved per unit volume.

Momentum equation

The momentum equation for a Newtonian fluid is:

$$\frac{\partial(\rho \boldsymbol{v})}{\partial t} + \boldsymbol{v} \cdot \nabla(\rho \boldsymbol{v}) = -\nabla p + \nabla \cdot \bar{\bar{\tau}} \qquad 2.36$$

$$\bar{\bar{\tau}}_{ij} = 2\mu \left[\epsilon_{ij} - \tfrac{1}{3} \nabla \cdot \boldsymbol{v} \delta_{ij} \right] \qquad 2.37$$

here $\bar{\bar{\tau}}$ is the viscous stress tensor, μ the dynamic viscosity of a Newtonian fluid, ϵ_{ij} the strain rate tensor and δ_{ij} is the Kronecker delta. A fluid is characterized as Newtonian when the dynamic viscosity μ doesn't depend on the velocity or stress state of the fluid, rather than its temperature and pressure. Most low-Z gases and common liquids, such as water, are approximated as Newtonian ones.

Equation 2.36 is the equivalent of Newton's 2nd Law for fluid flow. It states that the rate of change of momentum equals the sum of forces acting on the fluid contained inside the Control Volume (per unit volume). The pressure gradient term is dominant for a highly under-expanded flow, such as the one resulting from the nozzle expansion in our case. The inclusion of viscosity in the Navier-Stokes equations allows for the modeling of flows that exhibit internal friction and viscous effects, which can be significant, especially at the nozzle walls. The gravity term is not important in a nozzle design problem, so practically is omitted.

Energy equation

The energy equation (First Thermodynamic Law) in conservation form is given as:

$$\frac{\partial(\rho e_t)}{\partial t} + \nabla \cdot [\boldsymbol{v}(\rho e_t + p)] = \nabla \cdot [k\, \nabla T + (\bar{\bar{\tau}} \cdot \boldsymbol{v})] \qquad 2.38$$

where $e_t = e_{in} + v^2/2$, is the total internal energy of the gas per unit mass. In this case, the pressure term represents the work done by pressure forces on the fluid, k is its thermal conductivity and the related term accounts for the heat conduction within the fluid, and the viscosity term is again expressed for a Newtonian fluid.

2.9 NUMERICAL METHODS

The full set of equations describe a fluid flow are coupled nonlinear differential equations, and their analytical solution is possible only for simplified cases. To close the system and exclude non-physical solutions a state equation and the Second Thermodynamic Law are also used. The solutions for complicated flows, such as the problem examined in this dissertation, are approximated via numerical simulations, where the equations are discretized and the corresponding algebraic system is solved at specific locations of a computational mesh, following well established schemes, such as the Finite Volume Method (FVM) (Laney, 1998).

In Chapter 4, the flow via a nozzle is studied using ANSYS Fluent, a well-established CFD commercial solver. In Fluent, FVM is applied, where the conservation form of the governing equations is used. The variables selected according to the terms contributing to the model, are calculated at the centroids of the cells (cell-centered discretization scheme), which must be sufficiently small to capture flow characteristics. To accurately simulate a specific physical problem, iterative algorithms are used to arrive in a converged solution. CFD simulations are computationally expensive; this is why, weather the geometry of the problem allows for simplifications, symmetry is considered.

CFD simulations are ideal under the continuum approximation, which ensures that the studied properties vary continuously. This is quantified by a dimensionless parameter, known as Knudsen number, $K_n = \frac{\lambda_{MF}}{L}$, where λ_{MF} is the mean free path of a gas molecule and L a characteristic length of the flow, such as the nozzle exit radius. According to our calculations, the continuum assumption is valid for the range of pressures simulated here, as $K_n \ll 1$.

Chapter 3: LWFA theory

In LWFA an ultrafast (~$25\ fs$) and ultra-intense (*I*>*10*^{18} W/*cm*^{2}) laser pulse is interacting with a gas to accelerate electrons. The dynamic evolution of the process is non-linear, thus highly complicated. In this chapter, phenomena related to the pulse characteristics and the plasma formed, necessary to describe the process and their relations are presented. Also, various electron injection mechanisms and laser propagation effects in plasma, as also acceleration limitations are discussed. Finally, Betatron radiation scaling relations are introduced.

3.1 A GAUSSIAN LASER PULSE IN A VACUUM AND IMPORTANT LASER QUANTITIES

A laser pulse in LWFA experiments is approximated by a Gaussian function in space and time (bi-Gaussian). The electric field $\boldsymbol{E}$, of a bi-Gaussian pulse propagating in z axis is given by the following relation (Milonni & Eberley, 1988):

$$\mathbf{E}(r,z,t) = \frac{E_0}{2} exp\left[-\frac{r^2}{w^2(z)}\right] exp\left[-\frac{(t-z/c)^2}{\tau_0^2}\right] cos\left\{\left[\omega_0 t - k_0 z - k_0 \frac{r^2}{2R(z)} + \psi_g(z)\right] e_\perp\right\} + \text{c.c.} \qquad 3.1$$

where E_0 is the electric field amplitude, $\mathrm{w(z)}$ is the width of the beam at position z,

$$w(z) = w_0 \sqrt{1 + (\frac{z}{z_R})^2} \qquad 3.2$$

and w_0 is the beam waist, namely the smallest value of beam radius at the focus ($z = 0$), while $z_R = (\pi w_0^2)/\lambda_0$ is the Rayleigh length, representing the position at which the transverse area of the pulse is doubled, λ_0 is the wavelength of the pulse, $c = 3 \times 10^8$ m/s is the speed of light in vacuum, τ_0 is the pulse duration at Full Width at Half Maximum (FWHM), k_0 and ω_0 are the wavenumber $k_0 = {}^{2\pi}/_{\lambda_0}$ and the angular frequency $\omega_0 = ck_0$. Also, $R(z)$ is the radius of curvature of the wavefront and $\psi_g(z) = \arctan\left({}^{z}/_{z_R}\right)$ is the Gouy phase shift of the pulse. Finally, $e_\perp$ is the unit vector of the polarization direction ($e_\perp = e_x$ for a linearly polarized wave).

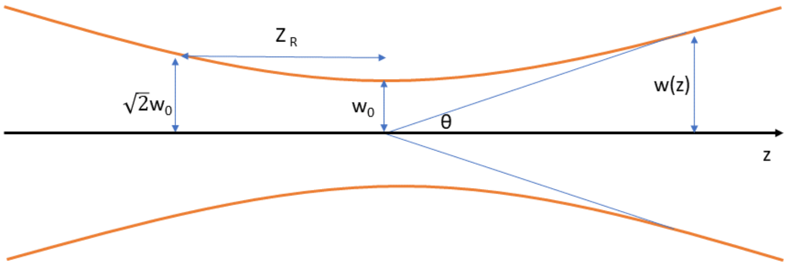

Figure 3-1: The spatial evolution of a Gaussian pulse at focus. The beam waist w_0 and the Rayleigh length z_R are highlighted.

Electric $\boldsymbol{E}$ and magnetic $\boldsymbol{B}$ fields are often expressed as a combination of a vector potential $\boldsymbol{A}$ and a scalar potential Φ. Following the approach of (Cros, 2014) for $\nabla\boldsymbol{A} = 0$, a choice for the vector potential known as Coulomb gauge according to gauge invariance theory (Jackson & Okun, 2001)) $\boldsymbol{E}$ and $\boldsymbol{B}$ are given by:

$$\boldsymbol{E} = -\nabla\Phi - \frac{\partial \boldsymbol{A}}{\partial t} \qquad 3.3$$

$$\boldsymbol{B} = \nabla \times \mathbf{A} \qquad 3.4$$

In a vacuum $\Phi = 0$, thus both fields depend only on $\boldsymbol{A}$.

To deal with the laser-plasma interaction, some related quantities are introduced. The laser normalized peak vector potential a_0 is defined by the relation:

$$a_0 = \frac{eA_0}{m_e c} = \frac{eE_0}{m_e c \omega_0} \qquad 3.5$$

where e and m_e are electron charge and mass respectively. The laser intensity I_L, is defined as the averaged Pointing vector $\boldsymbol{S}$, over a cycle:

$$I_L =< \mathbf{S} >= c^2 \varepsilon_0 < \mathbf{E} \times \mathbf{B} >= \frac{c\varepsilon_0 |\boldsymbol{E}|^2}{2} \qquad 3.6$$

where $\varepsilon_0 = 8.85 * 10^{-12}$ F/m, the vacuum permittivity. The measurable laser pulse quantities are τ_0, w_0 and the mean pulse energy $\mathcal{E}_L$. Thus, for a Gaussian pulse the laser power P_L is calculated as:

$$P_L = 2\sqrt{\frac{ln2}{\pi}}\frac{\mathcal{E}_L}{\tau_0} \approx \frac{\mathcal{E}_L}{\tau_0} \qquad 3.7$$

while the peak laser intensity is given as:

$$I_0 = 2\frac{P_L}{\pi w_0^2}. \qquad 3.8$$

Then, by substituting 3.6 for peak laser intensity to 3.5 and for $\omega_0 = {}^{2\pi}/_{\lambda_0}$

$$a_0 = \sqrt{\frac{e^2}{2\pi^2 \varepsilon_0 m_e^2 c^5}\lambda_0^2 I_0} \cong 0.86\lambda_0[\mu m]\sqrt{I_0\left[\frac{10^{18}W}{cm^2}\right]}. \qquad 3.9$$

Practically, for a laser like Zeus ($\lambda_0 = 0.8\ \mu m$), with $\mathcal{E}_L = 1\,J$ and $\tau_0 = 25\,fs$ the power is $P_L = 40\ TW$. Given a measured beam waist $w_0 = 15\ \mu m$ its intensity is calculated as $I_0 = 1.2 \times 10^{19}\ W/cm^2$, and $a_0 = 2.35$.

When such an ultra-intense laser interacts with a gaseous target, e.g., a He gas-jet, the gas becomes ionized. Even the intensity of the leading edge of the laser pulse exceeds the threshold intensity demanded to ionize both electrons of He atom, which, according to (Fill, 1994), is equal to $I_{th} = 6 \times 10^{15}\ \mathrm{W/cm^2}$. Therefore, when the main pulse arrives interacts with a He-plasma; this is why in the following section the electron motion in a laser field will be discussed.

3.2 SINGLE ELECTRON MOTION IN THE LASER FIELD

When the laser meets a relativistic electron, the electron momentum $\boldsymbol{P}$ is given by the relation:

$$\boldsymbol{P} = \gamma m_e \boldsymbol{V} \tag{3.10}$$

where $\boldsymbol{V}$ is the electron velocity, $\gamma = (1-\beta^2)^{-1/2}$ is the Lorentz factor, and $\beta = {}^{V}\!/_{c}$ is the normalized electron's velocity. The electron motion is described by the Lorentz force equation:

$$\frac{d\boldsymbol{P}}{dt} = -e(\boldsymbol{E} + \boldsymbol{V} \times \boldsymbol{B}). \tag{3.11}$$

Following a plane wave approximation for the laser field which propagates along z-axis and the electric field oscillates on the x-axis ($\boldsymbol{B}$-field along y-axis) then:

$$\boldsymbol{E}(z) = E_L\, cos(k_0 z - \omega_0 t)\, \boldsymbol{e}_x. \tag{3.12}$$

And, by using equation 3.3, for $A_0 = {}^{E_L}\!/_{\omega_0}$:

$$\boldsymbol{A}(z) = A_0\, sin(k_0 z - \omega_0 t)\, \boldsymbol{e}_x. \tag{3.13}$$

The magnetic field is connected to the electric field via the relation $|\boldsymbol{B}| = |\boldsymbol{E}|/c$. In the non-relativistic regime, where $\beta \ll 1$ the magnetic field term in equation 3.11 can be ommited, thus:

$$\frac{d\boldsymbol{P}}{dt} = -e\boldsymbol{E} = -e\frac{\partial(A_0\, sin(k_0 z - \omega_0 t)\, \boldsymbol{e}_x}{\partial t}. \tag{3.14}$$

Dividing by cm_e and substituting by equation 3.5, and for an electron with zero initial velocity at $z = 0$ 3.14 becomes:

$$\beta = -\alpha_0\, sin(\omega_0 t) \tag{3.15}$$

According to equation 3.15, the resulting electron motion is an oscillation, due to the electric field, without moving forward. When $\alpha_0 \geq 1$ then the $\boldsymbol{V} \times \boldsymbol{B}$ term can no longer be ignored, as electrons' oscillation velocity approaches c, and electron trajectories become (Gibbon, 2005):

$$x_e = -\frac{\alpha_0}{k_0}\, cos(k_0 \xi) \tag{3.16}$$

$$z_e = \frac{a_0^2}{8k_0}\,[2k_0\xi - sin(2k_0\xi)]. \tag{3.17}$$

In equations 3.16 and 3.17 ξ is given by $\xi = z - ct$, defined as the position of an observer travelling with the velocity of the laser pulse. Relation 3.17 indicates that the electron oscillates twice at the laser frequency, but also moves forward in the longitudinal direction. In relations 3.16 and 3.17 the motion scales with a_0 and a_0^2 respectively, thus for $a_0 \gg 1$ longitudinal motion becomes much higher than the transverse motion.

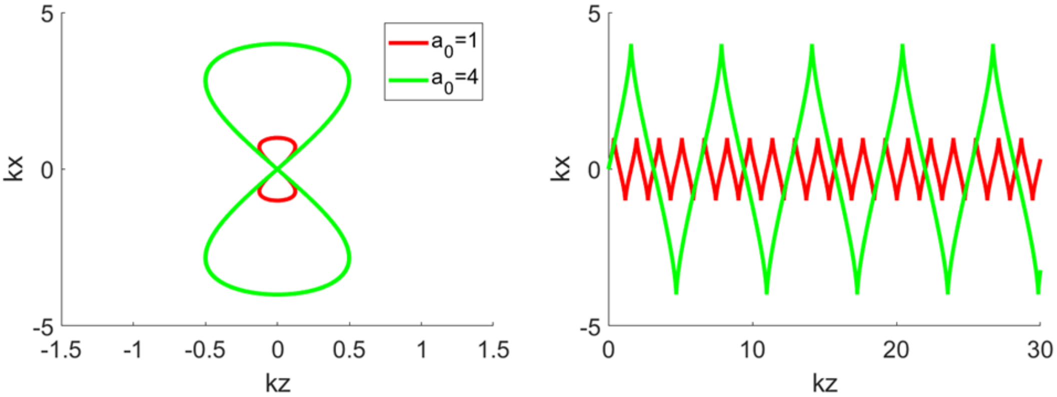

Figure 3-2: Electron relativistic trajectories in the laser field in the laser frame (left) and in the laboratory frame for $a_0 = 1$ and $a_0 = 4$.

According to this analysis, when the electron is in the relativistic regime, it moves forward along the laser propagation direction, however there is no energy gain from the laser. Practically, the laser plane wave approximation is not valid in LWFA experiments, where the laser is tightly focused, thus it strongly varies in the transverse plane.

3.3 PROPAGATION OF EM WAVES IN A PLASMA

From plasma theory, it is known that dispersion relation of an EM wave with frequency ω_0 in a plasma is given by the relation (F. F. Chen, 1983):

$$\omega_0^2 = \omega_p^2 + c^2k^2 \tag{3.18}$$

where ω_p is a characteristic frequency, the plasma frequency, denoting the oscillation frequency of the electrons around an equilibrium position, in a plasma with density n_e:

$$\omega_p = \sqrt{\frac{n_e e^2}{m_e \varepsilon_0}}. \tag{3.19}$$

If $\omega_0 > \omega_p$ the wavenumber k is a real number, and the wave propagates into the plasma. On the contrary, when $\omega_0 < \omega_p$ k is imaginary, and the wave can no longer propagate. The density at which a laser meets the limit $\omega_0 = \omega_p$, is called the critical density and is calculated by the following relation:

$$n_c[10^{21}cm^{-3}] = \frac{\omega_0^2 m_e \varepsilon_0}{e^2} = \frac{1.12}{\lambda_0^2[\mu m]}. \qquad 3.20$$

Plasma is called underdense (overdense) when n_e<n_p (n_e>n_p). For a laser like Zeus (λ_0=0.8 μm) the critical density is $n_c = 1.75 \times 10^{21} cm^{-3}$. In an overdense plasma the laser light is reflected.

LWFA takes place in the underdense regime, where after the laser propagation, plasma waves are formed. Based on equation 3.18, the phase and group velocity of an EM field in the plasma are calculated:

$$u_{ph} = \frac{\omega_0}{k} = \sqrt{c^2 + \frac{\omega_p^2}{k^2}} \qquad 3.21$$

$$u_g = \frac{d\omega_0}{dk} = \frac{c^2}{\sqrt{c^2 + {\omega_p^2}/{k^2}}}. \qquad 3.22$$

The plasma phase velocity is equal to its driver's velocity, namely the laser group velocity thus:

$$\beta_p = {u_g}/{c} = \sqrt{1 - {n_e}/{n_c}} \text{ and } \gamma_p = \frac{1}{\sqrt{1-\beta_p^2}} = \sqrt{\frac{n_c}{n_e}} \qquad 3.23$$

where β_p is the normalized phase velocity and γ_p is the Lorentz factor of the plasma wave. Practically, a lower electron density causes a higher plasma phase velocity and relativistic factor. In addition, the refractive index of a plasma is defined as a function of plasma density, by utilizing 3.21:

$$\eta_p = \frac{c}{u_{ph}} = \sqrt{1 - \frac{\omega_p^2}{\omega_0^2}} = \sqrt{1 - \frac{n_e}{n_c}}. \qquad 3.24$$

3.4 PLASMA WAVES

The ponderomotive force is related to the second-order electron motion averaged over one optical laser cycle. For an electron, the 3D ponderomotive force can be expressed as (Kruer, 2003):

$$\boldsymbol{F_p} = -m_e c^2 \nabla \langle \frac{a^2}{2} \rangle = -m_e c^2 \nabla \frac{a_0^2}{2}. \qquad 3.25$$

Due to the ponderomotive force, plasma waves are formed. Practically, according to equation 3.25, charged particles are driven out from the high laser intensity region. However, ions that are significantly heavier than electrons respond slower, and their motion is neglected for this analysis. In LWFA, the longitudinal electric field is generated by the periodic distribution of the electrons that oscillate behind the laser pulse. When the plasma frequency is significantly smaller than the laser frequency, the plasma phase velocity is comparable to the laser group velocity in the medium, and the plasma wave is called relativistic. The relativistic plasma wave, or WakeField, plays a crucial role in the acceleration of electrons. Its oscillation length, known as the plasma wavelength, is calculated in practical units by the relation:

$$\lambda_{\mathbf{p}}[\mu\mathrm{m}] \cong 33 \times (n_e[10^{18}cm^{-3}])^{-1/2} \tag{3.26}$$

and the amplitude of the longitudinal accelerating field in practical units is:

$$\mathrm{E}_{\mathbf{p}}[\mathrm{GeV/m}] \cong 96 \times (n_e[10^{18}cm^{-3}])^{1/2}\frac{\delta n_e}{n_e} \tag{3.27}$$

which maximizes for maximum density perturbation δn_e.

3.5 LWFA REGIMES

The basic parameters, which define electron acceleration, are the laser characteristics and plasma properties. The normalized peak vector potential is the parameter used to distinguish the LWFA regimes. The regimes describe the wave formation and further electron acceleration process by using different models. Mainly 3 regimes are widely used. The linear regime describes the acceleration for $a_0 < 1$ via a 1D linear wakefield approximation (Dawson, 1959), the 1D non-linear regime for $a_0 \geq 1$ (Akhiezer & Polovin, 1956), and 3D non-linear regime for $a_0 > 2$ (Lu et al., 2007). The details of 1D models will not be discussed here, however the peak electric field derived by each one of them is given as:

$$\mathrm{E_{max,linear}} = \frac{\mathrm{m_e c \omega_p}}{\mathrm{e}} \tag{3.28}$$

$$\mathrm{E_{max,1D,non-linear}} = \frac{\mathrm{m_e c \omega_p}}{\mathrm{e}}\sqrt{2(\gamma_\mathrm{p} - 1)}. \tag{3.29}$$

3.5.1 The Bubble regime

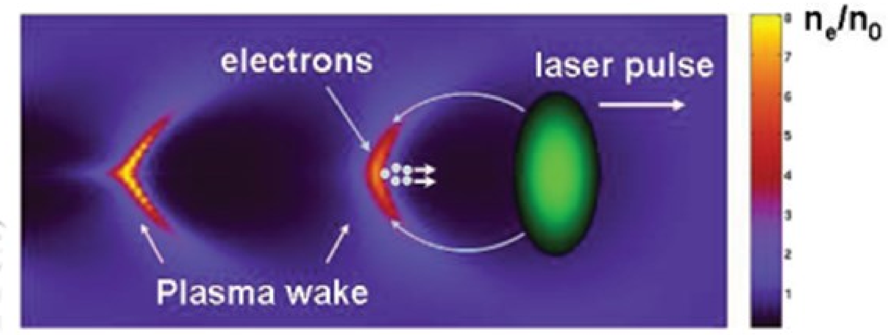

Figure 3-3: Behind the laser pulse a bubble, void from electrons is formed. Electrons are injected from its rear side and accelerated. Adopted by (Malka, 2013).

The Bubble regime is well-known and is based on 3D PIC studies (Lu et al., 2007; Pukhov & Meyer-ter-Vehn, 2002). When the ponderomotive force is high enough to evacuate all plasma electrons from the laser path, the structure formed resembles to a bubble. According to (Lu et al., 2007), the bubble size can be estimated by equalizing the laser ponderomotive force to the plasma bubble Lorentz force, thus:

$$r_b \approx 2\frac{\sqrt{a_0}}{k_p}. \tag{3.30}$$

After a plasma wavelength the electrons are pulled back, forming a density spike when they cross the propagation axis. At the location of the highest accelerating field, the wave breaks (wavebreaking) and electrons are injected into the bubble. For optimum bubble formation, efficient electron injection, and subsequent acceleration the laser characteristics and plasma wavenumber must fulfill a matching condition:

$$c\tau_0 \leq w_0 \; and \; w_0 \approx r_b. \tag{3.31}$$

Under this condition, a perfect bubble is formed. When the laser is not strong enough to create a perfect bubble, self-focusing and self-compression of the pulse along propagation may help to fulfill the conditions. According to this model, electrons injected to the bubble, gain energy, given by the relation:

$$\Delta E = \frac{2}{3}\mathrm{m_e c^2}\left(\frac{\omega_0}{\omega_p}\right)^2 a_0 \approx \mathrm{m_e c^2}\left(\frac{P}{m_e^2 c^5}\right)^{1/3}\left(\frac{n_c}{\mathrm{n}_e}\right)^{2/3} \tag{3.32}$$

and in practical units

$$\Delta E[GeV] = 1.7\left(\frac{P[TW]}{100}\right)^{1/3}\left(\frac{10^{18}}{n_e[cm^{-3}]}\right)^{1/3}\left(\frac{0.8}{\lambda_0}\right)^{4/3} \tag{3.33}$$

while the charge is given as

$$Q(nC) = 0.4\frac{\lambda[\mu m]}{0.8}\sqrt{\frac{P[TW]}{100}}. \tag{3.34}$$

3.6 LASER MODULATION IN A PLASMA

As plasma density is modified by the plasma wave excitation, the laser pulse is consequently modified. For $a_0 \geq 1$, some significant propagation effects arise, e.g., self-focusing and self-compression, which correspond to changes in the transverse size and duration of the laser pulse respectively and play an important role. Another remarkable effect is laser filamentation.

3.6.1 Self-focusing

When electrons are subjected to strong laser fields, they acquire relativistic energies. This is why the relativistic factor γ(r) must be considered to modify the plasma density. For an underdense plasma of a uniform density n_{e0}, and a plasma wave with a large amplitude the plasma density is given by:

$$\omega_p^2(r) = \frac{\omega_{p0}^2}{\gamma(r)}\frac{n_e(r)}{n_{e0}} \tag{3.35}$$

by replacing 3.35 to 3.24 we have:

$$\eta(r) \approx 1 - \frac{1}{2}\frac{n_e(r)}{\gamma(r)n_c}. \tag{3.36}$$

Thus, refractive index is modified by the density distribution and the relativistic factor. According to (Esarey et al., 2009) the refractive index for a weakly relativistic case is given by the relation:

$$\eta(r) = 1 - \frac{\omega_p^2}{2\omega_0^2}(1 - \frac{a^2}{2} + \frac{\Delta n_e}{n_0} + \frac{\delta n_e}{n_0}) \tag{3.37}$$

where the term $a^2/_2$ corresponds to the relativistic laser guiding, $^{\Delta n_e}/_{n_0}$ is the term related to the preformed plasma channel along the radius, and $^{\delta n_e}/_{n_0}$ is the term related to the plasma wave guiding. Practically, plasma focuses the gaussian laser beam along the propagation axis, acting as a convex lens. There is a critical power above which self-focusing is happening (Mangles et al., 2012):

$$P_c = \frac{8\pi\varepsilon_0 m_e^2 c^5 \omega_0^2}{e^2\omega_p^2} = 17\frac{\omega_0^2}{\omega_p^2}\,[GW]. \tag{3.38}$$

For Zeus interacting with a plasma with density $n_{e0} = 5\ 10^{18} cm^{-3}$ the critical power is almost $6\ TW$, far beyond laser Zeus power.

3.6.2 Self-compression

The modulations in the density and consequently in the refractive index responsible for self-focusing are also happening longitudinally. The locally varying group velocity along the laser pulse propagation axis can cause a compression of the pulse, together with the generation of new frequencies in the laser spectrum, a phenomenon known as self-phase modulation (Gordon et al., 2003). Self-focusing and self-compression may be useful when the initial laser pulse intensity is too low to resonantly drive a wakefield.

3.6.3 Filamentation

A phenomenon called filamentation of the laser beam occurs when the focal length is too short, so that $w_0 < \lambda_p$ (Thomas et al., 2007), or when imperfections of the laser beam exist (Andreev et al., 2007). In this case the beam is broken into smaller beamlets, which drive smaller plasma waves on both sides of the laser beam. The adjacent structures may contain high power, able to drive additional wakefields. Also, injection is possible in the main and at the additional accelerating structures; however lower peak energy and higher energy spread of the accelerated electrons is expected, as self-guiding length may be shortened due to the laser power spread ($P < P_C$).

3.7 WAVEBREAKING AND ELECTRON INJECTION

As already discussed, electric fields in LWFA experiments can achieve great values in the order of GV/m. As the electric field increases, there is a limit, known as the wave-breaking, which takes place when the electron oscillation amplitude is so large that they can escape the collective motion. According to (Kostyukov et al., 2009) the electron self-injection happens when the wave breaks, namely electrons are trapped in the wake and accelerated. Electron trapping in the accelerating field happens only if their velocity approaches the phase velocity of the wave. According to (Mangles et al., 2012) to obtain self-injection for a given density, the power aP contained within the FWHM of the beam spot is calculated by the following condition:

$$\frac{aP}{P_c} = \frac{1}{16}\left[\ln\left(\frac{2n_c}{3n_e}\right) - 1\right]^3 . \qquad 3.39$$

Self-injection is a simple and efficient method to inject electrons in the bubble. However, self-injection can last up to the point that the space-charge fields created by the trapped electrons deform the accelerating structure, resulting to wide energy and angular divergence electron beams (Couperus et al., 2017), an effect well known as beam loading.

Finally, the injection process determines the electron beam characteristics (energy, energy spread, angular divergence). Also, from an experimental point of view, fulfilling the matching conditions is not always the case. This is why other injection methods have been established (Faure, 2014). During an experiment, various injection mechanisms may take place simultaneously.

3.7.1 Ionization injection

Usually in LWFA experiments the gas target used is a low Z gas (He or H_2). In this case, due to the small ionization potential of their electrons, the gas is already fully ionized by the leading edge of the pulse. Thus, the peak of the laser pulse will later interact with the preformed plasma and self-injection will occur. Although, when a high-Z gas is used, the intensity at the leading edge of the pulse might not be adequate for the ionization of the inner shell electrons of the gas. Some (or all, depending on their ionization potential) inner shell electrons will be ionized later, by the higher intensity of the peak of the laser pulse. Practically, these electrons become free inside any position of the plasma bubble formed by the outer electrons and accelerated. This mechanism is known as ionization injection. Many experiments have been conducted using various gases and gas mixtures (McGuffey et al., 2010; Mirzaie et al., 2015). However, electron beams created based on this mechanism provide high number of electrons but at the same time they suffer from wide energy spread (Grigoriadis et al., 2021). Practically, ionization injection takes place all over the bubble, providing electrons travelling for different acceleration lengths, thus gaining different amounts of energy.

3.7.2 Injection in a density down-ramp

As discussed in the Introduction, the use of a tailored density profile, with a high-density region followed by a density drop, the so-called down-ramp, is a well-established mechanism, which can provoke localized injection at the density drop region. When a lower-density plateau region follows the down-ramp region, then acceleration is also optimized. In (Bulanov et al., 1998; Suk et al., 2001) the mechanism of injection in a density down-ramp were examined via PIC simulations. Initially the laser propagates at the high-density region, where the bubble is formed. Then, along the down-ramp the plasma density decreases, thus plasma wavelength increases. This leads to a reduced phase velocity at the back of the bubble, while the phase velocity at the front of the bubble is higher, thus the bubble expands longitudinally. Then wave breaking occurs and electrons are injected along the down-ramp. Experimentally this has been realized by the two different setups described in section 1.2.1 (Ekerfelt et al., 2017; Hansson et al., 2015; Thaury et al., 2015). Also, the machining beam concept is based on the same mechanism (Brijesh et al., 2012; Faure et al., 2010).

3.7.3 Optical injection

This method refers to a modified experimental concept, where two laser pulses are used. The first pulse, known as the driver pulse, is destined to form the wakefield but without reaching the self-injection limit. In this case, to trap electrons they must be de-phased with respect to the plasma wave. This is achieved by using an additional pulse, the "injector pulse", which collides with the wakefield, destined to locally trigger injection. In this case a heating process occurs, resulting from the beating of the second, lower intensity pulse with the initial one (Faure et al., 2006). By modifying the delay between the two pulses the acceleration distance is tuned. Although optical injection was successfully achieved, its experimental implementation is complicated and thus is not commonly used.

3.8 ENERGY GAIN IN THE PLASMA WAVE

After injection occurs, acceleration of a beam starts. An electron accelerated in a plasma wave gains energy equal to the product of the accelerating field $E_p$and the acceleration length L_{acc}:

$$W = eE_pL_{acc}. \tag{3.40}$$

In the simplest approach, the upper energy limit is calculated by multiplying the peak electric field achieved before the wave breaking by considering as L_{acc} the distance between the injection position and the end of the gas. However, three mechanisms may limit L_{acc}, the electron dephasing, the pulse depletion length, and the laser diffraction.

3.8.1 Electron dephasing length

At some distance in the accelerating field, the trapped electron beam may reach a velocity higher than the laser group velocity. Consequently, after this distance the beam outruns the accelerating field and starts to decelerate. This distance is the dephasing length, as the beam is no longer in phase with the wake. In the bubble regime, the dephasing distance in the co-moving frame is given by the relation (Lu et al., 2007)

$$L_d^{3D} = \frac{r_b}{1-\beta_p} = \frac{2}{3}\frac{\omega_0^2}{\omega_p^2}r_b = \frac{4}{3}\frac{\omega_0^2}{\omega_p^2}\frac{\sqrt{a_0}}{k_p} \tag{3.41}$$

which is a function of the bubble radius given by 3.30. According to equation 3.41, L_d^{3D} depends on laser intensity and plasma density, providing the opportunity to tune it. L_d^{3D} for laser Zeus, when performing with an a_0=2 and a plasma of $n_{e0} = 4{,}5\ 10^{18} cm^{-3}$, is around $5\ mm$.

3.8.2 Pump depletion length

As the laser pulse propagates, it becomes depleted by transferring its energy to the wakefield. At the pump depletion length, the energy transfer stops, as well as the acceleration. For the bubble regime is given by the relation (Lu et al., 2007):

$$L_{pd}^{3D} = \frac{\mathrm{c}}{u_{etc}} c\tau_0 = \frac{\omega_0^2}{\omega_p^2} c\tau_0 \qquad 3.42$$

where $u_{etc} = {c\omega_p^2}\big/{\omega_0^2}$ according to (Decker et al., 1996) is the etching velocity, namely the erosion velocity of the laser head that excites the wave before the self-focusing effect occurs. L_{pd}^{3D} for laser Zeus and a plasma of $n_{e0} = 5\ 10^{18} cm^{-3}$ is around $5\ mm$. It is important to mention here that while low density leads to longer dephasing and depletion lengths, there is a density threshold, above which self-injection becomes inefficient (Mangles et al., 2007, 2012).

3.8.3 Laser diffraction limitation

As any focused beam, the laser will be diffracted at a certain distance and its intensity will be reduced. The diffraction length in vacuum is connected to the $L_{diff} = 2z_R$. However, this distance is strongly modified due to self-focusing. Practically, the beam remains relatively focused for several Raileigh lengths.

3.9 BETATRON RADIATION

In LWFA the year 2004 is referred as a milestone, as the first high-energy electron beams were achieved. At the same year the so-called Betatron Radiation was observed for the first time. The group of (Rousse et al., 2004) presented a soft x-ray beam of synchrotron-like spectrum with few $mrad$ divergence and duration of few tenths of fs.

According to the synchrotron radiation definition, relativistic electrons wiggling in a periodic field emit photons (Bolton et al., 2018). The total radiation emitted by the relativistic electrons per frequency ω, per solid angle Ω is given by the following relation (Jackson J. D., 1977):

$$\frac{\partial^2 I}{\partial\omega\partial\Omega} = \frac{e^2}{16\pi^3\varepsilon_0 c}\left|\int_{-\infty}^{+\infty} e^{i\omega\left[t-\frac{\boldsymbol{n}*\boldsymbol{r}(t)}{c}\right]} \frac{\boldsymbol{n}\times[(\boldsymbol{n}-\boldsymbol{\beta})\times\dot{\boldsymbol{\beta}}}{(1-\boldsymbol{\beta n})^2}\ dt\right|^2 \qquad 3.43$$

where $\boldsymbol{\beta} = \frac{\boldsymbol{u}}{c}$ is the normalized velocity of the electron, $\boldsymbol{n}$ is the unit vector in the direction of observation, $\boldsymbol{r}(t)$ the electron. According to this relation the yield is maximized when $\boldsymbol{\beta n} = 1$, namely when electrons' velocity approaches c, while is parallel to the direction of observation. In addition, there is no radiation without acceleration, namely the whole spectrum vanishes for $\dot{\boldsymbol{\beta}} = 0$.

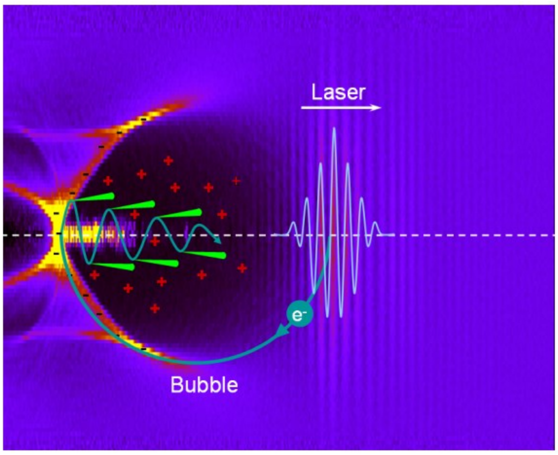

Figure 3-4: Electrons injected in the bubble oscillate transversely and emit x-ray photons of small divergence at the laser propagation direction. This radiation is known as Betatron. Adopted from (Jinchuan, 2013).

While the LWFA takes place, if injected electrons are slightly of axis, at the same time undergo transverse oscillations in the plasma wake, thus they radiate, as seen in Figure 3-4. This motion is happening due to the radial restoring force that electrons experience in the bubble caused by the charge separation. This motion is similar to the one of electrons entering a periodic magnetic field in an undulator, used to create synchrotron radiation. The wavelength of the magnetic field in an undulator is λ_{MAG} and is related to the magnet's length, thus the resulting photons' wavelength is $\lambda_X = {}^{\lambda_{MAG}}/_{(2\gamma)^2}$, where γ is the relativistic factor of the electron. This radiation is limited by the magnet's length, which can't be less than few mm.

The oscillation frequency for the Betatron motion is given by (Rousse et al., 2007)

$$\omega_\beta = \frac{\omega_p}{\sqrt{2\gamma}}. \qquad 3.44$$

In this case the photons' fundamental wavelength λ, for near axis oscillations with a Betatron wavelengh λ_B, calculated as $\lambda = {}^{\lambda_B}/_{(2\gamma)^2}$, however λ_B is in the micron-scale, thus electrons of smaller relativistic factors in comparison to the electrons inserted in the periodic magnetic field of an undulator, radiate photons on the x-ray energy range.

An analytical description of the theory related to Betatron Radiation emission can be found in (Corde et al., 2013). Here we will briefly present some basic scaling of Betatron Radiation, according to LWFA parameters. According to (Wood et al., 2017) the Betatron spectrum can be approximated by the on-axis synchrotron spectrum, given by the relation:

$$\frac{d^2I}{dE\,d\Omega} \sim \gamma^2 \left(\frac{E}{E_c}\right)^2 K_{2/3}^2 \frac{E}{2E_c} \qquad 3.45$$

where $K_{2/3}$is a second kind modified Bessel function and E_c is the critical photon energy achieved by this mechanism. E_c in practical units is given by the following relation:

$$E_C = \hbar\omega_c = 5 * 10^{-21}\gamma^2 n_e[cm^{-3}] r_\beta[\mu m] \qquad 3.45$$

where ω_c is the critical frequency of the spectrum, and r_β the amplitude of the Betatron oscillation, which is related to the electron injection method (Faure et al., 2006). The average photon number with an energy E_c is:

$$N_\chi = 5.610^{-3} N_\beta K \qquad 3.46$$

where N_β is the number of betatron oscillations that an electron will conduct, and K is the strength parameter:

$$K = \frac{2\pi\gamma r_\beta}{\lambda_\beta} = 1{,}33 * 10^{-10}\gamma^{1/2}\, n_e^{1/2}[cm^{-3}] * r_\beta[\mu m] \qquad 3.47$$

where K is a similar concept to the wiggler strength parameter in synchrotron radiation. The previous relations describe the so-called wiggler regime, where $K >> 1$, the radiation spectrum is synchrotron-like, emitted in a narrow cone with a photon emission angle $\theta = K/\gamma$. If $K << 1$ the undulator regime is occurring, where the photon emission angle $\theta = 1/\gamma$, and the photons are emitted at the fundamental wavelength. As Betatron radiation is emitted by a micron scale area, it presents high spatial coherence, thus is ideal for high resolution imaging.

3.10 PIC SIMULATIONS

The real dynamics of LWFA is a 3D non-linear problem, where for all plasma particles, Lorentz equation must be solved using the Maxwell's equations to approach the EM fields. The fields must be continuously updated, according to the self-consistent fields created by the plasma. As discussed before, 1D linear and 1D non-linear approximations have been developed to describe its dynamics. However, the 3D problem can't be analytically solved. A precious tool often used is PIC simulations.

In this dissertation, EPOCH, a plasma physics simulation code was used. In PIC codes, several physical particles are represented using a smaller number of pseudo-particles, thus the problem can be addressed computationally (Arber et al., 2015). In EPOCH the EM fields generated by the laser, together with the motion of these pseudo-particles are calculated using a finite difference time domain technique. Especially in EPOCH a modified leapfrog scheme is used, where the fields are updated at full- and half-time steps. The calculations take place at a fixed resolution mesh point, defined by the plasma characteristics. More precisely, the plasma Debye Length must be resolved to avoid numerical instability. This characteristic plasma length defines the volume of a sphere over which an electrostatic potential is attenuated by a factor of $1/e$ by charge re-distribution, and is given by the relation (Chen, 1983):

$$\lambda_D = \sqrt{\frac{\epsilon_0 k_B T_e}{n_e e^2}} \qquad 3.48$$

where k_B is the Boltzmann constant and T_e the electron temperature.

A full-time step begins with charge and current density calculation from the macroparticles' properties and interpolated at the grid points. Then, based on them, EM fields are calculated at the same and neighbouring grid points. Then, macroparticles are moving due to the EM fields and their new positions are calculated. Based on the new positions, a new time step begins with the new charge and current density calculation.

Chapter 4: CFD simulations setup and results for conical Nozzles

The role of the gas and plasma density in bibliography and LWFA theory has been highlighted. The way that LWFA is connected to the gas and plasma density is complicated and there is no unique solution for such an experiment, as various gas profiles lead to different LWFA injection and acceleration conditions and, thus, to different electron beam characteristics.

In this Chapter the CFD simulations are presented, conducted for understanding the gas flow parameters and accordingly design a series of nozzles, which aim to provide some tunability to the IPPL electron source.

4.1 PHYSICAL PROBLEM

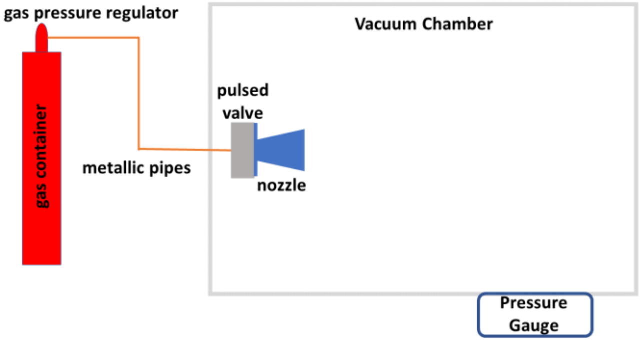

Figure 4-1: Concept of the simulation: Using a pressure regulator the backing pressure is set. The gas flows via a metallic pipe to a pulsed gas valve and exhausts to the vacuum chamber via a nozzle. The pressure gauge located at one of the chambers' ports measures an indicative pressure value, related to the outlet pressure.

In LWFA experiments a high-pressure gas container (up to $200\ bar$) connected with a pressure regulator (up to $60\ bar$) provides a gas flow via metallic pipes to a pulsed solenoid valve. A nozzle attached to the valve forms the gas expansion taking place in a vacuum chamber, continuously pumped. The valve opening duration is $400\ \mu s$, and the flow has been measured to be adequately steady for over $300\ \mu s$. From now on, the gas valve with the nozzle attached will be addressed as gas jet assembly. The pressure measured using a vacuum gauge positioned at the chamber port (about $1\ m$ away from the gas jet assembly exhaust area) never exceeds $10^{-5}\ mbar$. Under such conditions, the pressure ratio along the gas jet assembly is ultra-high and the flow is highly under-expanded.

In the Laser Plasma Accelerators (LPA) one can take advantage of the nozzle geometry to shape the gas profile. The most common nozzle design in LWFA experiments is the De Laval nozzle, a convergent-divergent nozzle that drives a supersonic flow. The influence of the convergent geometry is not as important as the so-called throat, where the diameter is the smallest (Lemos et al., 2009; Semushin & Malka, 2001). Various groups have conducted extensive 2D-axisymmetric CFD simulations as discussed in section 1.3.1, to study various axisymmetric geometries, with the work presented in the doctoral thesis of Schmid being the most complete (Schmid, 2009).

In this study the gas valve was provided, thus, to create supersonic nozzles, we built upon the geometry of the existing valve. Taking advantage of the precisely modelled inner valve geometry, we designed a set of mainly conical extensions, which, in combination with the inner valve geometry, act as Convergent-Divergent (CD) nozzles.

4.2 SIMULATION GEOMETRY MESH AND BOUNDARY CONDITIONS

For the simulation geometry the convergent part is attached to an area, which represents the reservoir where the backing pressure is applied, treated as a pressure inlet. The nozzle exit is in contact with an area that represents the vacuum chamber, where the nozzle exhausts, up to the end of the simulation domain selected to be treated as a pressure outlet. In the inner nozzle wall no slip boundary condition is applied.

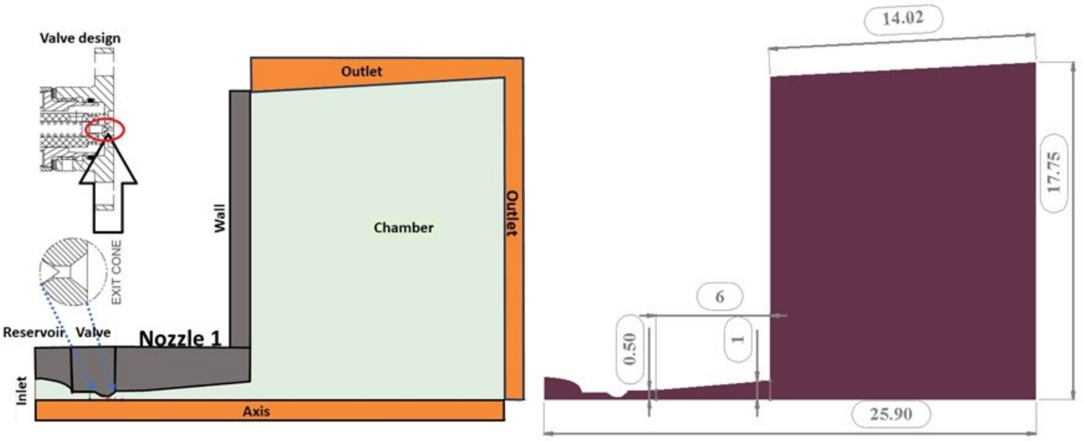

Figure 4-2: left: Conceptual Flow Domain. Right: The exact dimensions at various locations.

In Figure 4-2, the simulation geometry for one of the designed nozzles is illustrated. At the left, the boundary areas are highlighted, while at the right the exact dimensions are marked. As illustrated, the part of the valve from the nozzle tip and downstream is included, placed exactly after the constant pressure reservoir. The valve is an Ultra-low leak Extreme performance Valve, from Parker solenoid valve series. This part incorporates already a CD area, with a minimum diameter of $280\ \mu m$. This exact area was selected to be the throat of the integrated nozzle, which was further developed mainly as a cone. This served also to avoid the production of an ultra-small diameter via 3D printing, which is a very difficult task (Döpp et al., 2016).

The nozzle illustrated in Figure 4-2, named Nozzle 1 according to table 1, has 7.5 mm total length, with a front cylindrical section of 1.5 mm length and 1 mm diameter, and a following divergent conical section of 6 mm length, with a 2 mm diameter at the nozzle exit. The length of the flow domain downstream the nozzle exit is about 14 mm. Even though the formed jet expands along a larger distance, the hyperbolic nature of the flow equations allows for omitting its simulation.

In Table 1 the geometrical characteristics of the 5 designed nozzles are displayed. All the five nozzles have a cylindrical area of $1\ mm$ diameter with length equal to its base length and then a conical area. Their exit diameter is from $2\ to\ 3\ mm$, and one of them, Nozzle 5 has a straight part following the divergent-one, to examine a case similar to the one proposed and analyzed in (Mollica, 2016; Rovige et al., 2021). According to these studies, an oblique shock is expected to be formed due to the straight area, which will create a high-density peak away from the nozzle exit.

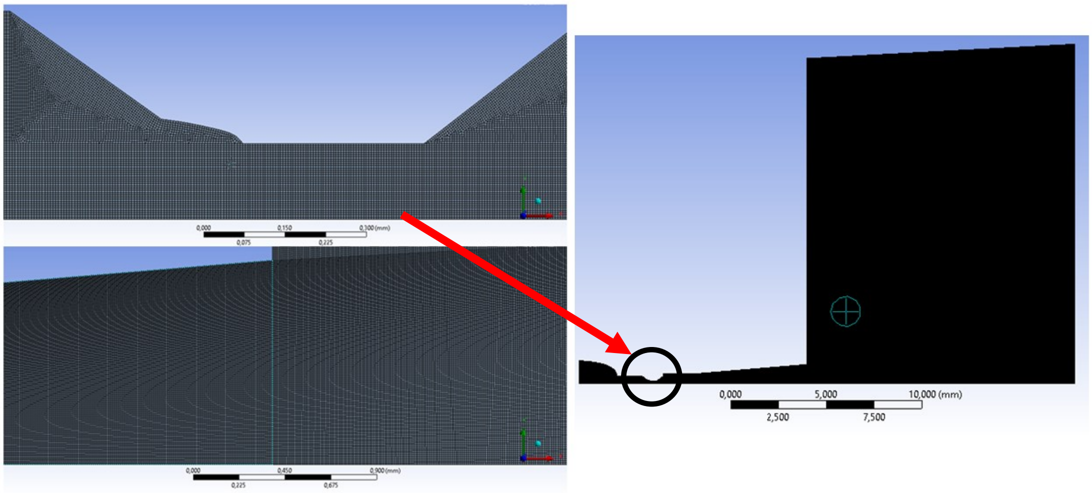

Figure 4-3: The 2D mesh is unstructured, quadrilateral dominant. The mesh after the close to the wall area is finer, to capture viscous effects.

In Figure 4-3 the mesh constructed for the 2D simulation is presented. The mesh is unstructured, consisting mainly of quadrilateral elements, although triangular elements are used at the regions of significant curvature, such as the area at the throat of the inner valve. For this specific geometry, it consists of more than 10^6 elements. A mesh independence study (see Appendix A) demonstrates that the applied discretization was sufficient.

	1	*2*	*3*	*4*	*5*
Cone length (mm)	6	8	3	6	6
Base length (mm)	1.5	3	1.5	1.5	2
Exit diameter (mm)	2	3	2	2.5	3
Straight part (mm)	-	-	-	-	2

Table 1: Geometric features of the designed nozzles

4.3 DENSITY BASED SOLVER

The problem was approximated as a 2D axisymmetric and steady state one. ANSYS Fluent provides two solvers, pressure-based and density-based, that solve the equations in a different sequence. For compressible flow problems density-based solver is preferred. As seen in Figure 4-4, the density-based solver is coupled, thus solves in the same step continuity, momentum, and energy equations (2.35,2.36 and 2.38) and afterwards, the turbulence equations are solved (Ansys Inc, 2013).

In the simulations, double precision accuracy was used. A convergence criterion for the residual value for each variable is set and until all reach this value ($< 10^{-4}$), the solver updates the fluid properties based on the current solution and moves to the next iteration. Before the first iteration, all values are initialized via a hybrid initialization. Additionally, a Full-Multigrid Initialization scheme on 5 coarser grids is used to facilitate convergence.

Implicit formulation is selected, and the flux type follows the Roe Flux Difference Splitting scheme (Roe-FDS). The turbulence model used was k-ω Shear Stress Transport (SST). In this model the transport equations for the turbulent kinetic energy k and the specific dissipation rate ω are calculated near the walls, to provide high accuracy, while a simpler model is solved in the inner flow area, to save computational time (Menter, 1994).

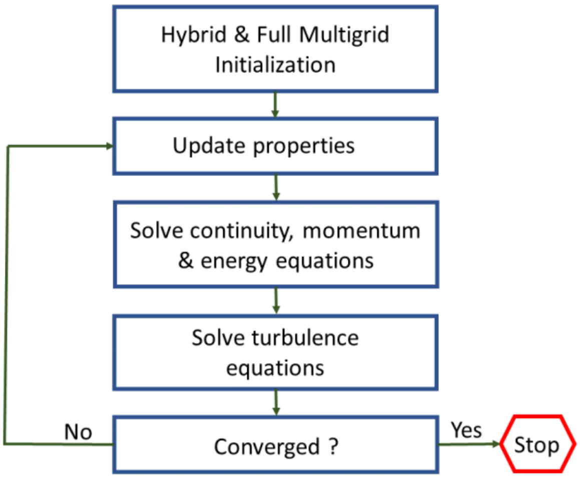
Hybrid & Full Multigrid Initialization
Update properties
Solve continuity, momentum & energy equations
Solve turbulence equations
Converged ?
No
Yes
Stop

Figure 4-4: Steps of the Density Based solver of ANSYS Fluent.

For flow, turbulent kinetic energy and specific dissipation rate calculations second order upwind schemes were applied. However, to accelerate convergence, solution steering technique was enabled, which allows to reduce solution accuracy by creating a blend of first and second order upwind schemes (in our case 30-80 %).

4.4 SIMULATION RESULTS

The basic model selected, based on bibliography research, is calculating gas density using on ideal gas equation of state for constant values of gas properties (here for $p = 1\ bar$ and $T = 300\ K$) (Aniculaesei, 2015; Mollica et al., 2016; Schmid, 2009). The gas properties values are presented in Table 2. The use of various gasses in our experiments (Grigoriadis et al., 2021) motivated a comparative study for various gas types.

Gas	Specific heat (J/kg K)	Thermal conductivity (W/m K)	Viscosity (kg/m s)	Molecular weight (amu)
He	5190	0.156	1.96×10^{-5}	4.002
Ne	1030	0.0498	3.13×10^{-5}	20.17
N_2	1040	0.026	1.76×10^{-5}	28.012
Ar	520	0.0179	2.23×10^{-5}	39.94

Table 2: gas properties for p=1 bar and T=300 K (Https://Www.Engineeringtoolbox.Com/; Https://Www.Engineersedge.Com)

In Figure 4-5 details of the simulated flow inside the gas jet assembly with Nozzle 1 are highlighted. The inlet backing pressure applied was $40\ bar$ and the outlet pressure was set to $1\ mbar$. Initially, at the gas reservoir and the first part of the valve the gas density remains constant. As the gas enters the gas valve and comes close to the throat, the flow changes from subsonic ($M < 0.3$) to sonic ($M = 1$). Then, exactly after the valve throat, where the first small divergent area is located (which is part of the inner valve) and inside the cylindrical area of Nozzle 1, the pressure ratio is ultra-high, and a barrel shock is developed. Located upstream of the Mach disk, lies an area where the Mach number approaches a value of 10. Inside the divergent part of Nozzle 1, downstream the barrel shock, an oblique reflected shock occurs and further on, multiple expansion and compression waves are generated, forming a weaker diamond-like shock, which dissipates downstream the nozzle before its exit. The Mach number continues to rise inside and downstream the Nozzle's 1 exit.

Gas crossing the Mach disk is then subsonic, while the gas passing through the barrel and oblique reflected shock remains supersonic, resulting to a slip line between the subsonic area in the jet core and the supersonic at the shear layer, similar to the formations noticed in via PLIF imaging, at the outer area of a highly underexpanded jet (Wilkes et al., 2005). Modelling and simulation of the exact geometry, including the commercial valve part revealed such formations, which govern the flow, as preliminary simulation tests, simulating Nozzle 1 without considering the valve geometry, didn't reveal the strong barrel shock.

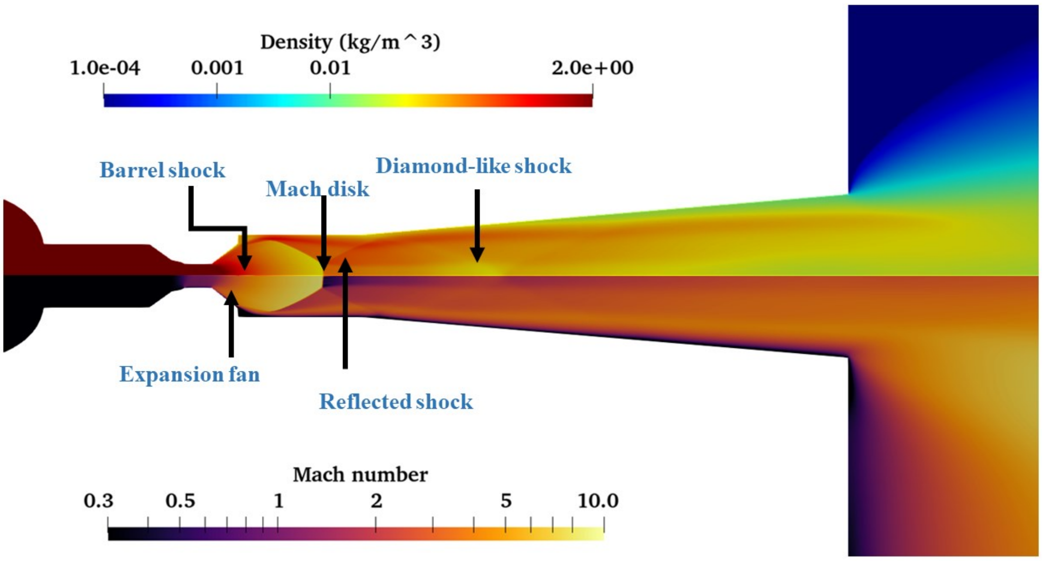
Density (kg/m^3)
1.0e-04
0.001
0.01
2.0e+00
Barrel shock
Mach disk
Diamond-like shock
Expansion fan
Reflected shock
Mach number
0.3
0.5
1
2
5
10.0

Figure 4-5: Detail of the simulation domain inside Nozzle 1: density map (top) and Mach number map (bottom). Flow formations inside the inner valve and nozzle region are highlighted: a barrel shock, followed by a diamond-like shock are observed inside the nozzle. Maximum values of Mach number are in the order of 10.

In Figure 4-6 the simulated variation of the gas density and Mach number along the symmetry axis is presented, for the same case. Density decreases with an almost constant rate, up to the areas where abrupt geometry changes happen, such as the valve throat, or the transition to the divergent part. The rate of change in density is inverse to the rate of change of the Mach number. The discontinuities in Mach number and density correspond to the location where shock waves are formed. The first strong discontinuity is the Mach disk, while the second weaker one is the diamond shock.

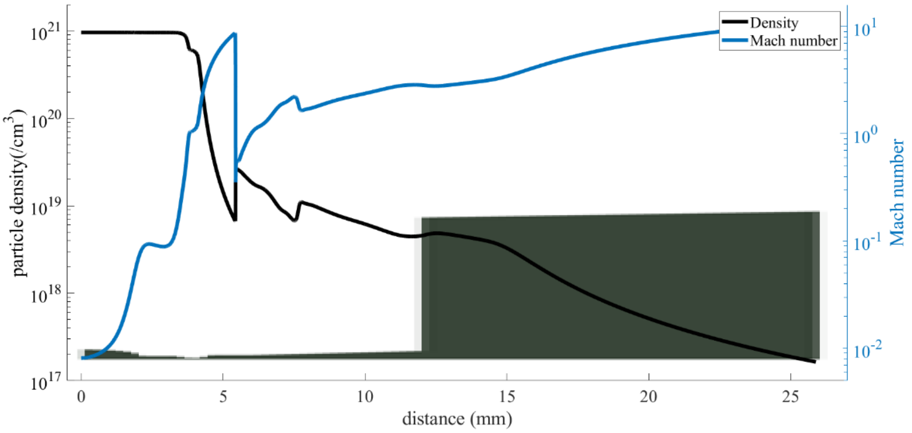

Figure 4-6: Density (black) and Mach number (blue) along the symmetry axis of the simulation domain (bottom), for He and $40\ bar$ backing pressure.

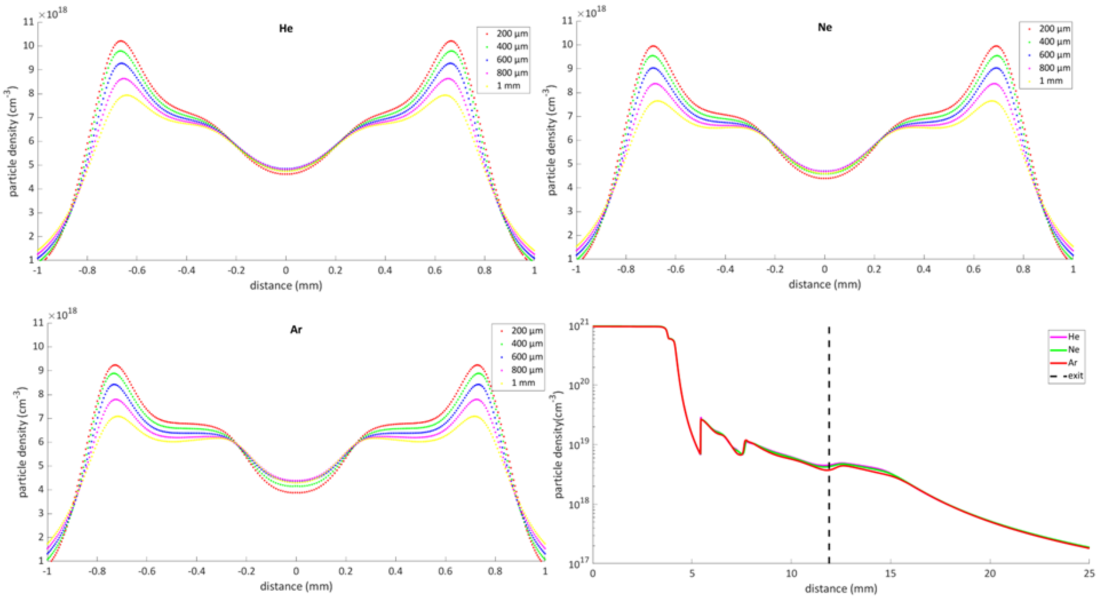

Figure 4-7: Gas density profiles $200, 400, 600, 800\ and\ 1000\ \mu m$ downstream the Nozzle 1 exit for He, Ne and Ar, for $40\ bar$ backing pressure and outlet pressure $1\ mbar$). Density along the axis of symmetry, for the 3 gases.

In Figure 4-7, the gas density profiles of He, Ne, and Ar at $200, 400, 600, 800\ and\ 1000\ \mu m$ downstream the Nozzle 1 exit, for the same boundary conditions, are plotted. The overall density decreases by increasing distance from the nozzle's exit for all gasses, while He presents the higher and Ar the lower. In the last plot, the density along the symmetry axis is plotted for He (magenta), Ne (green), and Ar (red). The density variation for the 3 gasses is almost identical.

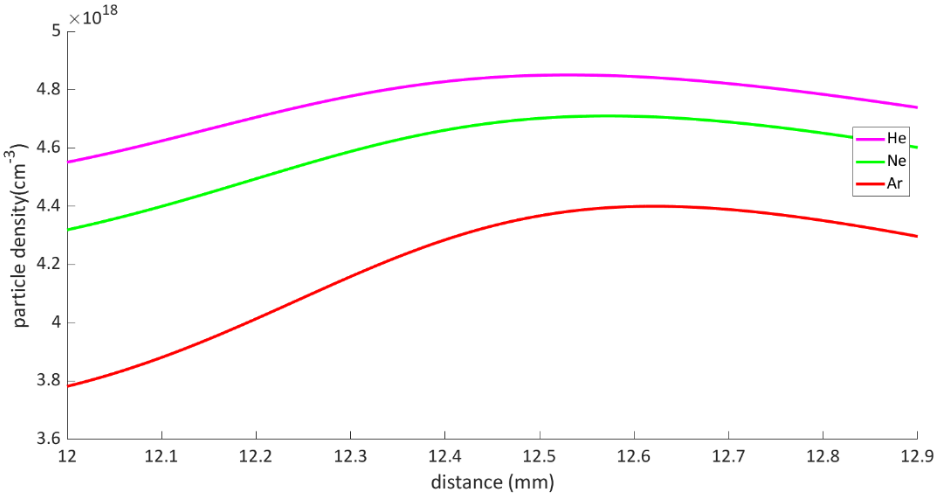

Figure 4-8: Density along axis for He, Ne and Ar $1mm$ downstream the Nozzle 1 exit. A small density increase is noticed, due to the reflections of the expansion waves to the shear layer. The selected area is zoomed, as being the mostly used in LWFA experiments.

In Figure 4-8 a zoom for $1\ mm$ distance downstream the Nozzle 1 exit of this plot is depicted. The selected area corresponds to the area of interest for LWFA experiments. The flow is characterized by the transition from the inner nozzle to the outer domain, namely the low-pressure chamber, thus there are no more geometrical restrictions posed (solid boundary). In this region, a small increase in density, lasting for a short length, is noticed. This is attributed to the existence of the shear layer, where expansion waves are reflected.

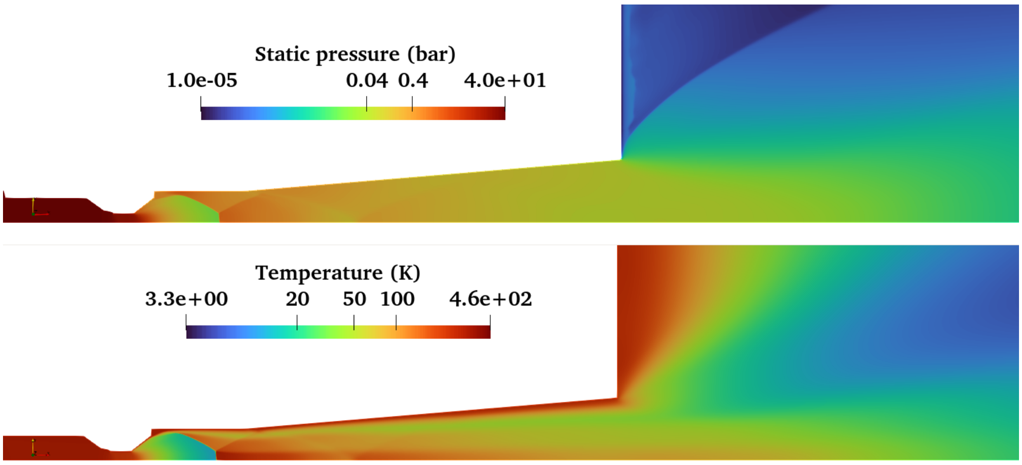

Figure 4-9: Pressure and temperature in the flow domain. The values vary significantly and upstream the Mach disk the static pressure is below the critical value, while the temperature is slightly above.

However, by examining other important quantities, such as pressure and temperature, displayed in Figure 4-9, one can see that there is a significant variation along the simulation domain, which may strongly affect gas properties. Also, upstream the Mach disk, the critical point conditions may be locally met. This is why a study of the model reliability was conducted, presented in the next paragraphs.

4.4.1 Kinetic theory model

In (Henares et al., 2019) gas jet targets destined for ion acceleration experiments, thus expected to be over-dense, according to the definitions discussed in section 4.3, are examined. The range of backing pressures examined in their study is ultra-wide ($1 - 1000\ bar$), thus different tabulated values of the gas properties are used for different inlet pressures. Although closer to each simulation ran, the properties have a 2D distribution according to the local value of the temperature.

In this paragraph the differences in the flow, when the gas properties are calculated by using the kinetic theory model, included in ANSYS Fluent, are examined (Ansys Inc, 2013). This model was used to run a simulation for Nozzle 1, with He, at the exact same boundary conditions as in the previous paragraph, which are considered reference conditions for most of the following studies. According to the kinetic theory model, viscosity is given by the equation

$$\mu_i = 2.67\ 10^{-6} \frac{\sqrt{M_W T}}{\sigma^2 \Omega_\mu}, \qquad 4.1$$

where M_W is the molecular weight, $\Omega_\mu = \Omega_\mu(T^*)$ is the diffusion collision integral and $T^* = \frac{T}{(\varepsilon/k_B)}$. The quantity σ (Å) stands for the Lennard-Jones characteristic length and $\varepsilon/_{k_B}$ (K) stands for the Lennard-Jones energy parameter. Lennard-Jones potentials are intermolecular potentials which model soft repulsive and attractive interactions for neutral molecules and their value is given for each element by the relation (Lennard-Jones, 1931)

$$V_{LJ}(r) = 4\varepsilon\left[\left(\frac{\sigma}{r}\right)^{12} - \left(\frac{\sigma}{r}\right)^{6}\right] \qquad \mathbf{4.2}$$

where r is the intermolecular distance, ∂ is the distance where $V\ (\sigma) = 0$ and ε is the depth of the well, as shown in Figure 4-10. The values used for He in this study are $\sigma = 2{,}52\ \text{Å}$ and $\epsilon = 9.87\ K$ found in (J. O. Hirschfelder et al., 1954).

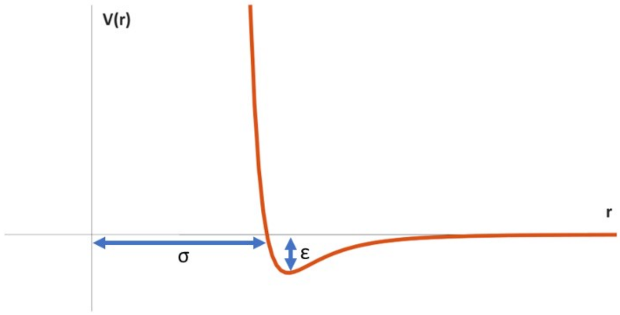

Figure 4-10: Lennard-Jones potential characteristic form; σ is the distance at which the potential is equal to zero, and $\boldsymbol{\varepsilon}$ is the depth of the well.

Considering kinetic theory, the specific heat capacity of a gas i, is calculated by the relation:

$$c_{p,i} = \frac{1}{2}\frac{R}{M_W}(f_i + 2), \qquad 4.3$$

where f_i is the number of degrees of freedom of the gas. Thermal conductivity k_i is calculated via the relation:

$$k_i = \frac{15}{4}\frac{R}{M_W}\mu\left(\frac{4}{15}\frac{c_{p,i}M_W}{R} + \frac{1}{3}\right), \qquad 4.4$$

The results obtained using kinetic theory model to calculate gas properties (top) together with the results obtained with the values of table 1 (bottom) are displayed in Figure 4-11. He holds 3 degrees of freedom anyway, thus, c_p value displayed in 4-11(a) is constant for both cases. In figure 4-11(b) and (c) the viscosity and thermal conductivity values are displayed. According to kinetic theory model, both vary for over 2 orders of magnitude.

In addition, in Figure 4-11(d), (e) and (f) the density, Mach number, and pressure for constant (bottom) and calculated according to the kinetic theory model (top) values of μ, c_p and k are presented. The effect of the model in those quantities, which are important to our study, is very small and in the contour maps is eliminated.

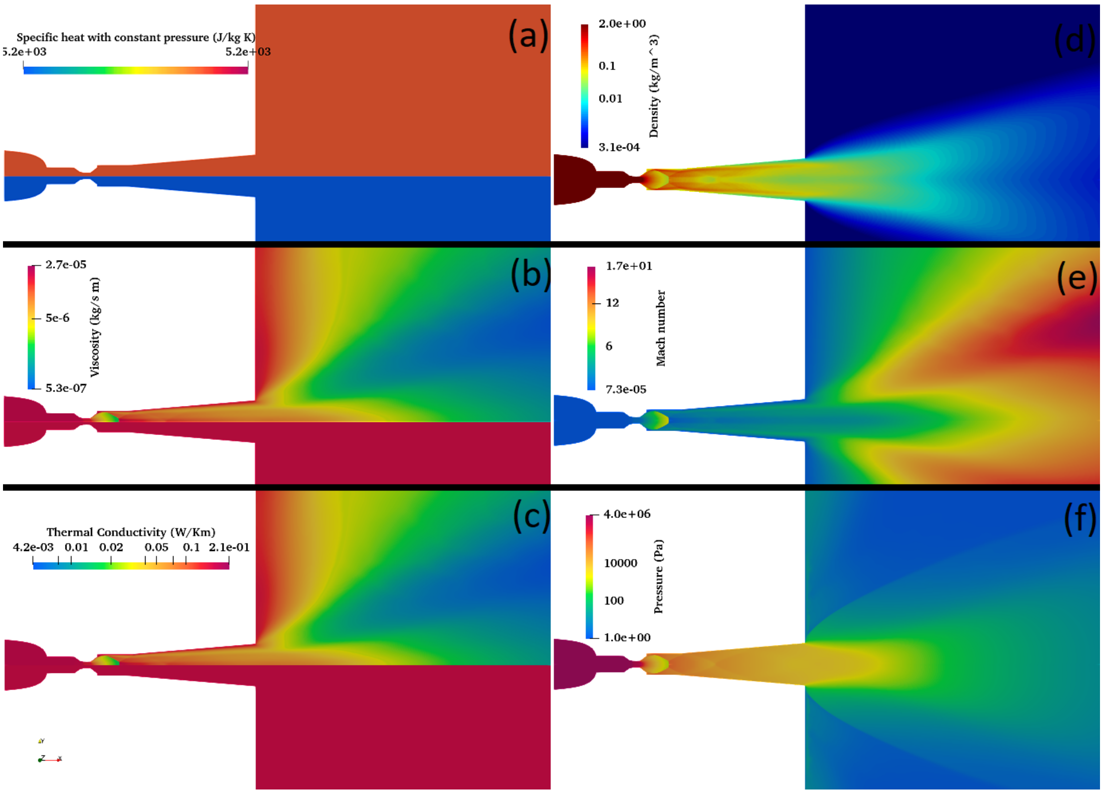

Figure 4-11: The comparison of the quantities a) C_p, b) μ, c) k, d) ρ, e) M and f) p for two different simulation cases. In case 1 the values of c_p, μ and k are constant (bottom), while in case 2, are calculated by the kinetic theory model. Although the values of μ and k vary almost two orders of magnitude, the variation of ρ, M and p is below the resolution of the contour maps.

To highlight the effect of the model on the gas density and Mach number, in Figure 4-12 (top) the profiles $400\ \mu m$ downstream the nozzle are plotted, as well as the same quantities along the symmetry axis at the area corresponding to the one suitable for LWFA experiments (bottom). The changes noticed in the examined values are minor ($\sim 1\ \%$). Considering equation 2.36, we infer that the pressure gradient is the governing term, while heat conduction and viscosity terms are of minor contribution at the case examined.

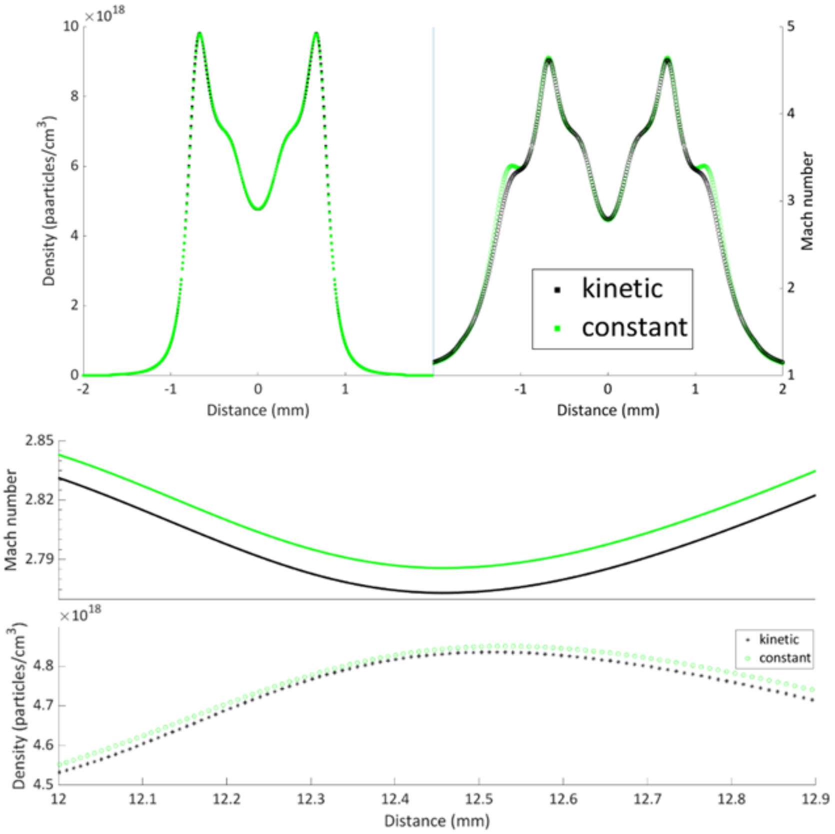

Figure 4-12: Top: Particle density (left) and Mach number (right) profiles $400\ \mu m$ downstream the nozzle exit; Bottom: Mach number and density variation along the axis, for constant values of the gas properties according to table 2 (green) and for properties calculated according to the kinetic-theory model (black).

4.4.2 Density calculation with Peng-Robinson real gas model

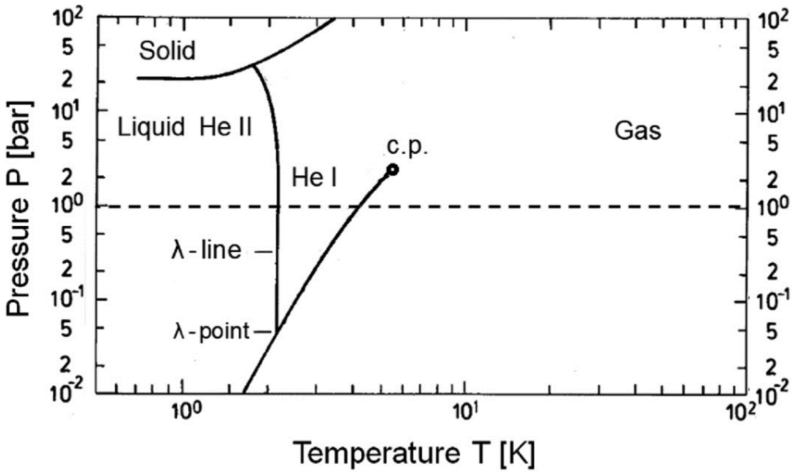

Figure 4-13: p-T phase diagram of ⁴He. The critical point is at $p_c = 2.27\ bar$ and $T_c = 5.2\ K$ (Slenczka & Toennies, 2022).

The validity of the ideal gas approximation is also examined here. Real gases and especially noble gases tend to behave like an ideal gas for a wide range of thermodynamic conditions. However, the particles that compose the gas under relatively low pressure and extremely low temperature conditions exert intermolecular forces and when the critical point is achieved the gas starts to liquefy.

In Figure 4-13 the phase diagram of He is displayed. The critical point of He is at a very low-temperature, T_c=5.2 K and P_c=2.27 bar. The triple point λ is also highlighted, and the $\lambda - line$, which particularly for He, instead of denoting the co-existence of gas, liquid (He I) and solid state, denotes the co-existence gas, liquid (He I) and superfluid state (He II) (Slenczka & Toennies, 2022).

A test was conducted by applying a real gas model for the density calculation. The Peng-Robinson model (Peng & Robinson, 1976) is expressing equation of state via the relation:

$$p = \frac{RT}{V-b} - \frac{a}{V^2 + 2bV - b^2} \qquad 4.5$$

where V is the molar volume, while a and b are given by:

$$a = \left(0.4\frac{R^2T_c^2}{p_c}\right)\left[1 + (0.4 + 1.5\omega - 0.27\omega^2)\left(1 - \left(\frac{T}{T_c}\right)^{1/2}\right)\right]^2 \qquad 4.6$$

$$b = \frac{RT_c}{p_c} \qquad 4.7$$

and ω is the acentric factor, being equal to 0.39 for He. The ANSYS Fleunt material database was used to determine the demanded properties for the application of this model.

To highlight the effect of the model on the gas density and Mach number, in Figure 4-14 (top) the profiles $400\ \mu m$ downstream the nozzle is plotted, as well as the same quantities, along the symmetry axis at the area corresponding to the one suitable for LWFA experiments (bottom). The gas density at the peaks of $400\ \mu m$ profiles is reduced by almost $< 3\%$, while at the middle area is increased by $\sim < 8\%$. The difference remains high along the axis. The differences noted here are considerable. The density profiles expected are slightly modified, however, as the model has a higher computational cost, and its contribution is now known, the following parametric studies were conducted by using the ideal gas assumption.

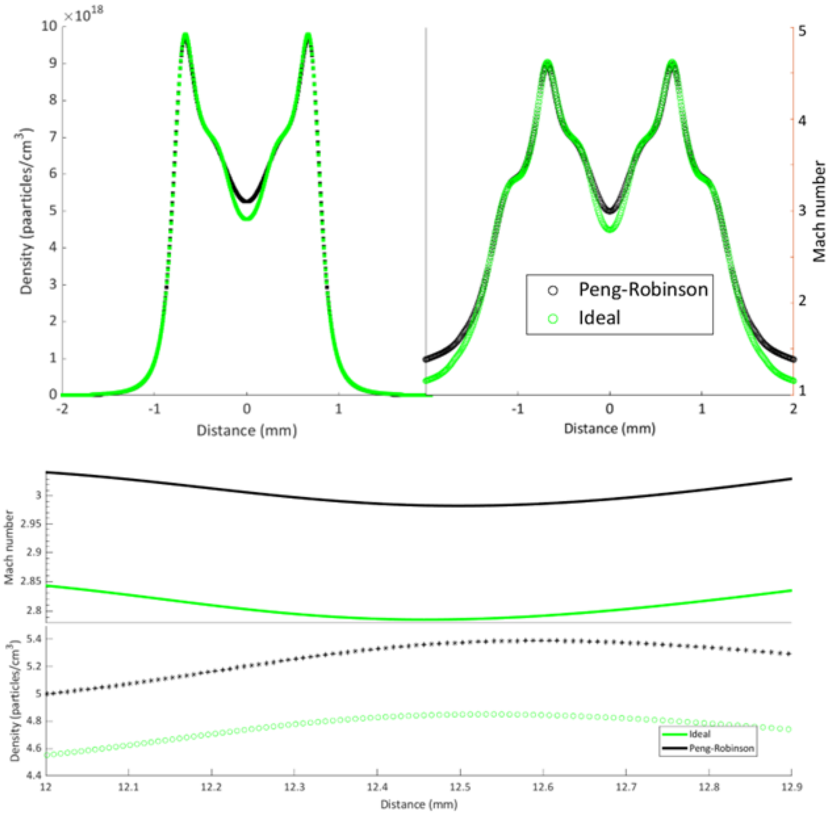

Figure 4-14: Particle density (left) and Mach number (right) profiles $400\ \mu m$ downstream the nozzle exit. Bottom: Mach number and density variation along flow axis for the density calculated from the ideal gas equation of state (green) and for the density calculated from the Peng-Robinson real gas equation of state (black).

4.5 EFFECT OF GAS PRESSURE

4.5.1 Inlet pressure parametric study

In LWFA a wide range of backing pressures is tested, while optimizing the experimental conditions. In this study, using Nozzle 1, the backing pressure was varied, and the density variations are highlighted. In Figure 4-15 the density contour map for $50\ bar$ backing pressure (top) is displayed together with the $25\ bar$ backing pressure (bottom) density contour map, under the same color scale, while the outlet pressure was kept constant. The flow features formed are similar for both cases, however, as backing pressure increases, the overall density increases, and the jet extends for a longer area.

In Figure 4-16 the simulated density $400\ \mu m$ downstream Nozzle 1 exit is plotted for $25\ to\ 50\ bar$ backing pressure. Although the profiles are similar, the peak to minimum value ratio is increased by increasing backing pressure. In addition, the density peaks lie closer to each other, as the backing pressure decreases. Practically, when a more uniform profile is desired, the operation of the same nozzle at lower packing pressure is a possible option.

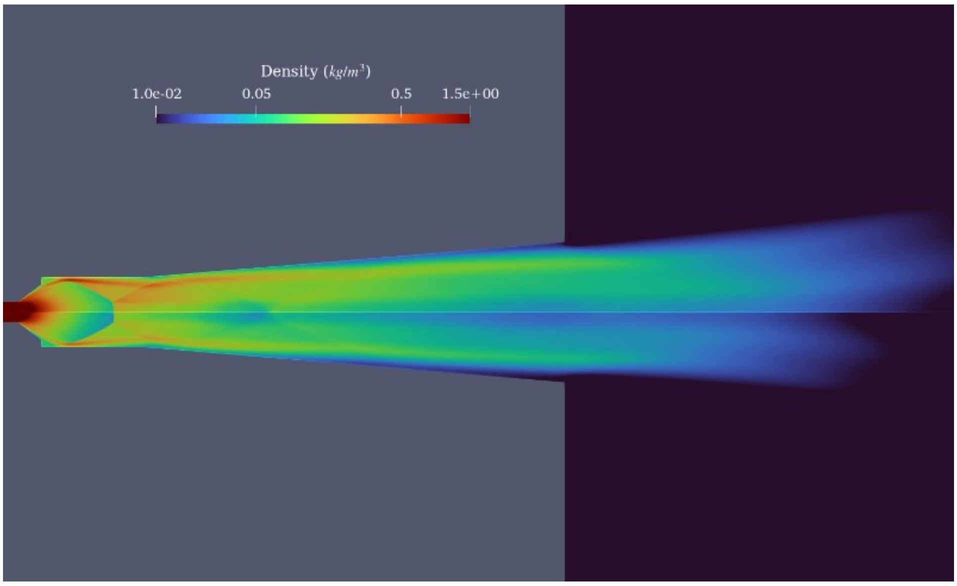

Figure 4-15: Density contour maps for He for $50\ bar$ (top) and $25\ bar$ (bottom) backing pressure. Similar flow features are formed. The overall density decreases by decreasing backing pressure, as also the length of the jet.

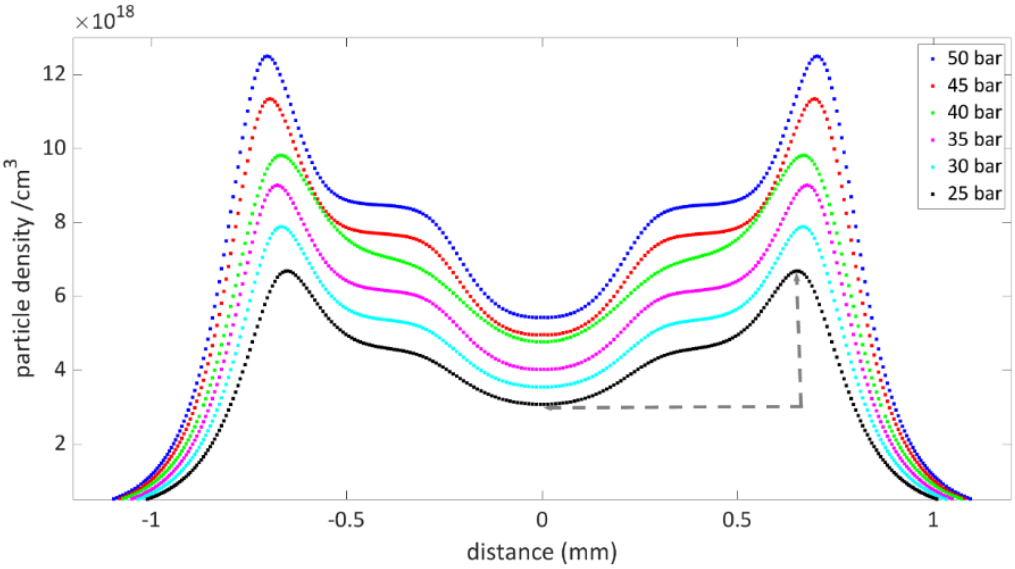

Figure 4-16: Particle density $400\ \mu m$ downstream the nozzle's exit, for $25\ to\ 50\ bar$ backing pressures. The peak to minimum value ratio is increased, as well as the distance between the peaks, as the backing pressure increases.

Finally, in Figure 4.17 the simulated particle density along axis for $25\ to\ 50\ bar$ backing pressure is plotted. The dashed line represents the nozzle's exit. We notice that after the first strong shock, which is located at the same position for all cases, the formations are located sligthly earlier for the lower backing pressures.

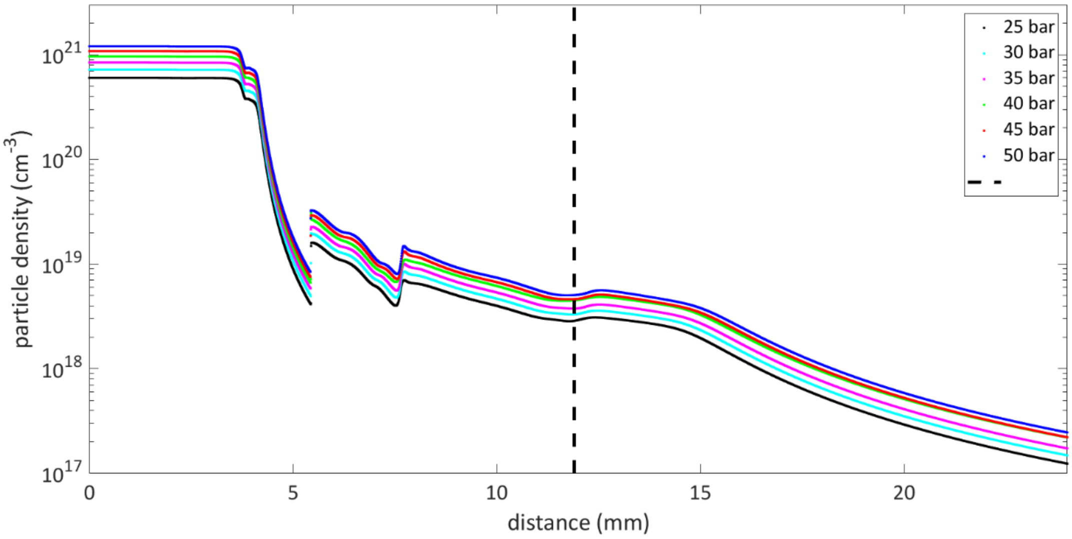

Figure 4-17: Particle density along axis for $25\ to\ 50\ bar$ backing pressures. The flow features after the first barrel shock are moving slightly downstream as the pressure increases.

4.5.2 Outlet pressure

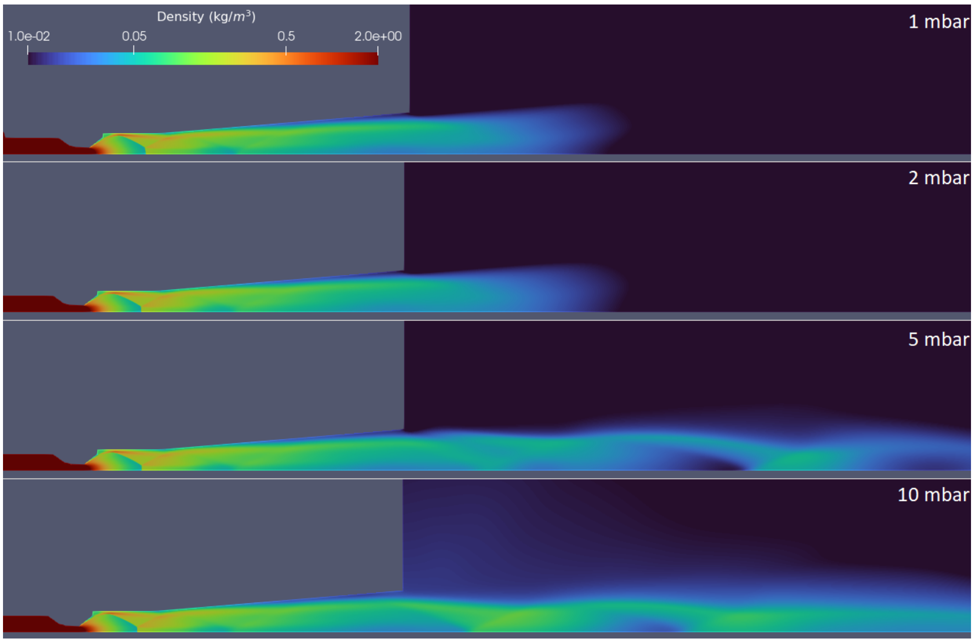

Figure 4-18: Density contour maps for Nozzle 1 with He, at $40\ bar$ backing pressure. From top to bottom, outlet pressure increases from $1\ to\ 10\ mbar$, initially without a great effect on density values, especially at the area close to the nozzle exit. Progressively diamond-like shocks with increasing periodicity are formed.

On the contrary to the backing pressure, which is manually picked during an experiment, the pressure at the outlet is a non-controllable value, as it depends on the amount of gas exhaust and the pumping conditions in the chamber. Also, by the measured value, only a rough estimation is possible, as the pressure gauge is fixed much further than the outlet, at the chamber ports (Figure 4-1). Thus, the selection of the pressure value at the outlet is a complicated process, where calibration simulations must be conducted, as discussed in (Fan-Chiang et al., 2020). However, nozzles weren't yet manufactured, therefore the range tested presented here was based mainly on bibliography.

Density contour maps, for a wide range of outlet pressures are presented in Figure 4-18. As the outlet pressure increases, additional diamond-like shocks are formed. The periodicity of these shocks is increasing with the outlet pressure. Also, smaller outlet values were tested, but without significant difference, especially near the nozzle's exit, where the area of interest is located.

Finally, based on previous measurements made by colleagues for another nozzle (Nozzle 0, provided with the gas valve) $1\,mbar$ was selected as the outlet pressure. Emphasis is given to the fact that this approximation can't match with all nozzle's geometries, simulation domains and backing pressures tested, however was a legit simplification, typically conducted in bibliography.

4.6 NOZZLES 2-5

As discussed above, various geometries have been tested. In Figure 4-19 the density contour maps for nozzles 2, 3, 4 and 5 (named according to Table 1, where their geometrical characteristics are presented) are displayed. Their designs are presented in Appendix B. The simulations were performed for He, at $40\,bar$ backing pressure and $1\,mbar$ at the outlet. The model was set as described in section 4.1. The flow characteristics for the 4 nozzles are similar to the ones' produced by Nozzle 1, shown in Figure 4-5.

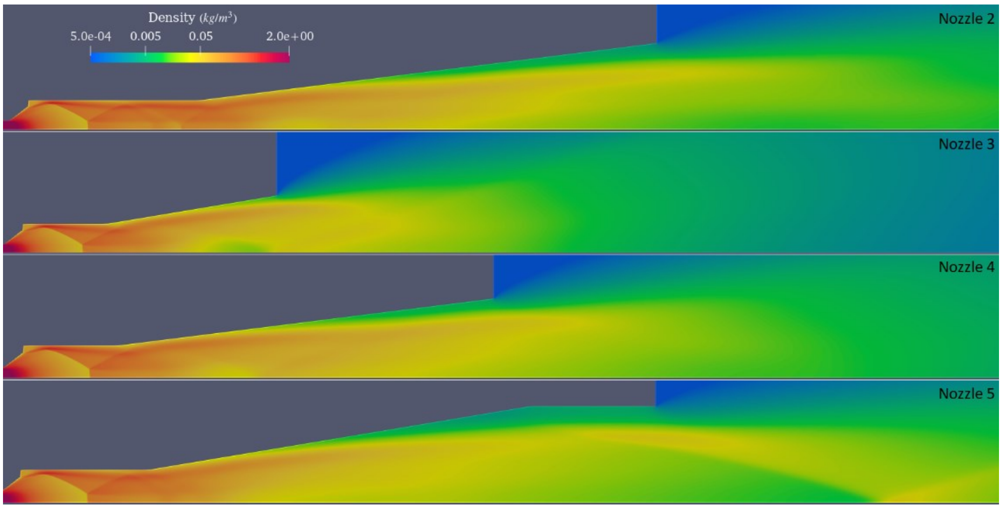

Figure 4-19: Density contour maps of Nozzles 2, 3, 4 and 5, for He, with $40\,bar$ backing pressure, and $1\,mbar$ at the outlet. Their dimensions are presented in Table 1.

First, a barrel shock is produced at the same position inside the cylindrical part of the nozzle for all nozzles. For Nozzle 2, inside the cylindrical part which extends longer (for $3\,mm$), a second less intense barrel shock, with a smaller Mach disk is formed. For all nozzles, the weaker, diamond-like, shock is produced in the conical area. For Nozzle 3, which has the shorter conical length a part of the high-density area of the diamond-like structure lies also out of the nozzle. In Nozzle 5, due to the straight duct area following the conical one, a diamond-like shock is formed further downstream the nozzle exit. The barrel shock is located at the same position; however, the nozzle has a longer cylindrical area after the throat ($2\ mm$), thus the diamond-like shock is formed closer. Such a nozzle is ideal for experiments where the nozzle must be placed in a lower position, as it produces a high-density area far downstream its exit. Also, Nozzle 5 is ideal for experiments where a density profile peak at the middle is preferred.

The density profiles of all nozzles $400\ \mu m$ downstream each nozzle exit are plotted in Figure 4-20. In general, the forms of the profiles at this distance are similar. The length of the profile increases for longer nozzle exit. At the same backing pressure, the density drops by increasing nozzle's exit diameter. Nozzles 2 & 4 provide smoother profiles.

Finally, in Figure 4-21 the particle density variation along axis, for the area $1mm$ upstream to $13\ mm$ downstream the nozzles exit are displayed. The diamond-like shock of Nozzle 3 lies downstream its exit, and of Nozzle 5 lies about $4\ mm$ downstream its exit.

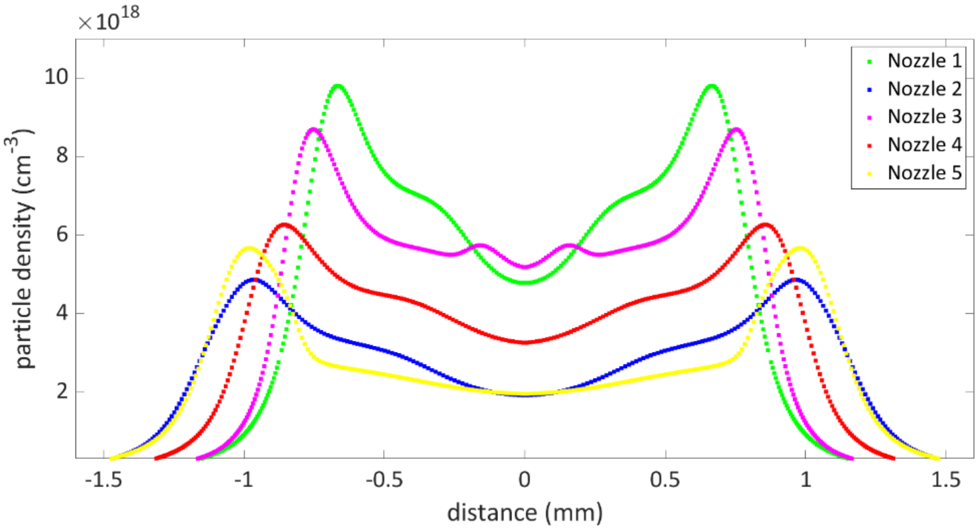

Figure 4-20: Particle density of all Nozzles of Table 1, $400\ \mu m$ downstream each nozzle's exit, for He, with $40\ bar$ backing pressure and $1\ mbar$ at the outlet. The profile lengths vary according to the exit diameter of each nozzle. The density profiles of Nozzles 2 & 4 are smoother.

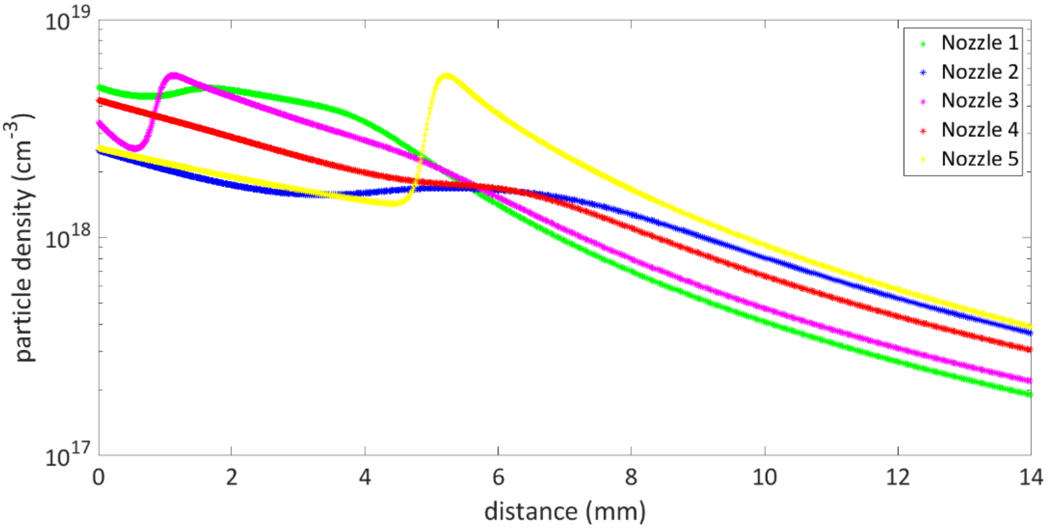

Figure 4-21: Particle density of all Nozzles of Table 1, along axis of symmetry, from $1\ mm$ upstream the exit to $14\ mm$ downstream, for He, with $40\ bar$ backing pressure, and $1\ mbar$ at the outlet.

4.7 REMARKS

Various designs of axisymmetric nozzles have been simulated under various boundary conditions. The resulting profiles are in the desired density range. This set of nozzles was designed to provide an opportunity to operate the existing LWFA electron source under various conditions. The nozzles were manufactured via 3D printing methods, and their density profiles were experimentally measured using interferometry technique. In chapter 6, where the density measurements are presented, the validation of the simulations is also discussed.

Each examined divergent nozzle contains the formed barrel-shock and the subsequent diamond-like expansion and compression waves. Such waves would be also formed (but with different characteristics) in the case when the divergent nozzles, designed by the author, were omitted (while keeping only the convergent-divergent EM valve); in such a case a typical underexpanded free-jet would be formed at the valve exit, while the reflections of the expansion waves would be at the shear layer of the free-jet. Here, the geometry of the adopted divergent nozzle "controls" the shape and the magnitude of the shock formations and determines the details of the density profile at the nozzle exit.

The tunability of the electron source, obtained by modifying the gas density profile is further examined via the experimental results presented in chapter 7. In addition, three non-axisymmetric nozzles have been designed and constructed (see Appendix B), aiming to create a down-ramp density profile. To simulate them 3D CFD simulations are necessary and have been conducted to some extent. However, the mesh construction to reproduce the resolution studied here, necessary to capture the small flow features in 3D domains is a laborious task, not yet accomplished in the context of this dissertation.

Chapter 5: Experimental setups

Figure 5-1: IPPL facility of HMU hosted at Rethymnon (top). The 45 TW laser system Zeus (bottom).

The experimental part of this thesis was implemented in IPPL of HMU (Https://Ippl.Hmu.Gr/). IPPL is a new, outstanding in a national level facility, hosting the most powerful laser in Greece. In Figure 5-1, the building of IPPL facility at Rethymnon is illustrated, together with the $45\ TW$ laser system Zeus room.

In chapter 6, the experimental characterization of the 3D-printed nozzles is presented and evaluated. In the following chapters, the behavior of the LWFA-based electron source, with respect to various density profiles, resulting from the nozzles designed, will be examined. In this chapter, a description of all the experimental setups implemented in this work, e.g., the Nomarski interferometry setup, laser Zeus, and the setups used for the LWFA and Betatron experiments, will be described. For the diagnostics of the experiments an operating principle is presented.

5.1 ZEUS LASER SYSTEM

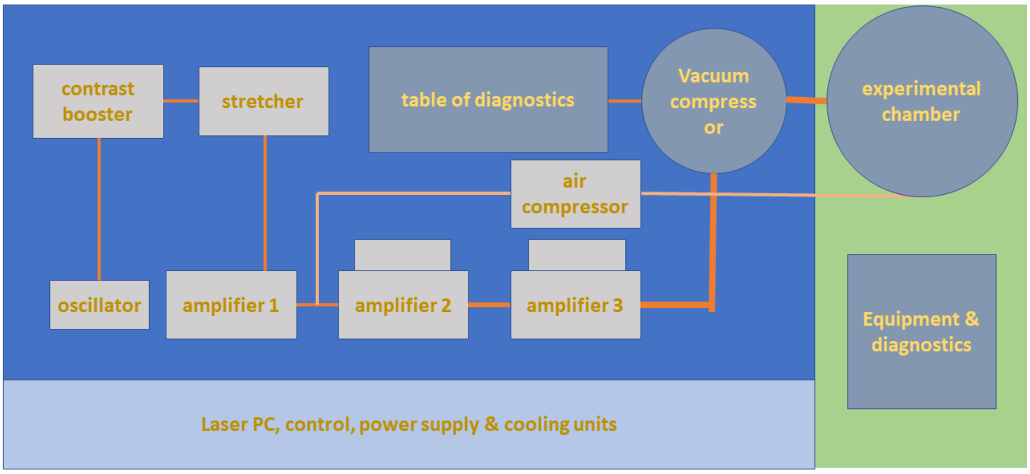

Figure 5-2: General layout of laser Zeus. The basic modules necessary to amplify the pulse up to 1.4 J energy using the CPA technique, are highlighted.

Laser Zeus, manufactured by Amplitude Technologies, is a $10\,Hz$ system that delivers pulses of up to $1{,}4\,J$ energy, $24\,fs$ pulse duration and its central wavelength is at $800\,nm$. The final, high-power laser pulse is achieved via several consecutive amplification stages. In Figure 5-2 a layout of the basic components of laser Zeus is presented.

The first module is the Ti:Sa oscillator named "Synergy Pro" (Https://Www.Spectra-Physics.Com/En/f/Synergy-Femtosecond-Oscillator). The following module is a contrast ratio booster, where the beam produced by the oscillator is amplified up to the μJ level and its contrast ratio is improved via a saturable absorber. To further amplify the laser pulse, the CPA technique is applied, as the ultra-short pulse produced by the oscillator would eventually exceed the damage threshold of the following optics. The stretcher is the module where the pulse is temporally stretched to the ps level, via a dispersive optical setup. The next module is amplifier 1, where the stretched pulse, after crossing an additional saturable absorber, enters a regenerative and a multi-pass amplifier achieving energy below $25\,mJ$. Then two additional multi-pass amplifiers (Amplifier 2 &3) follow, pumped by two Prepulse Nd:Yag laser systems. The base of the crystal installed in the Amplifier 3 module is cryogenically cooled to eliminate thermal effects that may create damage. After that, the final beam energy is typically higher than $1.2\,J$ and the beam is driven to the vacuum compressor, where its duration is reduced again back to around $25\,fs$ via a set of gratings. The beam diameter is also progressively growing, and its final diameter is $5.5\,cm$. Since the gratings are sensitive optics and the laser power is ultra-high, the compressor is operating always under vacuum conditions ($p < 10 - 5\,mbar$).

A vacuum tube of a few meters is connecting the compressor and the experimental chamber. A gate valve with a glass window is positioned in this tube to permit different pressure conditions between the two chambers (Figure 5-5). This feature provides the opportunity to open the experimental chamber and operate under atmospheric pressure with a low laser energy (up to $30\,mJ$), for preparatory measurements, such as alignment in the target area and measurements of the reflectivity of the chamber's optic elements, which are regularly conducted.

In the compressor chamber there is an option to send the laser beam either to the experimental chamber or to the table of diagnostics, via a motorized mirror. Via the diagnostics we access off-line information about the laser total energy, pointing, pulse duration, and contrast ratio. The information is used for any corrections at the laser operation and as reference values for the experiments.

In addition, exactly after amplifier 1, a secondary laser beam is generated, where a small portion of the laser beam of few mJ energy is separated. This lower energy beam is compressed at the air compressor module and arrives at the experimental chamber from a different optical path (via an extra delay line the synchronization of the two beams is achieved), and a pulse duration $\sim 25\,fs$. This beam is also used in our experiments to probe the laser-plasma interaction (probe beam).

5.2 MEASUREMENTS OF LASER CHARACTERISTICS

To operate the laser for LWFA experiments, measurements of the pulse characteristics take place. The mean energy exactly before the vacuum compressor is measured via a high accuracy laser energy meter, while a representative value is $800 - 1000\,mJ$ with $< 1\%$ peak to peak stability. The energy is multiplied by a factor of $\sim 0.6 - 0.8$, to estimate its value on target. This factor results from the reflectivity measurements of the following optics, conducted at the preparatory experimental phase. The pointing of the laser beam is recorded at a web camera to remain aligned with respect to the interaction area. The beam pointing stability is high and small corrections may be needed. Then, the pulse duration is measured in a daily basis using the FASTLITE Wizzler device (https://fastlite.com/produits/wizzler-ultrafast-pulse-measurement/). The technique used is Self-Referenced Spectral Interferometry (SRSI) (Moulet et al., 2010). In this technique, a part of the laser pulse is used to generate two similar, but different to the initial and each other pulses. After applying a Fourier-Transform Spectral Interferometry (Shen et al., 2017) treatment to the interference pattern of these pulse, the temporal shape of the pulse is calculated (figure 5.3b).

The Contrast Ratio of the pulse is also periodically measured. Although the peak of the laser pulse has a $\sim 25\,fs$ pulse duration, practically significant amount of Amplified Spontaneous Emission (ASE), ghost pulses and pulse pedestal are always present. Thus, the temporal pulse quality must be controlled as it plays an important role on experimental results (Mangles et al., 2006). Using Sequoia from Amplitude technologies (https://amplitude-laser.com/add_ons/metrology/sequoia/), a high dynamic range ($> 500\,ps$) 3d-order cross-correlation, we often measure the pulse contrast ratio. The laser pulse is splitted, and one of the parts is frequency doubled and delayed with respect to the other. Then, these two beams are driven through a third harmonic generator crystal. The wavelength of the cross-correlation signal of the two beams, and its evolution in time provides the pulse temporal profile. A typical set of measurements can be seen in Figure 5-3 c. The measured pulse contrast (black line) is improved using an extra optic, a saturable absorber, as referred before (red line). In

IPPL we have studied the effect of this improvement to the electron beam signal (Grigoriadis et al., 2022). According to our findings the absorber filters wavelengths of photons generated in the amplification cavity asymmetrically, resulting in a significant reduction of the ASE, improved the stability of the electron source and reduced the electron beam charge.

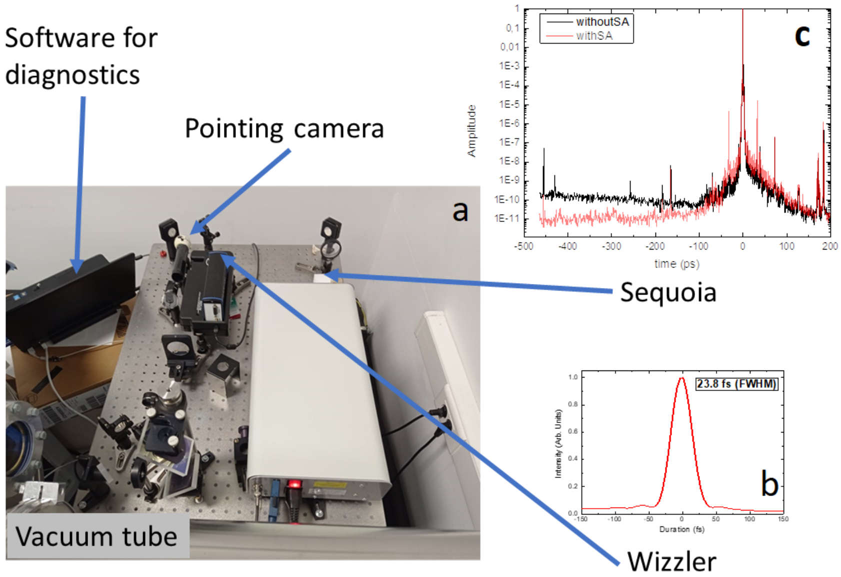
Software for diagnostics
Pointing camera
a
Vacuum tube
Sequoia
Wizzler
c
withoutSA
withSA
Amplitude
1
0,1
0,01
1E-3
1E-4
1E-5
1E-6
1E-7
1E-8
1E-9
1E-10
1E-11
-500
-400
-300
-200
-100
0
100
200
time (ps)
b
23.8 fs (FWHM)
Intensity (Arb. Units)
1.0
0.8
0.6
0.4
0.2
0.0
-150
-100
-50
0
50
100
150
Duration (fs)

Figure 5-3: a) Table of laser diagnostics. Off-line measurements highlight the laser condition, resulting in potential corrections which also are used as reference for the following experiments. b) Pulse duration measured by the Wizzler. c) Contrast ratio measurement with and without the additional saturable absorber, placed before the first amplifier.

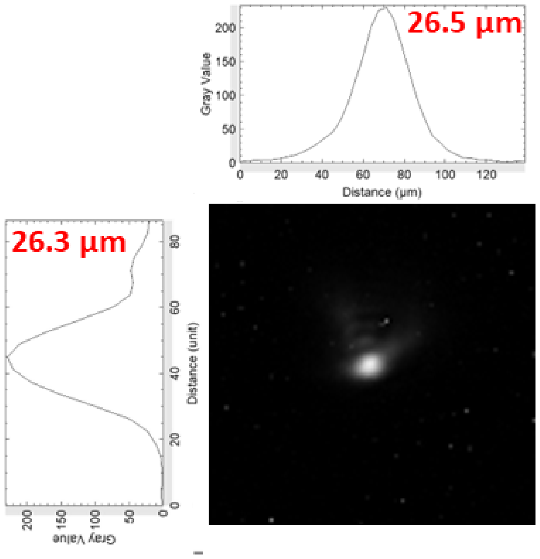

Figure 5-4: The spatial density profile of the focal spot at beam waist position. Its lineouts measured by the two perpendicular profiles at FWHM is 26.4 μm.

At the interaction area the beam is focused by an off-axis parabolic mirror. The measurement of the size of the laser beam at focus is also necessary for the laser intensity calculation. The beam waist was imaged by placing a highly filtered CCD camera at the interaction area. By moving the off axis parabolic mirror, we aim at the minimum beam waist and the optimum, almost circular shape, as a perfect circular shape is not easily achieved, due to wavefront aberrations caused by the optics.

5.3 LWFA EXPERIMENTAL SETUP

The basic setup for the LWFA experiments is hosted in the experimental chamber of IPPL, placed at the west laboratory. The west laboratory is adjacent to the laser Zeus room and the laser is coming to the chamber via a vacuum tube, as already explained. In Figure 5-5 a photo of the chamber of $1.5\ m$ diameter and $0.7\ m$ height is displayed. The experimental equipment necessary to perform the experiment is presented here. Two $4''$ diameter dielectric mirrors guide the laser beam to an $8°$ off-axis parabolic mirror, with a $1\ m$ focal length. The gas jet assembly is placed at the focus position. The off-axis parabolic mirror and the gas jet assembly were both positioned relative to the center of an ISO 200 port of the chamber, on motorized stages, permitting control of their position with accuracy $\sim 1\ \mu m$. The interaction of the high intensity laser beam creates a plasma column, and electrons are then accelerated towards the port. To capture the interaction, a shadowgraphy setup is installed in the chamber. Also, to measure the spectrum of the accelerated electrons, a Magnetic Spectrometer (MS) is installed. A pulse generator is used to synchronize the performance of the laser, the gas valve and the CCD cameras opening.

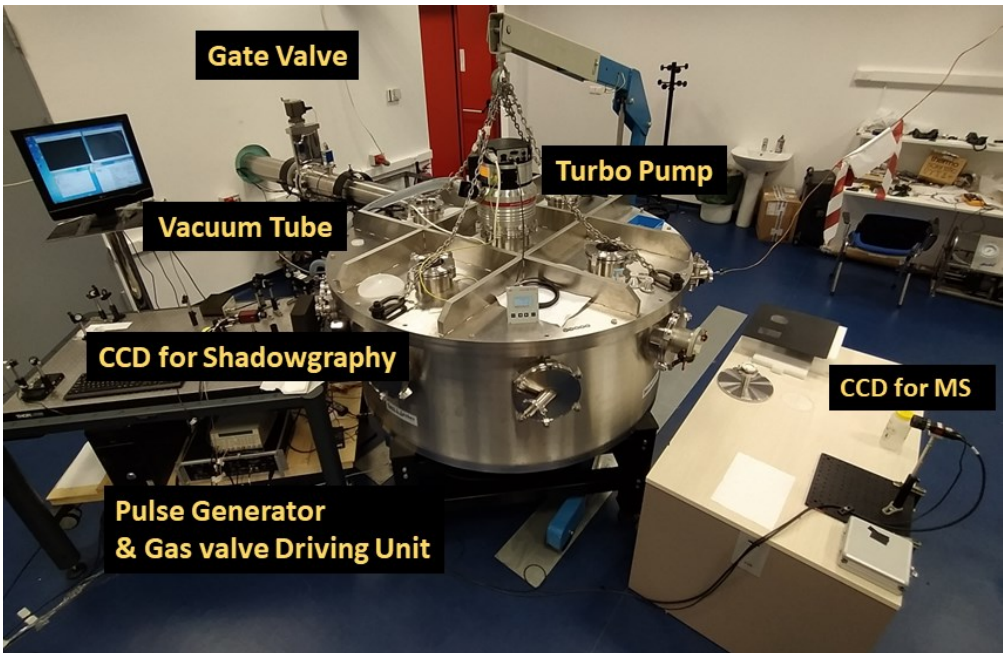

Figure 5-5: The laser is entering the experimental chamber via a vacuum tube. A gate valve placed at the tube provides the opportunity to keep the compressor chamber under vacuum conditions, while exposing the experimental chamber to atmospheric pressure. A turbo pump (accompanied by a mechanical pump) on top of the chamber's topping provides high vacuum conditions during the experiments. Two CCD cameras are highlighted: CCD camera for MS is dedicated to the detection of the trace of the electrons, after their path in the Magnetic Spectrometer (MS), and one for the shadowgraphy setup, placed on the optical diagnostic table. On the optical beam table, all the optics necessary to drive the probe beam are set. Finally, the pulse generator that controls the delays among the laser pulse, the gas valve opening, and the CCD cameras' opening time, is highlighted.

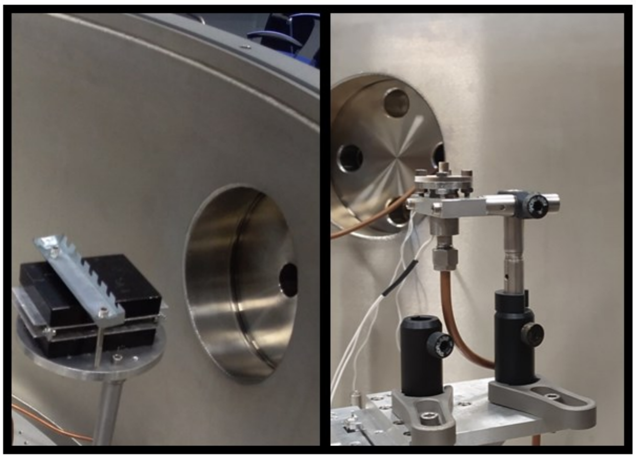

Figure 5-6: left) The pair of magnets of the MS. Right) The EM gas valve with a plastic, 3D printed nozzle attached.

5.3.1 Operation of the EM valve and synchronization

The Ultra-low leak Extreme performance Valve with exit cone (Parker) is shown in Figure 5-6. The designed nozzles are screwed on its top surface. The valve was controlled via the IOTA ONE 060-0001-900 Microfluid valve driver, shown in Figure 5-5. The valve's opening provided an adequatelly constant gas flow for a time span of $300\ \mu s$, according to our experimental measurements.

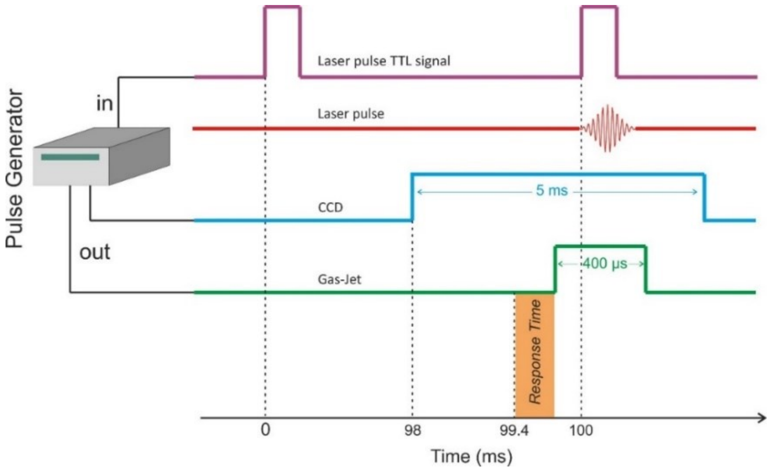

Figure 5-7: Synchronization diagram of the temporal delays of the gas jet assembly and the CCD cameras. A pulse generator triggered by the laser is used to adjust the time delays.

In Figure 5-7 the temporal syncronization of the LWFA setup is illustrated. When Laser Zeus operates in single-shot mode, two conseqjutive TTL pulses are generated with 100 ms delay. The firt one is used as a trigger signal for the pulse generator and the second one is simultaneous to the laser pulse. The pulse generator is then triggering through separate chanels to adjust the following delays:

i) the gas valve opening, so as to ensure steady flow condition at the gas jet assembly during the main laser pulse arrival,

ii) the CCD cameras, to ensure signal acquisation.

5.3.2 Shadowgraphy technique

Shadowgraphy, also known as strioscopy, is a widely used visualization technique to study the behavior of plasmas. The operating principle is simple, as by illuminating the plasma with a bright light source one observes the shadow cast by the plasma density gradients onto a detector (Tatarakis et al., 1998). In our case, the lower-energy laser beam of Zeus is used, called the probe beam, and the detector is a CCD camera (Allied Vision Pike).

Practically, the laser crosses perpendicularly the area containing the plasma created by the interaction of the main beam with the gas, thus it experiences different refractive indices due to density gradients, as observed in Figure 5-8. As a result, the laser light refracts, resulting in a shadow with different intensity regions. The relation that connects the incoming light intensity I_0 to the disturbed intensity I_d after crossing a plasma area along z axis with length L is given by the relation:

$$\frac{\Delta I_d}{I_0} = L\int_0^L \left(\frac{\partial^2}{\partial x^2} + \frac{\partial^2}{\partial y^2}\right)\eta(x,y,z)dz. \tag{5.1}$$

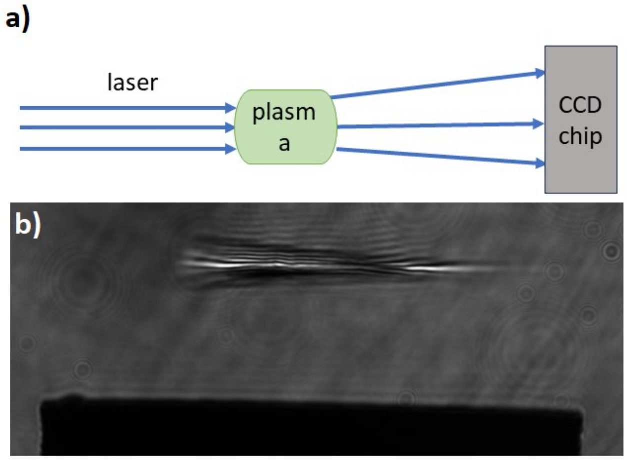

Figure 5-8: a) Operating principle of shadowgraphy technique. Probe beam of laser Zeus with an incoming intensity I_0 crosses the interaction area perpendicularly and the disturbed beam I_d is captured by a CCD camera. The density gradient resulting in different refractive indexes $\eta(x,y,z)$ causes the light to refract, revealing density structures formed by the interaction. b) A typical shadowgram captured in a LWFA experiment.

5.3.3 Magnetic spectrometer (MS)

A MS is a diagnostic that deflects electrons according to their velocity. The home-made MS consists of a pair of permanent Neodymium magnets of $11\ cm$ length, $9\ cm$ width and $20\ cm$ height, shown in Figure 5-6 left, fixed together at $1\ cm$ distance via a specially designed case (not shown here), a scintillating screen placed after the magnets, and a CCD camera. Due to lack of space, it is placed as close as possible after the interaction area, however, special care is taken, so as its magnetic field does not affect the gas valve operation.

The relativistic electrons cross the almost uniform magnetic field ($\sim 0.4\ T$) and due to the Lorentz force for $\boldsymbol{E} = 0$:

$$\gamma_e m_e \frac{d\boldsymbol{v}_e}{dt} = -e\boldsymbol{v}_e \times \boldsymbol{B} \qquad 5.2$$

are dispersed perpendicular to the magnetic field $\boldsymbol{B}$ and their velocity $\boldsymbol{v}_e$. Electrons with the highest velocity disperse less. The electrons then cross the scintillator (Lanex Regular screen) located at the port of the chamber. Its active layer consists of the powdered phosphor Gd_2O_2S:Tb and is $10 - 100\ \mu m$ thick. The electrons interact with the phosphor, with a known conversion efficiency (Kurz et al., 2018), producing photons with energy $545\ nm$. The photons are then collected on the CCD camera and the gray value, corresponds to the electron charge. The imaging system response was calibrated using a known source emitting at the same wavelength. The camera used was a Guppy PRO by Allied Vision, with a resolution of 1292×964 and pixel size of $3.75\ \mu m \times 3.75\ \mu m$, operating in $8\ bit$ grayscale.

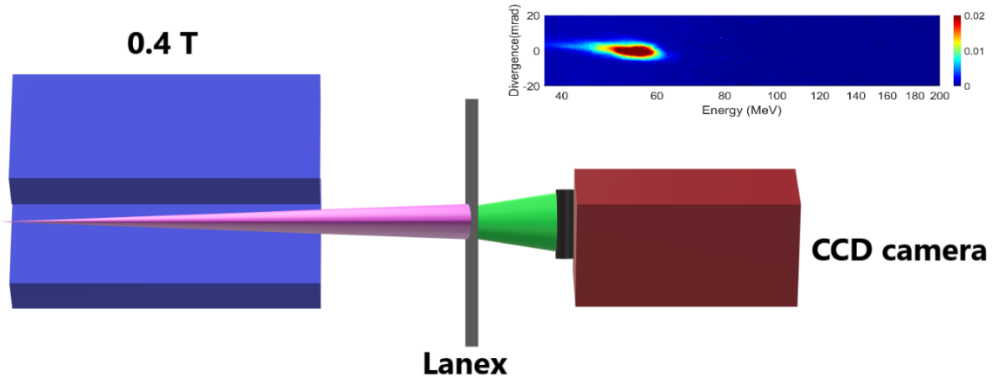

Figure 5-9: Operating principle of MS. Relativistic electrons cross a magnetic field of 0.4 T and are dispersed with respect to their velocity perpendicular to their initial direction. Their interaction with a scintillating screen produces photons of 545 nm wavelength, which are recorded to a CCD camera. The analysis of the recorded signal via a spectrum analysis code produces electron energy spectrum.

Then, the code SEAL, a spectrum analysis code, is used to calculate the relativistic electron trajectories, according to the magnetic field created by the pair of magnets and converts recorded electron beam traces to energy spectrum. The optical system calibration and the code SEAL are part of the work conducted for the PhD thesis of (Grigoriadis, 2023).

Finally, by the un-affected dimension of the electron beam, its angular divergence can be estimated, as can be seen in Figure 5-9.

5.4 INTERFEROMETRY TECHNIQUE

Interferometry is a measurement technique that takes advantage of the interference of two waves, to extract information related to the properties of the waves or to the objects they interact with. The basic principle of interferometry involves the interaction of at least two waves for producing an interference pattern. In LWFA experiments interferometry measurements are often used to measure the gas or plasma density profile.

In IPPL, the gas density was measured using a Nomarski-type interferometer. The main advantages of a Nomarski-type interferometer rely on the fact that there is no need for a reference branch, as will be explained. Hence, the space and optics needed are the least possible, the optical path is always equal, and there is high spatial and temporal coherence.

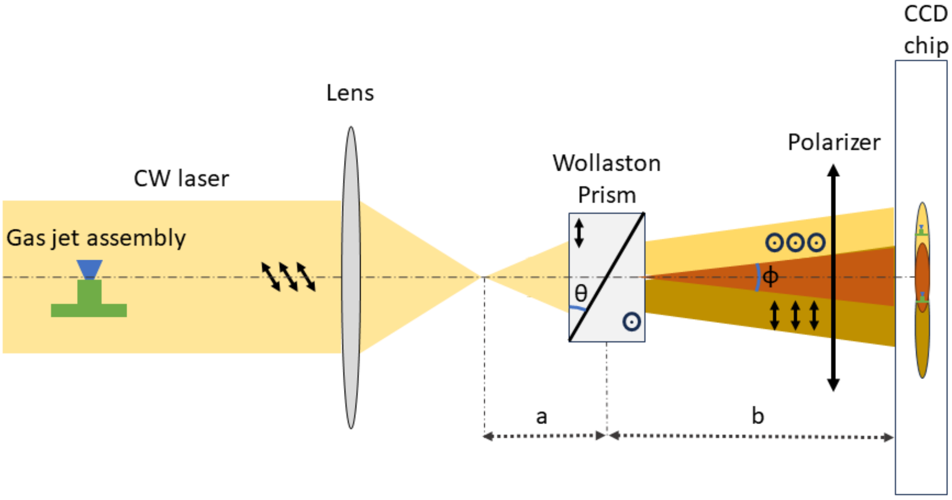

Figure 5-10: Operating principle of Nomarski interferometry set-up: The beam of a CW laser is driven over the 3D-printed nozzle, where the gas exhausts. Then, the beam crosses a Wolaston prism, where two spatially separated perpendicularly polarized beams are formed, which then cross a polarizer. The interference signal of the two beams is recorded onto a CCD camera.

The interferometry setup was developed at IPPL's experimental chamber. The beam of a linearly polarized CW He-Ne laser of $\lambda = 648\,nm$ wavelength was employed. The beam was expanded to over $1\,cm$ in diameter and directed towards the expansion region of the gas. The beam section passing through the disturbance was phase-shifted, due to the change in the refractive index. Then, the beam was focused and directed through a Wollaston-type birefringent prism. At this point, two spatially separated perpendicularly polarized beams were formed, namely the ordinary and extraordinary waves. After that, the beams were separated by a small angle φ:

$$\varphi = 2\theta(\eta_e - \eta_o) \qquad 5.3$$

where θ is the characteristic Wollaston angle and η_e and η_o are the refractive indexes of the extraordinary and the ordinary way respectively. To create an interference pattern, these two beams crossed a polarizer set at $45°$ angle. Finally, on the CCD camera chip two images are projected, partially overlapping. In the overlapping area the interference pattern is contained. The sketch of the Nomarski setup is illustrated in Figure 5-10. The separation distance d, among the fringes is controlled by prism location:

$$d = \frac{\lambda b}{\theta a}. \qquad 5.4$$

The Nomarski operation principle and a comparison among several interferometric setups for gas measurements is found in (Liu et al., 2021). The CCD exposure time was set to $4\ \mu m$. The phase shift recorded contains information related to the gas density.

5.4.1 Phase shift

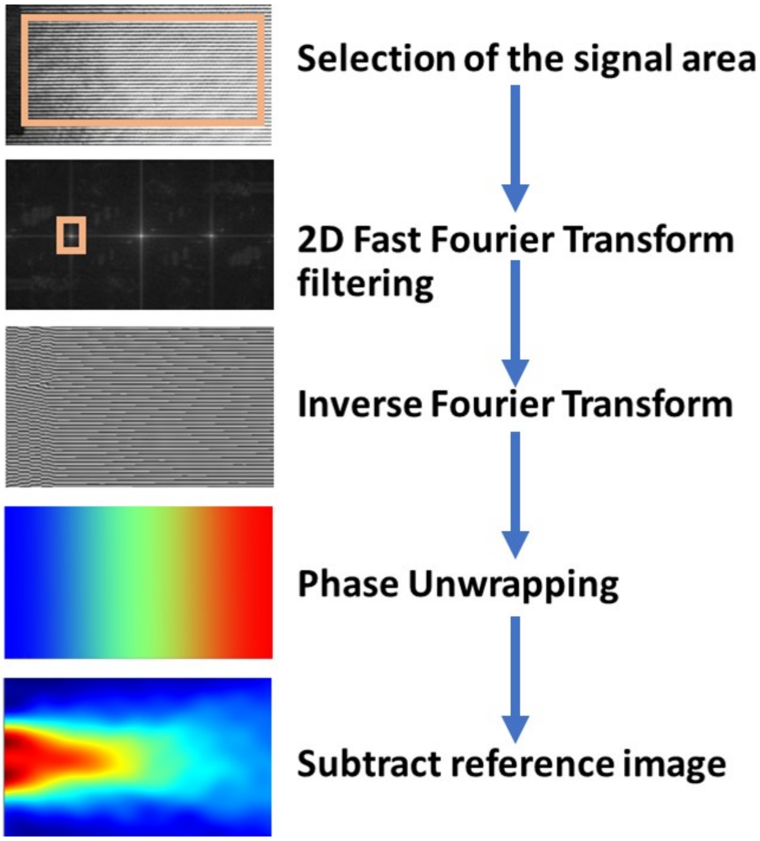
Selection of the signal area
2D Fast Fourier Transform filtering
Inverse Fourier Transform
Phase Unwrapping
Subtract reference image

Figure 5-11: Steps for obtaining a phase shift map. For the reported steps IDEA software was used (Hipp et al., 2004).

To acquire 2D phase shift maps from the interferograms, the IDEA software was utilized (Hipp et al., 2004). From the image obtained, initially the part where the overlapping area containing the distortion was cropped. To this part of the image, the 2D Fast Fourier Transform (2D FFT) algorithm was applied, and the frequencies, containing the gas density information, were selected. By exclusively considering these frequencies, an inverse 2D FFT was applied, generating a synthetic interferogram. Then, the Step Function phase unwrapping algorithm was utilized, to derive the 2D map representing the phase shift. The same procedure was repeated for another, undisturbed interferogram (without gas flow in the valve). Finally, the two images were subtracted, resulting to the phase shift, as illustrated in Figure 5-11.

5.4.2 Axisymmetric nozzles: Abel Inversion

The 2D phase shift obtained before, $f(y)$, has integral phase shift information, namely a projection on the y plane of the phase shift acquired along an optical path on x, in a specific height z, according to Figure 5-12.

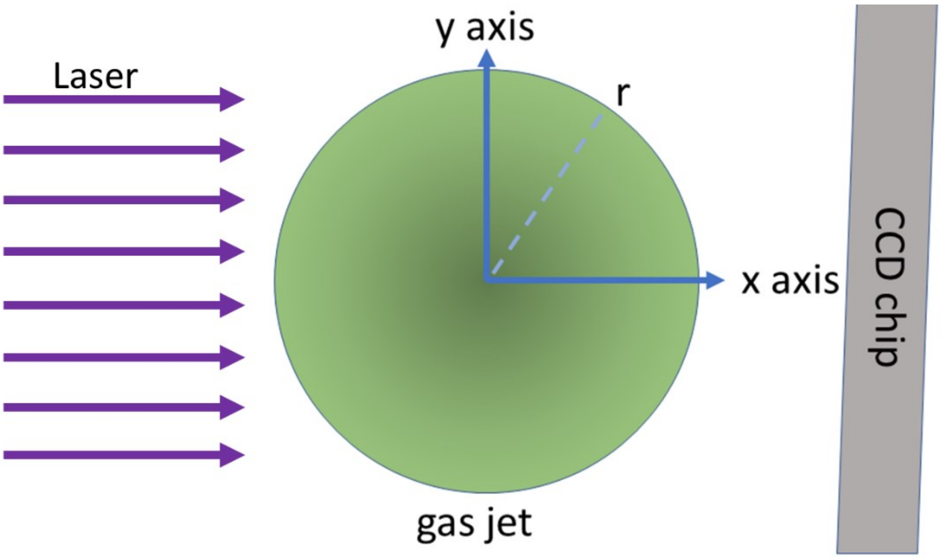

Figure 5-12: Abel Inversion reference geometry. The laser propagates parallel to the x-axis and passes through an area containing the axial symmetric gas jet. The projection of the phase shift F(y) is recorded on the CCD camera chip.

To obtain phase shift $g(r)$ at a position with radius r, in a specific height z, Abel Inversion is applied to the data, which is given by the relation:

$$g(r) = -\frac{1}{\pi}\int_{y}^{R}\frac{df(y)}{dy}\frac{dy}{\sqrt{r^2 - y^2}}dr. \qquad 5.5$$

The function $g(r)$ is related to the refractive index of a gas η:

$$g(r) = \frac{2\pi}{\lambda}(\eta(\mathrm{r}) - 1). \qquad 5.6$$

The index of refraction is connected to the gas atomic density n, and laser wavelength λ, via the Lorentz-Lorenz equation (Couperus et al., 2016):

$$\frac{\eta(\lambda)^2 - 1}{\eta(\lambda)^2 + 2} = \frac{n\alpha}{3\varepsilon_0} \qquad 5.7$$

where α is the mean polarizability of the gas and ε_0 is the vacuum permittivity. For low refractive index gases ($\eta \approx 1$ for all gasses used in this study, as illustrated in Table 3), and for a given λ, the relation is simplified as:

$$\eta - 1 = \frac{na}{2\varepsilon_0} \qquad 5.8$$

Dividing relation 5.8 with its version for Standard Temperature and Pressure (STP) conditions, becomes:

$$\frac{\eta - 1}{\eta_{\mathrm{STP}} - 1} = \frac{n}{n_{STP}} \qquad 5.9$$

where $n_{STP} = 2.68 \times 10^{19}\ cm^{-3}$, namely the gas density at STP, and finally, by replacing with relation 5.6 we obtain:

$$n(r) = \frac{\lambda\, n_0\, g(r)}{2\pi(\eta - 1)}. \tag{5.10}$$

Gas	η
He	1.000035
Ne	1.000067
Ar	1.000281
N₂	1.000298

Table 3: Refractive indexes of the gasses at STP (Https://Www.Engineeringtoolbox.Com/Refractive-Index-D_1264.Html).

A code developed by the colleague Alekos Skoulakis was used to calculate the Abel inversion numerical solution, using Gegenbauer polynomials ($a = 2$). This code considers asymmetries of the measured phase shift (Mosburg & Lojko, 1968) following the Freeman and Katz approach (Freeman & Katz, 1963). In this case, the symmetric part of the measured values is contained in the even function $f_g\ (y)$:

$$f_g(y) = \frac{f(y) + f(-y)}{2}, \tag{5.11}$$

while the asymmetric part is $f_u(y)$:

$$f_u(y) = \frac{f(y) - f(-y)}{2y}. \tag{5.12}$$

Then, after the Able Inversion, the radial distribution is expressed by:

$$g(\mathrm{r}) = \mathrm{g_g}(r) + r g_u(r), \tag{5.13}$$

$$g(-\mathrm{r}) = \mathrm{g_g}(r) - r g_u(r). \tag{5.14}$$

5.4.3 Non axisymmetric nozzles: Tomographic reconstruction

To obtain non-axisymmetric density profiles, a tomographic reconstruction algorithm, suitable for reconstruction of non-homogenous distributions, is necessary (Herman, 1980). In this case, multiple interferograms, obtained from different angles, are used.

According to the geometry displayed in Figure 5-13, given the integral data distributions $h(p,\theta)$, referred as projections, their relationship with the local distribution $f(r,\varphi)$, known as Radon Transform, is given by the relation (Radon, 1986)

$$h(p,\theta) = \int_{-\infty}^{+\infty} ds\, f\left(\sqrt{p^2 + s^2}, arctan\left(\frac{s}{p}\right) + \theta\right). \tag{5.15}$$

The inversion of this relation, implemented by Johann Radon, is known as the Radon Inversion, given by

$$f(r,\varphi) = \frac{1}{2\pi^2}\int_0^{\pi} d\theta \int_{-\infty}^{+\infty} \mathrm{dp} \frac{1}{r\cos(\theta - \varphi) - p}\frac{\partial h(p,\theta)}{\partial p}. \tag{5.16}$$

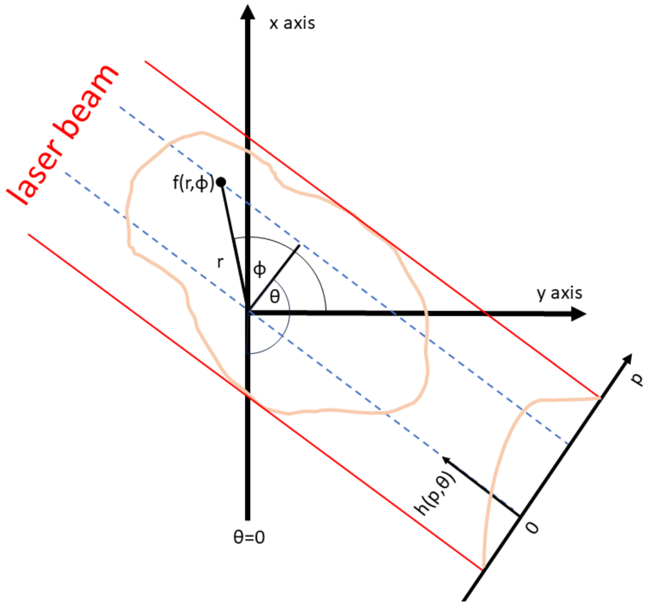

Figure 5-13: Reference geometry for tomography. Laser beam crosses the gas jet by various angles, creating the projections $h(p,\theta)$, which are used to calculate local phase shift distribution via the relation 5.16.

To solve equation 5.16, an infinite number of projections is required. Thus, numerical methods have been developed, instead. One of these methods, known for its applications in x-ray imaging, is called the filtered back-projection, based on mathematical convolution (Herman, 1980), and is available in IDEA software (Hipp et al., 2004).

To apply this method at least 3 phase shifts, resulting from three equidistant angle interferograms, with angles between 0 and 180 degrees are necessary. However, since an experimental setup is unsuitable for that, the software allows for interpolation of the results of non-equidistant angles.

The phase shifts are carefully cropped with reference to the image geometrical centre, and after the application of the algorithm, multiple slices of phase shift values $g(r)$, vertical to the initial interferograms, are obtained. Finally, by using relation 5.10, the density is calculated.

5.5 X-RAY DETECTION

Two x-ray photodiodes (Morros Compton CA) were used to detect x-ray photons. Their active area is circular, with a diameter of $1.2\ cm$. The photodiodes were reverse biased at $300\ V$ and connected to the oscilloscope, as can be seen in Figure 5-14. To ensure x-ray detection without any other signal or background (e.g., main laser photons), they were enclosed in special 3D-printed cases for shielding, while their free surface was covered by a $4.5\ \mu m$ thick Al foil, to block the IR laser photons. The transmission of this filter for a wide photon energy range is plotted in figure 5.14 c) (blue curve).

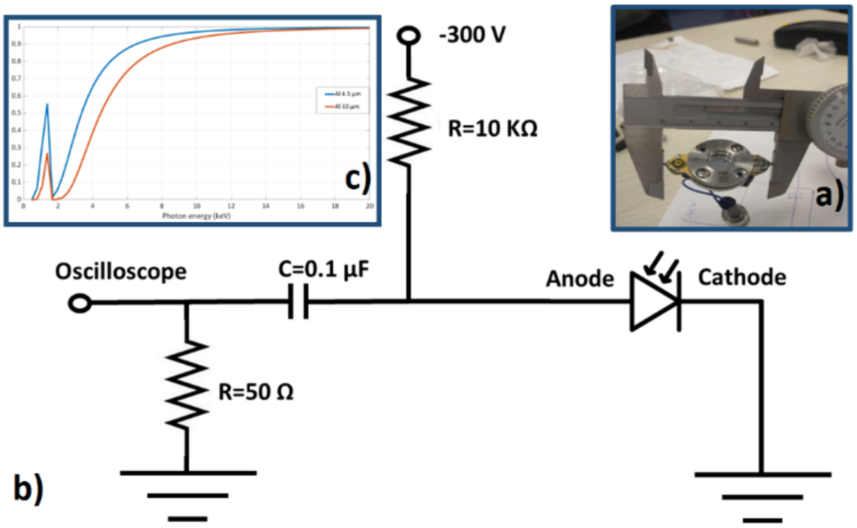
1
0.9
0.8
0.7
0.6
0.5
0.4
0.3
0.2
0.1
0
0
2
4
6
8
10
12
14
16
18
20
Photon energy (keV)
Al 4.5 μm
Al 10 μm
c)
-300 V
R=10 KΩ
a)
Oscilloscope
C=0.1 μF
Anode
Cathode
R=50 Ω
b)

Figure 5-14: a) The photodiode Morros Compton CA with active area 1.2 cm. b) The x-ray photodiode was reverse biased (-300 V) and connected to the oscilloscope. c) Al foil x-ray transmission curves (Https://Henke.Lbl.Gov/Optical_constants).

Chapter 6: Nozzle manufacturing and density measurements

The design and CFD study of several nozzles have been presented. The CAD files of the models were subsequently used for 3D-printing. In this chapter, we will describe the technologies implemented in 3D-printing of the nozzles and their performance. Part of this study was presented in the EEITE conference (Andrianaki et al., 2022a).

The gas density characterization was conducted via interferometry. To obtain particle density, two different techniques were applied, Abel inversion for axisymmetric nozzles and tomographic reconstruction for non-axisymmetric nozzles, as described in Chapter 5. The main results of the study for the design, based on CFD simulations and experimental evaluation of the axisymmetric, printed nozzles were published in (Andrianaki et al., 2023).

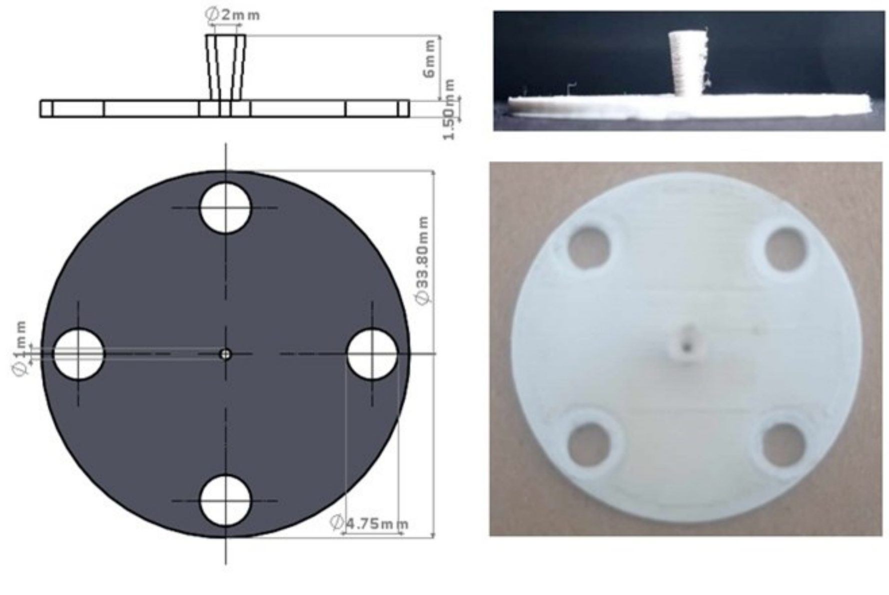

Figure 6-1: CAD drawing and prototype of Nozzle 1, printed via FDM technique.

6.1 NOZZLE MANUFACTURING WITH 3D PRINTING

LWFA experiments take place under a high vacuum ($\sim 10^{-6}\ mbar$), thus a nozzle must be vacuum compatible. Also, its smoothness should be very high, as any small unwanted remnant in the inner nozzle area can affect the gas flow; the flatness of the bottom base is necessary for the accurate fitting to the valve. Up to now mainly milling technology has been used to produce such nozzles. Metallic nozzles are known to be trusted for high-vacuum conditions, while small or moderate intensity laser pulses do not destroy the targets. The nozzles are typically purchased from specialized laboratories or companies, thus their cost and delivery time are high (Prencipe et al., 2017).

In our case, laser focal spot diameter is around $30\ \mu m$, and is usually focused on a distance greater than $200\ \mu m$ over the nozzle exit, while the focal area is extended for several Raileigh lengths, thus the nozzle is not interacting or affected by the laser. Given the fact that similar efforts have already been reported as successful (Döpp et al., 2016; Vargas et al., 2014), the nozzle geometries were 3D-printed. 3D-printing technology is ideal for prototyping, and was proved to be a low-cost, fast, and efficient (Conner et al., 2014; Wong & Hernandez, 2012). In this context, quality tests have been performed, using different printing technologies and printing settings.

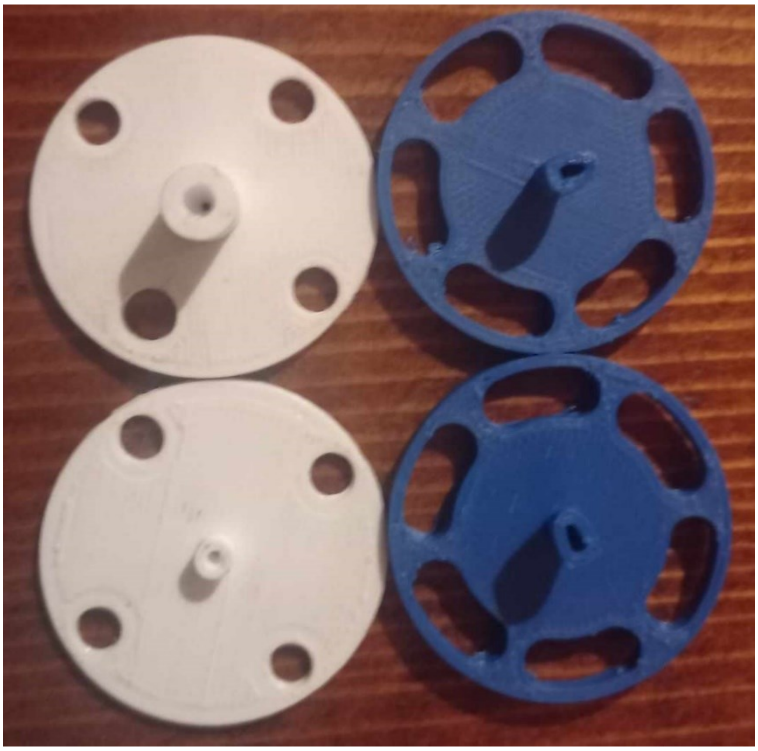

Figure 6-2: Nozzles produced via FDM 3D-printing.

Initially, the Fused Deposition Modelling (FDM) process was tested. In FDM a thermoplastic filament of diameter $> 1\ mm$ passes through an extruder and is heated and melted. Then the paste formed is ejected via a nozzle attached to the extruder and is placed on a surface, known as the printer's bed, that is also heated. The extruder and the bed are both moving, and the resulting part quality depends on the printer's characteristics, such as the printer's nozzle diameter, extruder and bed temperature, and layers' height. In our case, Prusa MK3 (Prusa Research, https://www.prusa3d.com) was available, with an $0.4\ mm$ nozzle, a printing layer height of $0.1\ mm$, while the printing filament was PETG. Some tests were conducted by varying printing settings to conclude that we produced the necessary details. In Figure 6-2 Nozzles 3, 5 and NS 1, 3 are depicted.

Stereolithography (SLA) process was also tested, as is known to deliver finer details. In SLA a tank filled with liquid resin is locally illuminated with UV light, thus the resin is hardened, and forms a layer at the printer's bed. The bed is progressively moving with respect to the UV light position and the next layer is created. The Photon Mono X (Anycubic, https://www.anycubic.com) was used, with a UV LED light source ($405\ nm$), creating a layer height of $0.01 - 0.15\ mm$. In SLA process, a printed part must be post-processed after removal from the printing bed (e.g., remove support material, hardening).

For the nozzles, printing was initially failing to create the smaller diameter of the inner geometry at the base of the cone, which was expected to be $800 - 1000\ \mu m$. Subsequently, printing under an angle, using supports as is shown in Figure 6-3, was tested. Although this way the desired hole was created, by removing the supportive material the flatness of the bottom base area was destroyed. Finally, the orientation of the printing part was inversed in Z-axis and supports longer than the nozzle height were used, so as to keep the nozzle exit unaffected. Finally, the critical areas of the nozzle were reproduced, and the bottom base surface was smooth, while the top base surface, which is out of interest, was rough.

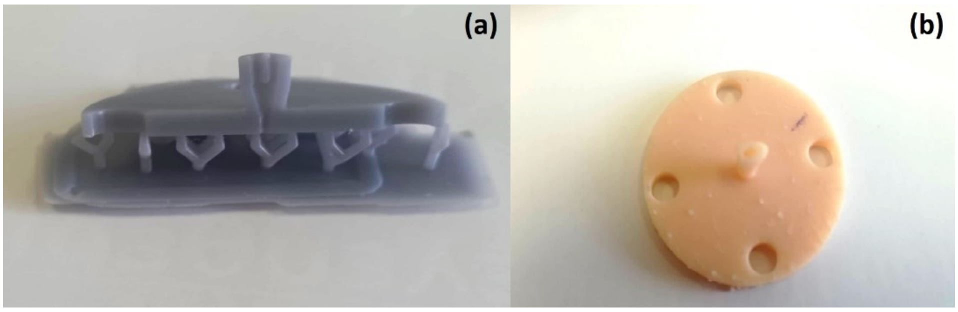

Figure 6-3: Nozzles printed via SLA process. a) Printing of half section of a nozzle to test the ability of the Anycubic SLA printer to reproduce inner nozzle details. Printing under an angle destroyed the bottom flatness. (b) Inverse-Z printing. The top area is rough after removing the supportive material.

Another test took also place using metal 3D-printing, namely the Laser Metal Deposition (LMD) process. In LMD, a powerful laser is used for melting a stainless-steel wire of $1\ mm$ thickness. The part is welded in the bed. The printing took place at the Laboratory of Computer Assisted Machining (CAM) of the School of Production Engineering and Management, Technical University of Crete (TUC), using MELTIO 450 (Meltio, https://meltio3d.com). Meltio uses 6 direct diode lasers of $976\ nm$ wavelength, which produce a total power of $1200\ W$. The process is taking place in an Ar filled environment. The printer allows for the mixing of two different materials, as two extruders are available.

The tests were unsuccessful, as the size of the extruder's nozzle was too large to print it properly. Therefore, the melted material was joined, without creating a hole at the nozzle's center. The proposed steps tested, such as reducing laser power, vary the distance of the wire and the bed, were not successful. Another proposed solution is to print the main part and afterwards to use CNC for the wholes. Although this solution would probably work, it didn't serve the main goal to simplify the nozzle construction process.

Another decisive disadvantage was the post-processing procedure required. As the part was welded in the bed it must be removed using a band saw, which was laborious and imprecise, resulting in a rough base bottom surface (Figure 6-4). The proposed solution is to add an extra layer that will be removed and polished at the post-processing procedure. Although operational, this solution adds extra complexity.

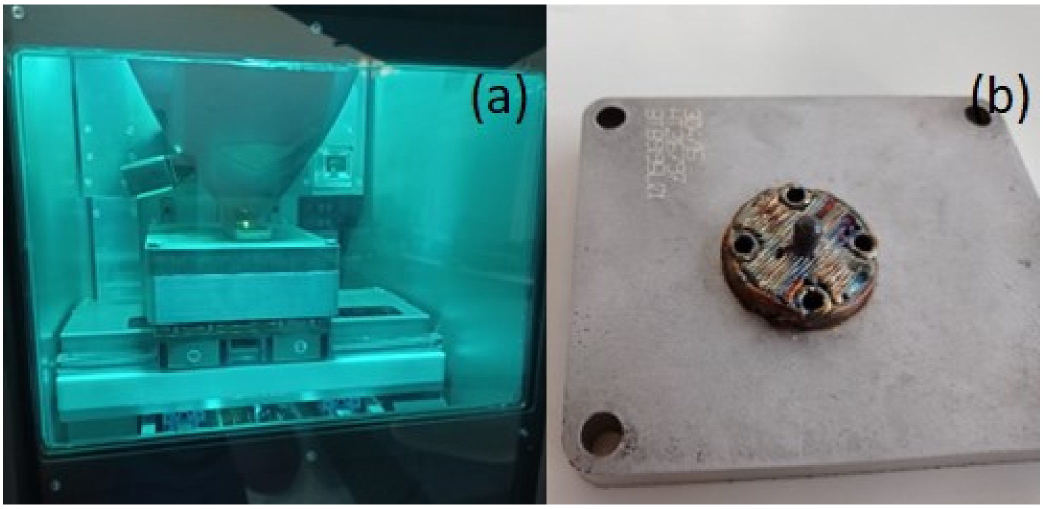

Figure 6-4: a) Printing chamber of Meltio M450 metallic 3D-printer, filled with gas Ar, through the protective window while printing. The laser is melting the 1 mm wire which is welded on the special bed. b) The welded part was unsuccessfully printed.

6.1.1 Comments on printing procedure

The printed geometries tested with the above processes are included in Appendix B. The criteria for the selection among the processes will be discussed in the following. Any university-scale laboratory with a table-top laser appropriate for LWFA experiments may have access to CAD software to create the geometrical drawing. The designs should be adapted to the printing method. To proceed further the options are owning a 3D-printer or outsourcing the designs. When outsourced, the cost for each plastic nozzle didn't exceed 4 Euros and the waiting time was at maximum few days.

FDM process is easy, even for beginners, and apart from the printer, no additional equipment is necessary, while the resulting nozzles were operational in LWFA experiments. However, when more complicated, non-axisymmetric designs were printed, the inner surfaces of the nozzles were coarser. For SLA, where supportive material was used and the hardening process (curing) is necessary, some expertise and additional equipment are required. SLA was successfully reproducing even the non-axisymmetric designs and the nozzles were operational in LWFA experiments. On the other hand, LMD needs a machine workshop to produce a nozzle. Also, the test nozzle failed to be successfully formed.

In addition, a comment on the reproducibility of printing procedure will follow. In Figure 6-5 the phase shifts, resulting from analysis of interferometric measurements for Nozzle 1 and Nozzle 2, printed with the same printer (Prusa MK3 ,FDM) and settings, are presented for Nozzle 1 (left) and 2 (right) for 40 bar (a and c) and 50 bar (b and d) backing pressures, respectively. Although both nozzles are functional in LWFA experiments, small defects in printing have arisen, resulting in a non-symmetric flow. Nozzle 1 systematically produced (for all kinds of gas tested and a range of backing pressures) more symmetrical phase shifts than Nozzle 2. Apiece 3D-printed nozzle evaluation tests should be conducted. However, it is important to report that in the literature, asymmetries for metallic nozzles produced via milling are also reported (Couperus et al., 2016; Landgraf et al., 2011).

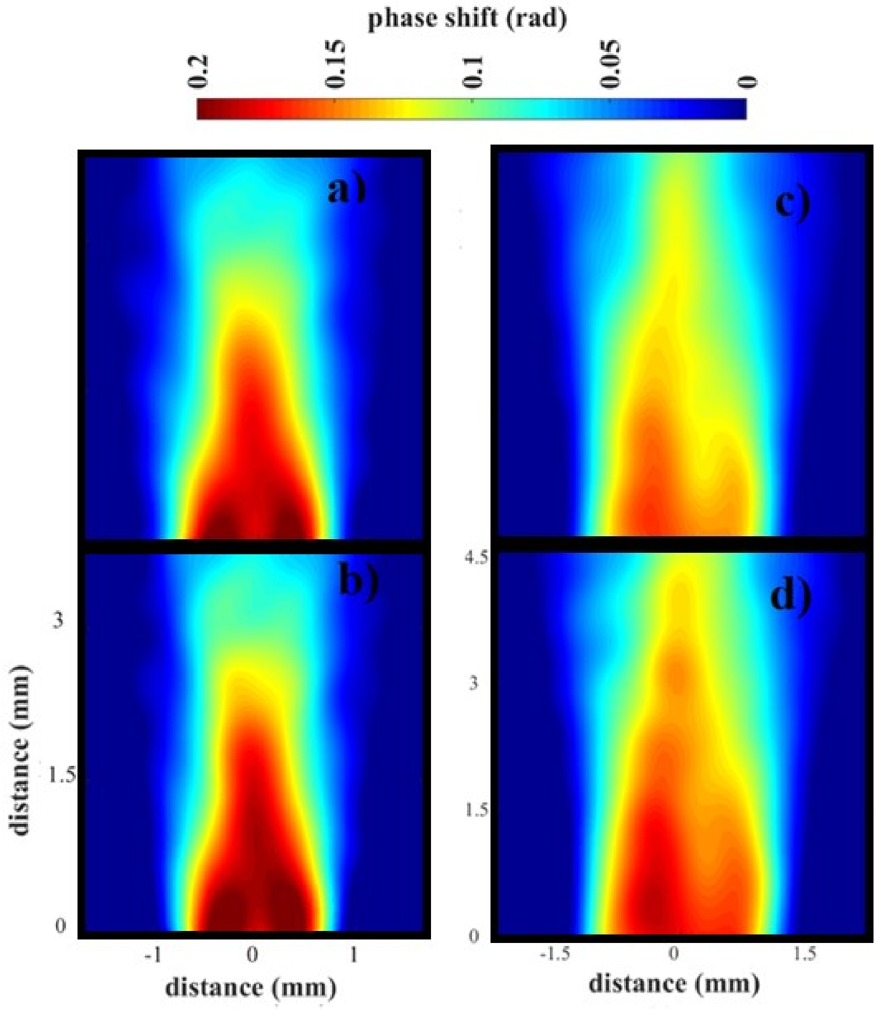

Figure 6-5: Phase shifts of Nozzle 1 ($2\ mm$ exit diameter) (a, b), and Nozzle 2 ($3\ mm$ exit diameter) (c, d), for He, at $40\ bar$ (a, c) and $50\ bar$ (b, d) backing pressure. Nozzle 2 systematically produced less symmetric phase shifts. Results obtained with IDEA software (Hipp et al., 2004).

6.2 RESULTS FOR AXISYMMETRIC NOZZLES

A parametric study was conducted for the 5 axisymmetric Nozzles. The range of backing pressure measured was from $25\ to\ 50\ bar$, which is the range that is typically examined in LWFA experiments. He, Ne, Ar and N_2 were measured via the interferometry technique, using the setup presented in section 5.4. The code discussed in paragraph 5.4.2, which highlights the measured asymmetries, was used to obtain density profiles. Some of our results, for Nozzles 1 and 2 which have already been used in LWFA experiments in IPPL, are presented.

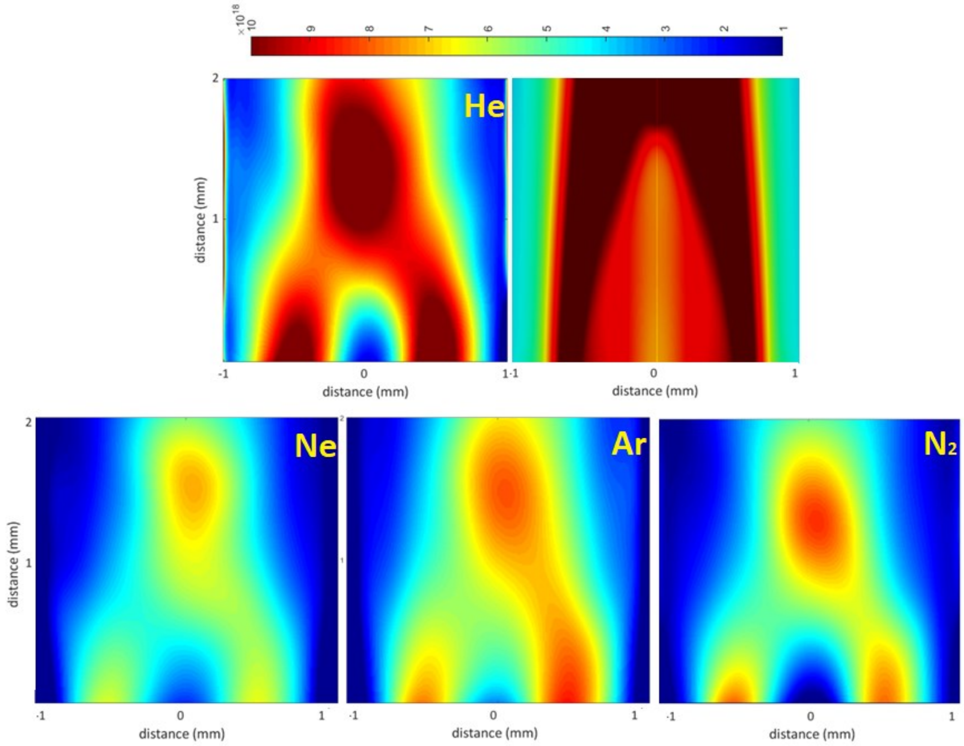

Figure 6-6: Bottom: Particle density contours in cm^{-3} for Nozzle 1 for Ne, Ar and N2 at $40\,bar$ backing pressure, measured with interferometry technique. Top: Particle density contours in cm^{-3} for Nozzle 1 for He at $40\,bar$ backing pressure, measured with interferometry technique and respective CFD simulation for He at $40\,bar$ backing pressure and 10 mbar outlet pressure.

In Figure 6-6 the measured particle density contours of He, Ne and Ar and N2 at $40\,bar$ backing pressure are presented. The simulated case is for $40\,bar$ He and $10\,mbar$ pressure at the outlet. The outlet pressure calibration study was discussed in paragraph 4.5.2. When these studies were conducted, the nozzles had not been constructed yet, and the case of $1\,mbar$ was selected as the reference one.

In Figure 6-7 the measured density profiles of He (top), Ne (middle) and Ar (bottom) at $40\,bar$ backing pressure are presented. Experimental profiles (magenta line) at 300 (left) and 500 (right) μm downstream the nozzle exit are presented, together with the profiles resulting from CFD simulations (green dashed line) at $300\,and\,500\,\mu m$, for each gas type, at $40\,bar$ backing pressure and $1\,mbar$ pressure at the outlet. This distance is selected as during the experiments we often select to fire the laser at this height over the nozzle. For all three gasses, a $2\,mm$ long density profile with a drop at the middle and peak at the edges were expected according to the CFD simulations. The experimental profiles are similar, peak values are in good agreement, however the peaks lie closer to the symmetry axis. The Ne experimental profile was unexpectedly low. A speculation is that the pressure regulator was stacked in a lower backing pressure value without being noticed.

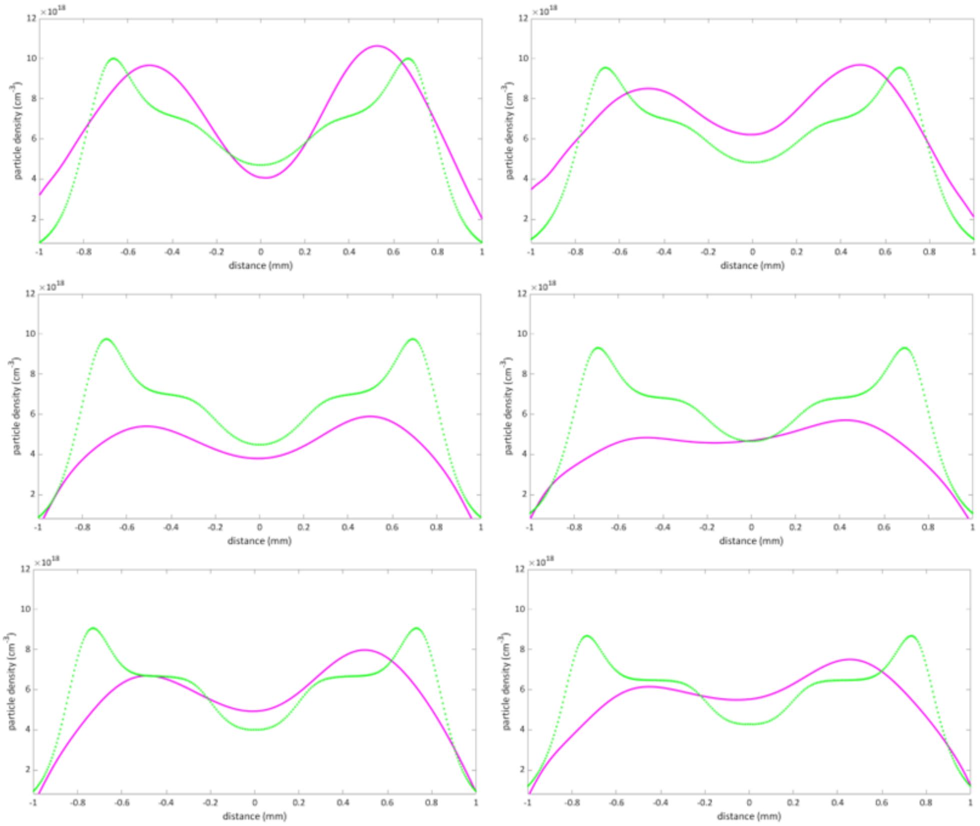

Figure 6-7: Density profiles for He (top), Ne (middle) and Ar (bottom) at $40\ bar$ backing pressure for Nozzle 1. Magenta lines are experimental results 300 (left) $500\ \mu m$ (right) downstream the nozzle's exit, and green lines are simulated values at the same distance respectively, for $40\ bar$ backing pressure and $1\ mbar$ at the outlet.

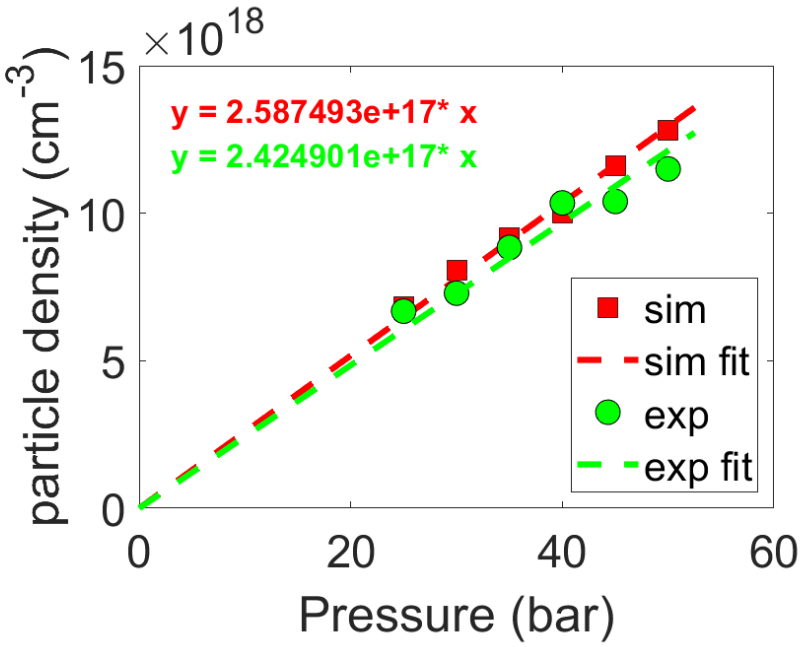

Figure 6-8: The peak density value variation of gas He with respect to the backing pressure applied at the valve for Nozzle 1, $300\ \mu m$ downstream the nozzle exit. Green spots and respective fitting curve is for the experimental results and red spots and respective fitting curve is for the CFD simulations.

In Figure 6-8 the peak density of gas He with respect to the backing pressure applied at the valve, for a $25\ to\ 50\ bar$ pressure range is plotted for values obtained $300\ \mu m$ downstream the nozzle exit. Peak particle density of the experimental data (green) and simulation results (red) are plotted and fitted with a linear fit. The expected linear increase of density with backing pressure is verified. The experimental results are more dispersed than the simulated ones. With a pressure increase, the distance between the simulation results and the experimental data increases.

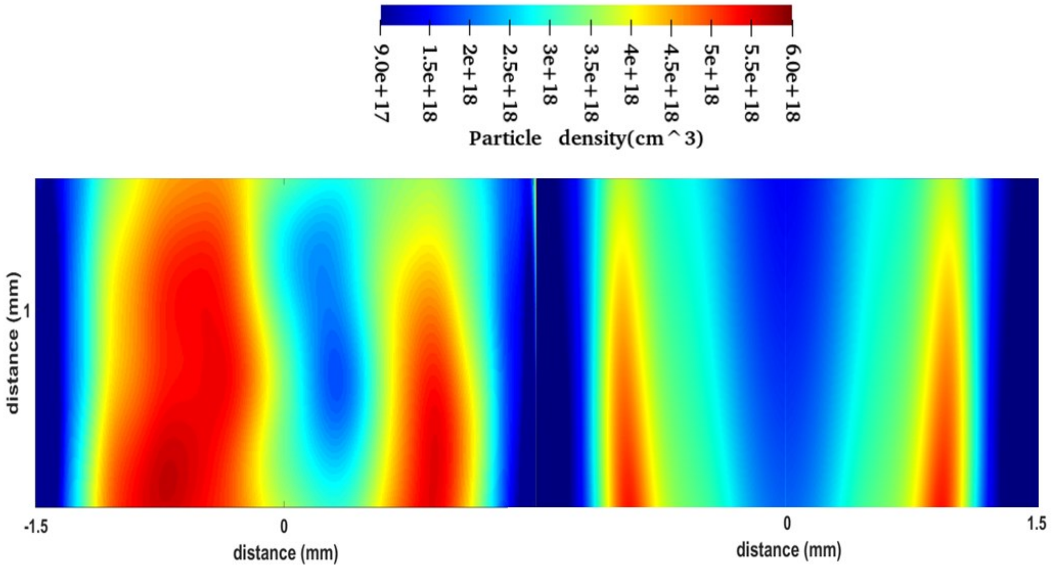

Figure 6-9: Experimental (left) and simulated (right) particle density contours for Nozzle 2, for He at $40\ bar$ backing pressure (1 mbar for the pressure outlet).

Nozzle 2 is the most used nozzle in IPPL LWFA experiments. The experimental density characterization via interferometry was conducted after its extensive use in various experiments. Non-visible defects caused either by its long-term operation, or the initial printing, caused the resulting highly non-axisymmetric phase shifts presented in Figure 6-5. Its 2D particle density contour map is displayed in Figure 6-9 (left), together with the simulated gas density for He, at $40\ bar$ backing pressure (right) (1 mbar for the pressure outlet). The results are adequately similar for the right side of the contour map, while the left one is not well reproduced.

In general, for nozzles 1, 2 and 4 the 2D particle density maps are similar to the simulations for the area close to the nozzle exit, which is typically used in the experiments. However, as explained in paragraph 4.5.2, the outlet pressure was defined by a calibration process and based on bibliography standard values, therefore the model is not an accurate reproduction of all experimental conditions. The gas density measurements were conducted without the use of the turbomolecular pump, in a higher chamber pressure than the one that LWFA experiments are conducted. The pressure was kept below $10^{-4}\ mbar$.

In Figure 6-10 the measured density profiles for Nozzles 2, 3 and 4, for gas He at $40\ bar$, $400\ \mu m$ downstream each nozzle's exit is plotted. The profiles of Nozzles

2 (blue line) and 4 (yellow line) are similar to the simulated ones, presented in Figure 4-17, while Nozzle 3 (orange line) has a totally different trend.

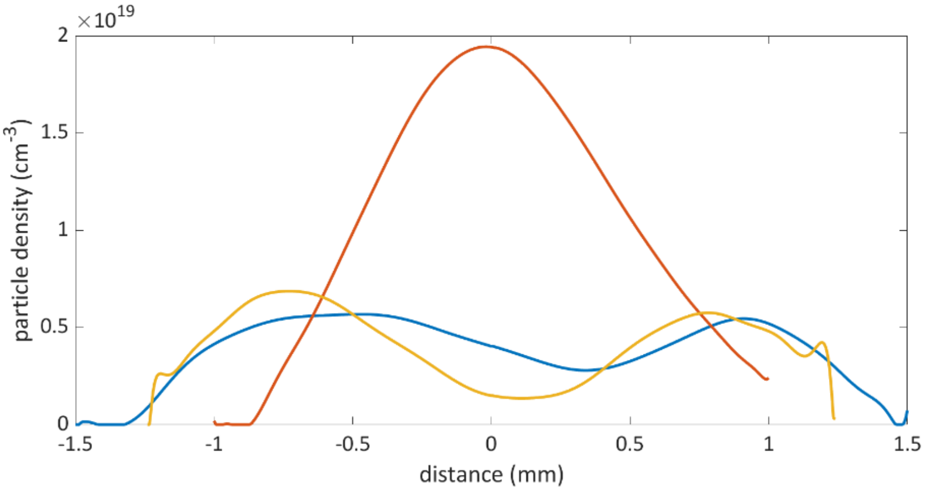

Figure 6-10: Particle density profiles for Nozzles 2 (blue line), 3 (orange line) and 4 (yellow line), $400\ \mu m$ downstream each nozzle exit for gas He, at $40\ bar$ backing pressure.

6.3 RESULTS FOR NON-AXISYMMETRIC NOZZLES

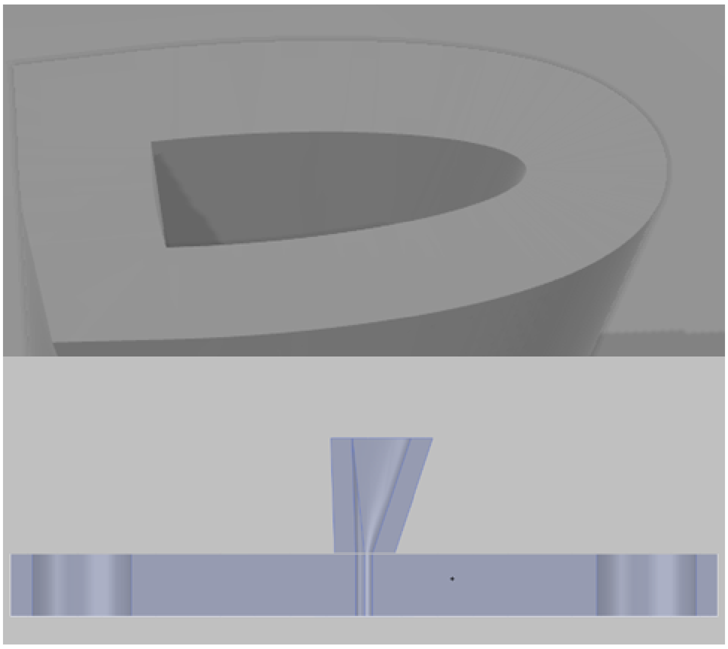

Figure 6-11: Bottom: Section view of NS1. Initially consists of a cylindrical area, elongated as an ellipse from one side and rectangular from the other side. Top: Side view of NS1 exit.

Besides the axisymmetric nozzles previously presented, 3 additional non-axisymmetric nozzles have been designed and 3D-prined; their design layouts are included in Appendix B (NS 1,2 &3). These nozzles initially follow the geometry of the valve, creating a cylindrical area, which then is elongated at one direction, destined to be the laser propagation axis, creating an ellipse. This ellipse is abruptly cut from one side, creating a rectangular surface, as can be seen in Figure 6-11.

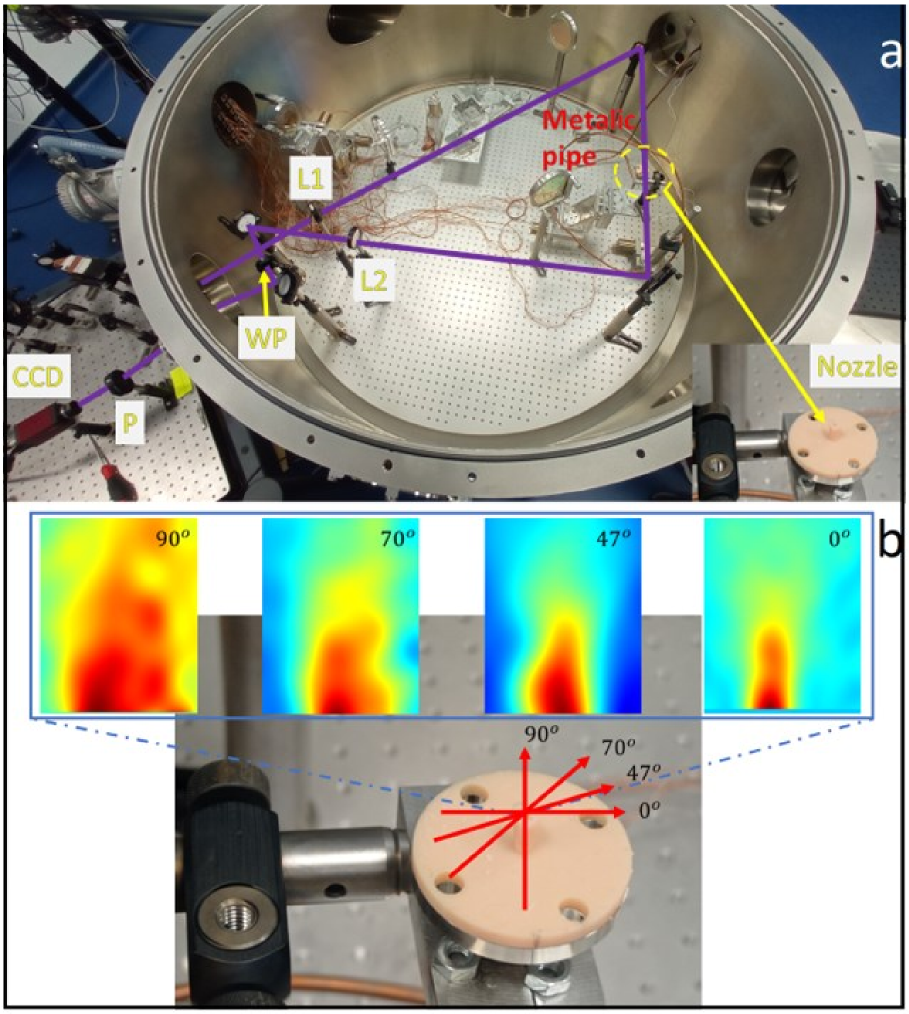

Figure 6-12: a) The experimental setup during interferometry experiments. The optics necessary to realize a Nomarski interferometer, as described in Figure 5-8, are highlighted. The base design, together with the long and stiff metallic pipe was annulling the ability to turn the nozzle at will. b) Nozzle AS1 and the phase shifts obtained at $0°, 47°, 70°, 90°$.

Here the results for nozzle NS1 are presented. The Nomarsky interferometry setup, described in section 5.4, was used. To further proceed for tomography, multiple interferograms obtained in equidistant angles were necessary. The simultaneous measurement for multiple angles would have created a complex optical setup, consisting of multiple similar optical paths; thus, we acquired the data from one optical path, by rotating the gas jet assembly. In Figure 6-12 the experimental chamber is depicted. The valve was connected to the gas high pressure container through a metallic pipe, which was difficult to rotate at will. Thus, after rotating, the obtained angles were measured to be at $0°, 47°, 70°, and\ 90°$. The images had to be carefully cropped with respect to the valve centre and finally, their phase shifts, shown in Figure 6-12, were interpolated in equidistant angles. Then, the convolution procedure was applied, to obtain phase shifts along sections vertical to the initial projections. Finally, density was calculated as explained in paragraph 5.4.3.

The results shown in Figure 6-13 are particle density contour maps at $200, 400, 600$ and $800\ \mu m$ downstream the nozzle's exit for N_2 at $30\ bar$ backing pressure. In Figure 6-14 (left) density profiles are plotted for all the above distances along the black line noted at the $200\ \mu m$ contour map of Figure 6.13 (which is assumed to be the laser path for the LWFA experiments). The density profile of the symmetric Nozzle 2, for N_2 at $30\ bar$ backing pressure $200\ \mu m$ downstream the nozzle exit is also displayed. In this case, the profile of Nozzle 2 has been extracted using a different method that averages left and right phase shift values, which totally vanishes any asymmetry.

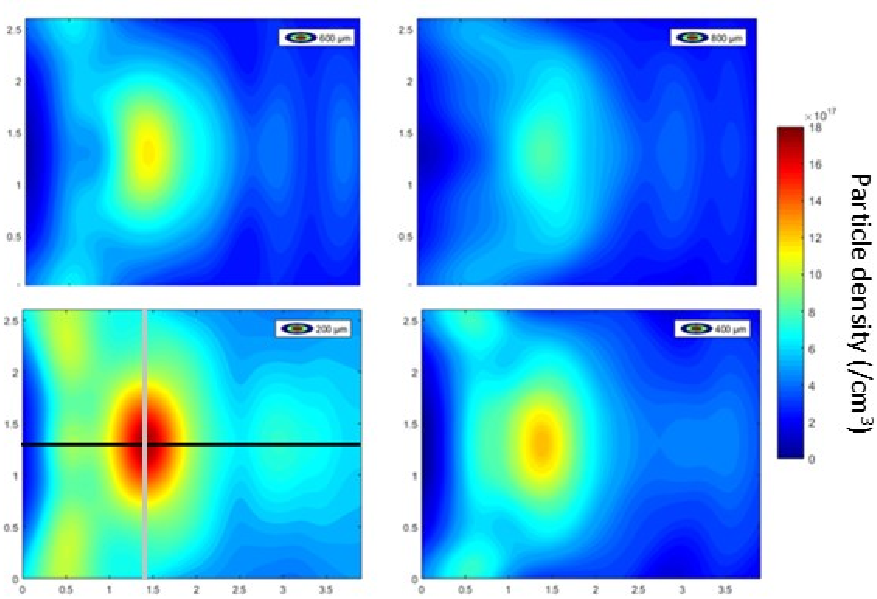

Figure 6-13: Density contour maps downstream the non-symmetric nozzle for N_2 at $30\ bar$ backing pressure $200, 400, 600, and\ 800\ \mu m$ downstream the nozzle exit.

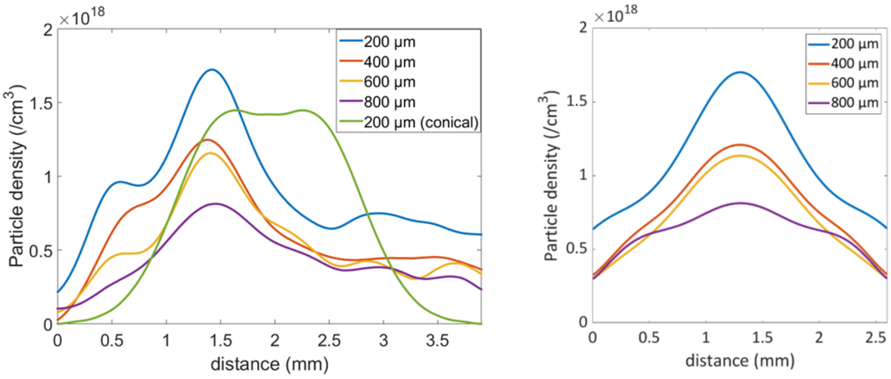

Figure 6-14: (Left) N_2 density profiles for 30 bar backing pressure along the black line displayed in Figure 6.8 at $200\ \mu m$, corresponding to the laser propagation direction for

$200, 400, 600, and\ 800\ \mu m$ downstream the exit of Nozzle NS 1 and N_2 density profile for $30\ bar$ backing pressure $200\ \mu m$ downstream the exit of Nozzle 2. (Right) density along the grey line displayed in Figure 6.8 at $200\ \mu m$ for $200, 400, 600, and\ 800\ \mu m$ downstream the exit of Nozzle NS 1.

As expected, a higher density area is formed, while the peak density is dropping by a down-ramp with approximately $500\ \mu m$ length. After that lies a constant, lower-density area. Finally, the peak density of Nozzle NS 1 is higher than the one provided by Nozzle 1 at the same distance downstream their exit. Also, in Figure 6-14 (right) density profiles are plotted for all the aforementioned distances along the grey line noted at the contour map of $200\ \mu m$ at Figure 6-13. Along this line, the profiles remain symmetrical with respect to the nozzle centre. The results of this study are included in (Andrianaki et al., 2022b).

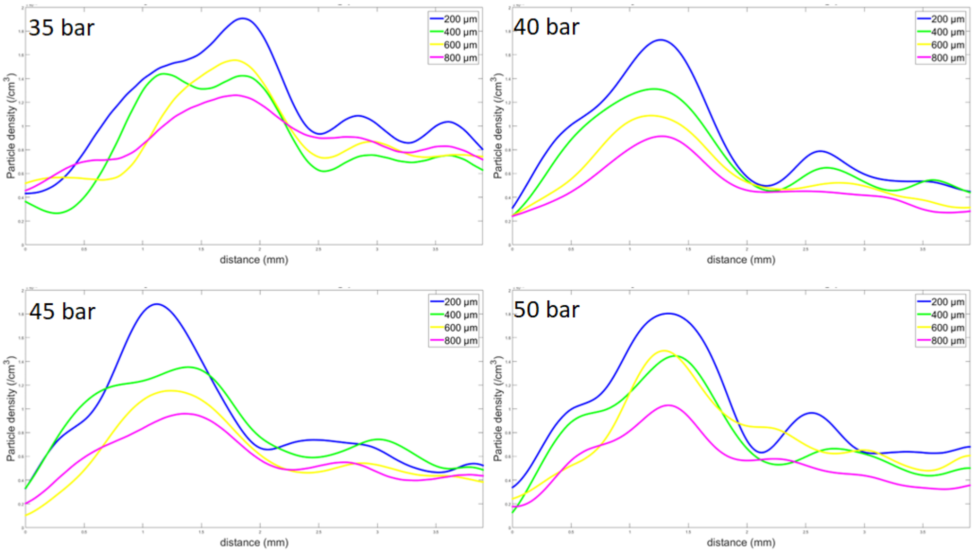

Figure 6-15: Density profiles at 200 (blue), 400 (green), 600 (yellow) and 800 (magenta) μm downstream the exit of NS 1 along the black line noted at the $200\ \mu m$ contour map of Figure 6-13. The density decreases by increasing the distance. Although pressure increases from $35\ to\ 50\ bar$ peak density remains almost unchanged.

In Figure 6-15 density profiles are plotted at 200 (blue), 400 (green), (yellow) and 800 (magenta) μm downstream the exit of NS 1 along the black line noted at the 200 μm contour map of Figure 6-13, which is assumed to be the laser path for the LWFA experiments. As a general observation, the down-ramp form is reproduced, however strong density fluctuations are measured, and the density doesn't increase by increasing backing pressure. This was unexpected, and therefore we plan to conduct additional measurements by improving the experimental setup.

In this context, a new base design was proposed. As it can be seen in Figure 6-16 (left), the exact rotation of the nozzle each 30 degrees, can be implemented using the proposed base design. This provides the opportunity to reposition the nozzle alone accurately and obtain 6 equidistant projections, without applying any unwanted tension to the metallic pipe. In addition, the design proposed at Figure 6-16 (right), is suitable for more than 12 equidistant projections.

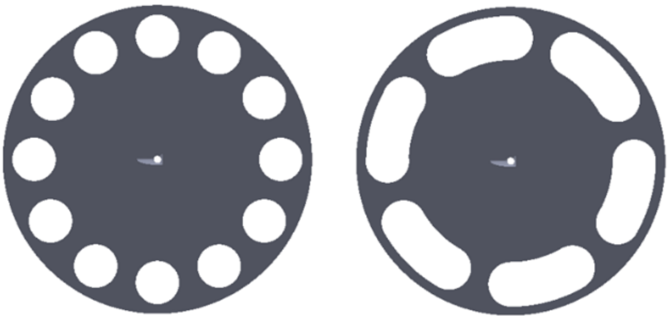

Figure 6-16: New base designs for asymmetrical nozzles. The designs are suitable for rotation at will in 6 or more equidistant angles, without rotating the gas jet assembly.

Chapter 7: LWFA experimental results by varying gas density profile

The role of the gas density profile in LWFA experiments has been extensively discussed. A set of nozzles suitable for LWFA experiments were designed, constructed and evaluated. In this chapter the results of LWFA experiments, for various density profiles, are presented and discussed. The aim is to achieve control over the electron source characteristics, such as energy, and energy spread. This will permit to provide a tuneable electron source, suitable for various applications. Preliminary results of this work have already been published in (Grigoriadis et al., 2022).

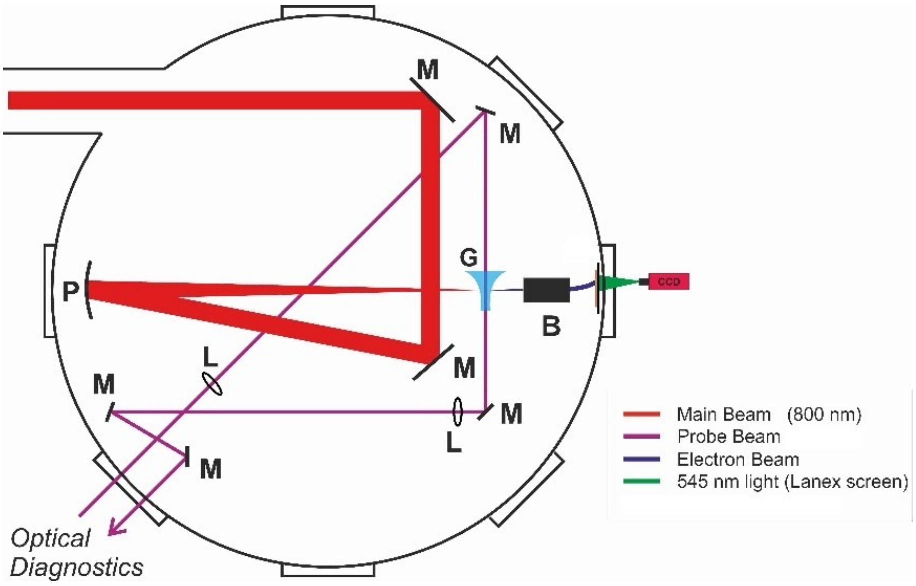

Figure 7-1: Layout of the experimental chamber during the LWFA experiments. Laser Zeus is driven and focused above the gas nozzle. The generated electron beam travels along the laser propagation direction and crosses the magnetic spectrometer. The electrons, dispersed according to their energy, are imaged on a scintillating screen. The probe beam travels perpendicular to the interaction area, to image the plasma channel formed by the interaction via shadowgraphy technique.

In Figure 7-1 the layout of the experimental chamber during the experiments is displayed. The description of the main equipment and diagnostics has already been presented in section 5.3. In brief, the laser arrives via a vacuum tube and is driven to the off-axis parabolic mirror, which focuses the beam to about $30\ \mu m$ diameter. When the laser arrives at the focus the gas exhausts, via the gas jet assembly and electrons via the LWFA mechanism are produced. The electrons are deflected according to their energy, using the MS. The plasma formed is imaged via shadowgraphy method.

Experiments of section 7.1 to 7.3 were conducted with He-gas for 3 different geometry nozzles (Nozzles 0, 1, and 2), while the resulting electron spectra for the source operating at the optimum backing pressure, for each nozzle are presented. Additionally, PIC simulation results for Nozzles 1 and 2, as well as for the non-axisymmetric nozzle NS 1 (section 7.4), are presented.

Experiments of section 7-6 were conducted with lower laser power and Nozzle 2, with gas N_2 for a range of backing pressures. The resulting electron energy spectra are mainly discussed, in the context of an electron source with some tunability.

7.1 NOZZLE 0

Nozzle 0 is an axisymmetric, cylindrical nozzle of $800\ \mu m$ exit diameter. It was constructed by gluing a commercial medical metallic needle to a 3D-printed base and is displayed in Figure 7-2 c). This nozzle was initially the unique available for the LWFA experiments. The optimum operating pressure was found experimentally to be at $12\ bar$, its density profile is illustrated in (Grigoriadis et al., 2022), with a peak neutral density at $2 \times 10^{19}\ cm^{-3}$. The laser energy was measured to be $1\,J$, the pulse duration $24\ fs$, and the focal spot diameter at FWHM $30\ \mu m$, resulting to a peak of $1.3 \times 10^{19}\ W/cm^2$.

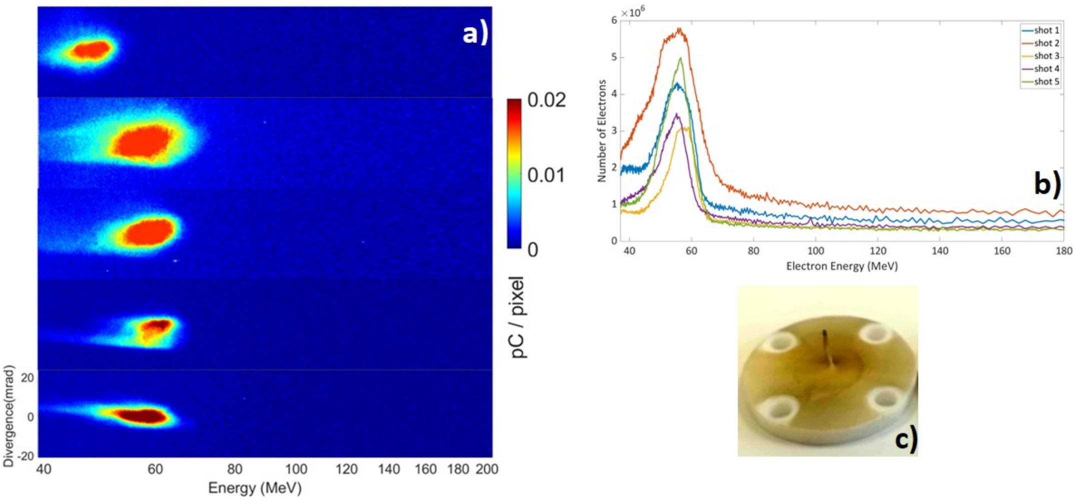

Figure 7-2: a) Electron energy spectra for 5 shots using Nozzle 0 (shots 1-5 from top to bottom). b) Spectra projection to the energy axis. The Semi-monoenergetic beams are produced with high stability. c) Picture of Nozzle 0.

In Figure 7-2 a) the energy and angular divergence electron spectra of 5 consecutive shots and their projection to the energy axis (Figure 7-2 b)) are displayed. Electrons beam energy is centred around $50 - 55\ MeV$ and the energy spread is ${}^{\Delta E}/_{E} \leq 20\ \%$. In addition, the beam angular divergence is around $10\ mrad$. The reproducibility of the electron spectrum is remarkable.

7.2 NOZZLE 1

Nozzle 1, designed by the author of this dissertation, has been extensively discussed in the previous chapters. Its performance in LWFA experiments at $40\ bar$

backing pressure is presented here. Its density profile, although not measured on-line, corresponds to the one presented in Figure 6-7 (top). The laser energy was measured to be $900\ mJ$, the pulse duration $25\ fs$, and the focal spot diameter at FWHM $30\ \mu m$, while laser intensity was relatively lower, $10^{19}\ W/cm^2$.

As depicted in Figure 7-3 a) and b), higher electron energies are achieved by using Nozzle 1 compared to Nozzle 0 (Figure 7.2). For instance, shots 4 and 5 are respectively centred at 76 and 97 MeV and their energy spread is also ${}^{\Delta E}/_{E} \leq 20\ \%$. The charge of the beams measured using Nozzle 1 is lower. Also, the angular divergence of the beam is not stable.

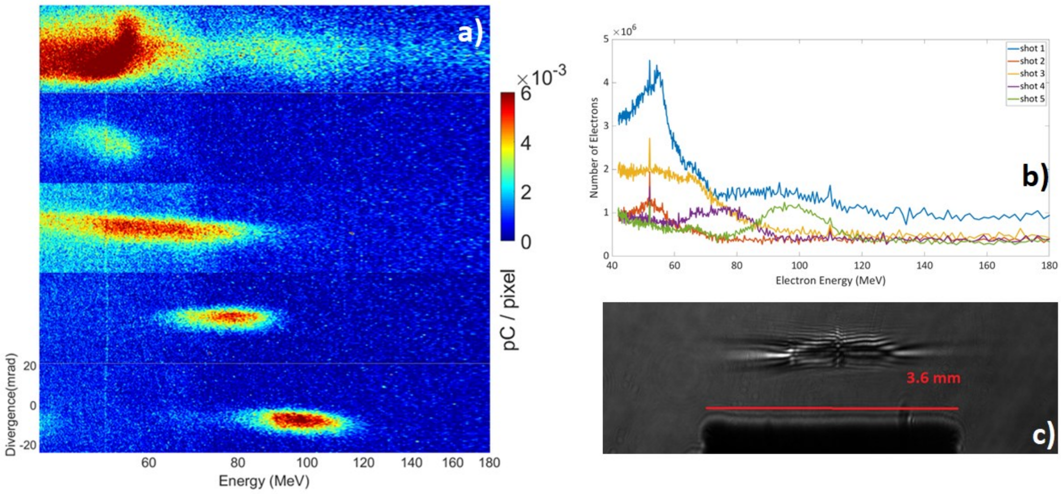

Figure 7-3: a) Electron energy spectra for 5 shots using Nozzle 1 (shots 1-5 from top to bottom). b) Spectra projection to the energy axis. c) shadowgram at the end of the interaction. The plasma channel has broken into sub-channels at the higher intensity area.

In Figure 7-3 c) a typical shadowgram obtained during the experiment is presented. For the shadowgram the delay was set at the end of the interaction, when the laser pulse has already crossed all the gas exhausted. We notice that the channel formed, has multiple breaks into smaller channels, especially at the central nozzle area, where the laser intensity is higher.

7.2.1 PIC simulations for Nozzle 1

PIC simulations were also conducted for Nozzle 1. The standard simulation setup, which has been found to approximate laser Zeus by previous PIC simulations, is utilized (Grigoriadis, Andrianaki, Tazes, et al., 2023; Tazes et al., 2020). The complete description of the electric field of a Gaussian pulse linearly polarized at the x-y plane, with laser parameters set to be $1\ J$ energy, $25\ fs$ pulse duration at FWHM are used, to apply a “simple laser“ boundary condition at the left side of the computational domain, while the other sides are set as open. The computational domain size was set to $120\ x\ 100\ \mu m,$ longer along the laser propagation axis, discretized by $2400\ x\ 500$ cells respectively, providing a higher resolution at this direction. Five macroparticles, shaped by 3rd order particle shape function per cell, were used. The target profile depicted in Figure 6-7 at $500\ \mu m$ downstream the nozzle exit is approximated according to Figure 7-4 top, as fully ionized He, a justified approximation, as He is already fully ionized by the prepulse.

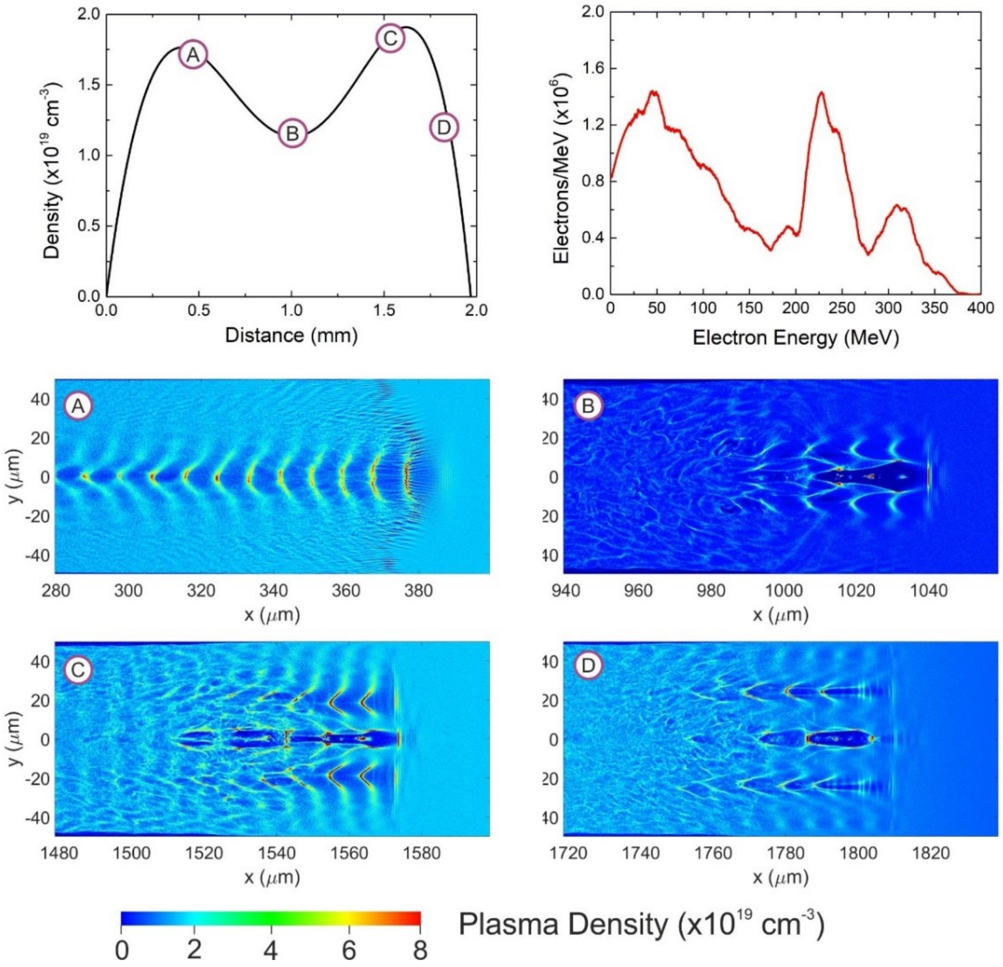

Figure 7-4: PIC simulation results for Nozzle 1. The density profile for $40\ bar$ backing pressure was approximated as fully ionized He (top left). In sub-plots A), to D) the snapshots of the plasma density, when the laser has crossed points A to D in the density profile, are plotted. At B) the beam is broken into beamlets, which drive additional waves. In the main accelerating structure of B), we see injected electron bunches, which further accelerate at C) and D), resulting in a wide energy spectrum with 3 distinct peaks (top right).

In Figure 7-4 A) - D), the plasma density is displayed, with A) to D), marked on the target profile symbolizing the position of the target profile at which the laser is arriving at each snapshot. In A) the laser drives several wakes, while in B) the laser beam breaks into smaller beamlets on both sides of the main beam, a phenomenon known as filamentation (Andreev et al., 2007; Thomas et al., 2007), which is a laser plasma modulation as already discussed in section 3.6.3. As illustrated, the beamlets drive additional, weaker wakes, and the remnant of the main beam drives the basic accelerating structure. In C) and D) the additional wakes preserve their structure, and no injection is occurring. On the other hand, at B), the central bubble structure driven by the main beam is elongated at the laser propagation direction, due to the plasma density decrease. This facilitates injection by lowering the injection threshold, thus several electron bunches have been injected in the bubble, acquiring energy.

According to (Thomas et al., 2007) filamentation is happening when the focal length is short, so as that $w_0 < \lambda_p$, resulting in broad electron spectra. Both w_0 and λ_p vary during the simulation, w_0 due to self-focusing and λ_p is a function of plasma density, which represents a non-uniform profile. As discussed in paragraph 3.6.3, filamentation may be also attributed to laser beam imperfections, however this is not the case at the simulation setup.

Here, the electron spectra obtained by the simulations is wide, with 3 distinct peaks centred at $60\ MeV$, another centred at $225\ MeV$ and a smaller one centred at $325\ MeV$. The maximum energy expected is at $375\ MeV$. The simulated energies exceed the experimental by far.

7.3 NOZZLE 2

Nozzle 2 has been utilized most frequently in IPPL experiments. Here its performance in LWFA experiments is discussed. In the results presented here operating backing pressure was set at $35\ bar$ and the laser intensity was calculated to be $1.1 \times 10^{19}\ W/cm^2$.

In Figure 7-5 a) and b) the spectra achieved with Nozzle 2 are presented. All shots have large energy spread, achieving energies up to $170\ MeV$. Shot 4 has also a distinct peak centered at $122\ MeV$. The energy spectra obtained are well reproducible. In addition, the angular divergence of the beams is smaller than for the other nozzles.

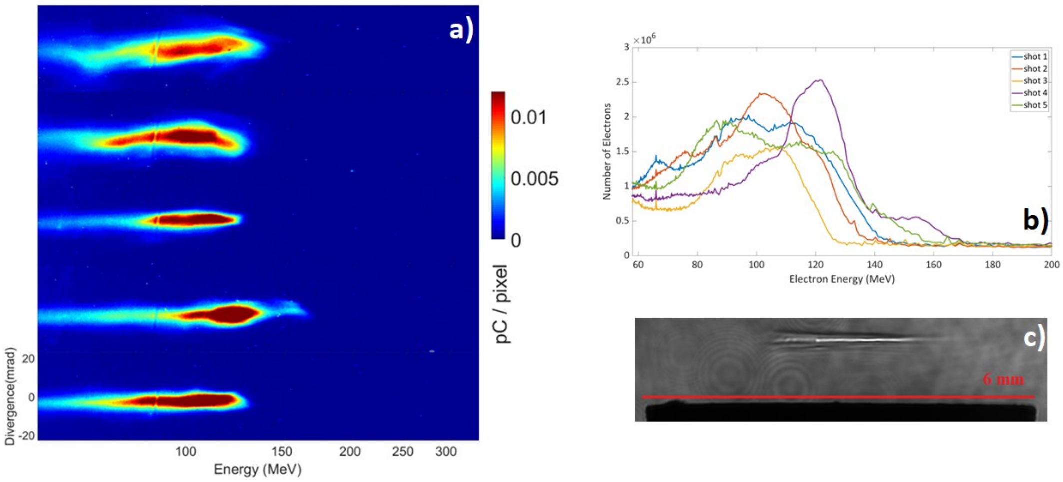

Figure 7-5: Electron energy spectra for 5 shots using Nozzle 2. High energy spread, high-energy beams are produced with good stability. b) Spectra projection to the energy axis. c) Shadowgram at the end of the interaction. The plasma channel is uniform.

7.3.1 Nozzle 2 - PIC simulations results

The laser setup is set as described in Section 7.2.1. The target profile is approximated according to Figure 7-6 top, as fully ionized He.

In A) - D), the plasma density is displayed, and A) to D) are marked points at the density profile, indicating the position that the laser arrives at each snapshot. At A) several wakes are formed. At B) the first and second bubble are elongated after travelling in a density down-ramp, and electrons have been injected in both. At C) and D) only the first bubble expands more, while the second one progressively vanishes. Finally, electron bunches injected from B) and also later, are accelerated by the first bubble. Maximum energy values are not obtained, as the energy window was limited up to $400\ MeV$ to reduce computational resources. A wide energy spectrum with some more populated areas is revealed. The simulated energies exceed the experimental by far.

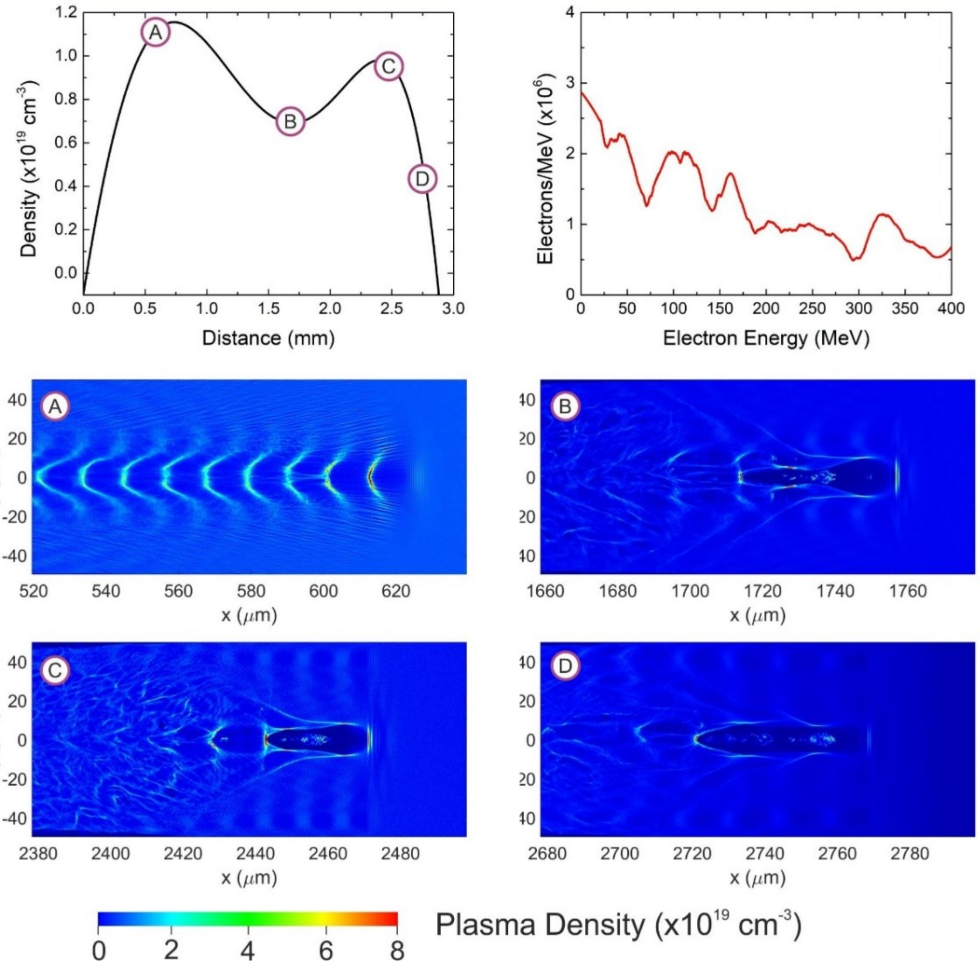

Figure 7-6: PIC simulations results for Nozzle 2. The density profile for $40\ bar$ backing pressure was approximated (top left). The resulting electron spectrum is plotted (top-right). In sub-plots A to D the snapshots of the plasma density when the laser has crossed points A to D in the density profile are plotted. First and second bubbles are elongated at B), where injection starts. In C) and D) the first bubble still expands in the longitudinal direction and injection continues.

7.4 NOZZLE NS 1 2D-PIC SIMULATIONS

The NS 1 is the next one to be tested in LWFA experiments. As illustrated in Figure 1-4, its density profile is interesting, as it follows the description of a down-ramp profile, with the additional low-density plateau, which is preferred for acceleration. Here, performed PIC simulations are presented, approximating its density profile from

Figure 6-14 as fully ionized He, as can be seen in Figure 7-7 top. The laser parameters were set as in the above cases. The symbolism follows the previous PIC results.

In this case, we may notice that for the first time, in B) the first bubble formed is not yet elongated, as the down-ramp density area has not been reached, and injection has not occurred yet. However, at C), which is approximately the end of the ramp, the bubbles are elongated, and electrons are injected. For NS 1 injection is localized, as no further injection is noticed in D). The electrons are efficiently accelerated and exceed the energy window limit. Their spectrum is wide, with a distinct peak at $100\ MeV$.

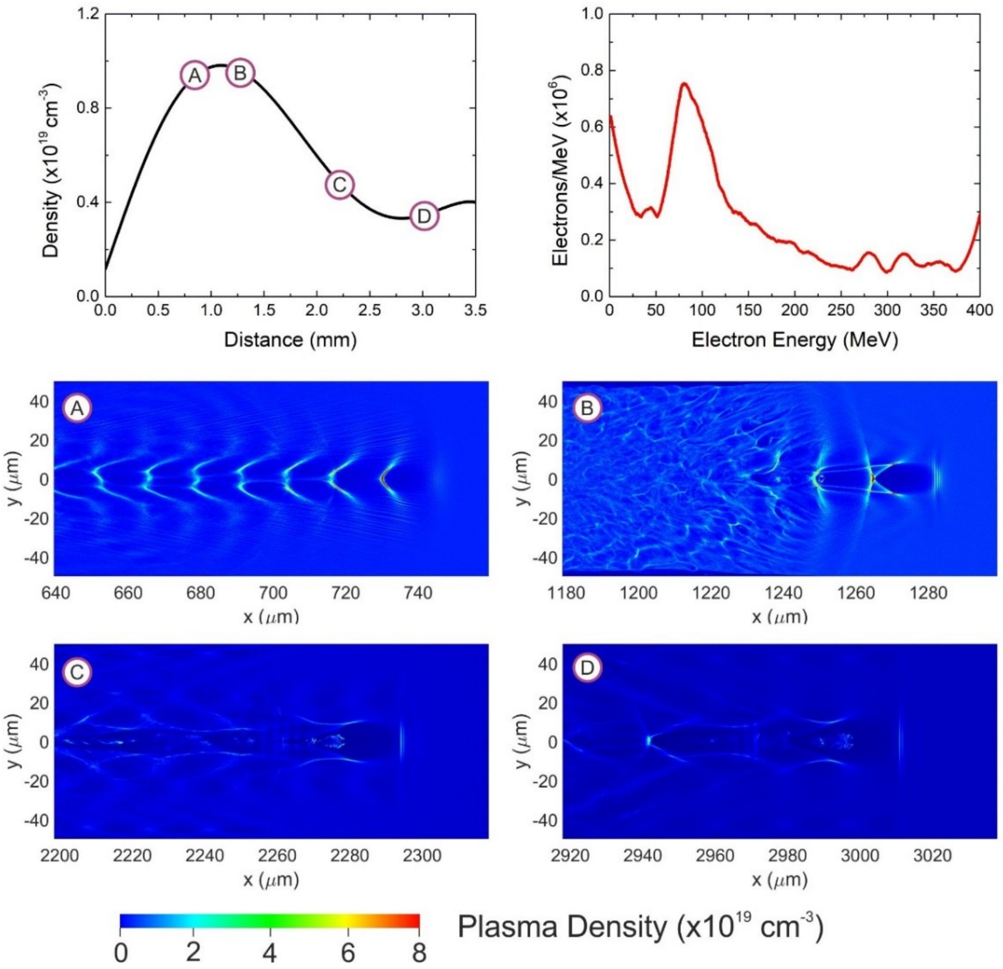

Figure 7-7: PIC simulations results for NS 1. The density profile used for fully ionized He was utilized (top left). The resulting electron spectrum is plotted (top-right). In sub-plots A) to D) the snapshots of the plasma density, when the laser has crossed points A to D in the density profile, are plotted. The first bubble formed is elongated at C), where electrons are injected. In D) the bubble is additionally stretched but no further injection occurs.

7.5 REMARKS

Nozzles 0,1 and 2 which provide different gas profiles result to different electron beam characteristics. Examining only the gas profile length, we notice that by increasing the gas jet length, the electron energy is increased. This would continue up to several limits, such as the bunch dephasing length, the laser pump depletion, and the diffraction limitation, discussed in section 3.8.

PIC simulation results overestimated the maximum energy expected in comparison to the experimental results for both cases. However, the electron energy range increases by increasing gas jet length, which was qualitatively reproduced by the PIC results. The channels imaged by shadowgrams of Nozzles 1 and 2 are significantly different. Channel of Nozzle 1 contains an extensive break into smaller channels. These formations may be attributed to the laser filamentation revealed also by PIC simulations.

The gas profiles of experiments with Nozzles 1 and 2 were measured to be far from uniform. In this study the exact profiles were simulated, which all contain density drops and could be characterized as parabolic. According to our simulation results, for both cases the density drop after the first peaks, served as down-ramps, where the plasma wavelength increased, the condition for wave breaking was fulfilled, and injection happened afterwards. As already discussed, the LWFA is further optimized when the down-ramp area is followed by a low-density plateau, where electrons will efficiently accelerate. On the contrary, density of Nozzles 1 and 2 increases after the ramps. In (Brijesh et al., 2012; Faure et al., 2010) they report that parabolic density profiles, created using a machining beam served in the same way, without reporting any influence of the second density peak. According to our PIC simulations, the existence of the second peak didn't manifest any specific detrimental or beneficial behavior too.

Finally, NS 1 provides a density profile designed for the optimization of acceleration after injection in a down-ramp. The comparison between Nozzle 1 and NS 1 is not so easy, as filamentation also affected the bubble evolution. Comparing the simulated electron spectra for Nozzle 2 and NS 1, electrons with wide energy spread are expected in both cases. However, for NS 1 lower number of electrons and a distinct high energy peak is expected.

7.6 N_2 TARGET-PRESSURE SCAN

During this experimental campaign gas N_2 was examined with Nozzle 2. As discussed in section 3.7.1, in this case together with the self-injection, ionization injection mechanism is also taking place. Especially for N_2, assuming that in the high laser intensity field will dissociate and behave like atoms, the intensity necessary to ionize the 5 outer electrons of N atom is $I_L \sim 10^{16}\ W/cm^2$, while for the 2 inner electrons, $I_L > 10^{19}\ W/cm^2$ is needed (Fill, 1994). This may occur only due to self-focusing effect, as explained in section 3.6.1, as the laser energy during this experiment was measured to be at $570\ mJ$, resulting to a peak intensity $I_L \sim 10^{18}\ W/cm^2$.

A parametric study for various backing pressures was conducted to characterize the electron source. The corresponding N_2 density at a distance $1.1\ mm$ downstream the nozzle exit, location at which the shots were conducted, for $30, 35, 40$ and $45\ bar$ backing pressure, is plotted in Figure 7-8 left. The gas density measurements were conducted off-line, while the shadowgraphy setup was set during the experiment. In 7-8 right, the representative shadowgrams for each backing pressure are displayed. The channels formed, similarly to the one of 7-3 (c) present an extensive break, which is slightly elongated as the backing pressure increases. Based on the channel formations, we speculate that laser filamentation occurred.

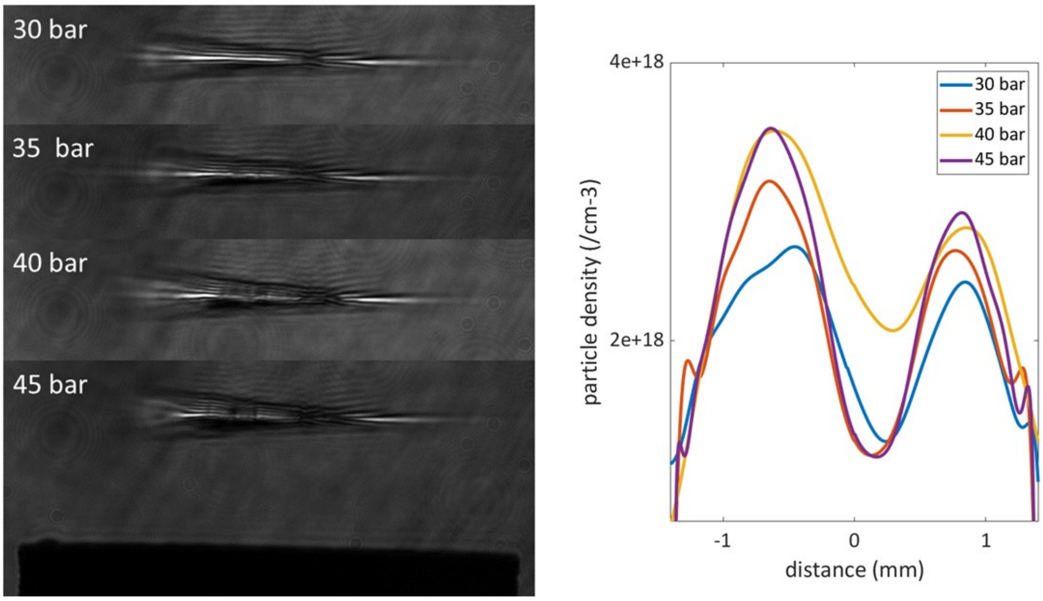

Figure 7-8: left) The shadowgrams at the end of the interaction for $30 - 45\ bar$ backing pressure. The length of the break noticed, increases with backing pressure increase. Right) The N_2 density profiles for Nozzle 2 at a distance $1.1\ mm$ downstream the nozzle exit, for $30 - 45\ bar$ backing pressure, measured with interferometry technique off-line.

In Figure 7-9 4 sets of 4 representative electron spectra for each backing pressure are presented. Due to experimental limitations, the minimum electron energy recorded at the camera was $36\ MeV$. We notice that in many cases we possibly lost an important part of the low-energy spectrum.

Below $30\ bar$ no electrons were detected. At $30\ bar$ beams of lower charge, with narrow angular divergence, were mainly noticed. In the most cases, semi-monoenergetic peaks were produced. At $35\ bar$, higher number of electrons are recorded, and their spectra and angular divergence are wider. Comparing these spectra to those of Figure 7-5 a), which were produced with gas He at $35\ bar$ backing pressure and significantly higher laser energy, one notices that maximum energy achieved is reduced by over $50\ MeV$.

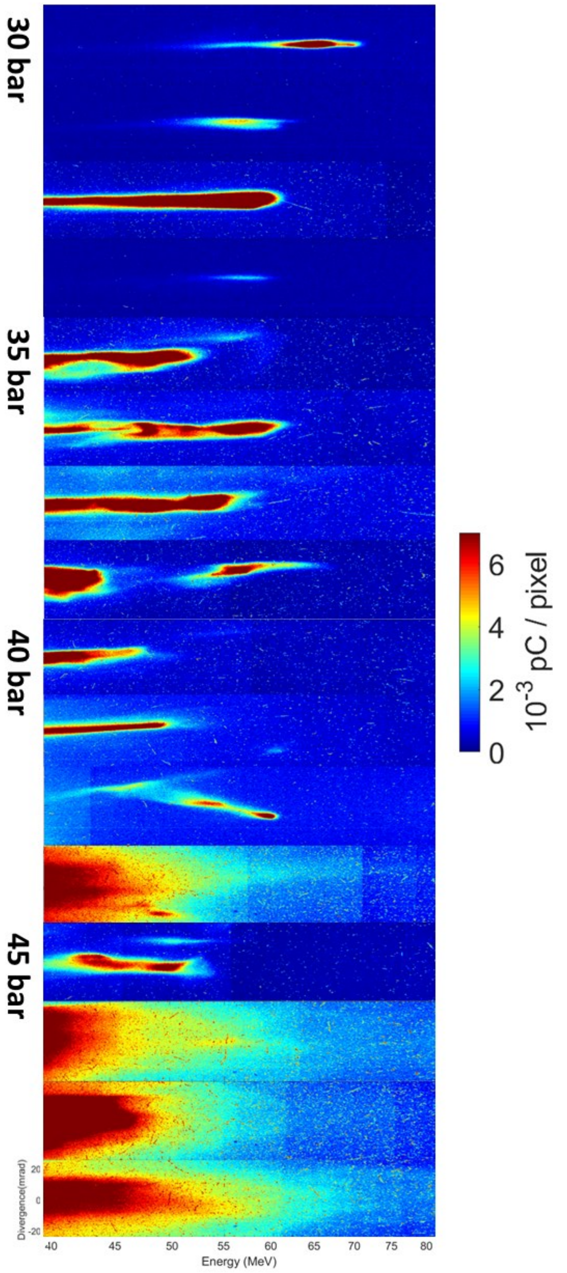

Figure 7-9: 4 representative electron spectra for $30, 35, 40\ and\ 45\ bar$ backing pressure. At $30\ bar$ lies the injection threshold, where high energy - low charge beams were detected.

As the backing pressure increases, we notice at $40\ bar$ for the first time, but also more repetitively at $45\ bar$, that the electrons lose their characteristic beam form and a continuum form is recorded, which is highly populated, with a very high angular divergence, exceeding detectors limits. In a similar experiment (Mangles et al., 2007a) they characterize this population as dark current. Also, there is a smaller but significant number of high-energy electrons. This continuum behaviour may be attributed to the beam loading effect. Beam loading takes place when the charge of the bunch is so high that modifies the accelerating field, resulting in lower quality bunch characteristics (Couperus et al., 2017). In addition, according to the results of (W. Li et al., 2013), the wide angular divergence spectra obtained in for higher backing pressure, may also be attributed to the acceleration of electrons by more than one filaments.

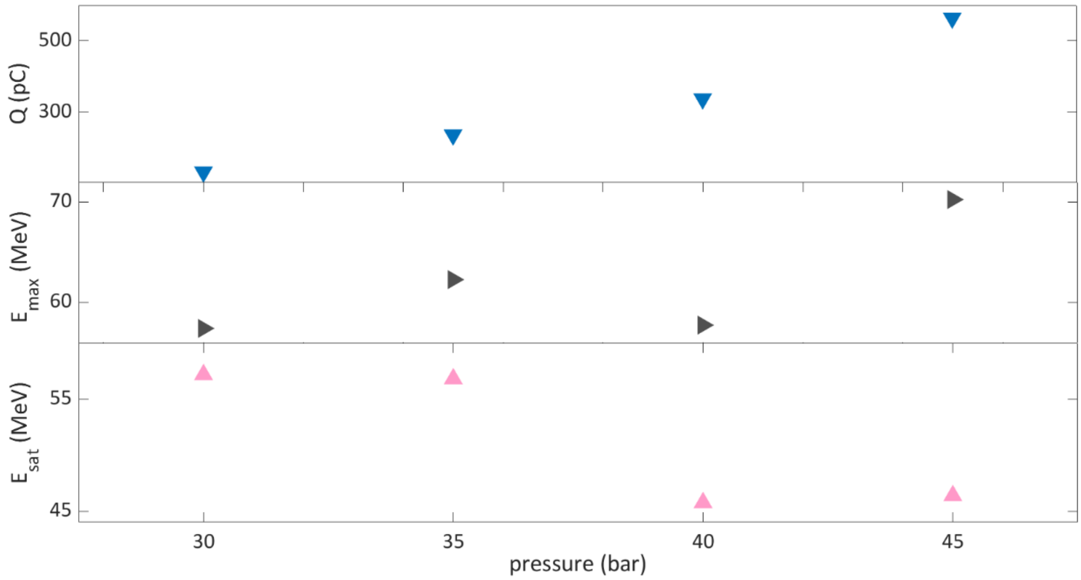

Figure 7-10: Mean total charge, mean maximum energy, and mean saturated maximum energy of electrons produced with an N_2 gas target for $30 - 45\, bar$ backing pressure. Charge increases significantly with backing pressure and creates the beam loading effect.

In Figure 7-10 mean total charge, mean maximum energy, and mean saturated maximum energy are plotted for $30\, bar$ (12 shots), $35\, bar$ (8 shots), $40\, bar$ (10 shots), and $45\, bar$ (8 shots). Although the mean saturated maximum energy reduced as expected, mean maximum energy increases, due to the continuum, lower charge spectrum.

Only PIC simulations in a non-fully pre-ionized plasma would clarify the contribution of ionization injection in the overall injection, however not conducted, due to their high demand for computational power. Given the density profiles of Figure 7-8 the density down-ramp may also be contributed to the injection, according to the previous discussion.

The experiment was conducted with the laser performing within the low energy regime. The electron source is far from optimized, especially in the high-pressure regime, where the beam characteristics are eliminated by the presence of the continuum spectrum. However, in some cases the high charge is a desired characteristic. Many studies are now conducted, aiming to manipulate the beam loading effect to improve the performance of LWFA (Couperus et al., 2017; Rechatin et al., 2010).

Chapter 8: X-ray Betatron identification experiment

Betatron x-ray beams are mainly considered a possible candidate for x-ray imaging. Moreover, they are examined as a non-invasive additional diagnostic for the LWFA evolution. In (Corde et al., 2012) they report to use Betatron beams to retrieve information about the wavebreaking, the electron injection location and whether the electron beam achieved the acceleration limits. Such valuable information can guide further steps for the creation of a tunable electron source.

In this context, in the year 2020, we modified the experimental LWFA setup to study simultaneously the relativistic electron spectra and Betatron-type x-ray radiation profiles, using various gases (He, N_2, Ne, and Ar). The main findings of this study have been published in (Grigoriadis et al., 2021).

In this chapter, the preliminary experiment for Betatron radiation identification is discussed. An experiment aiming to distinguish Betatron radiation from other x-ray production mechanisms (Corde et al., 2013) and identify its special characteristics was conducted, while the corresponding results are presented here and were reported in (Andrianaki et al., 2020)

8.1 THE BETATRON RADIATION IDENTIFICATION SETUP

The experimental setup is a modification of the one used in LWFA experiments. As a gas target, Nozzle 2 and He gas were used. According to (Rousse et al., 2004) along the laser and electron propagation radiation, a soft x-ray beam with low angular divergence is expected. This beam is produced when LWFA electrons wiggle transversely in the bubble, thus the conditions for efficient LWFA must be fulfilled.

To detect the x-ray signal, two pin-diodes, shielded for noise in the experimental chamber, were used. The diodes were filtered by Al foil of $4.5\ \mu m$ thickness, selected to block photons with energy $< 1\ keV$, according to the transmission curve presented in Figure 5-13. The diodes were positioned at the same distance from the x-ray source, D1 in a KF-40 flange, at the laser propagation direction, where the Betatron radiation was expected, while the second one, D2 was placed under various angles (the results presented here correspond to the angle perpendicular to the laser propagation direction) thus, the simultaneous detection of x-rays in various directions outwards the interaction region was obtained. The Al filter was mounted on a KF40 O-ring and placed in the tube for D1, while for D2 special care was taken at the design of the shielding case. As seen in Figure 8-1, a bypass tube was installed to permit pumping in the back side of the filter. To deflect the electron beam produced via the LWFA mechanism from the D1 active area, the pair of magnets used for MS was utilized.

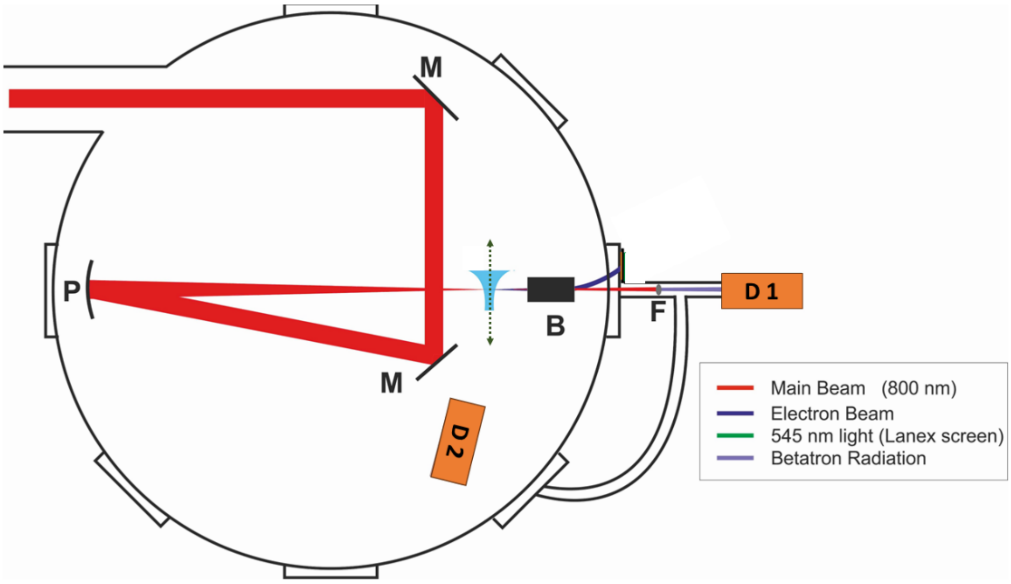

Figure 8-1: Layout of the experimental chamber during the Betatron radiation identification experiment. Laser Zeus is driven and focused above the gas nozzle. Laser final focusing optic (off-axis parabola) and the gas jet assembly are placed on a motorized base, permitting the source to move as a whole along the green array from -4 to $4\,mm$. Two photodiodes D1 and D2 are set, D1 at the laser propagation direction, D2 under various angles placed at the same distance from the source. The electron beam generated travels along the laser propagation direction and crosses the magnetic field of the spectrometer, which deflects them out of the active area of D1. The photodiodes were appropriately shielded and filtered from photons with energy below $1\,keV$, as presented in section 5.5.

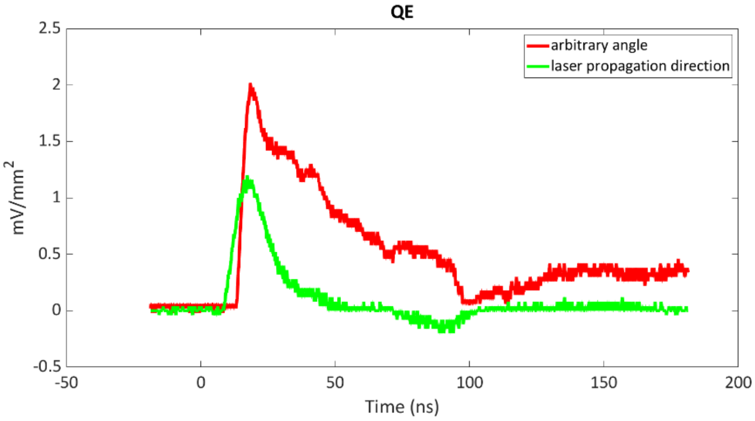

Figure 8-2: Quantum efficiency of D1 and D2 for stable photon source.

The two diodes were initially cross-calibrated, using a stable photon source (the secondary beam of laser Zeus) for their time response and their quantum efficiency. Their quantum efficiency was significantly different as can be seen in Figure 8-2, and the one with the lower value was selected as D1, as higher signals were expected at this direction. As the active area of the photodiodes is large, a metallic pinhole of $2\,mm$ diameter was placed in front of D1. The pin-diodes were triggered by the secondary beam of laser Zeus, a few ns before the interaction, and their signals were acquired using an ultrafast oscilloscope.

8.2 PRESSURE SCAN

For this experiment, the laser energy was measured to be $900\,mJ$, the pulse duration $26\,fs$, and the focal spot diameter around FWHM $30\,\mu m$, resulting to a peak intensity of 1.03×10^{19} W/cm^2. Betatron radiation is a non-linear effect and is produced when LWFA conditions are fulfilled. As already discussed, the operating backing pressure range of a LWFA source is limited. Thus, we varied backing pressure applied at the gas valve from 15 *to* $42\,bar$, and the signals recorded from diodes D1 and D2 are presented in Figure 8-3. In D2 the signal increased by increasing backing pressure. In D1 the signal was countable only for $30,\ 35$ and 42 bar. With the setup presented in Figure 8-1 the simultaneous measurement of electron spectrum was excluded, thus, based on our previous findings discussed in section 7.1.3, where the LWFA experimental results for Nozzle 2 operating with He were presented, we concluded that under similar conditions (gas He, similar laser intensity), the optimum electron source operating pressure was found to be at 35 bar. The signal in D1 is further increased for 42 bar. Although Betatron x-rays are produced by electrons accelerated in the wakefield, their number and critical energy is increased with the density, (relations 3.45 and 3.46), thus their yield is optimized under different conditions, as also shown in Figure 1-3, adopted from (Wood et al., 2017) and in (Ferri et al., 2018), where they used two consecutive gas jets, of significantly different gas density, to tune separately the LWFA and Betatron process.

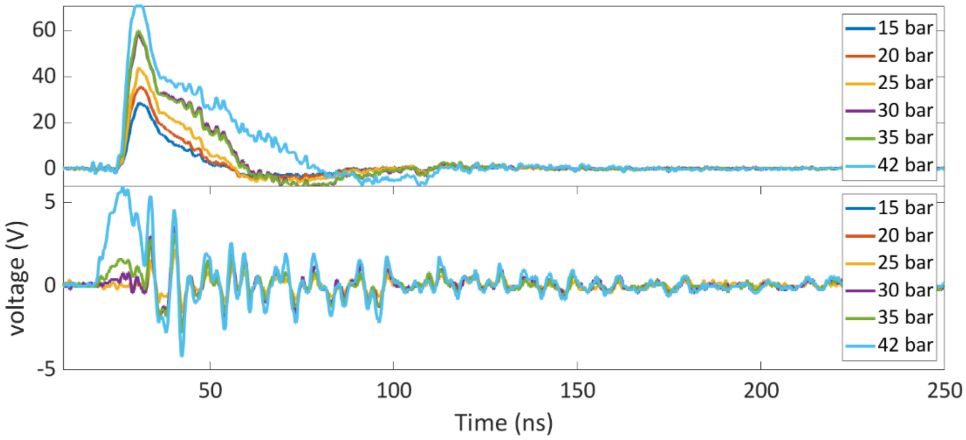

Figure 8-3: Signal (V) with respect to time for D1 (bottom) and D2 (top). In D1 the signal is distinguished from noise for a backing pressure higher than 35 bar.

Integrating the signal over time and using the cross-calibration factor, as also taking into account the active area of each photodiode, the signal with respect to the backing pressure applied at the gas valve was calculated and plotted in Figure 8-4. Signal in D2 (top) increases linearly with the backing pressure, while a non-linear behavior is noticed for D1 (bottom).

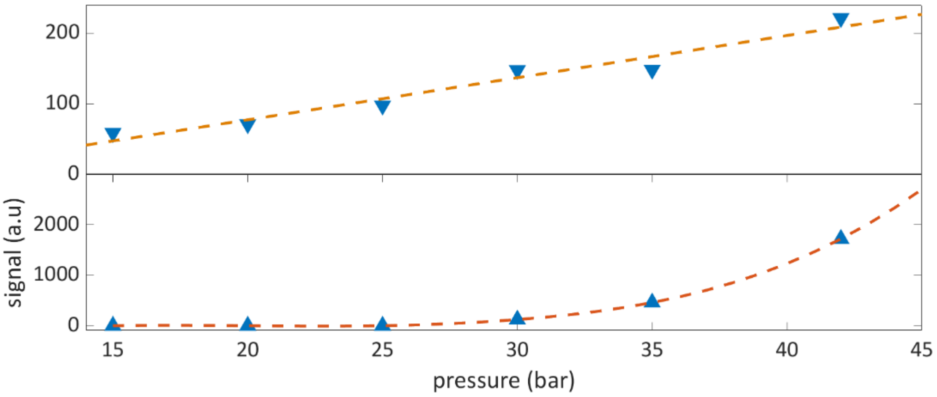

Figure 8-4: Integrated signal (a.u.) over time is plotted with respect to backing pressure applied to the EM valve.

8.3 X RAY POINTING

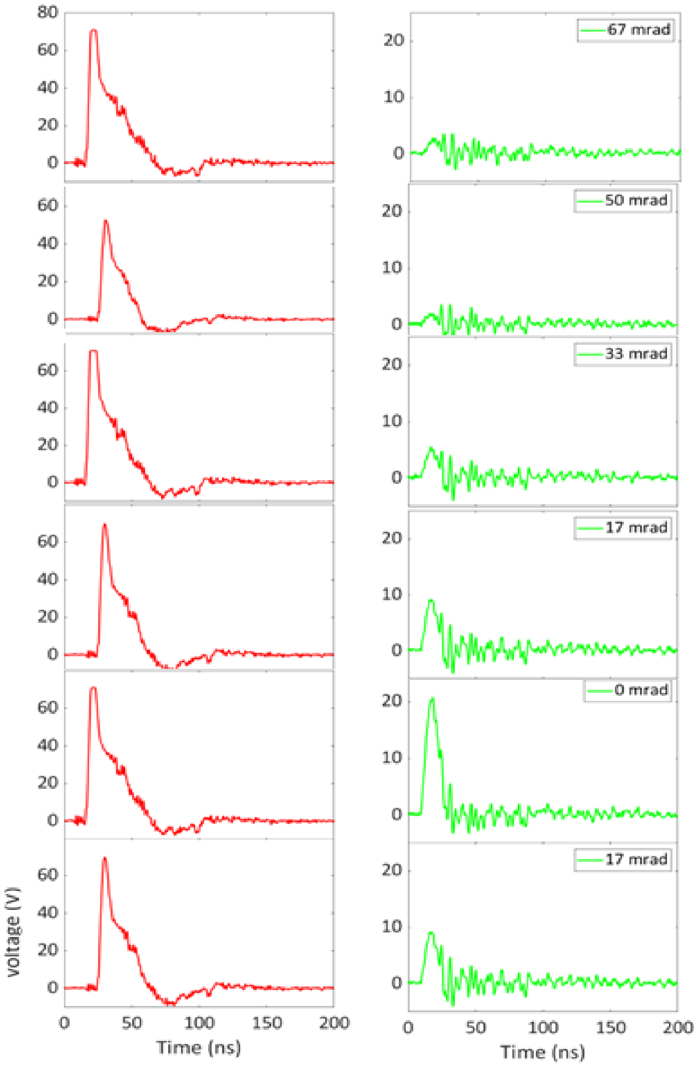

Figure 8-5: The signal over time recorded by D2 (left) and D1 (right) for source translation from $4\ to\ -1\ mm$ $(67\ to\ -17\ mrad)$ with respect to D1 centre. Signal in D2 is not affected by the source translation, while signal in D1 is dropping by increasing the angle.

According to the bibliography, Betatron radiation is expected to be a low-divergence, directional X-ray beam (Corde et al., 2013; Rousse et al., 2004). D1 was fixed in a KF-40 flange at the centre of a blind ISO 200 port. The gas jet assembly together with the focused laser beam, namely the x-ray source, were positioned in motorized stages, thus were able to move perpendicular to the center of D1 on both sides. Representative signals recorded at D1 (right) and D2 (left) by translating the source position over a *4 mm* from both sides with respect to the center of D1, corresponding to viewing angle from *0 to* ± 67 *mrad*, are plotted in Figure 8-5. The signal at D2 is independent from the source position, although translated covering a large distance, while the signal at D1 is maximum at the center and drops significantly as the source is moving to both sides.

Integrating the total signal over time and using the cross-calibration factor, as also taking into account the active area of each photodiode, the total signal with respect to the source translation is plotted in Figure 8-6. Signal in D2 remains unaffected while the signal in D1 reveals its directionality.

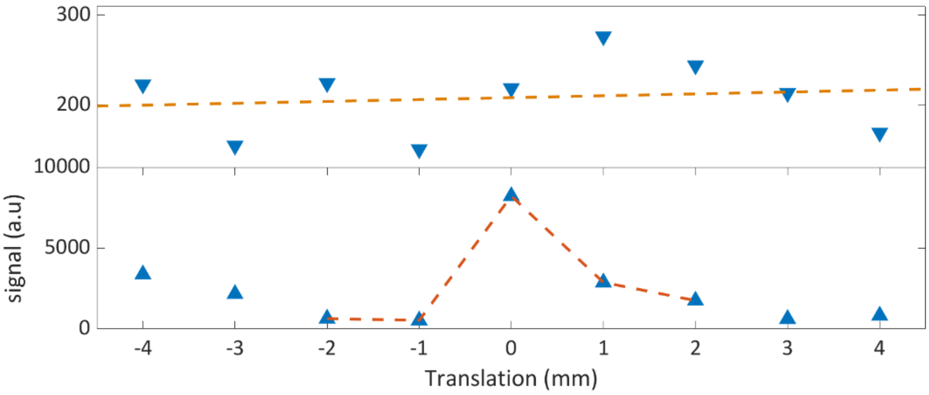

Figure 8-6: Integrated signal over time for D1 and D2, with respect to the translation position of the x-ray source relative to D1 centre.

An x-ray beam, co-propagating with the laser is recognized. Considering the directionality and the non-linear behavior with respect to backing pressure, this signal is attributed to the laser plasma Betatron-type radiation expected. The x-ray signal recorded in large angles, with respect to the laser beam direction, was unaffected by the x-ray source translation and was increasing linearly with the gas backing pressure. This signal is primarily attributed to the non-linear Thomson scattering (Corde et al., 2013).

For further investigation of Betatron Radiation, e.g., to obtain information about the number of x-ray photons and their spatial distribution is feasible by using a 2D detector. Thus, after the preliminary experiment, where we established the nature of the x-ray source at the laser propagation direction, we removed the photodiodes and placed at D1 position a Raptor Eagle XO CCD camera, able to capture visible, extreme UV and x-ray photons. The camera was also filtered from photons with energy $< 1\, keV$. In this case we also modified the ISO 200 port, to simultaneously detect the spectrum of the electron beam produced. By this setup the 2D x-ray beam profile was recorded. This study aimed to investigate how Betatron Radiation was affected by modifying the laser energy and by replacing He by multi-electron targets, namely the role effect of ionization injection mechanism and was extensively presented in (Grigoriadis Anastasios, 2023). The experimental results were also well reproduced by computationally demanding PIC simulations and are expected to be published soon.

Chapter 9: Conclusions and perspectives

In IPPL a relativistic electron source and an x-ray Betatron source have been established. To obtain controllability over the electron beam characteristics, which also define Betatron beam characteristics, a study for the influence of gas density profile in LWFA experiments is presented. The idea to design, manufacture and use our own nozzles, mainly based on CFD simulations, was realized. The designs were based on the existing gas valve, thus taking advantage of its geometrical features; additional (mainly) conical geometries were designed, to create as an integrated design, a CD nozzle geometry. This served also to omit the construction of the smallest feature of a CD nozzle, the throat, which would be very difficult to be accurately 3D-printed. The feasibility of the proposed concept, i.e. of designing and constructing only the divergent part of the nozzle by 3D printing (being far simpler, cheaper, and accurate than constructing additionally the throat region), was proved. The produced gas density profiles proved more than adequate for the performed LWFA experiments.

CFD simulations is a precious tool, which delivered reliable results, for a set of modified De-Laval type nozzles. The physical model proposed was counter-examined with other models and the importance of the use of a real gas equation of state was highlighted. The simulations presented in this dissertation are for 2D axisymmetric nozzles. However, non-axisymmetric nozzles have been also designed, thus 3D simulations are necessary for their assessment. Although some have been already conducted, a fine mesh, necessary to capture the smallest flow features, such as shocks, is not yet developed.

The 3D-printing manufacturing technology was tested. The nozzles were successfully manufactured, despite small defects which were noticed. The SLA technology proved to be the most reliable. The nozzle cost and delivering time was small. Interferometry was used to evaluate the gas density profiles and the results were mostly in good agreement with the corresponding CFD simulations.

The tomography technique was applied, to measure the profiles of the non-axisymmetric nozzles. The base of the non-axisymmetric nozzles was also re-designed, providing the opportunity for capturing multiple equidistant interferograms. In this way we aim to obtain more accurate gas density profiles. Also, the symmetrical nozzles will be examined via tomography to obtain accurate density profiles for them too.

Most of the density profiles for axisymmetric Nozzles 1-4 were peaked at the edges, while they present a density drop at the middle. The profile is reproducible for a wide range of backing pressures and distances from the nozzles exit. Their profile could be characterized as almost parabolic.

Nozzle 5 is a special case, where a diamond like shock in developed far downstream its exit. This nozzle is destined for experimental conditions at which the gas jet assembly should be positioned lower than the usual, or for a case where a density profile peaked at the middle is desired.

The non-axisymmetric Nozzle NS1 provided a high-density area, followed by a down-ramp and a plateau region. This profile, according to the bibliography and an initial PIC study, is suitable for LWFA acceleration with down-ramp injection. We are already planning the following experimental campaign to study its performance. Apart from the interesting electron density profile expected, according to the simulations the basic advantage reported by many groups is its reproducibility, which can be examined only experimentally.

According to our experimental findings, there is a tunability provided using different density profiles. In the experiments presented in Chapter 7, the maximum energy, as well as the energy spread increased by increasing the nozzle length. The high energy spread of the electron beam is typically addressed as a drawback. However, a reproducible high energy-range beam can be further manipulated to discriminate and utilize selected energy electrons (Park et al., 2016).

The pressure range of operation of Nozzle 2 with gas N_2, in the low laser energy laser regime was examined. The pressure threshold is at $30\, bar$, and for operation over $40\, bar$ the electrons lose their beam-like characteristics, and a continuum spectrum is obtained. Also, the number of electrons was increased by more than a factor of two by using nozzle 2 with gas N_2 under low energy and high backing pressure conditions. The exact contribution of the ionization injection mechanism is not clear without the conduction of PIC simulations.

The Betatron x-ray radiation was identified for the first time in IPPL. The non-linear increase of the signal with backing pressure and the dependence on the x-ray source position demonstrated the production of a Betatron-type source.

Based on the established electron and x-ray source, multiple experimental investigations will follow. Examining in more detail laser plasma interactions, and the resulting particle beams, several diagnostics will be established to provide more understanding of the mechanisms. The setup of an online interferometer and the use of another ultrafast ($\tau_0 < 7fs$) laser beam, available at IPPL, will provide time evolution information about the plasma density during the experiments. Also, the use of an additional scintillating screen, located before the magnetic field together with an additional imaging system, will permit to capture the pointing characteristics of the electron beam shot to shot. This is necessary to record electron beam pointing stability. Moreover, by establishing online laser diagnostics, the correlation of the laser, plasma and resulting electron beam characteristics will help to map the interaction with more precision and proceed with methods for active stabilization of the accelerator, according to (Maier et al., 2020).

In addition, more information about the Betatron beam is necessary. The x-ray energy spectrum should be measured; thus, an x-ray spectrometer must be constructed. The operating principle will be based on the Ross filter, where the use of multiple metallic filters, which present different transmission, are positioned at the same plane, covering different part of the x-ray beam, creating “photon energy windows” (Albert et al., 2013). The multi μm thickness filters have already been purchased and they will be established in a specially designed base before the chip of the x-ray CCD camera, along the Betatron beam direction.

In the gas target area, apart from examining the NS nozzles, another idea is the replacement of the gas jet assembly with an adjustable length gas cell. According to (Prencipe et al., 2017) this may drive in higher electron energy and more reproducible results. To create the appropriate gas density profile using a gas cell, CFD simulations should be conducted.

Finally, the existence of a relativistic electron source and a coherent x-ray beam is a great achievement, and the controllability of this source is valuable for potential applications. For instance, as the fruitful collaboration with the group of the Medical School of Crete and the University Hospital of Crete keeps going, the electron beam will be used to irradiate cancer cells as a next step. In addition, the laser produced Betatron radiation can serve as a probe in other laser-based experiments. In this case, as the two beams come from the same laser, synchronization will be simpler.

.

Appendices

Appendix A

Mesh independence study

A mesh independence study took place for the CFD simulations. When the number of mesh nodes increases, the computational cost increases too. This is why the coarsest mesh capable of resolving a problem is preferred. In many cases, a simulation converges in terms of residuals, but the results are dependent on the mesh size and nodes' positions. This is why a mesh independence study is necessary, at least for one specific run. After that, the sizing of the mesh can be adopted for the rest (similar) simulations. The mesh independence study was conducted for Nozzle 1.

After this study, the mesh was selected to consist of 1084653 nodes and 1080794 elements. The study presented here considers a coarse (~ 500.000 nodes), a medium (~ 700.000), and a high resolution ($\sim 2.000.000$) mesh. The simulation set-up described in section 4.3, for He gas at $40\ \mathrm{bar}$ backing pressure and $1\ \mathrm{mbar}$ at the outlet are used. A variable, in our case gas density, calculated at specific positions is used as a monitor parameter.

The corresponding density profiles for the 4 utilized meshes $200\ \mu\mathrm{m}$ downstream the nozzle exit, after the simulations reached convergence, are plotted in Figure 9-1. In Figure 9-2 the relative difference among each mesh with the selected-one are plotted, along the same line. The relative difference between the selected mesh and the one with the higher resolution is less than 1%, assuring that mesh independence is achieved; namely the results didn't undergo any significant change by altering the mesh, providing enough confidence for the simulation results.

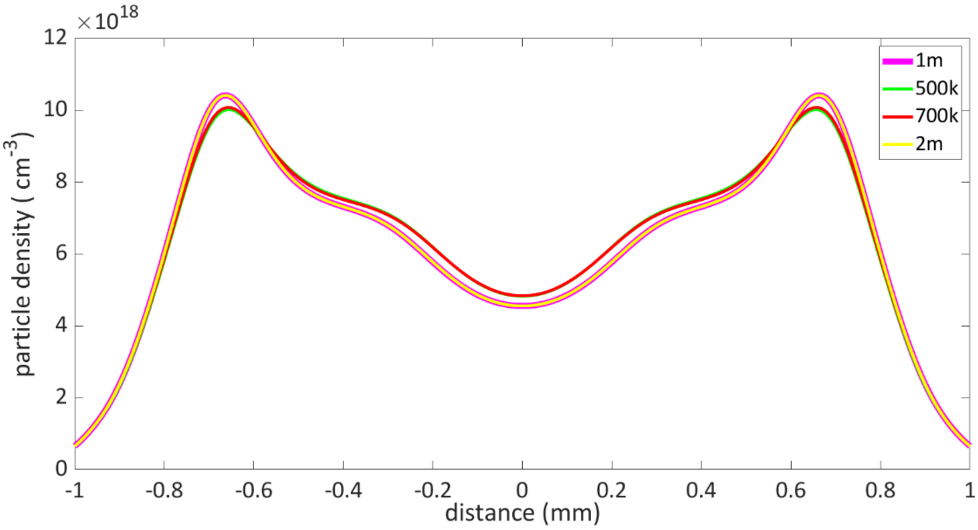

Figure 0-1: Particle density $200\ \mu m$ over the nozzle exit for Nozzle 1, with gas He at $40\ bar$ backing pressure.

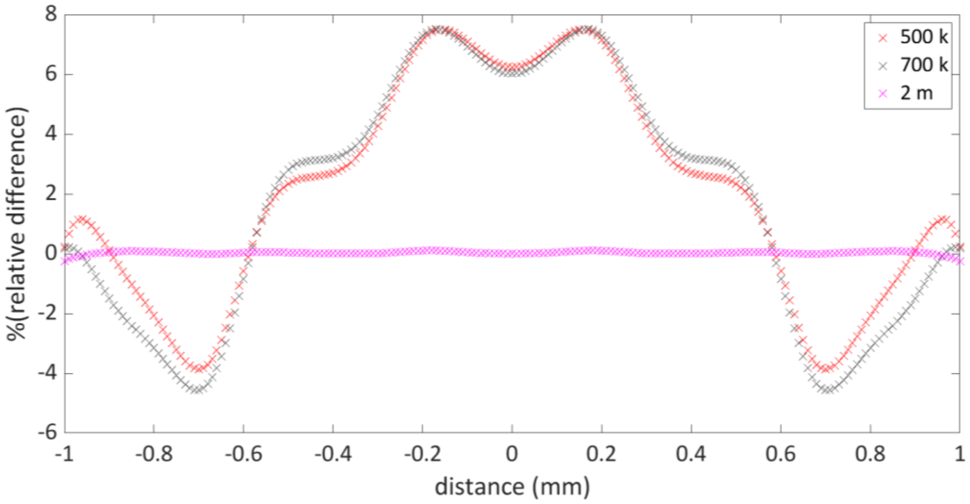

Figure 0-2: The relative difference percentage for the 3 test meshes relative to the selected one. The relative difference of the finer mesh with the utilized one is below 1%.

Appendix B

Nozzle drawings

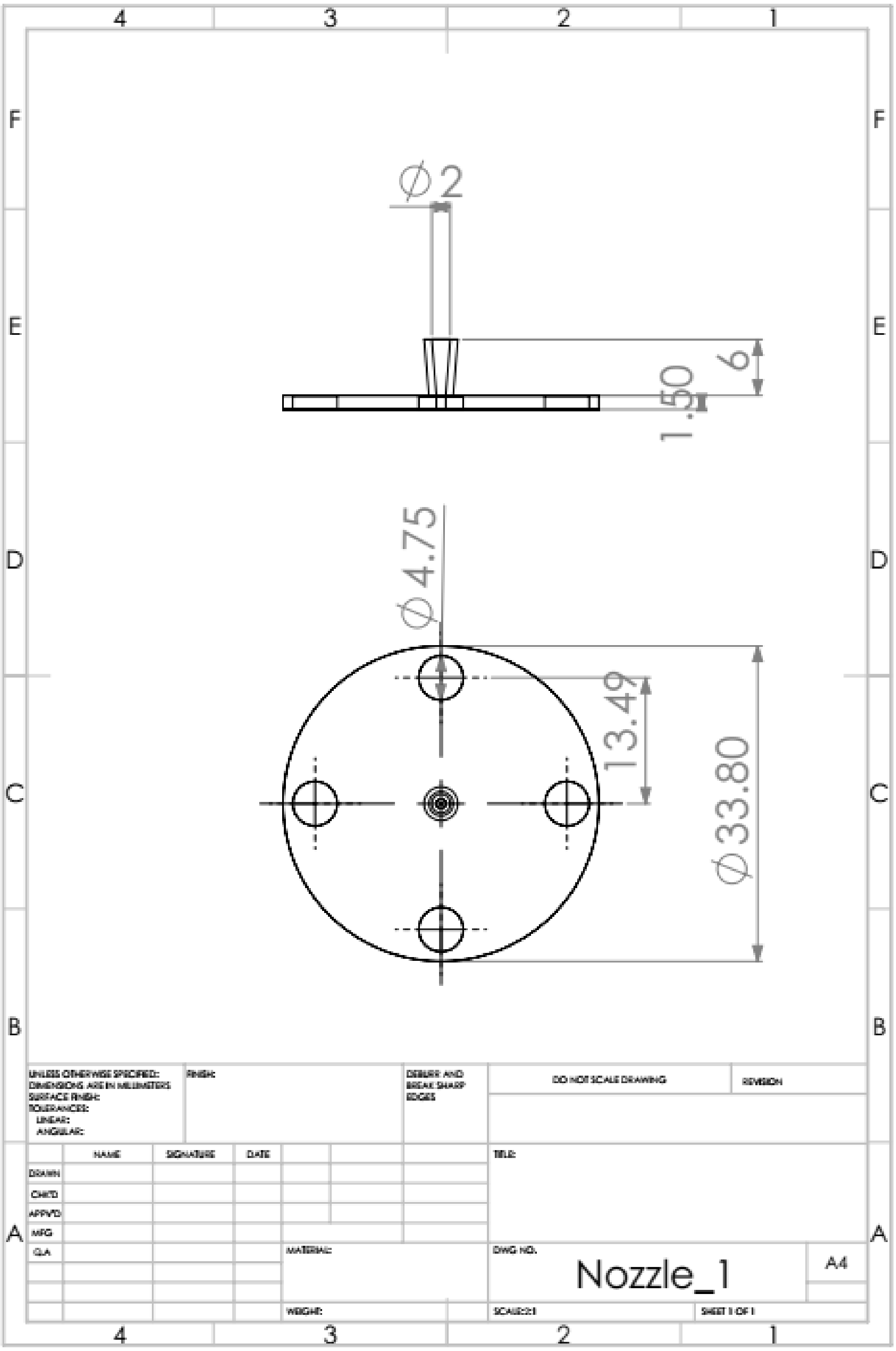
⌀2
6
1.50
⌀4.75
13.49
⌀33.80
4
3
2
1
F
E
D
C
B
A
UNLESS OTHERWISE SPECIFIED:
DIMENSIONS ARE IN MILLIMETERS
SURFACE FINISH:
TOLERANCES:
LINEAR:
ANGULAR:
FINISH:
DEBURR AND BREAK SHARP EDGES
DO NOT SCALE DRAWING
REVISION
NAME
SIGNATURE
DATE
DRAWN
CHK'D
APPV'D
MFG
Q.A
TITLE:
MATERIAL:
DWG NO.
Nozzle_1
A4
WEIGHT:
SCALE:2:1
SHEET 1 OF 1

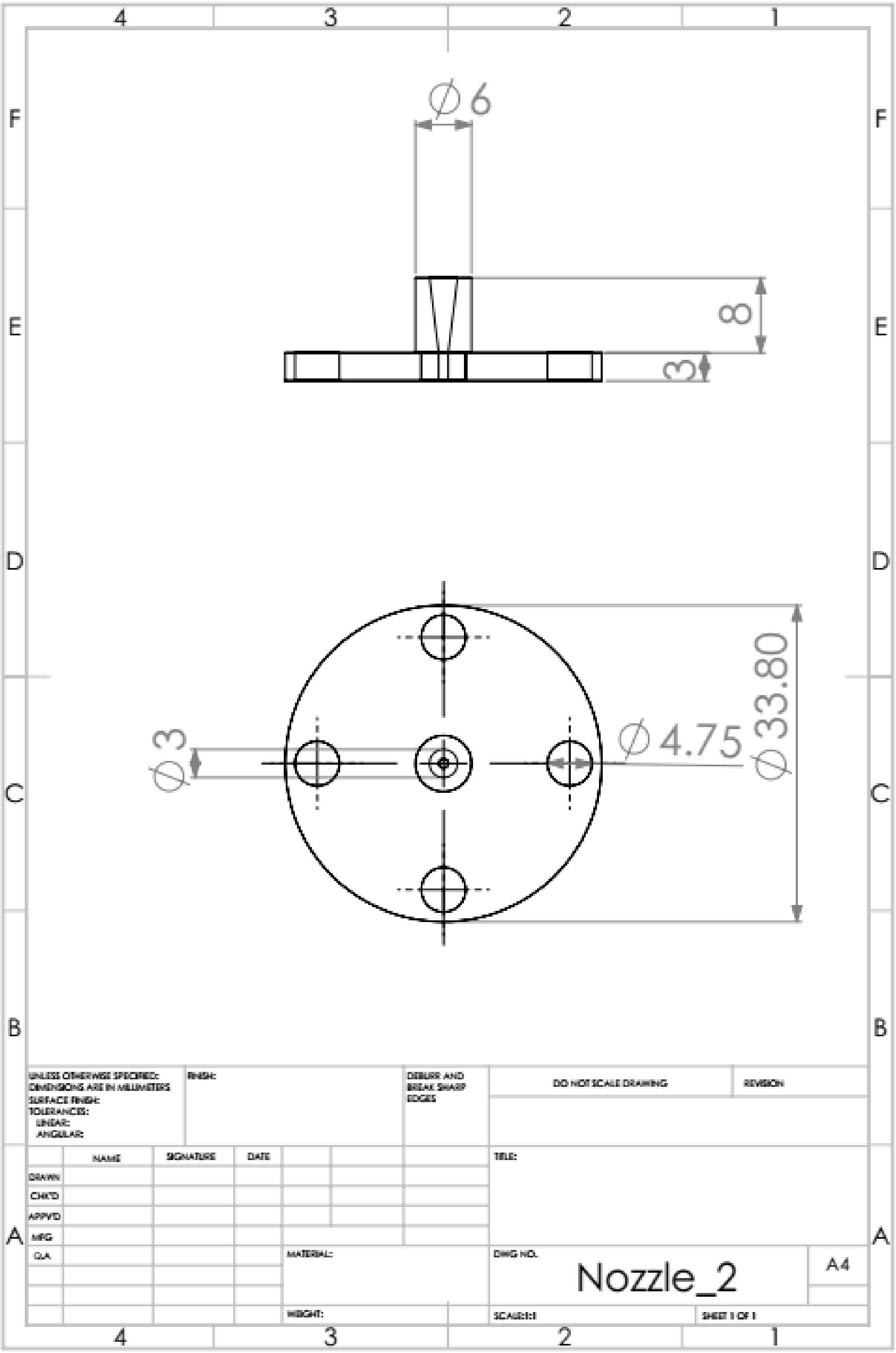
Ø6
8
3
Ø3
Ø4.75
Ø33.80
UNLESS OTHERWISE SPECIFIED:
DIMENSIONS ARE IN MILLIMETERS
SURFACE FINISH:
TOLERANCES:
LINEAR:
ANGULAR:
FINISH:
DEBURR AND BREAK SHARP EDGES
DO NOT SCALE DRAWING
REVISION
NAME
SIGNATURE
DATE
DRAWN
CHK'D
APPV'D
MFG
Q.A
TITLE:
MATERIAL:
WEIGHT:
DWG NO.
Nozzle_2
A4
SCALE:1:1
SHEET 1 OF 1
4
3
2
1
F
E
D
C
B
A

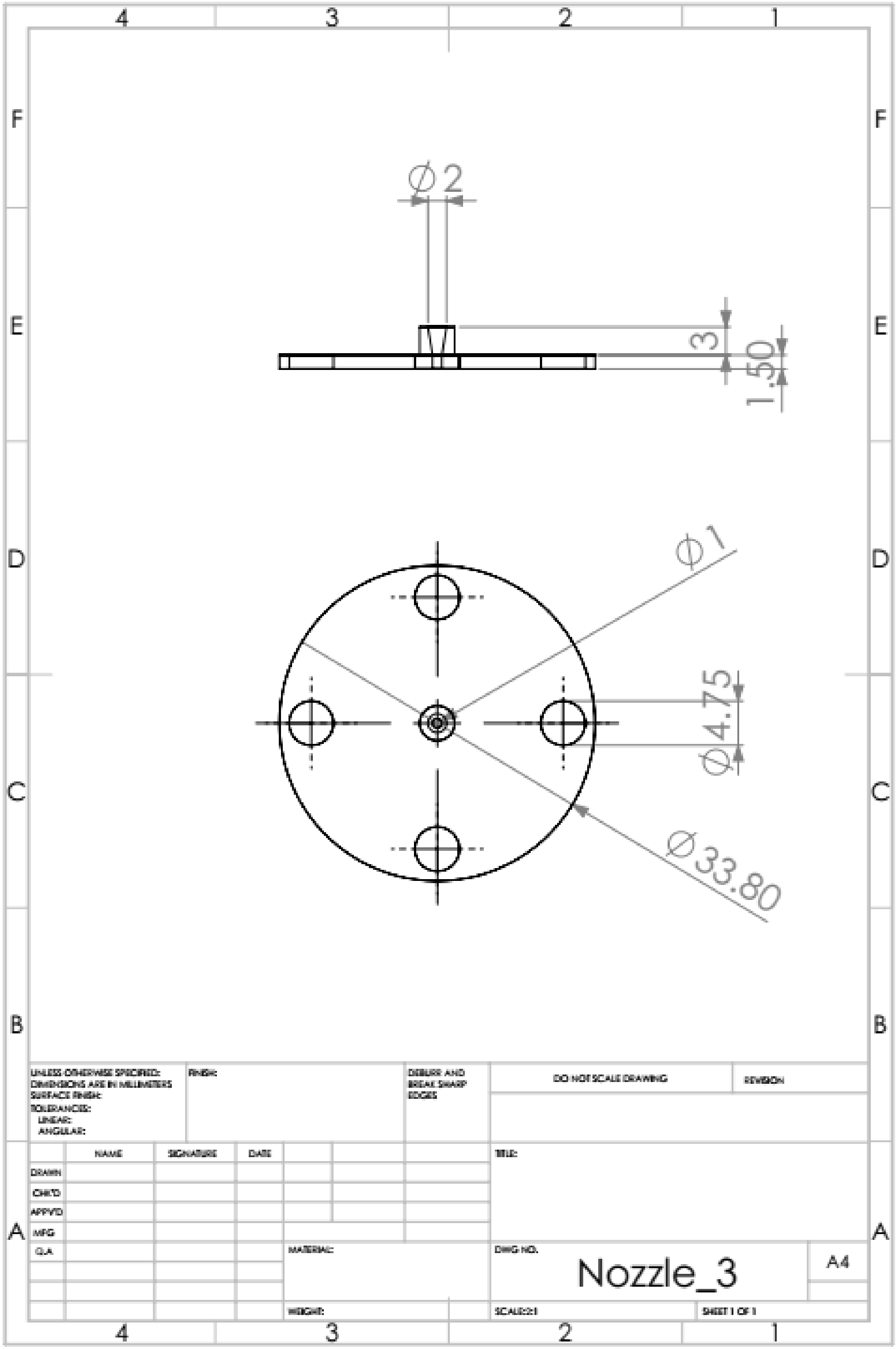
Ø2
3
1.50
Ø1
Ø4.75
Ø33.80
UNLESS OTHERWISE SPECIFIED:
DIMENSIONS ARE IN MILLIMETERS
SURFACE FINISH:
TOLERANCES:
LINEAR:
ANGULAR:
FINISH:
DEBURR AND BREAK SHARP EDGES
DO NOT SCALE DRAWING
REVISION
NAME
SIGNATURE
DATE
DRAWN
CHK'D
APPV'D
MFG
Q.A
MATERIAL:
WEIGHT:
TITLE:
DWG NO.
Nozzle_3
A4
SCALE:2:1
SHEET 1 OF 1
4
3
2
1
F
E
D
C
B
A

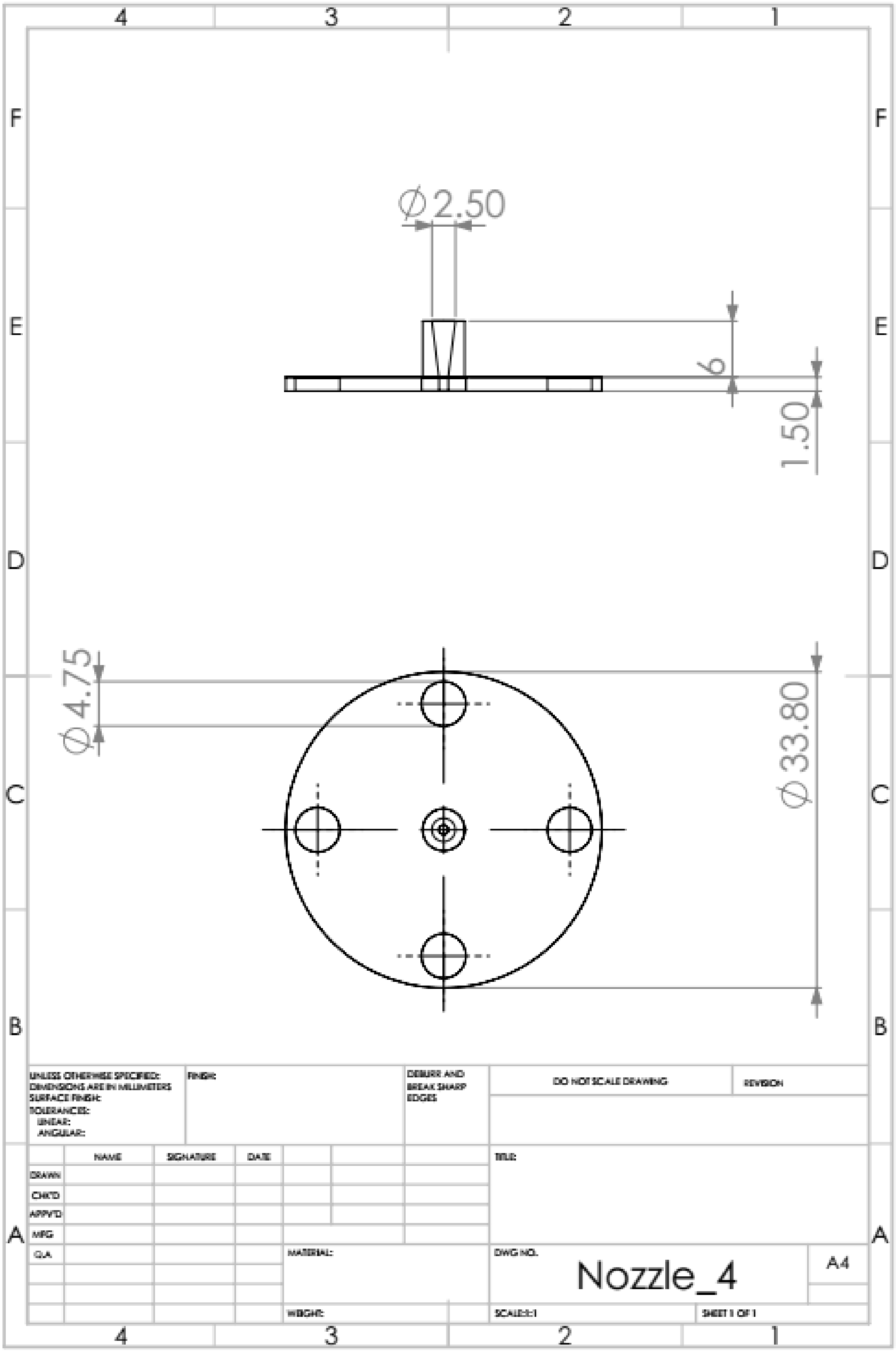
Ø2.50
6
1.50
Ø4.75
Ø33.80
4
3
2
1
F
E
D
C
B
A

UNLESS OTHERWISE SPECIFIED:
DIMENSIONS ARE IN MILLIMETERS
SURFACE FINISH:
TOLERANCES:
LINEAR:
ANGULAR:

FINISH:

DEBURR AND BREAK SHARP EDGES

DO NOT SCALE DRAWING

REVISION

	NAME	SIGNATURE	DATE
DRAWN			
CHK'D			
APPV'D			
MFG			
Q.A			

TITLE:

MATERIAL:

WEIGHT:

DWG NO.

Nozzle_4

A4

SCALE:1:1

SHEET 1 OF 1

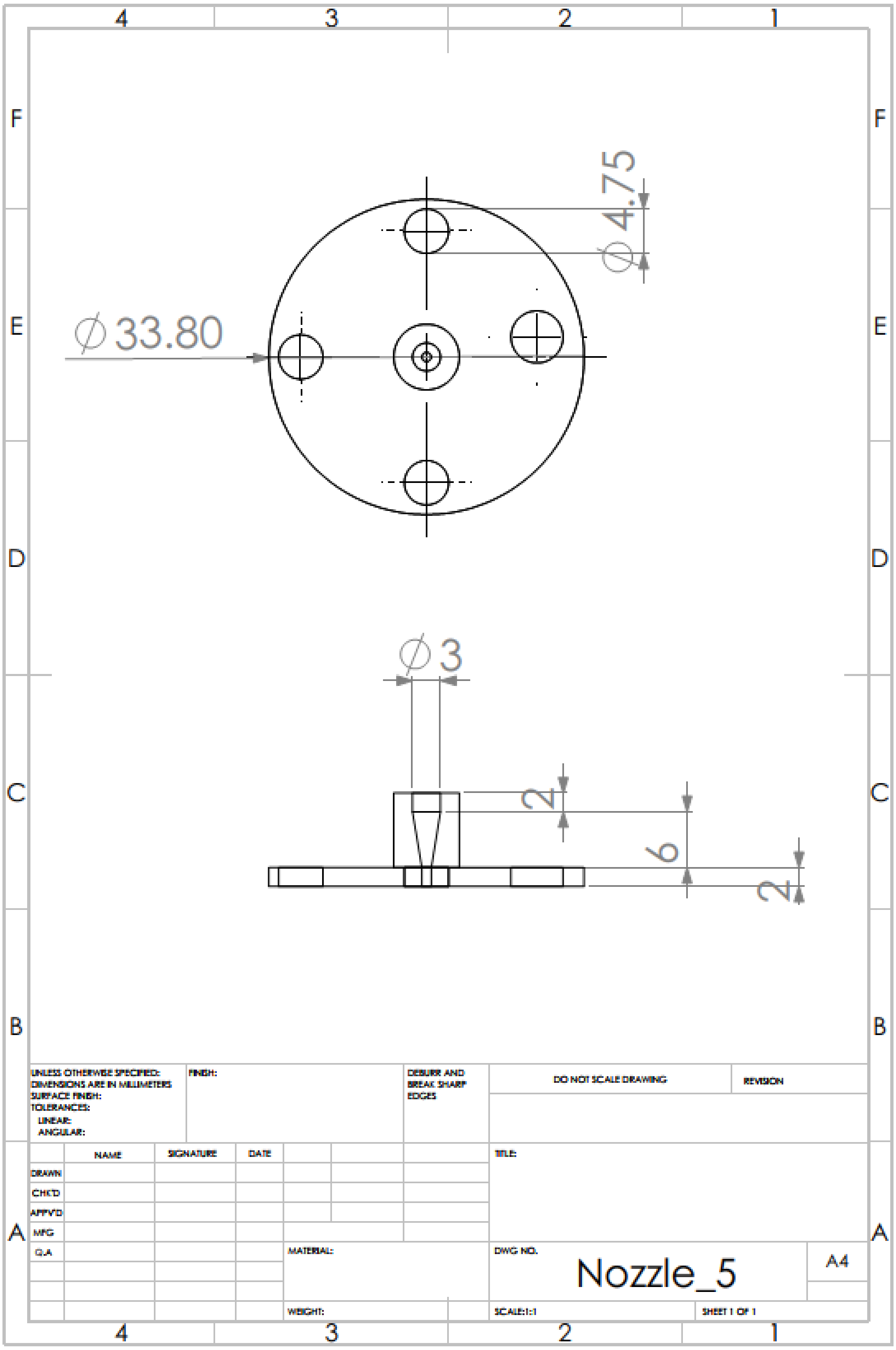

UNLESS OTHERWISE SPECIFIED:
DIMENSIONS ARE IN MILLIMETERS
SURFACE FINISH:
TOLERANCES:
LINEAR:
ANGULAR:

FINISH:

DEBURR AND
BREAK SHARP
EDGES

DO NOT SCALE DRAWING

REVISION

	NAME	SIGNATURE	DATE
DRAWN			
CHK'D			
APPV'D			
MFG			
Q.A			

TITLE:

MATERIAL:

WEIGHT:

DWG NO.

Nozzle_5

A4

SCALE:1:1

SHEET 1 OF 1

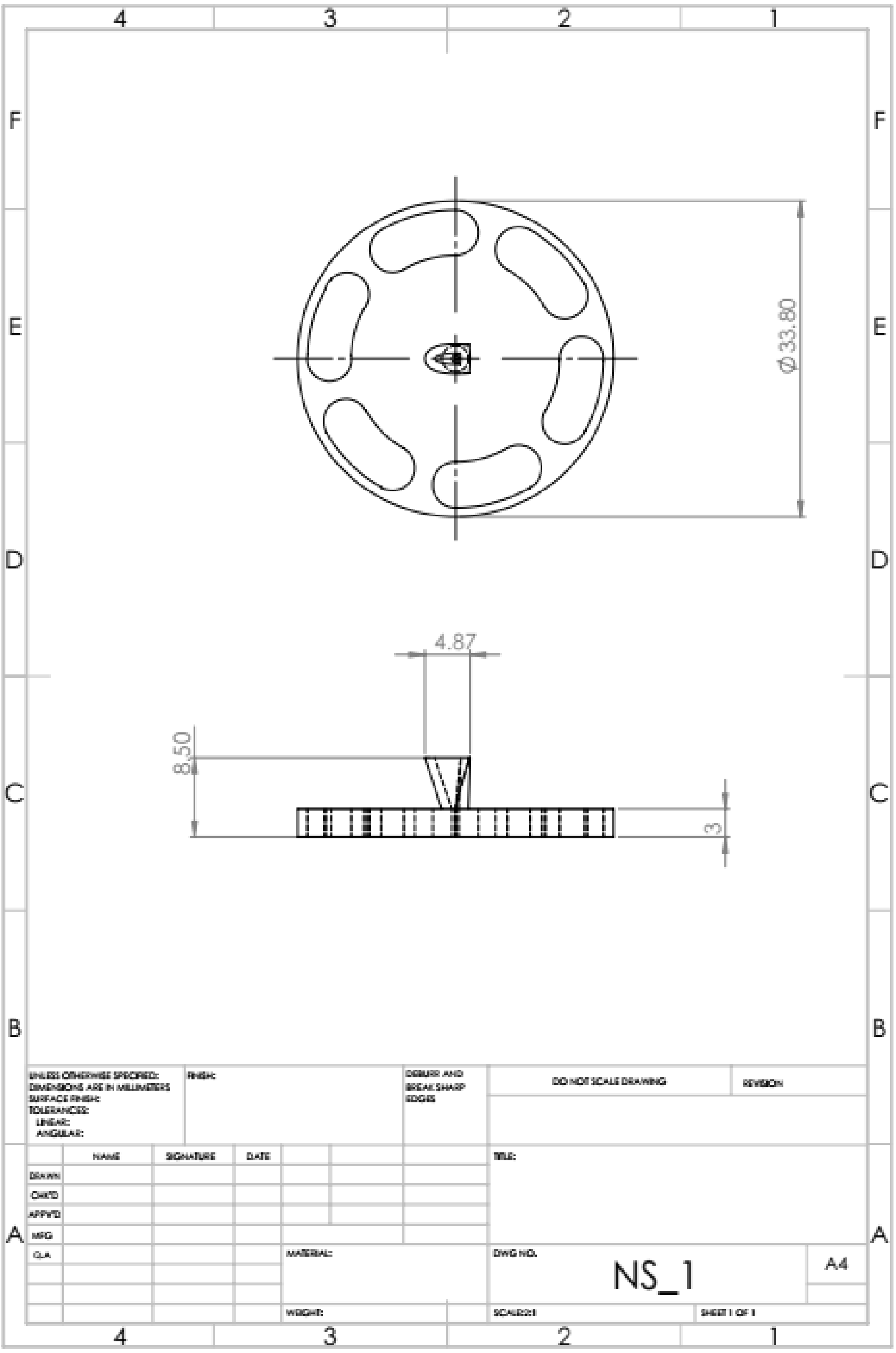
Ø33.80
4.87
8.50
3
UNLESS OTHERWISE SPECIFIED:
DIMENSIONS ARE IN MILLIMETERS
SURFACE FINISH:
TOLERANCES:
LINEAR:
ANGULAR:
FINISH:
DEBURR AND BREAK SHARP EDGES
DO NOT SCALE DRAWING
REVISION
NAME
SIGNATURE
DATE
DRAWN
CHK'D
APPV'D
MFG
Q.A
TITLE:
MATERIAL:
WEIGHT:
DWG NO.
NS_1
A4
SCALE:2:1
SHEET 1 OF 1

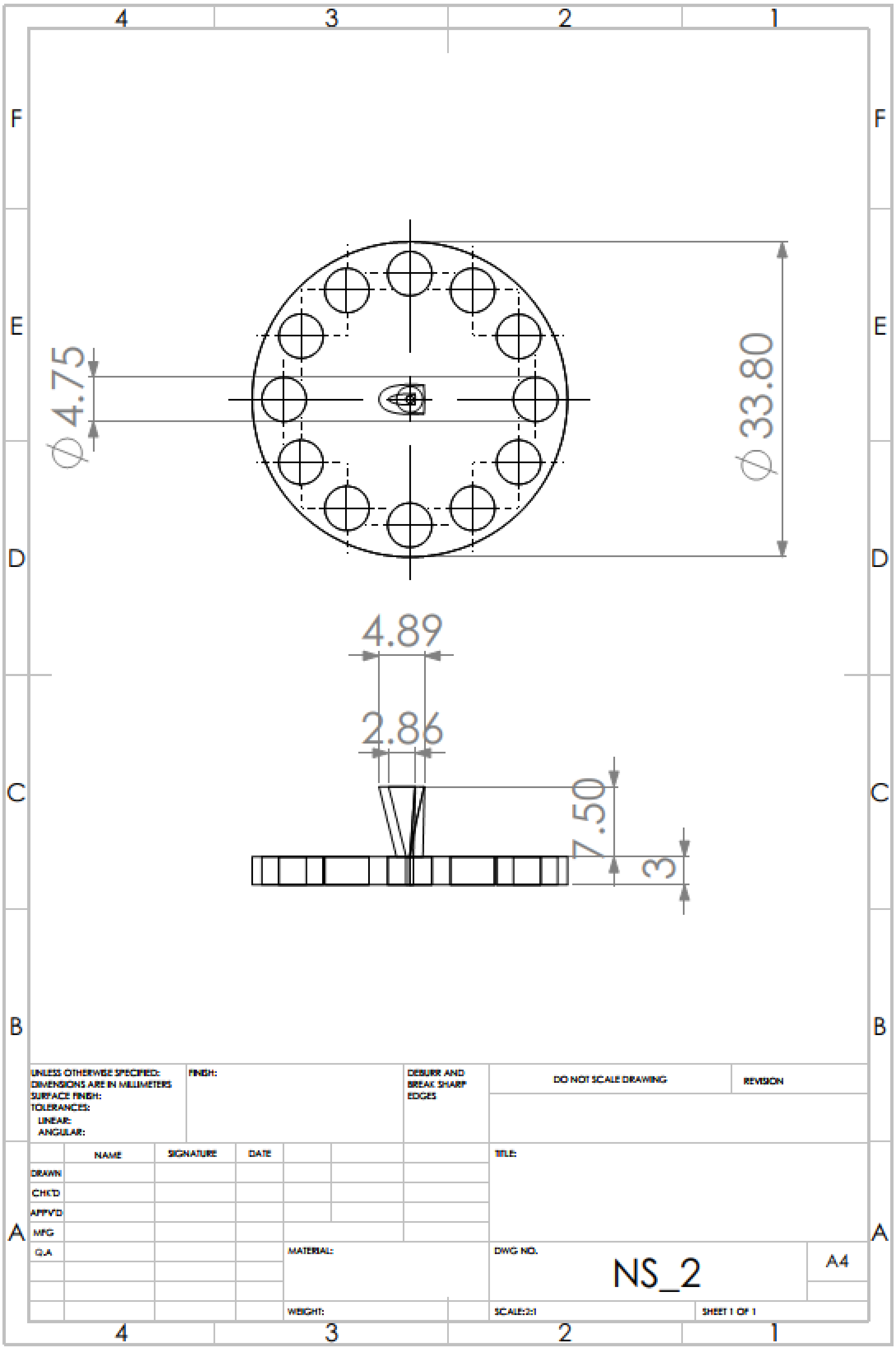
4
3
2
1
F
E
D
C
B
A
ϕ 4.75
ϕ 33.80
4.89
2.86
7.50
3
UNLESS OTHERWISE SPECIFIED:
DIMENSIONS ARE IN MILLIMETERS
SURFACE FINISH:
TOLERANCES:
LINEAR:
ANGULAR:
FINISH:
DEBURR AND BREAK SHARP EDGES
DO NOT SCALE DRAWING
REVISION
NAME
SIGNATURE
DATE
DRAWN
CHK'D
APPV'D
MFG
Q.A
TITLE:
MATERIAL:
DWG NO.
NS_2
A4
WEIGHT:
SCALE:2:1
SHEET 1 OF 1

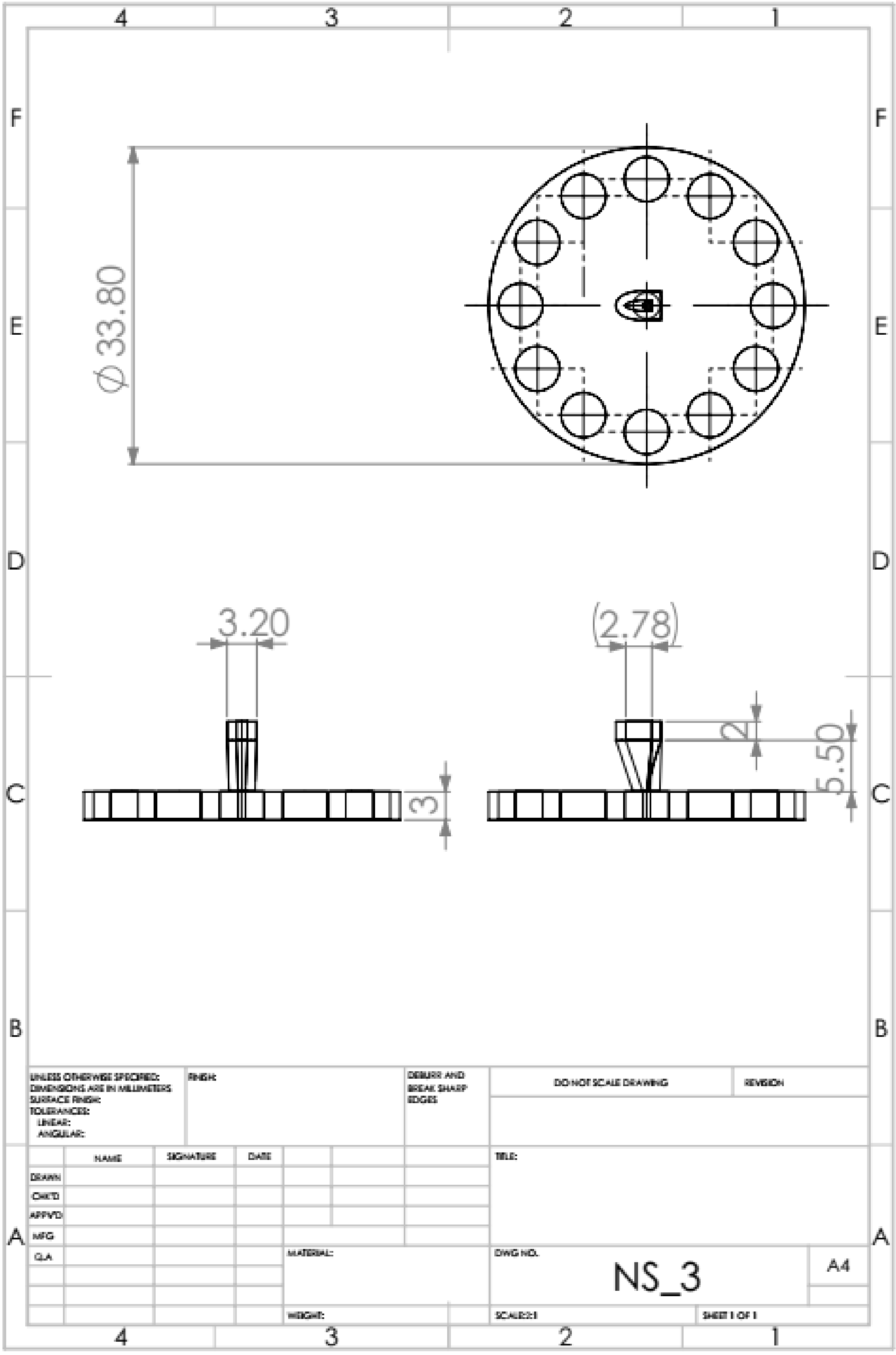
4
3
2
1
F
E
D
C
B
A
∅33.80
3.20
(2.78)
2
5.50
3
UNLESS OTHERWISE SPECIFIED:
DIMENSIONS ARE IN MILLIMETERS
SURFACE FINISH:
TOLERANCES:
LINEAR:
ANGULAR:
FINISH:
DEBURR AND
BREAK SHARP
EDGES
DO NOT SCALE DRAWING
REVISION
NAME
SIGNATURE
DATE
DRAWN
CHK'D
APPV'D
MFG
Q.A
TITLE:
MATERIAL:
WEIGHT:
DWG NO.
NS_3
A4
SCALE:2:1
SHEET 1 OF 1

Funding

03-07/2019

Participation in the project ‘ELI—LASERLAB Europe Synergy, HiPER & IPERION-CH.gr’ (MIS 5002735) which is implemented under the Action ‘Reinforcement of the Research and Innovation Infrastructure’, funded by the Operational Programme ‘Competitiveness, Entrepreneurship and Innovation’ (NSRF 2014-2020) and co-financed by Greece and the European Union (European Regional Development Fund).

Ευρωπαϊκή Ένωση
Ευρωπαϊκό Ταμείο
Περιφερειακής Ανάπτυξης

ΕΛΛΗΝΙΚΗ ΔΗΜΟΚΡΑΤΙΑ
ΥΠΟΥΡΓΕΙΟ
ΑΝΑΠΤΥΞΗΣ ΚΑΙ ΕΠΕΝΔΥΣΕΩΝ
ΕΙΔΙΚΗ ΓΡΑΜΜΑΤΕΙΑ ΔΙΑΧΕΙΡΙΣΗΣ
ΠΡΟΓΡΑΜΜΑΤΩΝ ΕΤΠΑ & ΤΣ
ΕΥΔ ΠΡΟΓΡΑΜΜΑΤΟΣ «ΑΝΤΑΓΩΝΙΣΤΙΚΟΤΗΤΑ»

ΕΠΑνΕΚ 2014-2020
ΕΠΙΧΕΙΡΗΣΙΑΚΟ ΠΡΟΓΡΑΜΜΑ
ΑΝΤΑΓΩΝΙΣΤΙΚΟΤΗΤΑ
ΕΠΙΧΕΙΡΗΜΑΤΙΚΟΤΗΤΑ
ΚΑΙΝΟΤΟΜΙΑ

ΕΣΠΑ
2014-2020
ανάπτυξη - εργασία - αλληλεγγύη

Με τη συγχρηματοδότηση της Ελλάδας και της Ευρωπαϊκής Ένωσης

02/2020 -05/21

Participation in research that was co-financed by Greece and the European Union (European Social Fund-ESF) through the Operational Programme ≪Human Resources Development, Education and Lifelong Learning 2014–2020≫ in the context of the project “Development and optimization of the betatron-type radiation source induced by ulta-intense laser electromagnetic fields” (MIS No. 5048172).

European Union
European Social Fund

Operational Programme
Human Resources Development,
Education and Lifelong Learning
Co-financed by Greece and the European Union

ΕΣΠΑ
2014-2020
ανάπτυξη - εργασία - αλληλεγγύη

05/22-09/23

The implementation of the doctoral thesis was co-financed by Greece and the European Union (European Social Fund-ESF) through the Operational Programme «Human Resources Development, Education and Lifelong Learning» in the context of the Act “Enhancing Human Resources Research Potential by undertaking a Doctoral Research” Sub-action 2: IKY Scholarship Programme for PhD candidates in the Greek Universities.

Ευρωπαϊκή Ένωση
European Social Fund

Operational Programme
Human Resources Development,
Education and Lifelong Learning
Co-financed by Greece and the European Union

ΕΣΠΑ
2014-2020
ανάπτυξη - εργασία - αλληλεγγύη

Bibliography

Akhiezer, A. I., & Polovin, R. V. (1956). Theory of wave motion of an electron plasma. *Soviet Phys. JETP*, *3*.

Albert, F., Pollock, B. B., Chen, Y.-H., Alessi, D., Ralph, J. E., Michel, P. A., & Pak, A. (2013). *Betatron X-rays from a laser wakefield accelerator in the ionization induced trapping regime*.

Anderson, J. D. Jr. (2003). *Modern Compressible Flow* (3d ed.). Mc Graw Hill.

Andreev, N. E., Gorbunov, L. M., Mora, P., & Ramazashvili, R. R. (2007). Filamentation of ultrashort laser pulses propagating in tenuous plasmas. *Physics of Plasmas*, *14*(8). https://doi.org/10.1063/1.2768030

Andrianaki, G., Grigoriadis, A., Beni, s E., & Papadogiannis, N. (2020). Pointing characteristics of x-rays generated by relativistic electron acceleration via 45 TW fs laser-He plasma. *OSA Technical Digest (Optica Publishing Group, 2020)*.

Andrianaki, G., Grigoriadis, A., Skoulakis, A., Tazes, I., Mancelli, D., Fitilis, I., Dimitriou, V., Benis, E. P., Papadogiannis, N. A., Tatarakis, M., & Nikolos, I. K. (2023). Design, manufacturing, evaluation, and performance of a 3D-printed, custom-made nozzle for laser wakefield acceleration experiments. *Review of Scientific Instruments*, *94*(10). https://doi.org/10.1063/5.0169623

Andrianaki, G., Grigoriadis, A., Tazes, I., Fitilis, I., Dimitriou, V., Benis, E. P., Nikolos, I. K., Papadogiannis, N. A., & Tatarakis, M. (2022a). *Custom-made 3d printed nozzles for Laser Wakefield Acceleration (LWFA) experiments in the Institute of Plasma Physics and Lasers (IPPL)*. https://www.prusa3d.com

Andrianaki, G., Grigoriadis, A., Tazes, I., Fitilis, I., Dimitriou, V., Benis, E. P., Nikolos, I. K., Papadogiannis, N. A., & Tatarakis, M. (2022b). The design and performance of an asymmetrical nozzle in Laser Wake Field electron acceleration. *48 Th EPS Plasma Conference* .

Aniculaesei, C. (2015). *Experimental Studies of Laser Plasma Wakefield Acceleration*.

Aniculaesei, C., Kim, H. T., Yoo, B. J., Oh, K. H., & Nam, C. H. (2018). Novel gas target for laser wakefield accelerators. *Review of Scientific Instruments*, *89*(2). https://doi.org/10.1063/1.4993269

Aniculaesei, C., Pathak, V. B., Kim, H. T., Oh, K. H., Yoo, B. J., Brunetti, E., Jang, Y. H., Hojbota, C. I., Shin, J. H., Jeon, J. H., Cho, S., Cho, M. H., Sung, J. H., Lee, S. K., Hegelich, B. M., & Nam, C. H. (2019). Electron energy increase in a laser wakefield accelerator using up-ramp plasma density profiles. *Scientific Reports*, *9*(1). https://doi.org/10.1038/s41598-019-47677-5

Ansys Inc (Ed.). (2013). *Ansys Fluent theory guide*.

Arber, T. D., Bennett, K., Brady, C. S., Lawrence-Douglas, A., Ramsay, M. G., Sircombe, N. J., Gillies, P., Evans, R. G., Schmitz, H., Bell, A. R., & Ridgers, C. P. (2015). Contemporary particle-in-cell approach to laser-plasma modelling. In *Plasma Physics and Controlled Fusion* (Vol. *57*, Issue 11). Institute of Physics Publishing. https://doi.org/10.1088/0741-3335/57/11/113001

Atkinson, D. B., & Smith, M. A. (1995). Design and characterization of pulsed uniform supersonic expansions for chemical applications. *Review of Scientific Instruments*, *66*(9), 4434–4446. https://doi.org/10.1063/1.1145338

Atzeni, S., Batani, D., Danson, C. N., Gizzi, L. A., Le Pape, S., Miquel, J. L., Perlado, M., Scott, R. H. H., Tatarakis, M., Tikhonchuk, V., & Volpe, L. (2022). Breakthrough at the NIF paves the way to inertial fusion energy. *Europhysics News*, *53*(1), 18–23. https://doi.org/10.1051/epn/2022106

Auluck, S., Kubes, P., Paduch, M., Sadowski, M. J., Krauz, V. I., Lee, S., Soto, L., Scholz, M., Miklaszewski, R., Schmidt, H., Blagoev, A., Samuelli, M., Seng, Y. S., Springham, S. V., Talebitaher, A., Pavez, C., Akel, M., Yap, S. L., Verma, R., … Laas, T. (2021). Update on the Scientific Status of the Plasma Focus. In *Plasma* (Vol. 4, Issue 3, pp. 450–669). MDPI. https://doi.org/10.3390/plasma4030033

Bingham, R., Mendonça, J. T., & Shukla, P. K. (2004). Plasma based charged-particle accelerators. In *Plasma Physics and Controlled Fusion* (Vol. 46, Issue 1). https://doi.org/10.1088/0741-3335/46/1/R01

Bolton, P. R., Parodi, K., & Schreiber J. (2018). *Applications of Laser-Driven Particle Acceleration*. http://taylorandfrancis.com

Brandi, F., Giammanco, F., Conti, F., Sylla, F., Lambert, G., & Gizzi, L. A. (2016). Note: Real-time monitoring via second-harmonic interferometry of a flow gas cell for laser wakefield acceleration. *Review of Scientific Instruments*, *87*(8). https://doi.org/10.1063/1.4960399

Brijesh, P., Thaury, C., Phuoc, K. T., Corde, S., Lambert, G., Malka, V., Mangles, S. P. D., Bloom, M., & Kneip, S. (2012). Tuning the electron energy by controlling the density perturbation position in laser plasma accelerators. *Physics of Plasmas*, *19*(6). https://doi.org/10.1063/1.4725421

Buck, A., Wenz, J., Xu, J., Khrennikov, K., Schmid, K., Heigoldt, M., Mikhailova, J. M., Geissler, M., Shen, B., Krausz, F., Karsch, S., & Veisz, L. (2013). Shock-front injector for high-quality laser-plasma acceleration. *Physical Review Letters*, *110*(18). https://doi.org/10.1103/PhysRevLett.110.185006

Bulanov, S., Naumova, N., Pegoraro, F., & Sakai, J. (1998). *Particle injection into the wave acceleration phase due to nonlinear wake wave breaking*.

Chen, F. F. (1983). *Introduction to Plasma Physics and Controlled Fusion* (third). Springer.

Chen, L. M., Yan, W. C., Li, D. Z., Hu, Z. D., Zhang, L., Wang, W. M., Hafz, N., Mao, J. Y., Huang, K., Ma, Y., Zhao, J. R., Ma, J. L., Li, Y. T., Lu, X., Sheng, Z. M., Wei, Z. Y., Gao, J., & Zhang, J. (2013). Bright betatron X-ray radiation from a laser-driven-clustering gas target. *Scientific Reports*, *3*. https://doi.org/10.1038/srep01912

Clark, E. L., Grigoriadis, A., Petrakis, S., Tazes, I., Andrianaki, G., Skoulakis, A., Orphanos, Y., Kaselouris, E., Fitilis, I., Chatzakis, J., Bakarezos, E., Dimitriou, V., Benis, E. P., Papadogiannis, N. A., & Tatarakis, M. (2021). High-intensity laser-driven secondary radiation sources using the ZEUS 45 TW laser system at the Institute of Plasma Physics and Lasers of the Hellenic Mediterranean University Research Centre. *High Power Laser Science and Engineering*, *9*. https://doi.org/10.1017/hpl.2021.38

Clark, E. L., Krushelnick, K., Davies, J. R., Zepf, M., Tatarakis, M., Beg, F. N., Machacek, A., Norreys, P. A., Santala, M. I. K., Watts, I., & Dangor, A. E. (2000). *Measurements of Energetic Proton Transport through Magnetized Plasma from Intense Laser Interactions with Solids*.

Cole, J. M., Wood, J. C., Lopes, N. C., Poder, K., Abel, R. L., Alatabi, S., Bryant, J. S. J., Jin, A., Kneip, S., Mecseki, K., Symes, D. R., Mangles, S. P. D., & Najmudin, Z. (2015). Laser-wakefield accelerators as hard x-ray sources for 3D medical imaging of human bone. *Scientific Reports*, *5*. https://doi.org/10.1038/srep13244

Conner, B. P., Manogharan, G. P., Martof, A. N., Rodomsky, L. M., Rodomsky, C. M., Jordan, D. C., & Limperos, J. W. (2014). Making sense of 3-D printing: Creating a map of additive manufacturing products and services. *Additive Manufacturing*, *1*, 64–76. https://doi.org/10.1016/j.addma.2014.08.005

Corde, S., Ta Phuoc, K., Lambert, G., Fitour, R., Malka, V., Rousse, A., Beck, A., & Lefebvre, E. (2013). Femtosecond x rays from laser-plasma accelerators. *Reviews of Modern Physics*, *85*(1), 1–48. https://doi.org/10.1103/RevModPhys.85.1

Corde, S., Thaury, C., Phuoc, K. T., Lifschitz, A., Lambert, G., Lundh, O., Brijesh, P., Arantchuk, L., Sebban, S., Rousse, A., Faure, J., & Malka, V. (2012). Betatron emission as a diagnostic for injection and acceleration mechanisms in laser plasma accelerators. *Plasma Physics and Controlled Fusion*, *54*(12). https://doi.org/10.1088/0741-3335/54/12/124023

Couperus, J. P., Köhler, A., Wolterink, T. A. W., Jochmann, A., Zarini, O., Bastiaens, H. M. J., Boller, K. J., Irman, A., & Schramm, U. (2016). Tomographic characterisation of gas-jet targets for laser wakefield acceleration. *Nuclear Instruments and Methods in Physics Research, Section A: Accelerators, Spectrometers, Detectors and Associated Equipment*, *830*, 504–509. https://doi.org/10.1016/j.nima.2016.02.099

Couperus, J. P., Pausch, R., Köhler, A., Zarini, O., Krämer, J. M., Garten, M., Huebl, A., Gebhardt, R., Helbig, U., Bock, S., Zeil, K., Debus, A., Bussmann, M., Schramm, U., & Irman, A. (2017a). Demonstration of a beam loaded nanocoulomb-class laser wakefield accelerator. *Nature Communications*, *8*(1). https://doi.org/10.1038/s41467-017-00592-7

Couperus, J. P., Pausch, R., Köhler, A., Zarini, O., Krämer, J. M., Garten, M., Huebl, A., Gebhardt, R., Helbig, U., Bock, S., Zeil, K., Debus, A., Bussmann, M., Schramm, U., & Irman, A. (2017b). Demonstration of a beam loaded nanocoulomb-class laser wakefield accelerator. *Nature Communications*, *8*(1). https://doi.org/10.1038/s41467-017-00592-7

Cros, B. (2014). Laser-driven plasma Wakefield: Propagation effects. *CAS-CERN Accelerator School: Plasma Wake Acceleration 2014, Proceedings*, 207–230. https://doi.org/10.5170/CERN-2016-001.207

Dawson, J. M. (1959). *Electron Oscillations in a Cold Plasma* (Vol. 113, Issue 2). Nonlinear.

Decker, C. D., Mori, W. B., Tzeng, K. C., & Katsouleas, T. (1996). The evolution of ultra-intense, short-pulse lasers in underdense plasmas. *Physics of Plasmas*, *3*(5), 2047–2056. https://doi.org/10.1063/1.872001

Döpp, A., Guillaume, E., Thaury, C., Gautier, J., Ta Phuoc, K., & Malka, V. (2016). 3D printing of gas jet nozzles for laser-plasma accelerators. *Review of Scientific Instruments*, *87*(7). https://doi.org/10.1063/1.4958649

Ekerfelt, H., Hansson, M., Gallardo González, I., Davoine, X., & Lundh, O. (2017). A tunable electron beam source using trapping of electrons in a density down-ramp in laser wakefield acceleration. *Scientific Reports*, *7*(1). https://doi.org/10.1038/s41598-017-12560-8

Esarey, E., Schroeder, C. B., & Leemans, W. P. (2009). Physics of laser-driven plasma-based electron accelerators. *Reviews of Modern Physics*, *81*(3), 1229–1285. https://doi.org/10.1103/RevModPhys.81.1229

Fan-Chiang, L., Mao, H. S., Tsai, H. E., Ostermayr, T., Swanson, K. K., Barber, S. K., Steinke, S., Van Tilborg, J., Geddes, C. G. R., & Leemans, W. P. (2020). Gas density structure of supersonic flows impinged on by thin blades for laser-plasma accelerator targets. *Physics of Fluids*, *32*(6). https://doi.org/10.1063/5.0005888

Faure, J. (2014). Plasma injection schemes for laser-plasma accelerators. *CAS-CERN Accelerator School: Plasma Wake Acceleration 2014, Proceedings*, 143–157. https://doi.org/10.5170/CERN-2016-001.143

Faure, J., Rechatin, C., Lundh, O., Ammoura, L., & Malka, V. (2010). Injection and acceleration of quasimonoenergetic relativistic electron beams using density gradients at the edges of a plasma channel. *Physics of Plasmas*, *17*(8). https://doi.org/10.1063/1.3469581

Faure, J., Rechatin, C., Norlin, A., Lifschitz, A., Glinec, Y., & Malka, V. (2006). Controlled injection and acceleration of electrons in plasma wakefields by colliding laser pulses. *Nature*, *444*(7120), 737–739. https://doi.org/10.1038/nature05393

Ferri, J., Corde, S., Döpp, A., Lifschitz, A., Doche, A., Thaury, C., Ta Phuoc, K., Mahieu, B., Andriyash, I. A., Malka, V., & Davoine, X. (2018). High-Brilliance Betatron γ - Ray Source Powered by Laser-Accelerated Electrons. *Physical Review Letters*, *120*(25). https://doi.org/10.1103/PhysRevLett.120.254802

Fill, E. E. (1994). *Focusing limits of ultrashort laser pulses: analytical theory* (Vol. 11).

Fitilis, I., Grigoriadis, A., Tazes, I., Petrakis, S., Andrianaki, G., Dimitriou, V., Bakarezos, E., Benis, E. P., Tsiapa, I., Boursianis, T., Kalaitzakis, G., Bontzos, G., Liakopoulos, D., Pappas, E., Detorakis, E., Clark, E. L., Maris, T. G., Papadogiannis, N. A., & Tatarakis, M. (n.d.). *Polymer-gel radiation dosimetry of laser-based relativistic electron sources for biomedical applications*. www.ippl.hmu.gr

Fourmaux, S., Kieffer, J.-C., & Krol, A. (2017). Ultrahigh resolution and brilliance laser wakefield accelerator betatron x-ray source for rapid in vivo tomographic microvasculature imaging in small animal models . *Medical Imaging 2017: Biomedical Applications in Molecular, Structural, and Functional Imaging*, *10137*, 1013715. https://doi.org/10.1117/12.2255080

Franquet, E., Perrier, V., Bruel, P., & Gibout, S. (2015). *Review on the underexpanded jets Greenhouse thermal design View project Thermal storage for eco-efficient process View project Free underexpanded jets in a quiescent medium: A Review*. https://doi.org/10.13140/RG.2.1.2640.6883

Freeman Mark P., & Katz S. (1963). Determination of a Radiance-Coefficient Profile from the Observed Asymmetric Radiance Distribution of an Optically Thin Radiating Medium,. *Journal of Optical Society of America*, *15*.

Geddes, C. G. R., Toth, C., Van Tilborg, J., Esarey, E., Schroeder, C. B., Bruhwiler, D., Nieter, C., Cary, J., & Leemans, W. P. (2004a). High-quality electron beams from a laser wakefield accelarator using plasma-channel guiding. *Nature*, *431*(7008), 538–541. https://doi.org/10.1038/nature02900

Geddes, C. G. R., Toth, C., Van Tilborg, J., Esarey, E., Schroeder, C. B., Bruhwiler, D., Nieter, C., Cary, J., & Leemans, W. P. (2004b). High-quality electron beams from a laser wakefield accelarator using plasma-channel guiding. *Nature*, *431*(7008), 538–541. https://doi.org/10.1038/nature02900

Gibbon, P. (2005). *Short pulse laser interactions with matter: an introduction*. Imperial College Press.

Golovin, G., Banerjee, S., Chen, S., Powers, N., Liu, C., Yan, W., Zhang, J., Zhang, P., Zhao, B., & Umstadter, D. (2016). Control and optimization of a staged laser-wakefield accelerator. *Nuclear Instruments and Methods in Physics Research, Section A: Accelerators, Spectrometers, Detectors and Associated Equipment*, *830*, 375–380. https://doi.org/10.1016/j.nima.2016.06.022

Golovin, G., Chen, S., Powers, N., Liu, C., Banerjee, S., Zhang, J., Zeng, M., Sheng, Z., & Umstadter, D. (2015). Tunable monoenergetic electron beams from independently controllable laser-wakefield acceleration and injection. *Physical Review Special Topics - Accelerators and Beams*, *18*(1). https://doi.org/10.1103/PhysRevSTAB.18.011301

Gonsalves, A. J., Nakamura, K., Daniels, J., Benedetti, C., Pieronek, C., De Raadt, T. C. H., Steinke, S., Bin, J. H., Bulanov, S. S., Van Tilborg, J., Geddes, C. G. R., Schroeder, C. B., Tóth, C., Esarey, E., Swanson, K., Fan-Chiang, L., Bagdasarov, G., Bobrova, N., Gasilov, V., … Leemans, W. P. (2019). Petawatt Laser Guiding and Electron Beam Acceleration to 8 GeV in a Laser-Heated Capillary Discharge Waveguide. *Physical Review Letters*, *122*(8). https://doi.org/10.1103/PhysRevLett.122.084801

Gonsalves, A. J., Nakamura, K., Lin, C., Panasenko, D., Shiraishi, S., Sokollik, T., Benedetti, C., Schroeder, C. B., Geddes, C. G. R., Van Tilborg, J., Osterhoff, J., Esarey, E., Toth, C., & Leemans, W. P. (2011). Tunable laser plasma accelerator based on longitudinal density tailoring. *Nature Physics*, *7*(11), 862–866. https://doi.org/10.1038/nphys2071

Gordon, D. F., Hafizi, B., Hubbard, R. F., Peñano, J. R., Sprangle, P., & Ting, A. (2003). Asymmetric Self-Phase Modulation and Compression of Short Laser Pulses in Plasma Channels. *Physical Review Letters*, *90*(21), 4. https://doi.org/10.1103/PhysRevLett.90.215001

Grigoriadis, A., Andrianaki, G., Fitilis, I., Dimitriou, V., Clark, E. L., Papadogiannis, N. A., Benis, E. P., & Tatarakis, M. (2022). Improving a high-power laser-based relativistic electron source: The role of laser pulse contrast and gas jet density profile. *Plasma Physics and Controlled Fusion*, *64*(4). https://doi.org/10.1088/1361-6587/ac4b06

Grigoriadis, A., Andrianaki, G., Tatarakis, M., Benis, E. P., & Papadogiannis, N. A. (2021). Betatron-type laser-plasma x-ray sources generated in multi-electron gas targets. *Applied Physics Letters*, *118*(13). https://doi.org/10.1063/5.0046184

Grigoriadis, A., Andrianaki, G., Tatarakis, M., Benis, E. P., & Papadogiannis, N. A. (2023). The role of laser chirp in relativistic electron acceleration using multi-electron gas targets. *Plasma Physics and Controlled Fusion*, *65*(4). https://doi.org/10.1088/1361-6587/acbb25

Grigoriadis, A., Andrianaki, G., Tazes, I., Dimitriou, V., Tatarakis, M., Benis, E. P., & Papadogiannis, N. A. (2023). Efficient plasma electron accelerator driven by linearly chirped multi-10-TW laser pulses. *Scientific Reports*, *13*(1), 2918. https://doi.org/10.1038/s41598-023-28755-1

Grigoriadis Anastasios. (2023). *Acceleration of Electrons to Relativistic Velocities Using an Ultra-Intense Laser* [PhD]. University of Ioannina.

Guillaume, E., Döpp, A., Thaury, C., Lifschitz, A., Grittani, G., Goddet, J., Tafzi, A., Chou, S. W., Veisz, L., Malka, V., & Electron, al. (2015a). *Electron Rephasing in a Laser-Wakefield Accelerator*. https://doi.org/10.1103/PhysRevLett.115.155002ï

Guillaume, E., Döpp, A., Thaury, C., Lifschitz, A., Grittani, G., Goddet, J., Tafzi, A., Chou, S. W., Veisz, L., Malka, V., & Electron, al. (2015b). *Electron Rephasing in a Laser-Wakefield Accelerator*. https://doi.org/10.1103/PhysRevLett.115.155002ï

Hafz, N., Lee, H. J., Kim, J. U., Kim, G. H., Suk, H., & Lee, J. (2003). Femtosecond X-Ray Generation via the Thomson Scattering of a Terawatt Laser From Electron Bunches Produced From the LWFA Utilizing a Plasma Density Transition. *IEEE Transactions on Plasma Science*, *31*(6 II), 1388–1394. https://doi.org/10.1109/TPS.2003.820680

Haines, M. G. (2011). A review of the dense Z-pinch. In *Plasma Physics and Controlled Fusion* (Vol. 53, Issue 9). https://doi.org/10.1088/0741-3335/53/9/093001

Hansson, M., Aurand, B., Davoine, X., Ekerfelt, H., Svensson, K., Persson, A., Wahlström, C. G., & Lundh, O. (2015). Down-ramp injection and independently controlled acceleration of electrons in a tailored laser wakefield accelerator. *Physical Review Special Topics - Accelerators and Beams*, *18*(7). https://doi.org/10.1103/PhysRevSTAB.18.071303

He, Z. H., Thomas, A. G. R., Beaurepaire, B., Nees, J. A., Hou, B., Malka, V., Krushelnick, K., & Faure, J. (2013). Electron diffraction using ultrafast electron bunches from a laser-wakefield accelerator at kHz repetition rate. *Applied Physics Letters*, *102*(6). https://doi.org/10.1063/1.4792057

Hemker, R. G., Hafz, N. M., & Uesaka, M. (2002). Computer simulations of a single-laser double-gas-jet wakefield accelerator concept. *Physical Review Special Topics - Accelerators and Beams*, *5*(4), 8–15. https://doi.org/10.1103/PhysRevSTAB.5.041301

Henares, J. L., Puyuelo-Valdes, P., Hannachi, F., Ceccotti, T., Ehret, M., Gobet, F., Lancia, L., Marquès, J. R., Santos, J. J., Versteegen, M., & Tarisien, M. (2019). Development of gas jet targets for laser-plasma experiments at near-critical density. *Review of Scientific Instruments*, *90*(6). https://doi.org/10.1063/1.5093613

Herman, G. T. (1980). *Image Reconstruction from Projections. The Fundamentals of Computerized Tomography*. Academic Press.

Hidding, B., Beaton, A., Boulton, L., Corde, S., Doepp, A., Habib, F. A., Heinemann, T., Irman, A., Karsch, S., Kirwan, G., Knetsch, A., Manahan, G. G., de laOssa, A. M., Nutter, A., Scherkl, P., Schramm, U., & Ullmann, D. (2019). Fundamentals and applications of hybrid LWFA-PWFA. *Applied Sciences (Switzerland)*, *9*(13). https://doi.org/10.3390/app9132626

Hipp, M., Woisetschläger, J., Reiterer, P., & Neger, T. (2004). Digital evaluation of interferograms. *Measurement: Journal of the International Measurement Confederation*, *36*(1), 53–66. https://doi.org/10.1016/j.measurement.2004.04.003

https://aerospaceweb.org. (n.d.).

https://henke.lbl.gov/optical_constants/. (n.d.).

https://home.cern/science/accelerators/future-circular-collider. (n.d.).

https://ippl.hmu.gr/. (n.d.). Https://Ippl.Hmu.Gr/.

https://www.engineeringtoolbox.com/. (n.d.).

https://www.engineeringtoolbox.com/refractive-index-d_1264.html. (n.d.).

https://www.engineersedge.com. (n.d.).

https://www.spectra-physics.com/en/f/synergy-femtosecond-oscillator. (n.d.). Https://Www.Spectra-Physics.Com/En/f/Synergy-Femtosecond-Oscillator.

Huang, K., Li, Y. F., Li, D. Z., Chen, L. M., Tao, M. Z., Ma, Y., Zhao, J. R., Li, M. H., Chen, M., Mirzaie, M., Hafz, N., Sokollik, T., Sheng, Z. M., & Zhang, J. (2016). Resonantly Enhanced Betatron Hard X-rays from Ionization Injected Electrons in a Laser Plasma Accelerator. *Scientific Reports*, *6*. https://doi.org/10.1038/srep27633

Hue, C., WAN, Y., Levine, E., & Malka, V. (2022). *Control of electron beam current, charge and energy spread using density downramp injection in laser wakefield accelerators*. http://arxiv.org/abs/2209.04853

Huntington, C. M., Thomas, A. G. R., McGuffey, C., Matsuoka, T., Chvykov, V., Kalintchenko, G., Kneip, S., Najmudin, Z., Palmer, C., Yanovsky, V., Maksimchuk, A., Drake, R. P., Katsouleas, T., & Krushelnick, K. (2011). Current filamentation instability in laser wakefield accelerators. *Physical Review Letters*, *106*(10). https://doi.org/10.1103/PhysRevLett.106.105001

Inman, J. A., Danehy, P. M., Nowak, R. J., & Alderfer, d. W. (2009). The Effect of Impingement on Transitional Behavior in Underexpanded Jets. *47th AIAA Aerospace Sciences Meeting and Exhibit*.

J. O. Hirschfelder, C. F. Curtiss, & R. B. Bird. (1954). *Molecular Theory of Gases and Liquids*. John Wiley & Sons.

Jackson J. D. (1977). *Classical Electrodynamics* (Inc. John Wiley & Sons, Ed.).

Jackson, J. D., & Okun, L. B. (2001). *Historical roots of gauge invariance*.

Jinchuan JU. (2013). *Electron acceleration and betatron radiation driven by laser wakefield inside dielectric capillary tubes*. Universite Paris-Sud.

Joshi, C., Corde, S., & Mori, W. B. (2020). Perspectives on the generation of electron beams from plasma-based accelerators and their near and long term applications. In *Physics of Plasmas* (Vol. 27, Issue 7). American Institute of Physics Inc. https://doi.org/10.1063/5.0004039

Kim, J. U., Hafz, N., & Suk, H. (2004). Electron trapping and acceleration across a parabolic plasma density profile. *Physical Review E - Statistical, Nonlinear, and Soft Matter Physics*, *69*(2 2). https://doi.org/10.1103/PhysRevE.69.026409

Kmecova, M., Sikula, O., & Krajcik, M. (2019). Circular Free Jets: CFD Simulations with Various Turbulence Models and Their Comparison with Theoretical Solutions. *IOP Conference Series: Materials Science and Engineering*, *471*(6). https://doi.org/10.1088/1757-899X/471/6/062045

Kokurewicz, K., Brunetti, E., Welsh, G. H., Wiggins, S. M., Boyd, M., Sorensen, A., Chalmers, A. J., Schettino, G., Subiel, A., DesRosiers, C., & Jaroszynski, D. A. (2019a). Focused very high-energy electron beams as a novel radiotherapy modality for producing high-dose volumetric elements. *Scientific Reports*, *9*(1). https://doi.org/10.1038/s41598-019-46630-w

Kokurewicz, K., Brunetti, E., Welsh, G. H., Wiggins, S. M., Boyd, M., Sorensen, A., Chalmers, A. J., Schettino, G., Subiel, A., DesRosiers, C., & Jaroszynski, D. A. (2019b). Focused very high-energy electron beams as a novel radiotherapy modality for producing high-dose volumetric elements. *Scientific Reports*, *9*(1). https://doi.org/10.1038/s41598-019-46630-w

Kononenko, O., Lopes, N. C., Cole, J. M., Kamperidis, C., Mangles, S. P. D., Najmudin, Z., Osterhoff, J., Poder, K., Rusby, D., Symes, D. R., Warwick, J., Wood, J. C., & Palmer, C. A. J. (2016). 2D hydrodynamic simulations of a variable length gas target for density down-ramp injection of electrons into a laser wakefield accelerator. *Nuclear Instruments and Methods in Physics Research, Section A: Accelerators, Spectrometers, Detectors and Associated Equipment*, *829*, 125–129. https://doi.org/10.1016/j.nima.2016.03.104

Kostyukov, I., Nerush, E., Pukhov, A., & Seredov, V. (2009). Electron self-Injection in multidimensional relativistic-plasma wake fields. *Physical Review Letters*, *103*(17). https://doi.org/10.1103/PhysRevLett.103.175003

Kruer William. (2003). *The Physics of Laser Plasma Ineractions*. Westview Press.

Kurz, T., Couperus, J. P., Krämer, J. M., Ding, H., Kuschel, S., Köhler, A., Zarini, O., Hollatz, D., Schinkel, D., D'Arcy, R., Schwinkendorf, J. P., Osterhoff, J., Irman, A., Schramm, U., & Karsch, S. (2018). Calibration and cross-laboratory implementation of scintillating screens for electron bunch charge determination. In *Review of Scientific Instruments* (Vol. 89, Issue 9). American Institute of Physics Inc. https://doi.org/10.1063/1.5041755

Labate, L., Palla, D., Panetta, D., Avella, F., Baffigi, F., Brandi, F., Di Martino, F., Fulgentini, L., Giulietti, A., Köster, P., Terzani, D., Tomassini, P., Traino, C., & Gizzi, L. A. (2020a). Toward an effective use of laser-driven very high energy electrons for radiotherapy: Feasibility assessment of multi-field and intensity modulation irradiation schemes. *Scientific Reports*, *10*(1). https://doi.org/10.1038/s41598-020-74256-w

Labate, L., Palla, D., Panetta, D., Avella, F., Baffigi, F., Brandi, F., Di Martino, F., Fulgentini, L., Giulietti, A., Köster, P., Terzani, D., Tomassini, P., Traino, C., & Gizzi, L. A. (2020b). Toward an effective use of laser-driven very high energy electrons for radiotherapy: Feasibility assessment of multi-field and intensity modulation irradiation schemes. *Scientific Reports*, *10*(1). https://doi.org/10.1038/s41598-020-74256-w

Landgraf, B., Schnell, M., Svert, A., Kaluza, M. C., & Spielmann, C. (2011). High resolution 3D gas-jet characterization. *Review of Scientific Instruments*, *82*(8). https://doi.org/10.1063/1.3624694

Laney, B. C. (1998). *Computational Gasdynamics* (first). Cambridge University Press.

Leemans, W. P., Nagler, B., Gonsalves, A. J., Tóth, C., Nakamura, K., Geddes, C. G. R., Esarey, E., Schroeder, C. B., & Hooker, S. M. (2006). GeV electron beams from a centimetre-scale accelerator. *Nature Physics*, *2*(10), 696–699. https://doi.org/10.1038/nphys418

Lemos, N., Albert, F., Shaw, J. L., Papp, D., King, P., Milder, A. L., Marsh, K. A., Pak, A., Joshi, C., Polanek, R., Pollock, B. B., Hegelich, B. M., Moody, J. D., Park, J., Tommasini, R., Williams, G. J., & Chen, H. (2017). *Bremsstrahlung x/gamma-ray source driven by an electron beam from a self-modulated laser wakefield accelerator Plasma Physics and Controlled Fusion Bremsstrahlung hard x-ray source driven by an electron beam from a self-modulated laser wakefield accelerator*.

Lemos, N., Lopes, N., Dias, J. M., & Viola, F. (2009). Design and characterization of supersonic nozzles for wide focus laser-plasma interactions. *Review of Scientific Instruments*, *80*(10). https://doi.org/10.1063/1.3233895

Lennard-Jones, J. E. (1931). *No. 240 COHESION*.

Li, S., Hafz, N. A. M., Mirzaie, M., Elsied, A. M. M., Ge, X., Liu, F., Sokollik, T., Tao, M., Chen, L., Chen, M., Sheng, Z., & Zhang, J. (2014). Generation of electron beams from a laser wakefield acceleration in pure neon gas. *Physics of Plasmas*, *21*(8). https://doi.org/10.1063/1.4892557

Li, W., Liu, J., Wang, W., Chen, Q., Zhang, H., Tian, Y., Zhang, Z., Qi, R., Wang, C., Leng, Y., Li, R., & Xu, Z. (2013). Observation of laser multiple filamentation process and multiple electron beams acceleration in a laser wakefield accelerator. *Physics of Plasmas*, *20*(11). https://doi.org/10.1063/1.4831759

Liu, C., Tripathi, V., & Eliasson, B. (2019). *High-Power Laser-Plasma Interaction*. Cambridge University Press.

Liu, Q., Ma, M., Zhang, X., Zhao, B., Lv, C., Meng, X., Wang, Z., He, C., Tian, B., Xi, X., Liu, F., & Guo, B. (2021). Application of Nomarski interference system in supersonic gas-jet target diagnosis. *AIP Advances*, *11*(1). https://doi.org/10.1063/5.0027317

Liu, Q. S., Ma, M. J., Zhao, B. Z., Zhang, X. H., Lv, C., Meng, X. H., Zhang, J., Ban, X. N., Wang, Z., Xi, X. F., Tian, B. X., He, C. Y., & Guo, B. (2021). Effect of multiple parameters on the supersonic gas-jet target characteristics for laser wakefield acceleration. *Nuclear Science and Techniques*, *32*(7). https://doi.org/10.1007/s41365-021-00910-1

Lorenz, S., Grittani, G., Chacon-Golcher, E., Lazzarini, C. M., Limpouch, J., Nawaz, F., Nevrkla, M., Vilanova, L., & Levato, T. (2019). Characterization of supersonic and subsonic gas targets for laser wakefield electron acceleration experiments. *Matter and Radiation at Extremes*, *4*(1), 015401. https://doi.org/10.1063/1.5081509

Lu, W., Tzoufras, M., Joshi, C., Tsung, F. S., Mori, W. B., Vieira, J., Fonseca, R. A., & Silva, L. O. (2007). Generating multi-GeV electron bunches using single stage laser wakefield acceleration in a 3D nonlinear regime. *Physical Review Special Topics - Accelerators and Beams*, *10*(6). https://doi.org/10.1103/PhysRevSTAB.10.061301

Maier, A. R., Delbos, N. M., Eichner, T., Hübner, L., Jalas, S., Jeppe, L., Jolly, S. W., Kirchen, M., Leroux, V., Messner, P., Schnepp, M., Trunk, M., Walker, P. A., Werle, C., & Winkler, P. (2020). Decoding Sources of Energy Variability in a Laser-Plasma Accelerator. *Physical Review X*, *10*(3). https://doi.org/10.1103/PhysRevX.10.031039

Maiman T. H. (1960). Stimulated Optical Radiation in Ruby. *Nature*, *187*, 493–494.

Maksimchuk, A., Gu, S., Flippo, K., Umstadter, D., & Bychenkov, V. Y. (2000). *Forward Ion Acceleration in Thin Films Driven by a High-Intensity Laser*.

Malka, V. (2012). Laser plasma accelerators. *Physics of Plasmas*, *19*(5). https://doi.org/10.1063/1.3695389

Malka V. (2013). Review of laser wakefield accelerators. *IPAC* .

Malka, V., Coulaud, C., Geindre, J. P., Lopez, V., Najmudin, Z., Neely, D., & Amiranoff, F. (2000). Characterization of neutral density profile in a wide range of pressure of cylindrical pulsed gas jets. *Review of Scientific Instruments*, *71*(6), 2329–2333. https://doi.org/10.1063/1.1150619

Mangles, S. P. D. (2017). *An Overview of Recent Progress in Laser Wakefield Acceleration Experiments*. https://doi.org/10.5170/CERN-2016-001.289

Mangles, S. P. D., Genoud, G., Bloom, M. S., Burza, M., Najmudin, Z., Persson, A., Svensson, K., Thomas, A. G. R., & Wahlström, C. G. (2012). Self-injection threshold in self-guided laser wakefield accelerators. *Physical Review Special Topics - Accelerators and Beams*, *15*(1). https://doi.org/10.1103/PhysRevSTAB.15.011302

Mangles, S. P. D., Murphy, C. D., Najmudin, Z., Thomas, A. G. R., Collier, J. L., Dangor, A. E., Divall, E. J., Foster, P. S., Gallacher, J. G., Hooker, C. J., Jaroszynski, D. A., Langley, A. J., Mori, W. B., Norreys, P. A., Tsung, F. S., Viskup, R., Walton, B. R., & Krushelnick, K. (2004). Monoenergetic beams of relativistic electrons from intense laser-plasma interactions. *Nature*, *431*(7008), 535–538. https://doi.org/10.1038/nature02939

Mangles, S. P. D., Thomas, A. G. R., Kaluza, M. C., Lundh, O., Lindau, F., Persson, A., Najmudin, Z., Wahlström, C. G., Murphy, C. D., Kamperidis, C., Lancaster, K. L., Divall, E., & Krushelnick, K. (2006). Effect of laser contrast ratio on electron beam stability in laser wakefield acceleration experiments. *Plasma Physics and Controlled Fusion*, *48*(12 B). https://doi.org/10.1088/0741-3335/48/12B/S08

Mangles, S. P. D., Thomas, A. G. R., Lundh, O., Lindau, F., Kaluza, M. C., Persson, A., Wahlström, C. G., Krushelnick, K., & Najmudin, Z. (2007a). On the stability of laser wakefield electron accelerators in the monoenergetic regime. *Physics of Plasmas*, *14*(5). https://doi.org/10.1063/1.2436481

Mangles, S. P. D., Thomas, A. G. R., Lundh, O., Lindau, F., Kaluza, M. C., Persson, A., Wahlström, C. G., Krushelnick, K., & Najmudin, Z. (2007b). On the stability of laser wakefield electron accelerators in the monoenergetic regime. *Physics of Plasmas*, *14*(5). https://doi.org/10.1063/1.2436481

Massimo, F., Lifschitz, F., Thaury, C., Malka, V., Lifschitz, A. F., Thaury, C., & Malka, V. (2017). *Plasma Physics and Controlled Fusion*. *59*(8), 10. https://doi.org/10.1088/1361-6587/aa717dï

McGuffey, C., Thomas, A. G. R., Schumaker, W., Matsuoka, T., Chvykov, V., Dollar, F. J., Kalintchenko, G., Yanovsky, V., Maksimchuk, A., Krushelnick, K., Bychenkov, V. Y., Glazyrin, I. V., & Karpeev, A. V. (2010). Ionization induced trapping in a laser wakefield accelerator. *Physical Review Letters*, *104*(2). https://doi.org/10.1103/PhysRevLett.104.025004

Menter, F. R. (1994). Two-equation eddy-viscosity turbulence models for engineering applications. *AIAA Journal*, *32*(8), 1598–1605. https://doi.org/10.2514/3.12149

Milonni Peter, & Eberley H.Joseph. (1988). *Laser Physics* (John Wiley & Sons, Ed.).

Mirzaie, M., Hafz, N. A. M., Li, S., Liu, F., He, F., Cheng, Y., & Zhang, J. (2015). Enhanced electron yield from laser-driven wakefield acceleration in high-Z gas jets. *Review of Scientific Instruments*, *86*(10). https://doi.org/10.1063/1.4931780

Mishra, S., Rao, B. S., Moorti, A., & Chakera, J. A. (2022). Enhanced betatron x-ray emission in a laser wakefield accelerator and wiggler due to collective oscillations of electrons. *Physical Review Accelerators and Beams*, *25*(9). https://doi.org/10.1103/PhysRevAccelBeams.25.090703

Mollica, F. (2016). *Spécialité doctorale "Physique des plasmas" présentée et soutenue publiquement par Ultra-intense laser-plasma interaction at near-critical density for ion acceleration.*

Mori, M., Kondo, K., Mizuta, Y., Kando, M., Kotaki, H., Nishiuchi, M., Kado, M., Pirozhkov, A. S., Ogura, K., Sugiyama, H., Bulanov, S. V., Tanaka, K. A., Nishimura, H., & Daido, H. (2009). Generation of stable and low-divergence 10-MeV quasimonoenergetic electron bunch using argon gas jet. *Physical Review Special Topics - Accelerators and Beams*, *12*(8). https://doi.org/10.1103/PhysRevSTAB.12.082801

Mosburg Earl R., & Lojko Matthew S. (1968). *Solution of the Able Integral Transform for a cylindrical luminous region with optical distortions at its boundary.*

Moulet, A., Grabielle, S., Cornaggia, C., Forget, N., & Oksenhendler, T. (2010). *Single-shot, high-dynamic-range measurement of sub-15 fs pulses by self-referenced spectral interferometry.*

Moulton, P. F. (1986). *Spectroscopic and laser characteristics of Ti:A1 2 0 3* (Vol. 3).

Nakanii, N., Huang, K., Kondo, K., Kiriyama, H., & Kando, M. (2023). Precise pointing control of high-energy electron beam from laser wakefield acceleration using an aperture. *Applied Physics Express*, *16*(2). https://doi.org/10.35848/1882-0786/acb892

Pak, A., Marsh, K. A., Martins, S. F., Lu, W., Mori, W. B., & Joshi, C. (2010). Injection and trapping of tunnel-ionized electrons into laser-produced wakes. *Physical Review Letters*, *104*(2). https://doi.org/10.1103/PhysRevLett.104.025003

Park, J. I., Ha, S. W., Kim, J. in, Lee, H., Lee, J., Kim, I. H., & Ye, S. J. (2016). Design and evaluation of electron beam energy degraders for breast boost irradiation. *Radiation Oncology*, *11*(1). https://doi.org/10.1186/s13014-016-0686-7

Peng, D.-Y., & Robinson, B. D. (1976). A New Two-Constant Equation of State . *Industrial & Engineering Chemistry Fundamentals*, *15*, 59–64.

Prencipe, I., Fuchs, J., Pascarelli, S., Schumacher, D. W., Stephens, R. B., Alexander, N. B., Briggs, R., Büscher, M., Cernaianu, M. O., Choukourov, A., De Marco, M., Erbe, A., Fassbender, J., Fiquet, G., Fitzsimmons, P., Gheorghiu, C., Hund, J., Huang, L. G., Harmand, M., … Cowan, T. E. (2017). Targets for high repetition rate laser facilities: Needs, challenges and perspectives. *High Power Laser Science and Engineering*, *5*. https://doi.org/10.1017/hpl.2017.18

Pukhov, A., & Meyer-ter-Vehn, J. (2002). Laser wake field acceleration: The highly non-linear broken-wave regime. *Applied Physics B: Lasers and Optics*, *74*(4–5), 355–361. https://doi.org/10.1007/s003400200795

Radon, J. (1986). On the Determination of Functions From Their Integral Values Along Certain Manifolds. In *IEEE TRANSACTIONS ON MEDICAL IMAGING* (Vol. 5, Issue 4).

Rechatin, C., Faure, J., Davoine, X., Lundh, O., Lim, J., Ben-Ismaïl, A., Burgy, F., Tafzi, A., Lifschitz, A., Lefebvre, E., & Malka, V. (2010). Characterization of the beam loading effects in a laser plasma accelerator. *New Journal of Physics*, *12*. https://doi.org/10.1088/1367-2630/12/4/045023

Rousse, A., Ta Phuoc, K., Shah, R., Fitour, R., & Albert, F. (2007). Scaling of betatron X-ray radiation. *European Physical Journal D*, *45*(2), 391–398. https://doi.org/10.1140/epjd/e2007-00249-7

Rousse, A., Ta Phuoc, K., Shah, R., Pukhov, A., Lefebvre, E., Malka, V., Kiselev, S., Burgy, F., Rousseau, J. P., Umstadter, D., & Hulin, D. (2004a). Production of a keV X-ray beam from synchrotron radiation in relativistic laser-plasma interaction. *Physical Review Letters*, *93*(13). https://doi.org/10.1103/PhysRevLett.93.135005

Rousse, A., Ta Phuoc, K., Shah, R., Pukhov, A., Lefebvre, E., Malka, V., Kiselev, S., Burgy, F., Rousseau, J. P., Umstadter, D., & Hulin, D. (2004b). Production of a keV

X-ray beam from synchrotron radiation in relativistic laser-plasma interaction. *Physical Review Letters*, *93*(13). https://doi.org/10.1103/PhysRevLett.93.135005

Rovige, L., Huijts, J., Vernier, A., Andriyash, I., Sylla, F., Tomkus, V., Girdauskas, V., Raciukaitis, G., Dudutis, J., Stankevic, V., Gecys, P., & Faure, J. (2021). *Symmetric and asymmetric shocked gas jets for laser-plasma experiments*. https://doi.org/10.1063/5.0051173

Sarri, G., Warwick, J., Schumaker, W., Poder, K., Cole, J., Doria, D., Dzelzainis, T., Krushelnick, K., Kuschel, S., Mangles, S. P. D., Najmudin, Z., Romagnani, L., M Samarin, G., Symes, D., Thomas, A. G. R., Yeung, M., & Zepf, M. (2017). Spectral and spatial characterisation of laser-driven positron beams. *Plasma Physics and Controlled Fusion*, *59*(1). https://doi.org/10.1088/0741-3335/59/1/014015

Schmid, K. (2009). *Supersonic Micro-Jets And Their Application to Few-Cycle Laser-Driven Electron Acceleration*.

Schmid, K., Buck, A., Sears, C. M. S., Mikhailova, J. M., Tautz, R., Herrmann, D., Geissler, M., Krausz, F., & Veisz, L. (2010). Density-transition based electron injector for laser driven wakefield accelerators. *Physical Review Special Topics - Accelerators and Beams*, *13*(9). https://doi.org/10.1103/PhysRevSTAB.13.091301

Schmid, K., & Veisz, L. (2012). Supersonic gas jets for laser-plasma experiments. In *Review of Scientific Instruments* (Vol. 83, Issue 5). https://doi.org/10.1063/1.4719915

Semushin, S., & Malka, V. (2001). High density gas jet nozzle design for laser target production. *Review of Scientific Instruments*, *72*(7), 2961–2965. https://doi.org/10.1063/1.1380393

Shen, X., Wang, P., Liu, J., Kobayashi, T., & Li, R. (2017). Self-referenced spectral interferometry for femtosecond pulse characterization. In *Applied Sciences (Switzerland)* (Vol. 7, Issue 4). MDPI AG. https://doi.org/10.3390/app7040407

Slenczka, A., & Toennies, J. P. (2022). *Molecules in Superfluid Helium Nanodroplets-Topics in Applied Physics* (Vol. 145). Springer. https://doi.org/10.1007/978-3-030-94896-2

Snavely, R. A., Key, M. H., Hatchett, S. P., Cowan, T. E., Roth, M., Phillips, T. W., Stoyer, M. A., Henry, E. A., Sangster, T. C., Singh, M. S., Wilks, S. C., Mackinnon, A., Offenberger, A., Pennington, D. M., Yasuike, K., Langdon, A. B., Lasinski, B. F., Johnson, J., Perry, M. D., & Campbell, E. M. (2000). *Intense High-Energy Proton Beams from Petawatt-Laser Irradiation of Solids*.

Strickland, D., & Mourou, G. (1985). *COMPRESSION OF AMPLIFIED CHIRPED OPTICAL PULSES ** (Vol. 56).

Suk, H., Barov, N., Rosenzweig, J. B., & Esarey, E. (2001a). Plasma electron trapping and acceleration in a plasma wake field using a density transition. *Physical Review Letters*, *86*(6), 1011–1014. https://doi.org/10.1103/PhysRevLett.86.1011

Suk, H., Barov, N., Rosenzweig, J. B., & Esarey, E. (2001b). Plasma electron trapping and acceleration in a plasma wake field using a density transition. *Physical Review Letters*, *86*(6), 1011–1014. https://doi.org/10.1103/PhysRevLett.86.1011

Sylla, F., Veltcheva, M., Kahaly, S., Flacco, A., & Malka, V. (2012). Development and characterization of very dense submillimetric gas jets for laser-plasma interaction. In *Review of Scientific Instruments* (Vol. 83, Issue 3). https://doi.org/10.1063/1.3697859

Tajima, T., & Dawson, J. M. (1979). *Laser Electron Accelerator* (Vol. 4, Issue 4).

Tatarakis, M., Aliaga-Rossel, R., Dangor, A. E., & Haines, M. G. (1998). Optical probing of fiber z-pinch plasmas. *Physics of Plasmas*, *5*(3), 682–691. https://doi.org/10.1063/1.872778

Tazes, I., Ong, J. F., Tesileanu, O., Tanaka, K. A., Papadogiannis, N. A., Tatarakis, M., & Dimitriou, V. (2020). Target normal sheath acceleration and laser wakefield acceleration particle-in-cell simulations performance on CPU & GPU architectures for high-power laser systems. *Plasma Physics and Controlled Fusion*, *62*(9). https://doi.org/10.1088/1361-6587/aba17a

Thaury, C., Guillaume, E., Lifschitz, A., Ta Phuoc, K., Hansson, M., Grittani, G., Gautier, J., Goddet, J. P., Tafzi, A., Lundh, O., & Malka, V. (2015). Shock assisted ionization injection in laser-plasma accelerators. *Scientific Reports*, *5*. https://doi.org/10.1038/srep16310

Thomas, A. G. R., Najmudin, Z., Mangles, S. P. D., Murphy, C. D., Dangor, A. E., Kamperidis, C., Lancaster, K. L., Mori, W. B., Norreys, P. A., Rozmus, W., & Krushelnick, K. (2007). Effect of laser-focusing conditions on propagation and monoenergetic electron production in laser-wakefield accelerators. *Physical Review Letters*, *98*(9). https://doi.org/10.1103/PhysRevLett.98.095004

Tomkus, V., Girdauskas, V., Dudutis, J., Gečys, P., Stankevič, V., Račiukaitis, G., Gallardo González, I., Guénot, D., Svensson, J. B., Persson, A., & Lundh, O. (2020). Laser wakefield accelerated electron beams and betatron radiation from multijet gas targets. *Scientific Reports*, *10*(1). https://doi.org/10.1038/s41598-020-73805-7

Tsai, H. E., Swanson, K. K., Barber, S. K., Lehe, R., Mao, H. S., Mittelberger, D. E., Steinke, S., Nakamura, K., Van Tilborg, J., Schroeder, C., Esarey, E., Geddes, C. G. R., & Leemans, W. (2018). Control of quasi-monoenergetic electron beams from laser-plasma accelerators with adjustable shock density profile. *Physics of Plasmas*, *25*(4). https://doi.org/10.1063/1.5023694

Vargas, M., Schumaker, W., He, Z. H., Zhao, Z., Behm, K., Chvykov, V., Hou, B., Krushelnick, K., Maksimchuk, A., Yanovsky, V., & Thomas, A. G. R. (2014). Improvements to laser wakefield accelerated electron beam stability, divergence, and energy spread using three-dimensional printed two-stage gas cell targets. *Applied Physics Letters*, *104*(17). https://doi.org/10.1063/1.4874981

Wilkes, J. A., Danehyt, P. M., & Nowakt, R. J. (2005). *Fluorescence Imaging Study of Transition in Underexpanded Free Jets*.

Wilkes, J. A., Glass, C. E., Danehy, P. M., & Nowak, R. J. (2006). Advanced Sensing and Optical Measurement Branch. In *AIAA Associate Fellow. § Research Scientist* (Vol. 493). AIAA Member.

Wong, K. V., & Hernandez, A. (2012). A Review of Additive Manufacturing. *ISRN Mechanical Engineering*, *2012*, 1–10. https://doi.org/10.5402/2012/208760

Wood, J. C., Chapman, D. J., Poder, K., Lopes, N. C., Rutherford, M. E., White, T. G., Albert, F., Behm, K. T., Booth, N., Bryant, J. S. J., Foster, P. S., Glenzer, S., Hill, E., Krushelnick, K., Najmudin, Z., Pollock, B. B., Rose, S., Schumaker, W., Scott, R. H. H., … Mangles, S. P. D. (2018). Ultrafast Imaging of Laser Driven Shock Waves using Betatron X-rays from a Laser Wakefield Accelerator. *Scientific Reports*, *8*(1). https://doi.org/10.1038/s41598-018-29347-0

Wood, J. C., Poder, K., Lopes, N. C., Cole, J. M., Alatabi, S., Kamperidis, C., Mangles, S. P. D., Sahai, A., Najmudin, Z., Kononenko, O., Palmer, C. A. J., Foster, P., Rusby, D., Symes, D. R., Warwick, J. R., & Sarri, G. (2017). *Enhanced Betatron Radiation from a Laser Wakefield Accelerator in a Long Focal Length Geometry*.

Zhou, O., Tsai, H. E., Ostermayr, T. M., Fan-Chiang, L., van Tilborg, J., Schroeder, C. B., Esarey, E., & Geddes, C. G. R. (2021). Effect of nozzle curvature on supersonic gas jets used in laser-plasma acceleration. *Physics of Plasmas*, *28*(9). https://doi.org/10.1063/5.0058963

Zucker, D. R., & Biblarz, O. (2002). *Fundamentals of gas dynamics* (I. John Wiley & Sons, Ed.; Second).